Imperial College London
Department of Materials

Layered Ruddlesden-Popper $La_{n+1}Ni_nO_{3n+1}$ (n = 1, 2 and 3) Epitaxial Films Grown by Pulsed Laser Deposition for Potential Fuel Cell Applications

Kuan-Ting Wu

2014

Supervised by Dr. Stephen Skinner and Prof. John Kilner

Submitted in part fulfilment of the requirements for the degree of
Doctor of Philosophy in Materials of Imperial College London
and the Diploma of Imperial College London

Declaration

I hereby declare that this thesis is a presentation of my original research work. For other material which is not my own work has been properly acknowledged.

— Kuan-Ting Wu

'The copyright of this thesis rests with the author and is made available under a Creative Commons Attribution Non-Commercial No Derivatives licence. Researchers are free to copy, distribute or transmit the thesis on the condition that they attribute it, that they do not use it for commercial purposes and that they do not alter, transform or build upon it. For any reuse or redistribution, researchers must make clear to others the licence terms of this work'

"Nobody ever figures out what life is all about, and it doesn't matter. Explore the world. Nearly everything is really interesting if you go into it deeply enough."

— Richard P. Feynman

Acknowledgements

I am very grateful to many people that have contributed either directly or indirectly to help me with my PhD research and this thesis during the past few years. First of all, my deepest respect and gratitude goes to my supervisor, Dr. Stephen Skinner, for all his support, professional mentorship and expert guidance throughout my PhD study. His cheerful enthusiasm and valuable advices are very crucial to me for getting to where I am now and eventually finishing my PhD. I would like express my appreciation for his patience and understanding when things were not going smoothly. I would also like thank him for giving me the opportunity to attend conferences and workshops. My gratitude also goes to my co-supervisor, Prof. John Kilner for his valuable guidance and advices on my research as well as on my career.

I would also like to acknowledge all the research officers and colleagues at Imperial College, who have given me great assistance for this work: Dr. Peter Petrov for managing the thin-film laboratory and allowing me successfully grow such complex, delicate materials, and Dr. Bin Zhou for training and helping me on the thin-film equipment, and all useful discussion as well as great assistance when the thin-film system were going wrong. In addition, I am deeply grateful to Mr. Richard Sweeney for training me to use XRD equipment, he is very understanding and allowed me to work long hours on the machine. I would like to express my sincere appreciation to Dr. Burriel Monica, Dr. Helena Téllez, Mr. Richard Charter, Dr. John Druce for SIMS and LEIS analyses, and all the professional assistance, advice and useful discussion. I would also like to thank Dr. Andrea Cavallaro for his absolutely expert assistance in XRD and thin-film deposition and useful discussion. My sincere appreciation also goes to Dr. Andrey V Berenov for the electrical conductivity measurements. The following people are appreciated for their help with the measurements and technical discussions: Dr. Mahmoud Ardakani and Mrs. Cati

Ware for helps with SEM, FIB, TEM. Dr. Richard Thorogate (University College London) for AFM measurements. I would also like to thank my collaborators: Dr. Y. Fan and Professor D. McComb at Department of Materials Science and Engineering in The Ohio State University, USA for HRTEM analysis.

I am also very grateful to my fantastic members (including former and current) in the Fuel Cell group: my buddies, Dr. John Druce, Dr. Téllez Helena, Lydia Fawcett, George Harrington for all their kindly extensive support. Also, others in particular, Ainara Aguadero, Ryan Bayliss, Stuart Cook, Samuel Taub, Matthew Sharp, Florent Tonus, Russell Woolley, Zhangwei Chen, Cassandra Harris, Mabel Lew, Cheng Li, Mathew Niania, etc. as well as other people in the office: Florian Le Goupil and Frederic Aguesse for their assistance and friendship.

In addition, many thanks are also owed to the great members of Queens Court 31 & 64 family and New 'Our Family': in particular, of course my greatest flatmate Rodger for his kind support through the past few years, Jing, Shirley, Jack, Stanley, Zoe, Peggy, Vivian, Alfie, Po-Yu, Jason, Doris, Betty, Chia-Chen, etc

To My Family

My sincerest and deepest gratitude also goes to those whose influence may not be so evident but who nevertheless provided the educational and emotional foundation, without which, this dissertation would have never been possible: My Parents, My Brother.

Kuan-Ting Wu
March 2014 London

Abstract

Layered Ruddlesden-Popper (RP) type $La_{n+1}Ni_nO_{3n+1}$ (n = 1, 2 and 3) oxides have recently been suggested as candidates for solid oxide fuel cell (SOFC) cathodes. However, the transport properties of the higher order (n = 2 and 3) phases have not been well-understood. The aim of this work is to achieve well-defined epitaxial $La_3Ni_2O_{7-\delta}$ and $La_4Ni_3O_{10-\delta}$ films deposited by the pulsed laser deposition (PLD) technique in order to fundamentally investigate their intrinsic anisotropic properties for SOFC applications.

This research involved PLD target synthesis and PLD deposition for these RP materials. The obtained films were evaluated through crystallographic, compositional, surface morphological and microstructural characterisation. Their electrical, oxygen diffusion and surface exchange properties were characterised by 4-point DC van der Pauw and the isotopic exchange depth profile (IEDP) with secondary ion mass spectrometry (SIMS) method. Finally, the surface and interface information were also obtained via SIMS and low energy ion scattering (LEIS) techniques.

An effect of target degradation during deposition was found to have significant influence on the microstructural and compositional variation with increasing film thickness. Successful epitaxial growth of the higher order phases (n = 2 and 3) of lanthanum nickelate have been demonstrated by PLD for the first time. The total planar electrical conductivity of these higher order RP epitaxial films exhibits a more promising conductivity value than $La_2NiO_{4+\delta}$. These dense higher order RP epitaxial films enabled the first information about the oxygen diffusion and surface exchange properties along the c-axis to be obtained. Also, an outermost surface structure of LaO-termination, followed by a Ni-enrichment in the sub-surface region for these RP materials was found by LEIS analysis. These studies provide useful information to help the further development of these materials and related RP-phases for the potential SOFC applications in the future.

Contents

Acknowledgement ……..…….....**i**

Abstract ……...……..……...…….…...**iii**

Contents ……..……....……...……**iv**

List of Figures ……...…...…….……**ix**

List of Tables ……...…….....……...…..**xxii**

Chapter 1 Introduction..... **1**

1.1 Energy Crisis and Environmental Impact 1

1.2 Fuel Cells..... 2

1.3 Solid Oxide Fuel Cells (SOFCs)..... 3

1.4 Research Motivation and Aim 10

1.5 Outline of Thesis..... 11

Chapter 2 Literature Review..... **13**

2.1 Architecture of Layered Ruddlesden-Popper (RP) Type Materials 13

2.2 Structure and Synthesis of RP $La_{n+1}Ni_nO_{3n+1}$ (n = 1, 2 and 3) Phases 15

2.3 Current Development of RP Phases in SOFC Application 18

2.4 Current Development of RP Thin-Films in SOFC Application..... 25

2.5 Summary 34

Chapter 3 Experiments and Characterisation Techniques **35**

3.1 Pulsed Laser Deposition (PLD) 35
3.1.1 Background of PLD 35
3.1.2 Thin-Film Growth 39
3.1.3 General Deposition Procedure 41
3.2 Synthesis of PLD Targets 42
3.3 Material Characterisation 44
3.3.1 Density Measurement of PLD Targets 44
3.3.2 Inductively-Coupled Plasma Atomic Emission Spectroscopy (ICP-AES) ... 45
3.3.3 X-ray Diffraction (XRD) 47
3.3.4 Film Thickness Measurement 52
3.3.5 Scanning Electron Microscope with Energy Dispersive X-ray Spectrometer (SEM-EDX) 52
3.3.6 Atomic Force Microscopy (AFM) 54
3.3.7 Transmission Electron Microscopy (TEM) 56
3.4 Transport Property Characterisation 58
3.4.1 Electrical Conductivity Measurements 58
3.4.2 Oxygen Transport Measurements 61
3.5 Surface and Interface Characterisation 64
3.5.1 Crater Depth Measurement 66
Chapter 4 Requirements of PLD Targets and Substrate 68
4.1 PLD Targets 68
4.1.1 Phase, Composition and Density Identification 68
4.1.2 Target Degradation and Particulate Formation 72
4.2 Substrate Requirements 78

4.3 Summary 83

Chapter 5 Growth and Characterisation of $La_{n+1}Ni_nO_{3n+1}$ (n = 1)..... 84

5.1 Optimisation of $La_2NiO_{4+\delta}$ Phase Growth..... 84

5.2 Charaterisation of $La_2NiO_{4+\delta}$ Epitaxial Films on STO and NGO..... 98

5.2.1 Crystallographic Analysis and Film Quality 98

5.2.2 Limitation of Identifying Film Crystal Structures 101

5.2.3 Film Orientation Characterisation..... 102

5.2.4 Out-of-Plane Parameter Characterisation..... 103

5.3 Electrical Conductivity Characterisation 105

5.4 Summary 109

Chapter 6 Growth and Characterisation of $La_{n+1}Ni_nO_{3n+1}$ (n = 2 and 3)..... 111

6.1 Optimisation of $La_3Ni_2O_{7-\delta}$ and $La_4Ni_3O_{10-\delta}$ Phase Film Growth 112

6.2 Charaterisation of $La_3Ni_2O_{7-\delta}$ and $La_4Ni_3O_{10-\delta}$ Epitaxial Films on NGO 126

6.2.1 Crystallographic Analysis and Film Quality 126

6.2.2 Film Orientation Characterisation..... 129

6.2.3 Out-of-Plane Parameter Characterisation..... 130

6.3 Influences on Microstructure..... 132

6.3.1 Effect of Film Thickness 133

6.3.1.1 Crystallographic Characterisation 134

6.3.1.2 Lattice Parameter and Strain Characterisation..... 138

6.3.1.3 Compositional Characterisation 146

6.3.1.4 Surface Morphological Characterisation 148

6.3.1.5 Microstructural Analysis..... 151

6.3.2 Effects of Post-annealing 155

6.4 Thermal Stability 160

6.5 Summary 162

Chapter 7 Transport Property of $La_{n+1}Ni_nO_{3n+1}$ (n = 2 and 3) **164**

7.1 Electrical Conductivity Analysis 165

7.1.1 Influence of Film Thickness 165

7.1.2 Cycling Measurement 174

7.1.3 Comparative Study 180

7.2 Oxygen Exchange and Transport Analysis 183

7.3 Summary 192

Chapter 8 Surface and Interface Characterisation of La-Ni-O Films **195**

8.1 Compositional Depth Profiling by SIMS 196

8.2 Surface Analysis by LEIS 200

8.2.1 Surface Analysis of As-Deposited $La_3Ni_2O_{7-\delta}$ and $La_4Ni_3O_{10-\delta}$ Films 201

8.2.2 Surface Analysis of After-Exchanged $La_3Ni_2O_{7-\delta}$ and $La_4Ni_3O_{10-\delta}$ Films ... 206

8.2.3 Surface Analysis of As-Deposited and Annealed $La_2NiO_{4+\delta}$ Films 212

8.3 Discussion 215

8.4 Summary 217

Chapter 9 Conclusion and Future Work **219**

9.1 Conclusion 219

9.2 Future Work 223

Appendices **226**

Bibliography **227**

List of Publications **244**

List of Figures

Figure 1.1 Five main types of fuel cells and their working temperatures and reaction mechanisms [9]..... 3

Figure 1.2 Schematic diagram for transport and reaction mechanism in a solid oxide fuel cell (SOFC) (adapted from [14]). 5

Figure 1.3 Illustrated comparison of (a) TPB and (b) MIEC where active areas (highlighted in red colour) for oxygen reduction reaction takes place. (adapted from [20])..... 9

Figure 2.1 Schematic crystal structures of the n = 1, 2 and 3 members of the Ruddlesden–Popper (RP) type $A_{n+1}B_nO_{3n+1}$ are shown. The denotation of n represents the number of stacked octahedral layers separated by a rock salt AO layer. BO_6 octahedra and A atoms are shown schematically. The unit cell of each structure is presented by a black rectangle. 14

Figure 2.2 Preparation of the four different $La_3Ni_2O_{7-\delta}$ phases with a wide range of oxygen stoichiometry δ = 0, 0.08, 0.16 and 0.65 (adapted from [51]). 17

Figure 2.3 High-temperature X-ray diffraction patterns of $La_3Ni_2O_{6.95}$ (a) and $La_4Ni_3O_{9.78}$ (b), showing the phase transition from orthorhombic to tetragonal symmetry [33]. 17

Figure 2.4 Schematic illustration of the $La_2NiO_{4+\delta}$ structure showing the vacancy and interstitialcy ionic transport directions. $LaNiO_3$ perovskite and LaO rock-salt layers are indicated. (adapted from [94])..... 19

Figure 2.5 oxygen ion diffusion along interstitialcy pathways in K_2NiF_4 phase. (a) represents the oxygen nuclear density distribution through analysing experimental neutron scattering data by maximum-entropy method at 1016°C for $(Pr_{0.9}La_{0.1})_2(Ni_{0.74}Cu_{0.21}Ga_{0.05})O_{4+\delta}$, reported by Yashima *et al.* [99]. O1 is equatorial oxygen, O2 is the apical oxygen, and O3 is the interstitial site. The O1 and O2 are present in NiO_6 octahedra whilst the O3 is in PrO rock-salt layer; (b) shows the theoretical simulation through molecular dynamics method at 827°C for $Pr_2NiO_{4+\delta}$ reported by Parfitt *et al.* [100]. O ions in red, Ni ions in blue and NiO_6 in green. 21

Figure 2.6 Comparison of θ/2θ X-ray diffraction patterns of $La_2NiO_{4.15}$, $La_3Ni_2O_{6.95}$ and $La_4Ni_3O_{9.78}$ bulk samples after annealing at 900°C for 2 weeks in air. Impurity phase formation for $La_2NiO_{4.15}$ after the heat treatment [33]. 22

Figure 2.7 (a) electrical conductivity (σ) and (b) ASR as a function of temperature for $La_2NiO_{4.15}$, $La_3Ni_2O_{6.95}$ and $La_4Ni_3O_{9.78}$ bulk samples..... 23

Figure 2.8 Total electrical conductivity of the c-axis oriented $La_2NiO_{4+\delta}$ epitaxial films deposited on STO and NGO substrates as a function of temperature and

different thickness in O_2, plotted together with literature data for single crystal and bulk ceramic measured in air. [40] 26
Figure 2.9 Schematic illustration of sample configuration for (a) transverse and (b) longitudinal oxygen tracer transport measurements (adapted from [41]) 28
Figure 2.10 Anisotropy of diffusion coefficients for $La_2NiO_{4+\delta}$ epitaxial films grown on STO and NGO in comparison with the literature data for $La_2NiO_{4+\delta}$ single crystal and dense ceramics [41]. 28
Figure 2.11 Anisotropy of surface exchange coefficients for $La_2NiO_{4+\delta}$ epitaxial films grown on STO and NGO in comparison with the literature data for $La_2NiO_{4+\delta}$ single crystal and dense ceramics [41]. 29
Figure 2.12 High temperature planar resistivity of the epitaxial films deposited with different La/Ni composition on NGO substrates. The average n value corresponding to each curve is labelled aside. The resistivity progressively varies with increasing n value and changes from semiconducting to metallic behaviour [91]..... 30
Figure 2.13 Schematic illustration and 3D AFM images of (a) $Nd_2NiO_{4+\delta}$(100)//YSZ(110) (a) and (b) $Nd_2NiO_{4+\delta}$(110)//YSZ(100) hetero-epitaxial films [115]. 32
Figure 2.14 SIMS image of ^{18}O intensity at the surface of $La_{1.5}Sr_{0.5}CoO_4/La_{0.6}Sr_{0.4}CoO_3$/CGO, after the diffusion annealing at 773 K for 180 s in 0.2 bar $^{18}O_2$ gas [117]. 34
Figure 3.1 Schematic illustration of PLD system setup (adapted from [129]) 37
Figure 3.2 Schematic illustration of PLA process: (a) laser pulse is initially absorbed, melting and vaporisation (shaded area indicates melted materials, and the short arrows represent motion of the solid-liquid interface), (b) vaporisation continues, the melt front propagates into the solid target, and laser plume starts to form, (c) absorption of incident beam through the expanding plum leads to plasma formation, (d) the melt front recedes after the laser pulse, resulting re-solidification [130]. 38
Figure 3.3 Schematic representation of the three typical thin-film growth modes: (a) is layer-by-layer growth mode (Frank-van der Merwe), (b) is layer-island growth mode (Stranski-Krastanov), and (c) island growth mode (Volmer-Weber) (adapted from [140]). 40
Figure 3.4 (a) The flow chart of the synthesis procedure and (b) the table of the sintering conditions for $La_2NiO_{4+\delta}$ (n = 1), (b) $La_3Ni_2O_{7-\delta}$ (n = 2) and (c) $La_4Ni_3O_{10-\delta}$ (n = 3) target preparation 44
Figure 3.5 An illustrated diagram of Bragg's Law for X-ray diffraction (adapted from [145]) 48

Figure 3.6 Schematic diagram showing the X'pert MRD system, indicating the 2θ, ω, φ and Ψ scan axes (adapted from [146])..... 49
Figure 3.7 Schematic illustration of the operation and setup of the AFM (adapted from [153]). 56
Figure 3.8 [110] viewing direction of layered RP-phases (space group: Fmmm) for (a) La_2NiO_4 (n = 1), $La_3Ni_2O_7$ (n = 2), and $La_4Ni_3O_{10}$ (n = 3)..... 58
Figure 3.9 Schematic illustration of two configurations of electrode contacts for 4-point DC van der Pauw measurements. I represents current; V represents voltage..... 60
Figure 3.10 Schematic illustration of the SIMS process (adapted from [167] 63
Figure 3.11 an illustrated diagram of LEIS process: incident primary ions (gray colour) collide with surface atoms (green, blue and red) and are scattered back at an angle of θ. The energy of backscattered ions is related to a function of the mass of incident primary ions, surface atoms and the collision angles. The experimental LEIS spectrum is also schematically shown. The red peak represents the energy of a heavy atom whereas the green one represents that of a light atom after collisions. 66
Figure 3.12 Schematic Diagram of the white light optical interferometer (adapted from [173])..... 67
Figure 4.1 θ/2θ X-ray diffraction patterns of (a) $La_2NiO_{4+\delta}$ (n = 1), (b) $La_3Ni_2O_{7-\delta}$ (n = 2) and (c) $La_4Ni_3O_{10-\delta}$ (n = 3) targets show the near pure-phase of these materials with a minority of NiO phase indicated by the symbol (▽)..... 69
Figure 4.2 SEM secondary electron (SE) images of surface morphology of $La_3Ni_2O_{7-\delta}$ (a) and $La_4Ni_3O_{10-\delta}$ (b) targets prepared by the modified Pechini nitrate-citrate method. Scale marker: 100 μm..... 71
Figure 4.3 Photographs of $La_4Ni_3O_{10-\delta}$ target (13 mm) on a target holder after a pulsed laser ablation process with 3000 pulses of ~0.6 J/cm^2 and before ablation process (upper right) 73
Figure 4.4 Normalised XRD patterns of (a) the original (before PLD) $La_3Ni_2O_{7-\delta}$ target, (b) the target after the use of PLA, and (c) the pellet after grinding the unwanted top-surface. (Inset: zoom of the range of 22-35° to show the impurity phases). ICSD code: 91141 ($La_3Ni_2O_7$), 158830 (La_2NiO_4); JCPDF code: 00-005-0602 (La_2O_3), 00-044-1159 (NiO). 75
Figure 4.5 Normalised XRD patterns of (a) the original (before PLD) $La_4Ni_3O_{10-\delta}$ target, (b) the target after the use of PLA, and (c) the pellet after grinding the unwanted top-surface. (Inset: zoom of the range of 22-35° to show the impurity phases). ICSD code: 80279 ($La_4Ni_3O_{10}$), 91141 ($La_3Ni_2O_7$), 158830 (La_2NiO_4); JCPDF code: 00-005-0602 (La_2O_3), 00-044-1159 (NiO). 75
Figure 4.6 La-Ni-O phase diagram (temperature vs composition) in air (pO_2 = ~0.2

atm). The theoretical positions of the stoichiometric La_2NiO_4, $La_3Ni_2O_7$ and $La_4Ni_3O_{10}$ phases are labeled in blue, green and pink colour, respectively (adapted from [78]) 76

Figure 4.7 SEM images of a $La_4Ni_3O_{10-\delta}$ thin-film to show particulate formation after the PLD. A part of the sample nearly directly exposed the centre of the plasma plume and a reduced evolution of particulate formation can be seen from area a to c, where the microstructure images represent as (a), (b) and (c), respectively. Scale marker: 200 μm (upper); 1 μm (lower three). 78

Figure 4.8 A schematic diagram of the epitaxial films oriented under tensile and compressive strain on STO and NGO substrates. 80

Figure 4.9 A schematic diagram of the basal arrangement of film-substrate orientation with the relevant lattice parameters a_p = 3.8606, 3.8331 and 3.8467 Å for $La_2NiO_{4.25}$, $La_3Ni_2O_7$ and $La_4Ni_3O_{10}$, respectively. Purple and yellow squares represent the basal planes of STO (001) and NGO (110) unit cells, respectively; blue, green and pink squares represent those of lanthanum nickelates. 81

Figure 4.10 Schematic representation of the orientation of the $La_2NiO_{4.25}$, $La_3Ni_2O_7$ and $La_4Ni_3O_{10}$ thin-films in relation to the NGO substrate normal direction [110], which corresponds to out of plane direction [00L] of these films. 81

Figure 5.1 θ/2θ XRD patterns of $La_2NiO_{4+\delta}$ films grown on STO (001) single crystal substrate by 750°C, 5000 laser pulses, and power density of 0.8 J/cm^2 with different oxygen pressure 400 mTorr (a), 250 mTorr (b), 100 mTorr (c), and 30 mTorr (d). The STO substrate peaks are indicated by solid circles (*), the c-axis oriented $La_2NiO_{4+\delta}$ film peaks are indexed by (00L), and the extra orientations of (H00) are designated by arrows. Al peaks originate from the aluminium sample cradle of XRD instrument and K_β peaks correspond to XRD background. 86

Figure 5.2 Schematic representation of the two orientations of the $La_2NiO_{4+\delta}$ thin-films in relation to the STO substrate normal direction [001], which corresponds to out of plane direction of these films..... 86

Figure 5.3 θ/2θ XRD patterns of $La_2NiO_{4+\delta}$ films grown on STO (001) single crystal substrate by 250 mTorr, 5000 laser pulses and power density of 0.8 J/cm^2 with various deposition temperatures (a) - (d). The STO substrate peaks are indicated by solid circles (*), the c-axis oriented $La_2NiO_{4+\delta}$ film peaks are indexed by (00L), and the extra orientations of (H00) are designated by arrows. Al peaks originate from the aluminium sample cradle of XRD instrument and K_β peaks correspond to XRD background. 88

Figure 5.4 SEM morphological images of $La_2NiO_{4+\delta}$ thin-films deposited on STO by 250 mTorr, 5000 laser pulses and power density of 0.8 J/cm^2 with various deposition temperatures of 780°C (a), 750°C (b), 700°C (c) and 650°C. Their

scale markers are 300 nm, 200 nm, 100 nm and 100 nm, respectively. 89

Figure 5.5 θ/2θ XRD patterns of $La_2NiO_{4+\delta}$ films grown on STO (001) single crystal substrate by 780°C, 250 mTorr, and power density of 0.8 J/cm^2 with 3000 (a) and 5000 (d) laser pulses. The STO substrate peaks are indicated by solid circles (*), the c-axis oriented La_2NiO_4 film peaks are indexed by (00L), and the extra orientations of (H00) are designated by arrows. Al peaks originate from the aluminium sample cradle of XRD instrument and K_β peaks correspond to XRD background. 90

Figure 5.6 SEM morphological images of $La_2NiO_{4+\delta}$ thin-films deposited on STO by 780°C, 250 mTorr and power density of 0.8 J/cm^2 with (a) 3000 and (b) 5000 laser pulses. Their scale markers are 300 nm and 200 nm, respectively. 90

Figure 5.7 θ/2θ XRD patterns of $La_2NiO_{4+\delta}$ films grown on STO (001) single crystal substrate by 780°C, 250 mTorr,, and 3000 laser pulses with various laser fluences of 0.6 J/cm^2 (a), 0.8 J/cm^2 (b) and 1.0 J/cm^2 (c). The STO substrate peaks are indicated by solid circles (*), the c-axis oriented $La_2NiO_{4+\delta}$ film peaks are indexed by (00L), and the extra orientations of (H00) are designated by arrows. 92

Figure 5.8 XRD patterns of $La_2NiO_{4+\delta}$ films grown on STO (001) single crystal substrate as a function of laser pulses of 5000 (a), 3000 (b) and 1000 (c). The STO substrate peaks are indicated by solid circles (*) and all (00L) reflections shown are attributed to the c-axis oriented $La_2NiO_{4+\delta}$ films. 93

Figure 5.9 SEM morphological images of $La_2NiO_{4+\delta}$ thin-films deposited on STO as a function of laser pulses of 5000 (a), 3000 (b) and 1000 (c). Their scale markers are 100 nm, 200 nm and 100 nm, respectively. 94

Figure 5.10 AFM images of $La_2NiO_{4+\delta}$ thin-film deposited on STO as a function of laser pulses (or thickness). (a) - (c) show 2D and 3D images of 1000 - 5000 pulses with image size: 1 μm × 1 μm, Z depth scale: (a) 13.2 nm, (b) 15.0 nm and (c) 20.4 nm from dark brown to white. (g) - (i) demonstrate the image distribution histograms of height (Z depth scale) data of each pixel plotted with number of events. The avg, height and RMS values are presented on the bottom of the image group. 96

Figure 5.11 θ/2θ XRD patterns of c-axis oriented $La_2NiO_{4-\delta}$ phases grown on STO (001) at 780°C (a) and on NGO (110) single crystal substrates at 750°C (b). The $SrTiO_3$ and $NdGaO_3$ substrate peaks are indicated by star (*) and solid circles (•), respectively. The c-axis oriented film peaks are indexed by (00L). Film thickness determined by Dektak 150 Surface Profiler is shown as an insert in top right of each pattern. 99

Figure 5.12 X-ray rocking curves of the c-axis oriented $La_2NiO_{4+\delta}$ (n = 1) films: (a) (004) reflection of 82 nm thick $La_2NiO_{4+\delta}$ film on $SrTiO_3$ and (b) (004) reflection

of 128 nm thick $La_2NiO_{4+\delta}$ film on $NdGaO_3$. 100

Figure 5.13 AFM images of the c-axis oriented $La_2NiO_{4+\delta}$ (n = 1) films (a) 82 nm thick $La_2NiO_{4+\delta}$ film on $SrTiO_3$, (b) 128 nm thick $La_2NiO_{4+\delta}$ film on $NdGaO_3$. Image size: 1 μm × 1 μm, depth scale: 20 nm from dark brown to white. 101

Figure 5.14 Phi(φ)-scan patterns for the c-axis oriented $La_2NiO_{4+\delta}$ (n = 1) films: {111} reflections registered at 2θ=24.093°, Ψ=73.09° for $La_2NiO_{4+\delta}$ films on $SrTiO_3$ and $NdGaO_3$ substrates shown in (a) and (b) respectively. 103

Figure 5.15 c-axis lattice parameter as function of (00L) planes for $La_2NiO_{4+\delta}$ films grown on STO (001) and NGO (110). The $La_2NiO_{4+\delta}$ film on STO is represented by solid circle (●); the film on NGO is represented by solid triangle (▲) with five units of the standard deviation errors from each individual fitted (00L) peak. The measured averages of c-axis parameters are labelled in the diagram. The analyses were based on the compared relationship of measured c-axis lattice parameters of each (00L) plane from the films with the values for the selected standard crystal structures of bulk materials (Orthorhombic [Fmmm]; Tetragonal [I4/mmm]) [189, 191]. The results show the c-axis parameters are influenced by strain from different substrates. 105

Figure 5.16 Total electrical conductivity of the c-axis oriented $La_2NiO_{4+\delta}$ epitaxial films deposited on STO and NGO substrates as a function of temperature from RT to 700°C in air (a), and Arrhenius plot of the electrical conductivity (b). 108

Figure 5.17 Total electrical conductivity of the c-axis oriented $La_2NiO_{4+\delta}$ epitaxial films deposited on STO and NGO substrates as a function of temperature in comparison with literature data from polycrystalline bulk [33], single crystal [111], and thin-films deposited by MOCVD [39]. 109

Figure 6.1 θ/2θ XRD patterns of $La_3Ni_2O_{7-\delta}$ films grown on NGO (110) single crystal substrates at 250 mTorr O_2, 3000 laser pulses and power density of 0.5 J/cm^2 with various deposition temperatures (a) - (c). The NGO substrate peaks are indicated by solid circles (•), the c-axis oriented $La_3Ni_2O_{7+\delta}$ film peaks are indexed by (00L) and some extra undefined peaks are indexed by stars (*)..... 113

Figure 6.2 AFM images of $La_3Ni_2O_{7-\delta}$ thin-film deposited on NGO as a function of deposition temperature. (a) - (c) show the images of films deposited at nominal temperatures of 780 – 700°C with an image sizes: 5 μm × 5 μm. Z depth scales are indicated from dark brown to white. The avg. RMS values are presented on the bottom of the images. 114

Figure 6.3 θ/2θ XRD patterns of $La_4Ni_3O_{10-\delta}$ films grown on NGO (110) single crystal substrate at 250 mTorr O_2, 3000 laser pulses and power density of 0.5 J/cm^2 with various deposition temperatures (a) - (c). The NGO substrate peaks are indicated by solid circles (•), the c-axis oriented $La_4Ni_3O_{10+\delta}$ film peaks are indexed by

(00L). The stars (*) represents the $La_3Ni_2O_{7-\delta}$ phase. 115

Figure 6.4 AFM images of $La_4Ni_3O_{10-\delta}$ thin-film deposited on NGO as a function of deposition temperature. (a) - (c) show the images of the films deposited at 750, 700 and 650°C with an image sizes: 5 μm × 5 μm. Z depth scales are indicated from dark brown to white. The avg. RMS values are presented on the bottom of the images. 116

Figure 6.5 θ/2θ XRD patterns of $La_3Ni_2O_{7-\delta}$ films grown on NGO (110) single crystal substrate in 250 mTorr O_2, 3000 laser pulses and deposition temperature of 750°C with various laser fluence (a) - (c). The NGO substrate peaks are indicated by solid circles (•), the c-axis oriented $La_3Ni_2O_{7-\delta}$ film peaks are indexed by (00L). .. 119

Figure 6.6 θ/2θ XRD patterns of $La_4Ni_3O_{10-\delta}$ films grown on NGO (110) single crystal substrate in 250 mTorr O_2, 3000 laser pulses and deposition temperature of 700°C with various laser fluence (a) - (c). The NGO substrate peaks are indicated by solid circles (•), the c-axis oriented $La_4Ni_3O_{10-\delta}$ film peaks are indexed by (00L). The stars (*) represents the $La_3Ni_2O_{7-\delta}$ phase. 120

Figure 6.7 θ/2θ XRD patterns of $La_4Ni_3O_{10-\delta}$ films grown on NGO (110) single crystal substrate in 250 mTorr O_2, 3000 laser pulses, deposition temperatures of 700°C, and laser fluence of 0.6 J/cm^2 with various laser repetition rate of 1, 3, 5 and 8 Hz. The NGO substrate peaks are indicated by solid circles (•), the c-axis oriented $La_4Ni_3O_{10-\delta}$ film peaks are indexed by (00L). Inset: the FWHM values as a function of laser repetition rate for the 0014 reflection. 122

Figure 6.8 A SEM image shows inhomogeneous surface morphology (indexed by black arrow) of $La_4Ni_3O_{10-\delta}$ deposited with the laser frequency of 1 Hz. Scale marker: 100 μm. 123

Figure 6.9 AFM images of $La_4Ni_3O_{10-\delta}$ thin-film deposited on NGO as a function of laser repetition rate of 1 Hz (a), 3 Hz (b), 5 Hz (c) and 8 Hz (d) with the image size: 1 μm × 1 μm. Z depth scales are indicated from dark brown to white. The avg, RMS values are presented on the top of the images. 124

Figure 6.10 θ/2θ XRD patterns of c-axis oriented $La_3Ni_2O_{7-\delta}$ phase at 750°C (a) and $La_4Ni_3O_{10-\delta}$ phases at 700°C (b) grown on NGO (110). The $NdGaO_3$ substrate peaks are indicated by solid circles (•). The c-axis oriented film peaks are indexed by (00L). Film thickness determined by Dektak 150 Surface Profiler is shown as an insert in top right of each pattern. 127

Figure 6.11 X-ray rocking curves: (a) (0010) reflection of 47 nm thick $La_3Ni_2O_{7-\delta}$ film on $NdGaO_3$; (b) (0014) reflection of 51 nm thick $La_4Ni_3O_{10-\delta}$ film on $NdGaO_3$..... 128

Figure 6.12 AFM images: (a) 47 nm thick $La_3Ni_2O_{7-\delta}$ film on $NdGaO_3$ and (b) 51 nm thick $La_4Ni_3O_{10-\delta}$ film on $NdGaO_3$. Image size: 1 μm × 1 μm, depth scale: both are 2 nm from dark brown to white. 128

Figure 6.13 Cross-section HAADF-STEM image of c-axis oriented $La_4Ni_3O_{10-\delta}$ film grown on NGO (110) substrate. Pt and Au cap is for the protection of the film under focused ion beam (FIB) preparation process. 129

Figure 6.14 Phi(φ)-scan patterns of in-plane diffraction for the c-axis oriented $La_{n+1}Ni_nO_{3n+1}$ (n = 2 and 3) films: (a) {206} reflections registered at 2θ=42.702°, Ψ=51.74° for $La_3Ni_2O_{7-\delta}$ film on $NdGaO_3$ substrate, and (b) {208} reflections registered at 2θ=42.702°, Ψ=51.74° for $La_4Ni_3O_{10-\delta}$ film on $NdGaO_3$ substrate..... 130

Figure 6.15 c-axis lattice parameter as function of (00L) planes for (a) $La_3Ni_2O_{7-\delta}$ and (b) $La_4Ni_3O_{10-\delta}$ films grown on NGO (110). Four clear peaks from each compound were refined by the Lorentz method. All errors are within the data points to a level of five standard deviations. The reference values as standard correspond to solid and dashed lines in the diagrams. [47, 208, 209] The measured averages of c-axis parameters are labelled by green and pink solid lines. 131

Figure 6.16 θ/2θ XRD scans of $La_2NiO_{4+\delta}$ (n = 1), $La_3Ni_2O_{7-\delta}$ (n = 2) and $La_4Ni_3O_{10-\delta}$ (n = 3) films deposited on NGO (110). The $NdGaO_3$ substrate peaks are indicated by solid circles (•). Inset: zoom of the range of 20-60°, labelled as the dashed square in the whole range pattern. The small arrows indicate the shift direction of the main peaks of each phase varies with n. 132

Figure 6.17 Thickness of (a) $La_3Ni_2O_{7-\delta}$ and (b) $La_4Ni_3O_{10-\delta}$ films grown on NGO (110) as a function of the number of laser pulses and their average deposition rates are 0.157±0.006 Å and 0.162±0.008 Å, respectively. The film thickness was determined using Dektak 150 Surface Profiler. 133

Figure 6.18 (a) θ/2θ XRD scans for $La_3Ni_2O_{7-\delta}$ films with various thicknesses ranging from 23 to 110 nm deposited on NGO (110). The $NdGaO_3$ substrate peaks are indicated by solid circles (•). The c-axis oriented film peaks are indexed by (00L). The dashed lines represent the positions of (00L) reflection from bulk oxide. (b) Zoom of the range of 20-60°, labelled as the dashed square in (a). The arrows indicate the shifting direction of (008), (0010) and (0012) peaks. 135

Figure 6.19 (a) θ/2θ XRD scans for $La_4Ni_3O_{10-\delta}$ films with various thicknesses ranging from 25 to 166 nm deposited on NGO (110). The $NdGaO_3$ substrate peaks are indicated by solid circles (•). The c-axis oriented film peaks are indexed by (00L). The star (*) and dashed lines represent the potential alternative phase (intergrowths) and the positions of $La_4Ni_3O_{10-\delta}$ (00L) reflection from bulk, respectively. (b) Zoom of the range of 20-60°, labelled as the dashed square in (a). The arrows display the shifting direction of (008), (0014) and (0016) peaks. The short solid green line indicates the (008) position of bulk $La_3Ni_2O_{7-\delta}$ phase. 137

Figure 6.20 Reciprocal space mapping in Q_x, Q_y coordinates with reciprocal lattice unit (rlu) of (1117) reflection of 47nm-thick $La_3Ni_2O_{7-\delta}$ (a) and (1123) of

51nm-thick $La_4Ni_3O_{10-\delta}$ (b) around (332) of NGO substrate. 139

Figure 6.21 (a) A plot of theoretical reciprocal lattice points of the $La_3Ni_2O_7$, $La_4Ni_3O_{10}$ and NGO phases, simulated by PANalytical X'Pert data collector software. The bigger semicircle is defined by the reciprocal lattice coordinates, Q_x and Q_y, with radius of $1/\lambda$ (λ is the X-ray wavelength) and in units of reciprocal lattice units (rlu, 1 rlu = $2/\lambda$). The two grey smaller semicircles represent the Laue zone where diffraction cannot be measured due to the geometric limitation of the equipment configuration. The construction of a Ewald sphere with radius of $1/\lambda$ depicts the relationship of incident and diffracted beams with the selected scan region for (1117) $La_3Ni_2O_7$, (1123) $La_4Ni_3O_{10}$ and (332) NGO reflections. (b) the zoom images of the selected scan region are illustrated with the scanning axes of ω and ω-2θ. Two satellites of (1116) $La_3Ni_2O_7$ and (1122) $La_4Ni_3O_{10}$ are also shown nearby (332) NGO in the selected region. 141

Figure 6.22 (a) Variation of the calculated a,b- and c-axis parameters of $La_3Ni_2O_{7-\delta}$ films with thickness of 23, 47, 82, and 110 nm. The horizontal dotted and dashed lines represent the bulk values of the average a,b-axis and c-axis parameters, respectively. (b) Variation of the estimated E_{xx}, E_{yy} and E_{zz} strains as a function of the film thickness. 143

Figure 6.23 (a) Variation of the calculated a,b- and c-axis parameters of $La_4Ni_3O_{10-\delta}$ films with thickness of 25, 51, 82, 104 and 166 nm. The horizontal dotted and dashed lines represent the bulk values of the average a,b-axis and c-axis parameters, respectively. (b) Variation of the estimated E_{xx}, E_{yy} and E_{zz} strain as a function of the thicknesses. 145

Figure 6.24 The variation of the cation ratio (La/Ni) for $La_3Ni_2O_{7-\delta}$ and $La_4Ni_3O_{10-\delta}$ as a function of film thickness. The horizontal dashed lines at 1.50 and 1.33 represent the expected cation ratio in $La_3Ni_2O_{7-\delta}$ and $La_4Ni_3O_{10-\delta}$, respectively. 147

Figure 6.25 AFM images of $La_3Ni_2O_{7-\delta}$ thin film deposited on NGO as a function of film thickness of 23 nm (a), 47 nm (b), 82 nm (c) and 110 nm (d) with the image size: 1 μm × 1 μm. Z depth scales are indicated from dark brown to white. The avg, RMS values are presented on the bottom of the images. 149

Figure 6.26 AFM images of $La_4Ni_3O_{10-\delta}$ thin film deposited on NGO as a function of film thickness of 25 nm (a), 51 nm (b), 82 nm (c), 104 nm (d) and 166 nm (e) with the image size: 1 μm × 1 μm. Z depth scales are indicated from dark brown to white. The avg, RMS values are presented on the bottom of the images. 150

Figure 6.27 Cross-section HAADF STEM image of the 166nm-thick $La_4Ni_3O_{10-\delta}$ film deposited on NGO (110). (a) the film primarily consists of intergrowths of n = 2 and 3 phases, occasionally n = 1 (labelled with different colours at X, Y and Z sections in the image). Three typically observed defects are indexed as domain

boundaries (white rectangle), extended faults (solid white arrows) and stacking faults (black arrows), labelled in region I, II and III respectively. The white dotted arrows correspond to the movement of LaO (rock-salt) layers when the propagation of the atomic columns undergoes the extended faults. (b) schematically represents that the film were grown along c-axis even though a variety of imperfection were encountered during deposition. The blue and red circles indicate lanthanum and nickel elements respectively. 152

Figure 6.28 θ/2θ XRD patterns of post-annealed and as-deposited films for $La_3Ni_2O_{7-\delta}$ (a) and $La_4Ni_3O_{10-\delta}$ (b) films grown on NGO (110) single crystal substrate. The NGO substrate peaks are indicated by solid circles (•), the c-axis oriented film peaks are indexed by (00L) and some extra peaks are indexed by stars (*) and represented as random intergrowths in the post-annealed films. 156

Figure 6.29 Cross-section HAADF STEM image of the as-deposited $La_4Ni_3O_{10-\delta}$ film epitaxially grown on NGO (110) substrate, showing that the c-axis oriented film was observed. A schematic cartoon represents the motif of the observed image. The solid blue circles correspond to lanthanum atoms; the octahedra with solid red circles inside correspond to NiO_6 blocks. 158

Figure 6.30 Cross-section HAADF STEM image of the post-annealed $La_4Ni_3O_{10-\delta}$ film epitaxially grown on NGO (110) substrate. (a) low-magnification image presents two dimensional planar defects lying perpendicular and parallel to the growth direction (c-axis). A cartoon also schematically represents the motif of the observed image. (b) high-magnification image clearly shows the crystal blocks are randomly distributed in square and rectangular fashion and coherently interleaved with LaO layer along the direction perpendicular and parallel to the growth direction, indexed by region I and II respectively. The two atomic arrangements are schematically exhibited in (c). The arrows correspond to the positions of LaO (rock-salt) layers. 159

Figure 6.31 comparative XRD patterns of a (a) 82nm-thick $La_3Ni_2O_{7-\delta}$ and (b) 81nm-thick $La_4Ni_3O_{10-\delta}$ film deposited on NGO substrate before and after a 4-point DC cycling electrical measurement from RT to 700°C in air for a month, including an aging treatments at 700°C in air for over 2 weeks (approximately 350 h in total). The Ag peaks originate from the electrode contacts for the electrical measurements. 162

Figure 7.1 Total electrical conductivity of the c-axis oriented $La_3Ni_2O_{7-\delta}$ epitaxial films with various thicknesses of 47, 82 and 110 nm deposited on NGO substrates as a function of temperature from RT to 700°C in air (a), Arrhenius plot of the electrical conductivity showing that the curves can be assigned to three region I, II and III (b), and fit of the curves at (c) region I (100-300°C), (d) II (300-500°C)

and (e) III (500-700°C) are presented with calculated activation energy (E_a) values. 168

Figure 7.2 Total electrical conductivity of the c-axis oriented $La_4Ni_3O_{10-\delta}$ epitaxial films with various thicknesses of 51, 82 and 166 nm deposited on NGO substrates as a function of temperature from RT to 700°C in air (a), Arrhenius plot of the electrical conductivity showing that the curves can be assigned to three region I, II and III (b), and fit of the curves at (c) region I (RT-250°C), (d) II (200-400°C) and (e) III (300-700°C) are presented with calculated activation energy (E_a) values..... 172

Figure 7.3 Total electrical conductivity of the c-axis oriented $La_3Ni_2O_{7-\delta}$ epitaxial films with various thicknesses of 47 nm (a), 110 nm (b) under two heating-cooling cycle measurements, and 82 nm (c) under three cycling measurements are shown as a function of temperature from RT to 700°C in air. Note that in (c), an aging treatment at 700°C in air for over two weeks (approximately 350 h in total) was carried out between Heating 3 and Cooling 3. 177

Figure 7.4 Total electrical conductivity of the c-axis oriented $La_4Ni_3O_{10-\delta}$ epitaxial films with various thicknesses of 51 nm (a), 166 nm (b) under two heating-cooling cycling measurements, and 82 nm (c) under three cycling measurements are shown as a function of temperature from RT to 700°C in air. Note that in (c), an aging treatment at 700°C in air for over two weeks (approximately 350 h in total) was carried out between Heating 3 and Cooling 3. 179

Figure 7.5 Total electrical conductivity of the c-axis oriented $La_2NiO_{4+\delta}$, $La_3Ni_2O_{7-\delta}$ and $La_4Ni_3O_{10-\delta}$ epitaxial films deposited on NGO substrates as a function of temperature in air plotted together with literature data from (a) polycrystalline bulk measured through van der Pauw method in air [33] and (b) epitaxial film of different phases deposited by PI-MOCVD characterised using AC impedance in O_2 atmosphere [91]. Note that for the literature data in (b), only $LaNiO_3$ and $La_2NiO_{4+\delta}$ are pure single phases and others are mixed, reported by the authors.... 182

Figure 7.6 Diffusion profile showing the normalised isotope fraction (C') of ^{18}O along the c-axis direction of the 44nm-thick $La_4Ni_3O_{10-\delta}$ / NGO sample exchanged at 400°C for ~29 min.. Note that the data (red solid dot) in region II selected to fit with the Eq.7.3, and then to extract the diffusion and surface exchange coefficients (D^* and k^* respectively) shown in the bottom figure. Top figure: a compositional depth profile (including Lao^-, NiO^- and GaO^-) of the sample for convenient observation in order to distinguish the diffusion position within the sample. 187

Figure 7.7 Diffusion profile showing the normalised isotope fraction (C') of ^{18}O along the c-axis direction of the 24nm-thick $La_4Ni_3O_{10-\delta}$ / NGO sample exchanged at 500°C for ~21 min. Note that the data (red solid dot) in region II selected to fit

with the Eq.7.3, and then to extract the k^* shown in the bottom diagram, but D^* is unable to be fitted. Top diagram: a compositional depth profile (including Lao^-, NiO^- and GaO^-) of the sample for convenient observation in order to distinguish the diffusion position from film surface to substrate. Middle diagram: the normalised ^{18}O isotope fraction depth profile. Bottom diagram: a zoom diagram of the middle one. 189

Figure 7.8 Diffusion profile showing the normalised isotope fraction (C') of ^{18}O along the c-axis direction of the 33nm-thick $La_4Ni_3O_{10-\delta}$ / NGO sample exchanged at 500°C for ~21 min. Note that the data (red solid dot) do fit well with the Eq.7.3. The k^* and D^* shown in the bottom diagram. Top diagram: a compositional depth profile (including Lao^-, NiO^- and GaO^-) of the sample for convenient observation in order to distinguish the diffusion position from film surface to substrate. Middle diagram: normalised ^{18}O isotope fraction depth profile. Bottom diagram: a zoom diagram of the middle one. 190

Figure 8.1 Compositional depth profiles for LaO^-, NiO^-, NdO^- and GaO^- secondary ion species in (a) 24nm-thick $La_4Ni_3O_{10-\delta}$ and (b) 33nm-thick $La_3Ni_2O_{7-\delta}$ films deposited on NGO after an oxygen isotope exchange at approximately 500°C. Region I, II, III and IV represent surface of film, film, film-substrate interface and substrate. The dashed lines identify the middle area between surface of film (I) and film (II); the middle interface area between film (III) and substrate (IV)..... 198

Figure 8.2 LEIS energy spectra of as-deposited $La_4Ni_3O_{10-\delta}$ film performed on the outer surface by (a) 3 keV He^+ and (b) 5 keV Ne^+ ion beams. 202

Figure 8.3 LEIS energy spectra of as-deposited $La_3Ni_2O_{7-\delta}$ film performed on the outer surface by (a) 3 keV He^+ and (b) 5 keV Ne^+ ion beams. 203

Figure 8.4 Normalised depth profiles of as-deposited $La_4Ni_3O_{10-\delta}$ film from Ne^+ spectra obtained after successive sputtering steps, showing (a) the raw yields of La and Ni, (b) apparent cation coverage and (c) cation (Ni:La) ratios plotted with ion fluence, i.e. Ar^+ ion sputtering rate. 205

Figure 8.5 Normalised cation depth profiles of as-deposited $La_3Ni_2O_{7-\delta}$ film from Ne^+ spectra obtained after successive sputtering steps, showing (a) the raw yield of La and Ni, (b) apparent cation coverage and (c) cation (Ni:La) ratios plotted with ion fluence, i.e. Ar^+ ion sputtering rate. 206

Figure 8.6 LEIS energy spectrum on the outer surface (a) and depth profile (b) of the after-exchanged $La_4Ni_3O_{10-\delta}$ film performed by a 3 keV He^+ ion beam. 207

Figure 8.7 LEIS energy spectrum on the outer surface (a) and depth profile (b) of the after-exchanged $La_3Ni_2O_{7-\delta}$ film performed by a 3 keV He^+ ion beam. 208

Figure 8.8 (a) LEIS energy spectra of after-exchanged $La_4Ni_3O_{10-\delta}$ film performed on the outer surface by 5 keV Ne^+ ion beams. Normalised cation depth profiles from

LEIS spectra obtained after successive sputtering steps, showing (b) the raw yield of La and Ni, (c) apparent cation coverage and (d) cation (Ni:La) ratios plotted with ion fluence, i.e. Ar^+ ion sputtering rate. 209

Figure 8.9 (a) LEIS energy spectra of after-exchanged $La_3Ni_2O_{7-\delta}$ film performed on the outer surface by 5 keV Ne^+ ion beams. Normalised cation depth profiles from LEIS spectra obtained after successive sputtering steps, showing (b) the raw yield of La and Ni, (c) apparent cation coverage and (d) cation (Ni:La) ratios plotted with ion fluence, i.e. Ar^+ ion sputtering rate. 210

Figure 8.10 Comparison of cation (Ni:La) ratios as a function of depth for as-deposited and after-exchanged $La_4Ni_3O_{10-\delta}$ samples. 211

Figure 8.11 Comparison of cation (Ni:La) ratios as a function of depth for as-deposited and after-exchanged $La_3Ni_2O_{7-\delta}$ samples. 211

Figure 8.12 LEIS energy spectra of as-deposited $La_2NiO_{4+\delta}$ film performed on the outer surface by (a) 3 keV He^+ and (b) 5 keV Ne^+ ion beams. 213

Figure 8.13 LEIS energy spectra of annealed $La_2NiO_{4+\delta}$ film performed on the outer surface by (a) 3 keV He^+ and (b) 5 keV Ne^+ ion beams. (c) depth profile of LEIS yield for La, Ni and a unknown elements analysed by 5 keV Ne^+ ion beams and obtained after successive sputtering steps plotted with ion fluence, i.e. Ar^+ ion sputtering rate. 214

Figure 8.14 Comparison of cation (Ni:La) ratios as a function of depth for as-deposited and annealed $La_2NiO_{4+\delta}$ samples. 215

List of Tables

Table 4.1 Cation ratios and density of $La_2NiO_{4+\delta}$ (n = 1), $La_3Ni_2O_{7-\delta}$ (n = 2) and $La_4Ni_3O_{10-\delta}$ (n = 3) targets determined by EDX and ICP-AES..... 70

Table 4.2 Summary of crystal structures, space groups, lattice parameters and mean mismatch with STO (001) and NGO (110) substrates for the layered RP-type $La_{n+1}Ni_nO_{3n+1}$ (n = 1, 2 and 3) compounds based on ICSD (Inorganic Crystal Structure Database) data. 80

Table 4.3 Surface roughness parameters of the adopted NGO substrates from different batches provided by Crystal GmbH, Berlin, Germany..... 82

Table 5.1 Optimal Growth Conditions for c-axis oriented $La_2NiO_{4+\delta}$ epitaxial films..... 97

Table 5.2 Summary of crystal structures, space groups, lattice parameters and mean lattice mismatch with STO (001) and NGO (110) substrates for the layered RP-type $La_2NiO_{4-\delta}$ (n = 1) compounds based on ICSD (Inorganic Crystal Structure Database) data. 99

Table 6.1 Cation ratios of the deposited $La_3Ni_2O_{7-\delta}$ (a) and $La_4Ni_3O_{10-\delta}$ (b) films with various deposition temperatures were determined by EDX. The theoretical La/Ni ratios for $La_3Ni_2O_{7-\delta}$ and $La_4Ni_3O_{10-\delta}$ are expected to be 1.50 and 1.33, respectively. 117

Table 6.2 Cation ratios and compositional deviation (%) of obtained (a) $La_3Ni_2O_{7-\delta}$ and (b) $La_4Ni_3O_{10-\delta}$ films with various laser fluences from 0.5 to 0.7 J/cm^2 were determined by EDX. The theoretical La/Ni ratios for $La_3Ni_2O_{7-\delta}$ and $La_4Ni_3O_{10-\delta}$ are expected to be 1.50 and 1.33, respectively. 118

Table 6.3 Optimal Growth Conditions for c-axis oriented $La_3Ni_2O_{7-\delta}$ and $La_4Ni_3O_{10-\delta}$ epitaxial films..... 125

Table 7.1 Summary of diffusion coefficient (D^*) and surface exchange coefficient (k^*) along c-axis of $La_3Ni_2O_{7-\delta}$ and $La_4Ni_3O_{10-\delta}$ films at ~400 and ~500°C, compared to the literature values of $La_2NiO_{4+\delta}$ film. 192

Chapter 1 Introduction

The purpose of this chapter is to introduce the general background of the research detailed in the thesis. Initially, the global energy crisis and environmental impact of today's society will be described, followed by introducing fuel cells as alternative energy devices. One type of fuel cell, the solid oxide fuel cell (SOFCs), will be specifically focused on along with a brief review of several conventional anode, electrolyte and cathode materials for SOFC applications. The following section will describe the research motivation and aims of the work in the thesis before outlining the organisation of the thesis.

1.1 Energy Crisis and Environmental Impact

In last two decades there has been an increasing awareness that the energy and environment globally present today's community with substantial issues and impact. These global effects are primarily driven by several factors as follows. The world population is continuingly growing, leading to the increasing demand for energy [1, 2]. The world energy demand has risen by approximately 50% from the year 1980 [3, 4]. However, the current energy generation is limited by the diminishing resources of fossil fuels (oil, coal and natural gas) [5]. Additionally, the massive usage of fossil fuels since the industrial revolution has resulted in many tremendous effects on the environment leading to climate change. One phenomenon in climate change is, for example, global warming. Global warming is caused by effluent gas emission, mainly CO_2, which is owing to the excess combustion of fossil fuels. During the past century, a rise of approximately 0.7°C has been recorded for the global mean surface temperature and the

trend has dramatically increased during the past 30~40 years [6]. The emissions from the usage of fossil fuels have also significantly polluted the atmosphere, leading to an influence on health for humankind and other lives all over the world. Most recently, climate change has further caused the increasing frequency of drastic natural catastrophes such as floods, droughts, heat waves, hurricanes, even earthquakes and tsunamis as seen in past decades [5, 6]. It is consequently of importance to manage the use of the limited fossil fuel resources and develop new power generation technologies as they will be critical for the future of the world. One of the remarkable alternative energy technologies, the fuel cell, is regarded as a highly clean and efficient energy conversion electrochemical device, which possesses great potential to significantly influence the global energy economy from fossil energy to a cleaner and more sustainable form.

1.2 Fuel Cells

Fuel cells are electrochemical energy conversion devices. They generally can utilise hydrogen as a fuel, providing the prospect of using energy via a clean and sustainable manner in various applications. Fuel cell technologies have been developed for widespread applications in recent years. The applications may be mainly considered under the following headings [7]: (1) small power systems (e.g. automobile and residential power systems), and (2) large power systems (e.g. generation power and waste treatment plants). Also, portable equipment (e.g. battery chargers and military equipment) has been studied and developed. At present, the SOFCs are the only type of fuel cell that possess significant potential for such a broad range of applications. There are five types of fuel cells as exhibited in **Figure 1.1**: solid oxide fuel cell (SOFC), molten carbonate fuel cell (MCFC), phosphoric acid fuel cell (PAFC), polymer electrolyte membrane fuel

cell (PEMFC), and alkaline fuel cell (AFC), which are generally classified by the nature of the electrolyte materials. For more detailed reviews of these other fuel cell types refer to two books, published by Larminie *et al*. [7] and O'Hayre *et al.*[8]. It should be noted that the work in this thesis will focus on new cathode materials for application in SOFC technology.

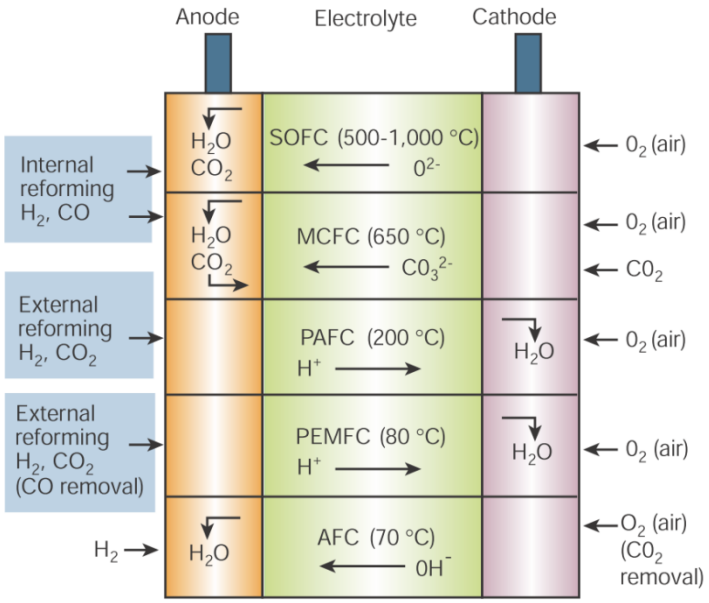


Figure 1.1 Five main types of fuel cells and their working temperatures and reaction mechanisms [9].

1.3 Solid Oxide Fuel Cells (SOFCs)

SOFCs are the most efficient electrochemical energy conversion devices that depend on a continuous feed of a fuel (particularly hydrogen) to produce chemical energy. The devices enable direct conversion of chemical energy into DC electrical energy and heat, and are consequently capable of overcoming combustion efficiency limits in thermodynamics (e.g. Carnot cycle in internal combustion engine) [10]. Pure water is produced as the exhaust at the anode side of the cells. A SOFC consists of entirely solid-state materials and operates under very high temperature (typically around

500~1000°C), and its structure contains four main components: an anode, solid ceramic oxide electrolyte, cathode, and external circuit (interconnects). A number of individual cells can be connected in series, parallel, series-parallel, or as a SOFC stack to provide appropriate electrical current and voltage for diverse applications [7].

Figure 1.2 is a schematic diagram briefly describing the transport and reaction mechanism in a SOFC system. Oxygen (or air) is supplied to the cathode where it is reduced to O^{2-} by an external supply of electrons. Oxygen ions migrate to the electrolyte surface and are transported through the solid electrolyte to the anode. On the other hand, hydrogen fuel is fed into the cell anode and is oxidised to release electrons (e^-). Then these electrons travel to the cathode via an external circuit to form a transport cycle. The by-products of this process are pure water (H_2O), heat and a small amount of carbon dioxide gas (CO_2). The oxidation reaction of the hydrogen fuel occurs at the anode as shown in Eq.1.1 and 1.2; the reduction reaction of oxygen take places at the cathode as presented in Eq.1.3 [7, 8]. The overall reactions are represented in Eq.1.4 and 1.5 [11]:

Anode side:

$$H_2 + O^{2-} \leftrightarrow H_2O + 2e^- \quad (1.1)$$

$$CO + O^{2-} \leftrightarrow CO_2 + 2e^- \quad (1.2)$$

Cathode side:

$$O_2 + 4e^- \leftrightarrow 2O^{2-} \quad (1.3)$$

Overall reactions:

$$H_2 + \frac{1}{2}O_2 \leftrightarrow H_2O \quad (1.4)$$

$$CO + \frac{1}{2}O_2 \leftrightarrow CO_2 \quad (1.5)$$

There are various advantages with SOFCs, which lead to a large number of applications. Firstly, it is believed that widespread use of SOFC systems in daily life will produce a reduced dependence on oil and fossil fuels in the future [11]. Then emissions of

pollutants, carbon dioxide in particular, can be also diminished. Secondly, the three important by-products of the cell reactions are heat, pure water (Eq.1.4), and low level of carbon dioxide (Eq.1.5), indicating that SOFCs are an environmental-friendly energy supplier. Additionally, coupled with heat recovery systems, SOFC systems present significantly higher efficiency for energy conversion of approximately 80% in comparison with conventional power generation systems such as combustion engines and turbine engines [12]. Very high-quality waste heat can be obtained owing to SOFCs normally operating at high temperature of around 1000°C; that is, very high energy efficiency can be achieved by such combined heat and power (CHP) systems [11, 13]. Due to operating at such high-temperature SOFCs also able to electrochemically oxidise CO, which is advantageous as hydrocarbon fuels are supplied to the cells [11]. Furthermore, solid ceramic oxides are used as electrolytes in SOFCs so that fuel choices can be flexible, which means no corrosion and reaction with the solid electrolytes [8]. Finally, SOFCs are considerably quieter than combustion engines because they have no moving parts in their operating processes; hence it can be installed indoors [7, 8].

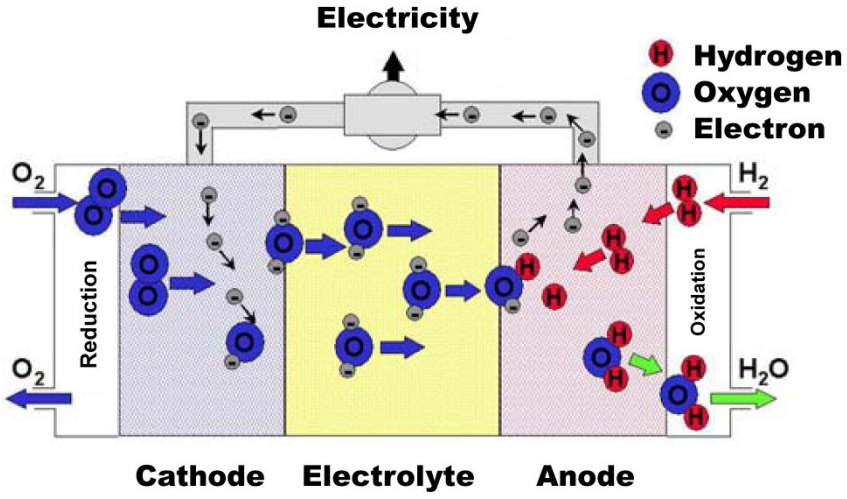


Figure 1.2 Schematic diagram for transport and reaction mechanism in a solid oxide fuel cell (SOFC) (adapted from [14]).

Although SOFCs have demonstrated excellent efficiency, fuel flexibility, and clean emission, they are not yet widely used for power generation. There are two main reasons: (1) the costs of the raw materials used in manufacturing SOFCs are still significantly high [10] and (2) the stability is not good at high operating temperatures (approximately 800~1000°C) [4]. To overcome these issues, a majority of current research has focused on lowering the operating temperature to the intermediate-temperature range (500~700°C) whilst retaining a high efficiency so as to solve the significant restrictions for the applications of intermediate temperature SOFCs such as material cost, compatibility, long-term stability and longevity [9, 11, 13]. To optimise performance of the cells, seeking suitable anode, electrolyte, and cathode materials, therefore, is a critical task for the development of IT-SOFCs. The requirements of each component and their current development will be briefly described as follows.

Anodes. A commonly used anode material is Ni/YSZ cermet (ceramic-metal composite), capable of no reaction with typical electrolyte materials; for example, YSZ (yttria stabilised zirconia) and CGO (gadolinium-doped ceria). The material also possesses excellent catalytic properties for fuel oxidation, highly porous structures to facilitate the mass transport of reactant and product gas, and appropriate thermal expansion coefficient (TEC) with the common electrolytes, while providing a high level of electronic conductivity as a good current collector [15]. However, there are some drawbacks for the Ni/YSZ-based anode; for instance, sulphur poisoning and carbon deposition when using natural gas as fuel due to the cracking of methane. More details can be found in a review article regarding the development of anode materials [15].

Electrolytes. The requirements of electrolytes for the use of solid oxide fuel cells (SOFCs) are high ionic conductivity, low electronic conductivity, appropriate thermomechanical properties (e.g. TEC), chemical stability in both oxidising and

reducing atmosphere, and long-term stability regarding dopant segregation. There are three common electrolyte materials such as yttria-stablised zirconia (YSZ), gadolinium-doped ceria (CGO) and magnesium-doped lanthanum strontium gallate (LSGM) being extensively studied for SOFC applications [16]. For ideal electrolytes applied in IT-SOFC, several requirements should be taken into account [11]: low electronic conductivity but high oxygen ionic conductivity (typically above 1×10^{-2} Scm^{-1}), good thermal and chemical stability to both electrode materials along with a good thermal expansion coefficient (TEC), a favourable fully-dense structure in order to reduce the overpotentials caused by the tortuous pathways and thereby maximise conductivity [17]. A comprehensive review, published by Goodenough [18] with regard to oxygen ion electrolytes is recommended, and for the most recent development of electrolyte materials for IT-SOFCs refer to references [19, 20].

Cathodes. For conventional SOFC cathodes, a number of general properties have to be exhibited [8, 11, 21]: suitable compatibility with electrolyte and interconnect materials; good thermal and chemical stability in air; excellent durability when operating at high temperature and temperature cycling; high catalytic activity for reduction of molecular oxygen to be dissociated into atoms, charged, and incorporated into electrolytes; high electronic conductivity for transferring electrons from the current collectors to the reaction area (in general > 100 Scm^{-1}) [22, 23]; and sufficient ionic conductivity (in particular for mixed ionic-electronic conductors).

As cathodes operate at high temperatures (traditionally ~1000°C), the kinetic reactions taking place at cathodes are sufficient, leading to a minor influence on the performance of cells. On the contrary, when operating at reduced temperatures (IT, 500-700°C) a significant increase in the polarisation losses of the cells is observed, which means that the rates of oxygen reduction reactions and charge transport proceed much

slower at low temperatures than at high ones. Therefore, it is imperative to develop alternative cathode candidates that effectively function at low operating temperatures for the practical application of IT-SOFC [11]. There are two distinct types of behaviour associated with cathode materials that have been studied: triple phase boundary (TPB) and mixed ionic-electronic conductor (MIEC) type cathodes [20], as schematically demonstrated in **Figure 1.3 (a)** and **(b)**.

The TPB-type cathodes are usually pure electronic conductors where the oxygen reduction reaction (ORR) takes place at the cathode/electrolyte/gas phase boundary, as shown in **Figure 1.3 (a)**. For this type of cathode, it is of importance to optimise the microstructure to maximise the TPB sites; i.e. to extend the active regions for ORR. The ORR is associated with several key processes such as dissociation of molecular oxygen into atoms, transport of charged oxygen and its incorporation into electrolytes. Therefore, TPB-type conductors must be operated at high temperature. On lowering the operating temperature, such conductors are no longer effective. A typical TPB-type conductor is the well-known (La,Sr)MnO_3 (LSM) that has been widely used as a cathode in various SOFC designs [22, 24] due to its good stability under oxidising atmospheres, high p-type electronic conductivity and close TEC with conventional YSZ-based electrolytes. Nevertheless, several drawbacks [11, 24] include not only having poor oxide ion conductivity owing to the lack of oxygen vacancies, but also having a reaction with the conventional YSZ electrolytes to form a $La_2Zr_2O_7$ insulating phase at high operating temperature resulting in cell degradation. Despite this, further improvement for LSM cathodes can be achieved via an YSZ/LSM composite, which have been extensively investigated [23-25].

Contrary to traditional TPB type electrodes, the MIEC-type cathodes are materials that exhibit both ionic and electronic conductivity through introducing both electronic

defects (i.e. electrons or holes) and ionic defects (i.e. oxygen vacancies or interstitials), as illustrated in **Figure 1.3 (b)**. Such properties permit the extension of the ORR area over part of the surface of the cathode materials, and thereby significantly the improvement of cell performance as operating at the lower temperature in particular. In the past two decades, a wide variety of perovskite-based MIECs such as doped $LaMnO_3$, $LaCoO_3$, $BaCoO_3$, and $LaFeO_3$ have been extensively investigated [13, 16, 19, 20, 23, 26-28]. Each series of materials may be appropriate for particular features of the cathode operation, but each of them has several deficiencies. For example, $(La,Sr)CoO_3$ (LSC) material possesses superior ionic and electronic conductivity while it has a high TEC, which is difficult to be used with conventional electrolytes (e.g. CGO) [11]. In order to address the deficiencies of LSC, substituting iron for cobalt produces $La_{1-x}Sr_xCo_{1-y}Fe_yO_{3-\delta}$ (LSCF), which exhibits good ionic and acceptable electronic conductivity, catalytic activity, and even lower TEC [23, 29].

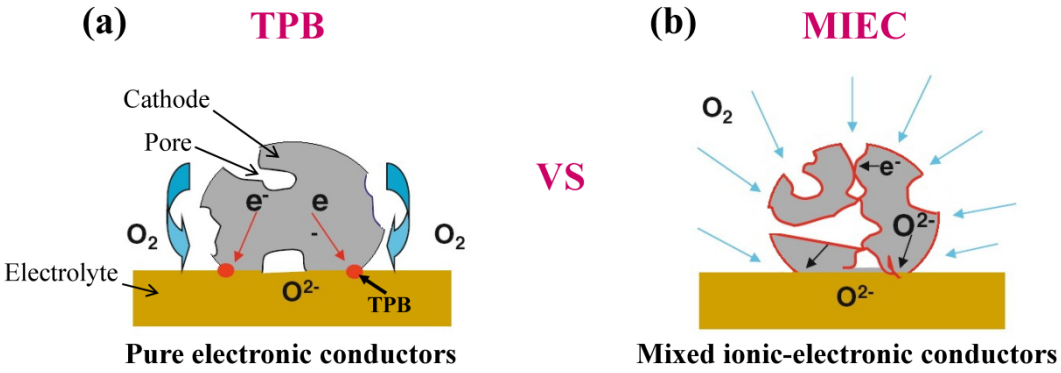


Figure 1.3 Illustrated comparison of (a) TPB and (b) MIEC where active areas (highlighted in red colour) for oxygen reduction reaction takes place. (adapted from [20])

In addition to perovskite-type cathode materials, there are a number of other new, promising candidates that have been intensively focused recently. These materials include layered double perovskite (e.g. $GdBaCoO_{5+\delta}$ and $PrBaCoO_{5+\delta}$) and perovskite-related Ruddlesden-Popper (RP) phases (e.g. $La_{n+1}Ni_nO_{3n+1}$ (n = 1, 2 and 3)). All these layered

oxide materials have been found to present encouraging performance as MIECs. More detailed information can be found in references [16, 19, 20, 30]. Note that the current development and properties related to RP-phase materials associated with the work of this thesis will be reviewed in Ch.2.

1.4 Research Motivation and Aim

As mentioned previously, layered RP-type $La_{n+1}Ni_nO_{3n+1}$ (n = 1, 2 and 3) have recently attracted significant attention as emerging alternatives to conventional perovskites for use as promising cathode materials for the next generation of IT-SOFCs [31-33]. For potential application as a cathode in operation at intermediate temperatures (500~700°C), earlier studies have demonstrated that $La_2NiO_{4+\delta}$ (n = 1) materials are predominantly electronic conductors with very promising ionic conductivity (σ_i = ~10^{-2} Scm^{-1}) [34] and acceptable electronic conductivity (σ_e = ~100 Scm^{-1}), compared to conventional cathode materials [23, 35]. In addition, long-term stability and compatibility of $La_2NiO_{4+\delta}$ with lanthanum gallate based (LSGM) electrolytes has been evaluated by Amow *et al.* [32, 33] who found that a Ni^{2+}/Ni^{3+} impurity phase formed when $La_2NiO_{4+\delta}$ was heated at 900°C for two weeks in air. Thus, $La_2NiO_{4+\delta}$ phases are not ideally suited for practical utilization for IT-SOFCs. Apart from $La_2NiO_{4+\delta}$, higher order RP phases, $La_3Ni_2O_{7-\delta}$ (n = 2) and $La_4Ni_3O_{10-\delta}$ (n = 3), are of interest for use as SOFC cathodes owing to their superior electrical conductivity, and good chemical and thermomechanical stability in operation at intermediate temperatures (500~700°C) [33].

However, to date there is an absence of information about intrinsic ionic conductivity of these higher order $La_3Ni_2O_{7-\delta}$ and $La_4Ni_3O_{10-\delta}$ compounds, which could be attributed to the challenge of synthesising dense, continuous polycrystalline samples,

as samples with only 50~60% of their theoretical density via conventional ceramic processes (e.g. solid state and sol-gel methods) have been achieved [33, 36]. To enable measurement of intrinsic electronic and particularly ionic transport properties, the greatest challenge is to synthesise dense, continuous or ideally epitaxial specimens of $La_3Ni_2O_{7-\delta}$ and $La_4Ni_3O_{10-\delta}$ through the pulsed laser deposition (PLD) technique. Furthermore, earlier studies on $La_2NiO_{4+\delta}$ have theoretically [37, 38] and experimentally [34, 39-42] confirmed their anisotropic transport properties (electronic and ionic). These studies also revealed that the anisotropy of oxygen diffusion and electrical conduction appears to improve the transport properties in comparison with non-layered compounds. Based on these earlier findings, both higher order $La_3Ni_2O_{7-\delta}$ and $La_4Ni_3O_{10-\delta}$ compounds are also expected to naturally have anisotropic transport properties because of their layered structures. Therefore, growing epitaxial films of the higher order compounds may facilitate the investigation of their intrinsic anisotropic properties. These fundamental studies not only allow understanding of the functional properties of the $La_3Ni_2O_{7-\delta}$ and $La_4Ni_3O_{10-\delta}$ materials but may also help the further development of these materials and related RP-phases for the potential SOFC or even micro-SOFC applications in the future.

1.5 Outline of Thesis

This thesis explores deposition and characterisation of the layered RP-type materials including $La_2NiO_{4+\delta}$, and particularly $La_3Ni_2O_{7-\delta}$ and $La_4Ni_3O_{10-\delta}$. The organisation of the thesis is as follows. The first chapter has briefly introduced the background, motivation and aims of the research. The second chapter is a brief overview about the RP-related materials and their current development. The following chapter (Ch.3) describes the experimental methods and characterisation techniques employed in this work.

There are five results chapters. The first part (Ch.4) is with regard to the synthesis and characterisation of the utilised $La_{n+1}Ni_nO_{3n+1}$ (n = 1, 2 and 3) PLD targets, followed by the description of the substrate requirements for PLD. The phenomena of target degradation is also highlighted. After the preparation of PLD targets, Ch.5 begins with the growth and characterisation of $La_2NiO_{4+\delta}$ in order to primarily determine the appropriate deposition conditions and substrate for higher order RP film (n = 2 and 3) growth. Based on these experiences from $La_2NiO_{4+\delta}$, a series of $La_3Ni_2O_{7-\delta}$ and $La_4Ni_3O_{10-\delta}$ epitaxial films have been achieved and the related influences on film microstructure caused by different deposition conditions are discussed in Ch.6. The transport properties of these obtained films are provided in the following Ch.7. At the end, the surface and interface information for these films are preliminarily investigated in Ch.8. In particular, the surface structure and cation coverage on the outer and even outermost surface are obtained by low energy ion scattering measurements.

The last chapter (Ch.9) summarises the conclusions with respect to the obtained results in this work. Future work about the series of RP materials is also suggested.

Chapter 2 Literature Review

As introduced in the previous chapter, the Ruddlesden–Popper (RP) series of layered oxides are considered to be promising candidates for the next generation of IT-SOFCs. Literature reviewed in this chapter provides basic knowledge of layered RP phases, and summarises the present developments of the series of materials for SOFC applications with specific focus on related studies of the $La_{n+1}Ni_nO_{3n+1}$ (typically n = 1, 2 and 3) family.

2.1 Architecture of Layered Ruddlesden-Popper (RP) Type Materials

Ruddlesden–Popper type materials have recently attracted significant attention as emerging alternatives to conventional perovskites for use as promising cathode materials for the next generation of IT- SOFCs [31-33]. The RP series of layered oxides, generally formulated $A_{n+1}B_nO_{3n+1}$ (typically n = 1, 2 and 3), is one of the best-known perovskite-related MIEC (mixed ionic-electronic transport conductor) materials. This series originated in the titanates, $Sr_{n+1}Ti_nO_{3n+1}$ reported by Ruddlesden and Popper in 1958 [43]. Illustrated in **Figure 2.1**, the crystal structure of the RP phases consists of n consecutive $(ABO_3)_n$ perovskite layers, alternating with AO rock-salt layers, stacking along the crystallographic c-axis, as represented by $(AO)(ABO_3)_n$. The A and B site cations are typically composed of rare/alkaline earth metals (La, Pr, Nd) and transition metals (Ni, Co, Cu) respectively. For this series of compounds, an ideally structural transformation has been shown between a tetragonal structure (*I4/mmm*) and orthorhombic distortions (*Fmmm*), which is based on rotation and inclination of oxygen

octahedral units (BO_6) along the c-axis due to variation in the oxygen non-stoichiometry [44-47].

Such layered MIECs display diverse defect chemistry, allowing non-stoichiometric defect structures (hypo- and hyper-stoichiometry, which can also be defined as oxygen deficiency and excess, respectively) due to their oxygen content through tailoring A- and B-site compositions. This feature makes these oxides very attractive for the fine-tuning of their electrical and electrochemical properties [32, 33, 46-57]. For the case of oxygen hyper-stoichiometry, particularly, the excess oxygen can occupy interstitial sites within the AO rock-salt layers.

Of recent particular interest in the case of materials for SOFC cathodes is the La-Ni-O family. The following review will primarily focus on the RP series of $La_{n+1}Ni_nO_{3n+1}$ (n = 1, 2 and 3) materials, including their structure, synthesis, and current development in SOFC applications.

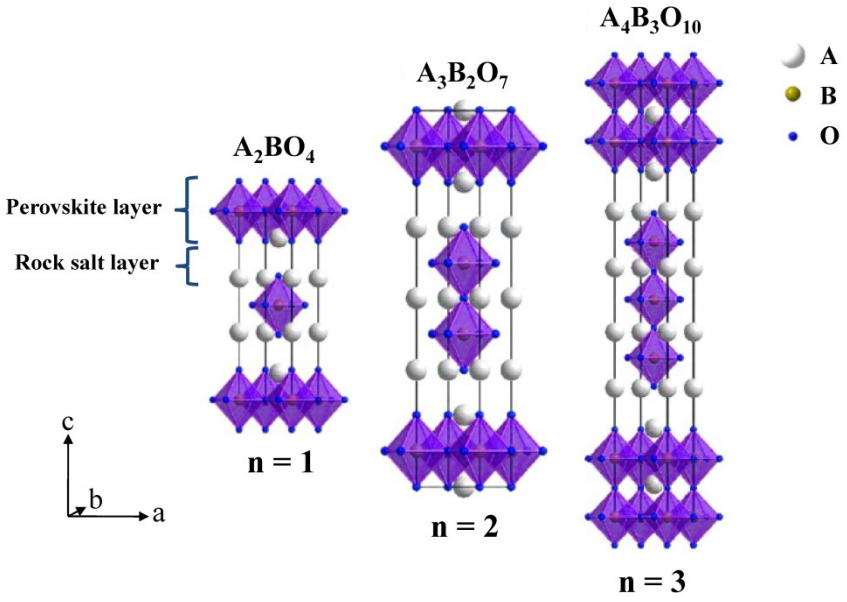


Figure 2.1 Schematic crystal structures of the n = 1, 2 and 3 members of the Ruddlesden–Popper (RP) type $A_{n+1}B_nO_{3n+1}$ are shown. The denotation of n represents the number of stacked octahedral layers separated by a rock salt AO layer. BO_6 octahedra and A atoms are shown schematically. The unit cell of each structure is presented by a black rectangle.

2.2 Structure and Synthesis of RP $La_{n+1}Ni_nO_{3n+1}$ (n = 1, 2 and 3) Phases

$La_2NiO_{4+\delta}$ is the first member of the RP $La_{n+1}Ni_nO_{3n+1}$ series, and has been extensively studied over the past few decades due to its high similarity with the high-temperature superconductor $La_2CuO_{4+\delta}$ [58] although there is no evidence of high-temperature superconducting behaviour in $La_2NiO_{4+\delta}$ [59-61]. The crystal structure of the compound consists of a $LaNiO_3$ perovskite block sandwiched by LaO rock-salt blocks, as seen in the n = 1 member of **Figure 2.1**. The material generally has two different crystallographic structures: tetragonal and orthorhombic with a variety of space groups, which have been extensively reported in Inorganic Crystal Structure Database (ICSD). The phase transitions between the two structures have been investigated in a whole range of temperature for $La_2NiO_{4+\delta}$ [62, 63], which can be briefly summarised as follows. A low temperature transition shows at ~80 K from a low temperature tetragonal (LTT) phase ($P4_2/ncm$ space group) to a low temperature orthorhombic (LTO) phase (*Bmab* or *Fmmm* space group) [64-66]. With increasing temperature to ~423 K, the LTO phase transforms to a high temperature tetragonal (HTT) phase (*I4/mmm* space group) [63]. It should be noted that these transition temperatures are highly dependent on the oxygen stoichiometry of the material [62, 63]. Also, these various space groups are associated with crystal symmetry, strongly related to the rotation and inclination of oxygen octahedral units (NiO_6), and hence relies on the oxygen stoichiometry of the films [62]. $La_2NiO_{4+\delta}$ is generally believed to be an oxygen-excess material, possessing a range of oxygen content (δ), typically from 0.14-0.25 [63, 67-69]. The excess oxygen is incorporated in interstitial sites of the structure, and consequently provides a high ionic conductivity, which will be discussed in detail in section 2.3.

In the case of $La_3Ni_2O_{7-\delta}$ and $La_4Ni_3O_{10-\delta}$ based on ICSD, the structures for both materials were generally regarded to be either tetragonal or orthorhombic [47, 51]. Zhang *et al.* [51] found that the structure of $La_3Ni_2O_{7-\delta}$ changed with a wide range of oxygen stoichiometry (δ = 0, 0.08, 0.16 and 0.65) from orthorhombic (*Fmmm*) to tetragonal structure (*I4/mmm*) under various oxidation and reduction treatments, as summarised in **Figure 2.2**. This wide range of oxygen stoichiometry (7.00-6.35) evidently indicates the flexibility of $La_3Ni_2O_{7-\delta}$ phase; i.e. the availability of highly distorted oxygen octahedra. Through neutron diffraction studies, the space group for stoichiometric $La_3Ni_2O_7$ was proposed to be a better fit to Cmcm, reported by Voronin *et al.* [44]. On the other hand, $La_4Ni_3O_{10-\delta}$ was also regarded to possess a structure between tetragonal (*I4/mmm*) for non-stoichiometric and orthorhombic (*Fmmm*) for stoichiometric material, reported by Zhange *et al.* [47]. Further detailed investigations via neutron diffraction analysis suggested a superior space group for stoichiometric $La_4Ni_3O_{10}$ was Cmca [44]. Subsequently, through in-situ high-temperature X-ray diffraction techniques, Amow *et al.* [32, 33] observed the phase transitions from orthorhombic to tetragonal for $La_3Ni_2O_{6.95}$ and $La_4Ni_3O_{9.78}$ at 589K and 758K, respectively (seen in **Figure 2.3 (a)** and **(b)**). $La_4Ni_3O_{10-\delta}$ can have a range of oxygen stoichiometry from 9.78 to 10.12 under various oxidation and reduction processes, reported by Carvalho *et al.* [70].

It should be noted that compared to $La_2NiO_{4+\delta}$ (n = 1), $La_3Ni_2O_{7-\delta}$ (n = 2) and $La_4Ni_3O_{10-\delta}$ (n = 3) are usually regarded as predominantly oxygen-deficient compounds (dominant by oxygen vacancies) rather than oxygen-excess ones (by interstitials) [33, 71]. Normally, under a typical ceramic preparation, the as-prepared $La_3Ni_2O_{7-\delta}$ and $La_4Ni_3O_{10-\delta}$ samples possess the oxygen content of 6.93-6.95 and 9.78-9.83, respectively [33, 72]. Also, the oxidation states of Ni for the stoichiometric compounds can be represented as $La_2(Ni^{2+})_1O_4$, $La_3(Ni^{2+})_1(Ni^{3+})_1O_7$, and $La_4(Ni^{2+})_1(Ni^{3+})_2O_{10}$ [73]. This

indicates that $La_2NiO_{4+\delta}$ is predominantly Ni^{2+}, and the Ni oxidation state increases with increasing n value from Ni^{2+} to Ni^{3+}. The variation of Ni oxidation state can be significantly influenced by oxygen content, and presumably cation composition ratio as well.

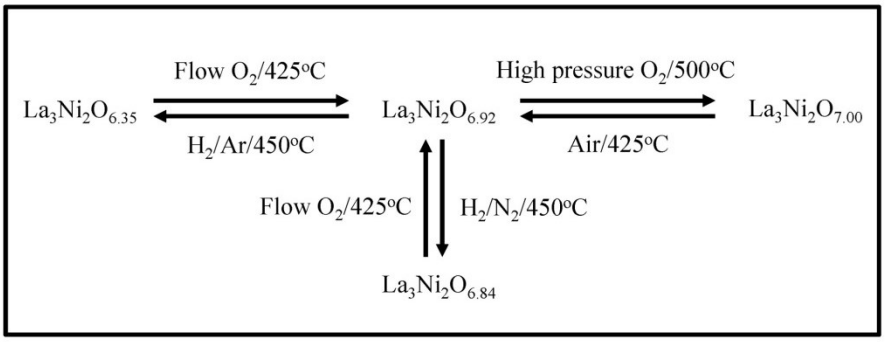


Figure 2.2 Preparation of the four different $La_3Ni_2O_{7-\delta}$ phases with a wide range of oxygen stoichiometry δ = 0, 0.08, 0.16 and 0.65 (adapted from [51]).

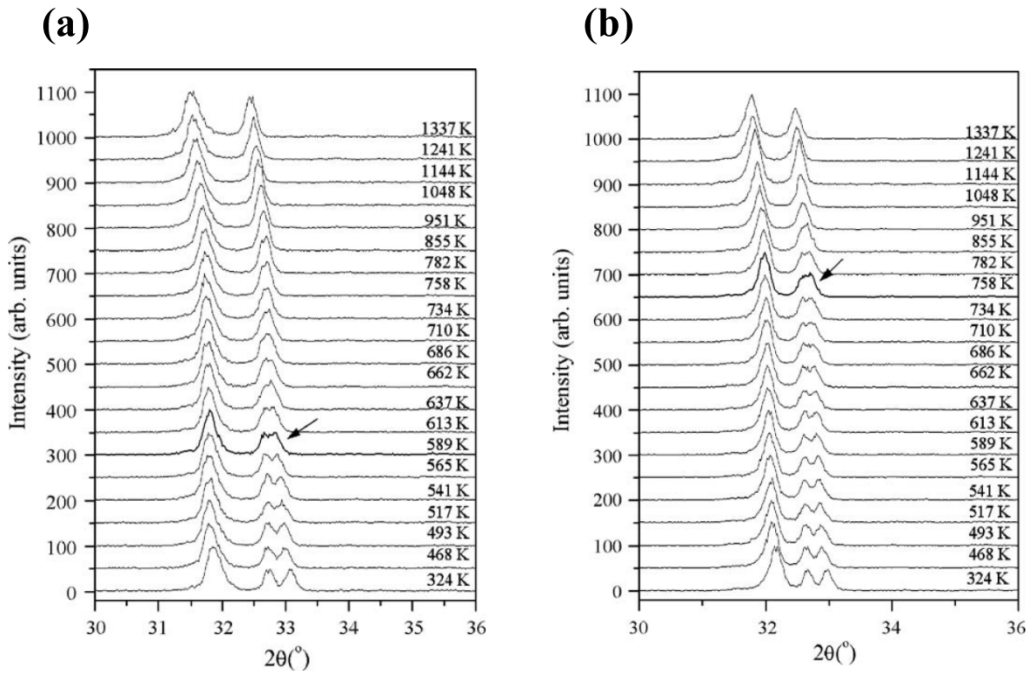


Figure 2.3 High-temperature X-ray diffraction patterns of $La_3Ni_2O_{6.95}$ (a) and $La_4Ni_3O_{9.78}$ (b), showing the phase transition from orthorhombic to tetragonal symmetry [33].

These members of the RP $La_{n+1}Ni_nO_{3n+1}$ series, in particular, $La_3Ni_2O_{7-\delta}$ and $La_4Ni_3O_{10-\delta}$, are difficult to synthesise as pure phases, and even stoichiometric forms. The synthesis process usually requires prolonged heating and reheating procedures [33, 51]. The reasons for the difficulties are that these heating compounds tend to not only form mixed intergrowths of different phases [47, 74-77], but also to easily lose or gain oxygen [46, 47, 51]. Thus, they are very sensitive to oxygen partial pressure and temperature as demonstrated on a series of stability and thermodynamic analyses by Zinkevich's and Bannikov's groups [72, 73, 78]. The other challenge in synthesis is to obtain dense bulk samples of the $La_3Ni_2O_{7-\delta}$ and $La_4Ni_3O_{10-\delta}$ phases. In earlier studies, the $La_2NiO_{4+\delta}$ phase has been widely synthesised by various techniques such as conventional ceramic processes (solid state and sol-gel methods) [32, 33, 79-81], metalorganic chemical vapour deposition [39, 47, 82], pulsed laser deposition (PLD) [83-85], and even floating zone technique for single crystals [34, 86, 87]. In contrast, a number of studies have achieved $La_3Ni_2O_{7-\delta}$ and $La_4Ni_3O_{10-\delta}$ phases in bulk forms through the traditional ceramic processes with prolonged and reheating procedures [32, 33, 46, 47, 51]. More recently, the synthesis of these compounds was improved via a single-step heat treatment of nano-sized metal hydroxide co-crystallites [88]. However, there are only a few studies of thin-films prepared through spray pyrolysis [89, 90] and pulsed injection metalorganic chemical vapour deposition (PI-MOCVD) [91], but no information on single crystals have been reported to date. These investigations will be further discussed in the following sections of the chapter.

2.3 Current Development of RP Phases in SOFC Application

Of particular interest in current research on SOFCs has been the n = 1 member of the RP series. A typical example is $La_2NiO_{4+\delta}$, which possesses the well-known K_2NiF_4-type structure, and usually believed to be an oxygen interstitial containing oxide. The oxygen interstitial sites in the compound are centered in the tetrahedron of surrounding metal La cations [92] (see **Figure 2.4**). An electric field exists between the $(La_2O_2)^{2+}$ and the $(NiO_2)^{2-}$ layers so that most of the interstitial oxide ions may be attracted to the LaO layers by the Coulomb potential, resulting in the anisotropic diffusion behaviour [34]. Sayagués *et al.* [93] have experimentally confirmed the presence of the excess oxygen and observed it to order at low temperature using high-resolution transmission electron microscopy (HRTEM).

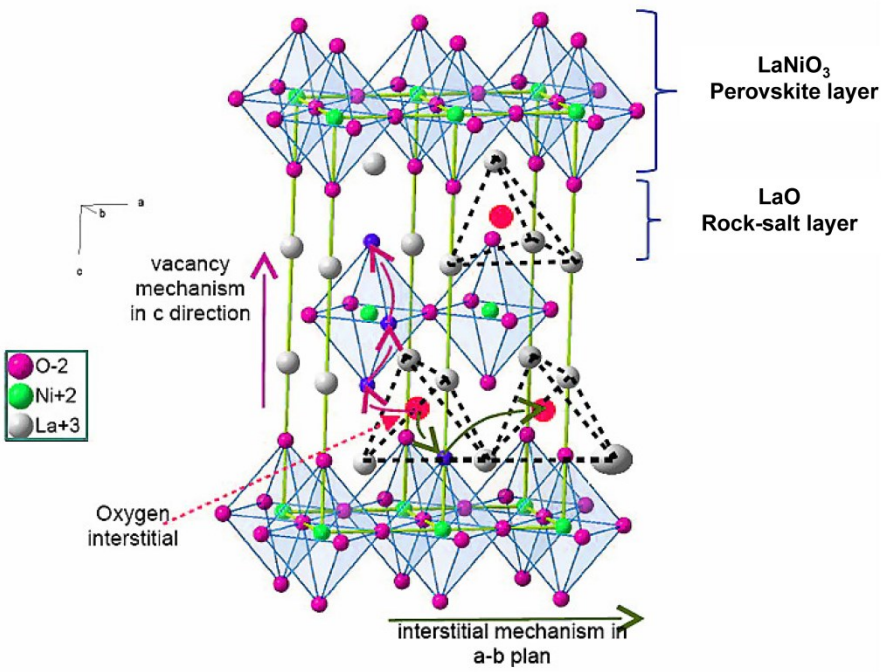


Figure 2.4 Schematic illustration of the $La_2NiO_{4+\delta}$ structure showing the vacancy and interstitialcy ionic transport directions. $LaNiO_3$ perovskite and LaO rock-salt layers are indicated. (adapted from [94])

There are extensive studies and evidence of anisotropic properties in K_2NiF_4-type materials. A number of groups have confirmed the anisotropic diffusion between the

c-axis and ab-axis-directions by means of a secondary ion mass spectrometry (SIMS) technique to determine the oxygen tracer diffusion properties in a number of K_2NiF_4-type compounds: polycrystalline $La_{2-x}NiO_{4+\delta}$ and $La_2Ni_{1-x}Co_xO_{4+\delta}$ [95, 96], single crystalline $La_2NiO_{4+\delta}$ [34], $Pr_2NiO_{4+\delta}$, $Nd_2NiO_{4+\delta}$ [57] and $La_{2-x}Sr_xCuO_{4+\delta}$ [97], and epitaxial $La_2NiO_{4+\delta}$ films [41]. Compared to these experimental investigations of La_2NiO_4, a series of theoretical studies were reported by Minervini, Frayret, and Chroneos [37, 38, 98]. For example, Minervini *et al.* [98] had theoretically investigated the accommodation and migration of excess oxygen by atomic scale computer simulation. According to their results, the oxygen diffusion would be strongly anisotropic with activation energies of $E_a(\perp a,b)$ = 2.9-3.5 eV and $E_a(\parallel a,b)$ = 0.3-0.9 eV, depending upon O^{2-} or O^- diffusion species. It is worth noting that such oxygen excess materials are the most interesting for SOFC cathode applications presently since they are much simpler than the substituted materials and show significant anisotropic oxygen transport rates because of their layered structure. As another example in $Pr_2NiO_{4+\delta}$-based materials, the type of material is generally regarded to have the behaviour analogous to $La_2NiO_{4+\delta}$. Yashima *et al.* have elegantly demonstrated oxygen nuclear density in $(Pr_{0.9}La_{0.1})_2(Ni_{0.74}Cu_{0.21}Ga_{0.05})O_{4+\delta}$ (PLNCG) analysing experimental neutron scattering data by maximum-entropy method, as can be observed in **Figure 2.5 (a)**. Their finding evidently indicated that the oxygen ion diffusion occurs along the interstitial sites (O3) in rock-salt layer and the apical sites (O2) in NiO_6 octahedra, as seen at the blue smearing of nuclear density in the figure. Subsequently, theoretical modelling of $Pr_2NiO_{4+\delta}$ by Parfitt *et al*. using the molecular dynamics method further confirmed the experimental results of PLNCG, as shown in **Figure 2.5 (b)**.

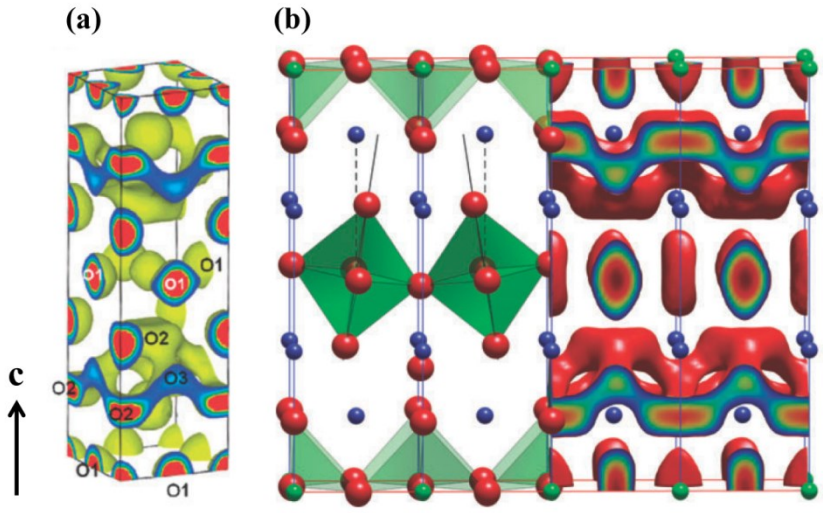


Figure 2.5 oxygen ion diffusion along interstitialcy pathways in K_2NiF_4 phase. (a) represents the oxygen nuclear density distribution through analysing experimental neutron scattering data by maximum-entropy method at 1016°C for $(Pr_{0.9}La_{0.1})_2(Ni_{0.74}Cu_{0.21}Ga_{0.05})O_{4+\delta}$, reported by Yashima *et al.* [99]. O1 is equatorial oxygen, O2 is the apical oxygen, and O3 is the interstitial site. The O1 and O2 are present in NiO_6 octahedra whilst the O3 is in PrO rock-salt layer; (b) shows the theoretical simulation through molecular dynamics method at 827°C for $Pr_2NiO_{4+\delta}$ reported by Parfitt *et al.* [100]. O ions in red, Ni ions in blue and NiO_6 in green.

However, for potential application as a cathode in operation at intermediate temperature (500~700°C), previous research has demonstrated that $La_2NiO_{4+\delta}$-based materials are predominant electronic conductors with very promising ionic conductivity (σ_i = ~10^{-2} Scm^{-1}) [34] with acceptable electronic conductivity (σ_e = 10-100 Scm^{-1} at 327-827°C) [23, 35]. Due to these properties, the $La_2NiO_{4+\delta}$-based materials are therefore comparable with the conventional cathode materials strontium-doped lanthanum manganite (σ_e = ~240 Scm^{-1} at 800°C; σ_i = ~10^{-4}-10^{-7} Scm^{-1} at 800-1000°C) and cobaltite (σ_e = ~1300-1600 Scm^{-1} at 800°C; σ_i = 0.093-0.76 Scm^{-1} at ~800°C) [23, 35, 101, 102]. In addition, long-term stability and compatibility of $La_2NiO_{4+\delta}$ with lanthanum strontium gallate magnesite (LSGM) and ceria gadolinium oxide (CGO) electrolytes have been reported by Amow *et al.* [32, 33] and Sayers *et al.* [103] respectively. For instance, a Ni^{2+}/Ni^{3+} impurity phase can form when $La_2NiO_{4+\delta}$ was heated at 900°C for 2 weeks in

air, as can be seen in **Figure 2.6** [33]. Thus, $La_2NiO_{4+\delta}$ is not ideally suited for practical utilization for IT-SOFCs.

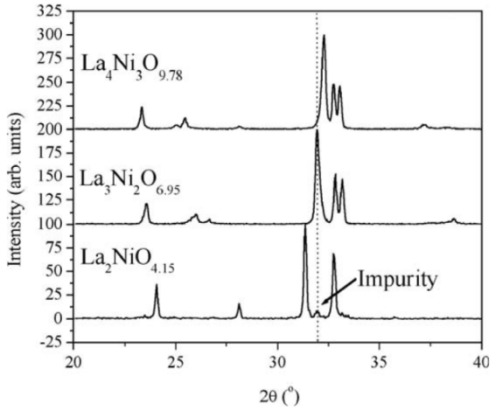


Figure 2.6 Comparison of θ/2θ X-ray diffraction patterns of $La_2NiO_{4.15}$, $La_3Ni_2O_{6.95}$ and $La_4Ni_3O_{9.78}$ bulk samples after annealing at 900°C for 2 weeks in air. Impurity phase formation for $La_2NiO_{4.15}$ after the heat treatment [33].

Apart from La_2NiO_4, the higher order RP phases, $La_3Ni_2O_7$ (n = 2) and $La_4Ni_3O_{10}$ (n = 3), are of interest for use as SOFC cathodes owing to their good long-term stability and compatibility, promising electrode performance, and superior electrical conductivity in operation at intermediate temperature. For example, there was no evidence of formation of significant impurities when $La_3Ni_2O_7$ and $La_4Ni_3O_{10}$ were aged at 900°C for 2 weeks in air (**Figure 2.6**) [33]. Amow *et al.* [33] reported that the electrical behaviour of $La_{n+1}Ni_nO_{3n+1}$ (n = 1, 2 and 3) appears to clearly vary with n values (**Figure 2.7 (b)**) although their data did not completely present the increasing trend with n values, which might be due to the use of low-density bulk samples (54-58%). They claimed that the electrical conductivity results may be improved by better quality of samples. Note that similar experiments were further conducted by Takahashi *et al.* [31], which will be described in the following content. Amow *et al.* also studied the symmetrical cells of these materials with LSGM as the electrolyte, and found that the area-specific resistance (ASR) decreased with increasing n values and $La_4Ni_3O_{10-\delta}$ (δ = 0.22) shows the lowest

ASR value (~1 Ωcm^2) at 800°C, as shown in **Figure 2.7 (b)**. Also, they comment that the trend of decreasing ASR with n apparently correlates with the increasing electrical conductivity with an increase in n, but it might be that the trend is also related to the systematic oxygen deficiency (δ) with the n values. This means that the more vacant oxygen sites in the perovskite layers, the greater the improvement of the oxygen ionic conduction. However, the latter viewpoint needs to be further investigated by means of oxygen tracer diffusion and isotope surface exchange measurement with secondary ion mass spectrometry (SIMS) techniques, and even by using neutron diffraction analysis to understand the distribution of oxygen vacancies in the series of compounds. In addition, despite $La_4Ni_3O_{10-\delta}$ displaying the lowest ASR of ~1Ωcm^2 at 800°C, this value is still higher than the desired value of 0.15 Ωcm^2 reported by Steele and Heinzel [9]. Thus, Amow *et al.* comment that the electrode performance of the higher order RP-phase $La_{n+1}Ni_nO_{3n+1}$ (n = 2 and 3) would be improved by optimising their density, microstructure and thickness.

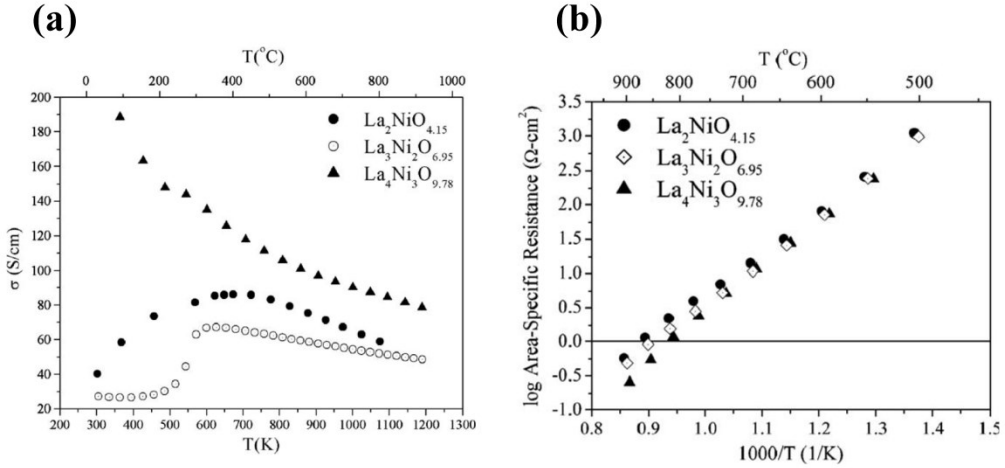


Figure 2.7 (a) electrical conductivity (σ) and (b) ASR as a function of temperature for $La_2NiO_{4.15}$, $La_3Ni_2O_{6.95}$ and $La_4Ni_3O_{9.78}$ bulk samples.

More recently, further studies on the electrode performance of the series of RP phases have been investigated. Pérez-Coll *et al.* [52] investigated the electrode/electrolyte

polarisation properties of La_2NiO_4 and $La_3Ni_2O_7$ as cathodes on a symmetrical cell with samarium-oxide-doped ceria $Ce_{0.8}Sm_{0.2}O_{2-\delta}$ (SDC) + 2% Co as electrolyte at 700-900°C. They found that the ASR of a $La_3Ni_2O_{7-\delta}$ cathode was lower than that of a $La_2NiO_{4+\delta}$ cathode. Furthermore, Takahashi *et al*. [31] reported a single fuel cell performance test regarding the *n* = 1, 2 and 3 members of RP-phase lanthanum nickel oxides at 500-700°C, composed of Ni–SDC//SDC//$La_{n+1}Ni_nO_{3n+1}$ (n = 1, 2 and 3) as an anode, electrolyte and cathode, respectively. The authors found that the ohmic and overpotential losses decreased with an increase in n value, but electrical conductivity increased with increasing n, in accordance with the results reported by Amow [33]. $La_4Ni_3O_{10}$ exhibited better cathode properties than those of the lower members at 700°C. Their cells delivered maximum power density of 10.2, 36.5, and 88.2 mW/cm^2 at 500, 600 and 700°C respectively. The power density values are still relatively low in comparison to conventional perovskite cathodes, but show some promise for future materials development. The results indicate that the performance of $La_3Ni_2O_7$ and $La_4Ni_3O_{10}$ electrodes is improved over La_2NiO_4. Moreover, Lou *et al*. [104] demonstrated that $La_3Ni_2O_7$/YSZ exhibits a promising ASR value of 0.39 Ωcm^2 at 750°C and a single cell of NiO-YSZ//YSZ//$La_3Ni_2O_7$ had a maximum power density of 848 mW/cm^2 at 750°C. Stable cell performance was also observed under a constant current of 0.6 A/cm^2 for over 30 hours at 750°C. They have suggested $La_3Ni_2O_7$ as a promising IT-SOFC cathode.

A couple of recent studies have also been reported for composite-type RP cathodes. Yoo *et al.* [71] infiltrated $La_{n+1}Ni_nO_{3n+1}$ (n = 1, 2 and 3) into YSZ scaffolds. They found that all samples present an increasing electrical conductivity with increasing n number, and thereby the $La_4Ni_3O_{10-\delta}$-YSZ is regarded as a recommended cathode candidate for IT-SOFC. Most recently, Woolley and Skinner [105] reported a series of novel $La_2NiO_{4+\delta}$/$La_4Ni_3O_{10-\delta}$ composites, and found that a 50:50 wt.% $La_2NiO_{4+\delta}$:$La_4Ni_3O_{10-\delta}$

mix exhibits the best ASR of 0.62 Ωcm^2 at 700°C.

Based on the knowledge described above, higher order RP $La_3Ni_2O_{7-\delta}$ and $La_4Ni_3O_{10-\delta}$ phases are suggested as SOFC cathodes. In the next section current development with regard to RP thin-film relevant to SOFC applications will be reviewed.

2.4 Current Development of RP Thin-Films in SOFC Application

Several studies have been performed using nearly fully dense polycrystalline, even ideally single crystals or epitaxial films to avoid the effects of microstructure and composition in the comprehension of the intrinsic properties of the materials as previously commented by Adler [17] and reported in several comprehensive review articles about thin-film technologies for SOFCs [36, 106-108] and micro-SOFCs [109, 110].

Ruddlesden-Popper (RP)-type oxides have attracted great interest as epitaxial thin films due to their intrinsic anisotropic transport properties. Before a fuel cell application can be considered for these thin-film RP oxides, many of the fundamental parameters governing fuel cell performance have to be determined. Evidently these may differ significantly from the bulk materials. Kim *et al.* [42] first successfully deposited the (100)-oriented epitaxial films of undoped $La_2NiO_{4+\delta}$ on $LaAlO_3$ (001) substrates by PLD. The authors demonstrated that the oxygen transport behaviour on a 300 nm film was through a control of surface exchange reaction during Electrical Conductivity Relaxation (ECR) measurements. Interestingly, they found a microstructure reorientation during ECR measurements and two new (200) and (220) reflections were detected by XRD after ECR, indicating that the effect of reorientation can significantly influence the surface exchange activity of the films. In a subsequent article [85], through AC impedance spectroscopy, the authors investigated the kinetic behavior of dense polycrystalline La_2NiO_4 thin-films

with a thickness of 300 nm, grown on yttrium stabilized zirconia (YSZ) single crystal substrates by PLD. They concluded that the electrode reaction is limited by the surface exchange reaction. Furthermore, very high quality epitaxial La_2NiO_4 films grown along the c-axis direction on single crystal $SrTiO_3$ (STO) (100) and $NdGaO_3$ (NGO) (110) substrates were attained by Garcia and Burriel *et al.* [39] via the use of chemical vapour deposition. The authors observed that the values of the electrical conductivity are remarkably improved by decreasing the film thickness such that the values are superior to the highest from bulk materials (~100 Scm^{-1}) [68, 95], and even the values from layers of 50 nm and thinner films are significantly higher than those from single crystal along the ab-axis (~200 Scm^{-1}) [111]. Subsequently, a maximum value for the electrical conductivity of this material (475 Scm^{-1}) in 33 nm thick films was reported by Burriel *et al.* [40]. A comparison of these electrical conductivity data is shown in **Figure 2.8**.

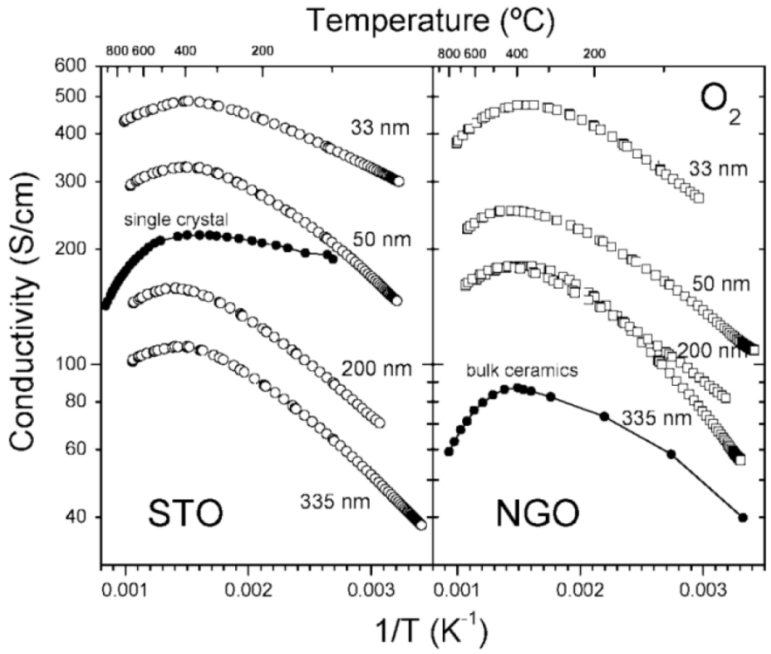


Figure 2.8 Total electrical conductivity of the c-axis oriented $La_2NiO_{4+\delta}$ epitaxial films deposited on STO and NGO substrates as a function of temperature and different thickness in O_2, plotted together with literature data for single crystal and bulk ceramic measured in air. [40]

Further work was performed by the same authors on determining the anisotropic tracer diffusion and surface exchange coefficients of the epitaxial $La_2NiO_{4+\delta}$ films by the oxygen isotopic exchange depth profile (IEDP) method. The authors developed a new and effective method for the measurement of transport properties in two directions, called transverse and longitudinal directions as shown in **Figure 2.9** [41]. Both tracer diffusion coefficients along the c-direction and ab-direction tend to increase with increasing thickness. It, however, seems that both surface exchange coefficients along the two different directions have no direct correlation with film thickness. This study corroborated that the oxygen diffusion and surface exchange exhibits highly anisotropic behavior and both display 2 to 3 orders of magnitude higher values along the ab-plane than those along the c-direction. **Figure 2.10** and **Figure 2.11** display a series of comparison of oxygen diffusion and surface exchange coefficients (D^* and k^*, respectively) from dense polycrystalline, single crystal and epitaxial $La_2NiO_{4+\delta}$ film samples [41]. Most recently, Lee *et al.* [112] reported that the surface exchange kinetics of the (100)-oriented epitaxial $La_2NiO_{4+\delta}$ thin films deposited by PLD was markedly correlated with film thickness and volumetric strain. Moreover, Santiso *et al*. [113] have recently developed a new method, time-resolved X-ray diffraction, to investigate the surface exchange kinetics of $La_2NiO_{4+\delta}$ and $La_2NiO_{4+\delta}/LaNiO_{3-\delta}$ bilayer films. The investigations were through in-situ analysis of the subtle lattice parameter variations when the oxygen stoichiometry of the films was changed under oxidation and reduction cycling, and different temperatures. The unique method complements the typical techniques such as ECR and IEDP to study oxygen exchange and transport properties of thin-film heterostructures.

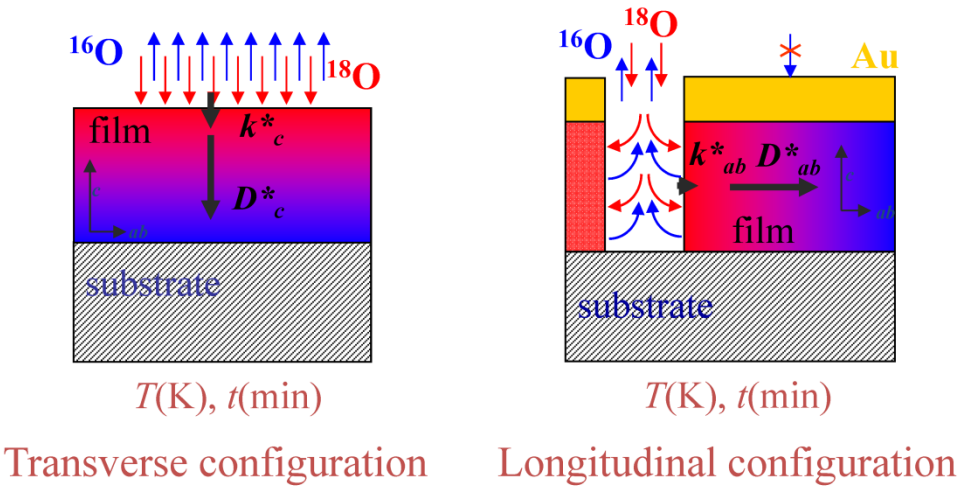


Figure 2.9 Schematic illustration of sample configuration for (a) transverse and (b) longitudinal oxygen tracer transport measurements (adapted from [41])

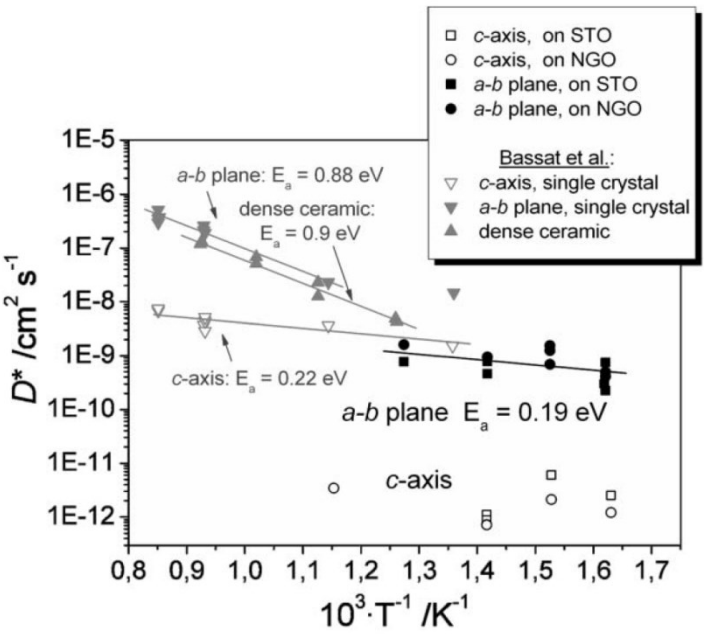


Figure 2.10 Anisotropy of diffusion coefficients for $La_2NiO_{4+\delta}$ epitaxial films grown on STO and NGO in comparison with the literature data for $La_2NiO_{4+\delta}$ single crystal and dense ceramics [41].

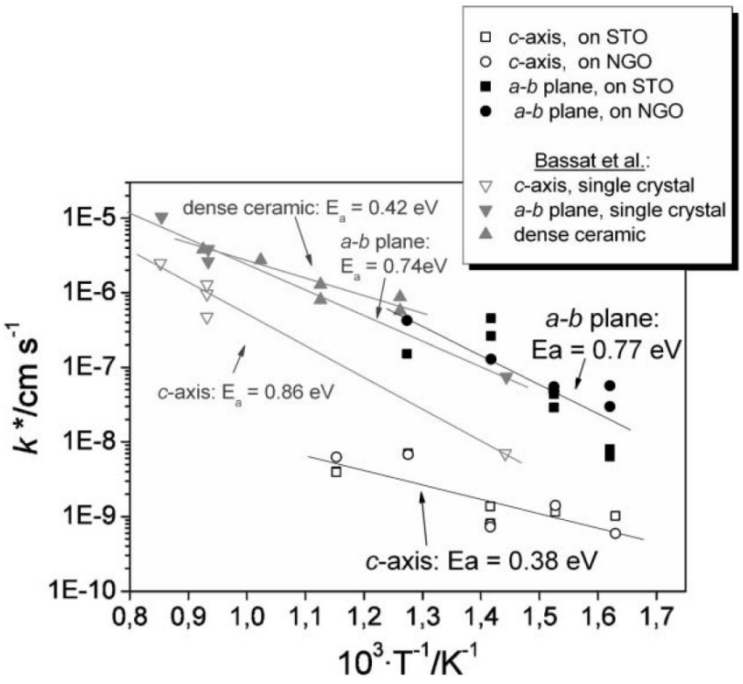


Figure 2.11 Anisotropy of surface exchange coefficients for $La_2NiO_{4+\delta}$ epitaxial films grown on STO and NGO in comparison with the literature data for $La_2NiO_{4+\delta}$ single crystal and dense ceramics [41].

Higher order RP phase lanthanum nickel oxide films (n = 2 and 3) have been first demonstrated by Raju *et al.* [89]. In their studies, oriented perovskite-type $LaNiO_3$, K_2NiF_4-type La_2NiO_4 and higher order RP-phase $La_3Ni_2O_7$ and $La_4Ni_3O_{10}$ films have been deposited on either Si(111) or $SrTiO_3$(100) via the method of Nebulized Spray Pyrolysis with a low processing temperature and the use of precursors of lanthanum and nickel acetylacetonate mixture. The research was the first knowledge available for depositing the n = 2 and 3 members of the monophasic RP-type lanthanum nickelate films, even though the cation stoichiometry of $La_3Ni_2O_7$ and $La_4Ni_3O_{10}$ are slightly off and there is some doubt whether the higher order RP films are oriented. Moreover, Burriel *et al.* [91] attempted to deposit the pure $La_3Ni_2O_7$ and $La_4Ni_3O_{10}$ thin-films by PI-MOCVD. However, despite mixed-phase films being obtained, particular films composed of pure La_2NiO_4 and $LaNiO_3$ forming a microstructure with disordered intermixed nanodomains were observed. These nanodomains progressively increased with the n value, and the

planar resistivity of the films shows a progressive change from the semiconducting to metallic behaviour (see **Figure 2.12**). The findings suggest that the transport properties in nanostructured epitaxial films of the $La_{n+1}Ni_nO_{3n+1}$ series could be enhanced by the nanodomains, as commented by the authors. This unfolds a new aspect to prepare new nanocomposite films with tailored properties. A recent study by Ryll *et al.* [90] demonstrated polycrystalline $La_4Ni_3O_{10-\delta}$ films deposited on sapphire and CGO substrates through spray pyrolysis. Their studies revealed that the crystal structure and microstructure were tailored by heat treatment processes, and hence significantly influence their electrical and electrochemical (ASR) properties.

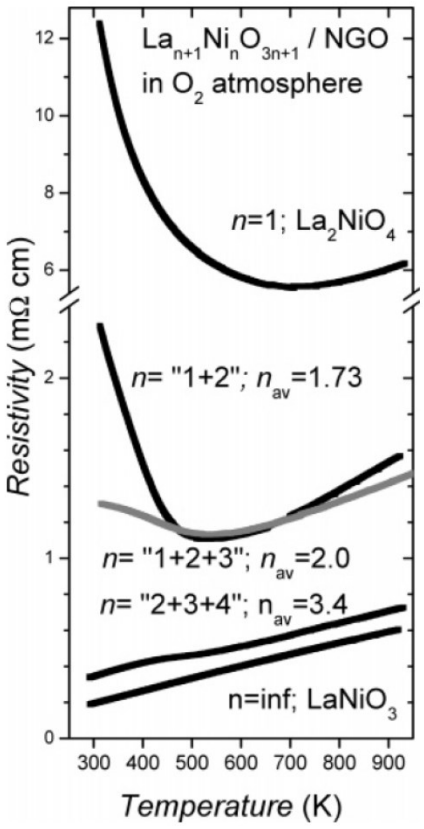


Figure 2.12 High temperature planar resistivity of the epitaxial films deposited with different La/Ni composition on NGO substrates. The average n value corresponding to each curve is labelled aside. The resistivity progressively varies with increasing n value and changes from semiconducting to metallic behaviour [91].

Recently the studies on heterostructures of the RP-phase oxide films are of great interest in the development of SOFC applications. RP-phases possess natural heterostructures with alternating blocks of perovskite and rock-salt. Thus, it is of interest to investigate whether growing heteroepitaxial films of these oxides will enhance electrical and electrochemical properties in SOFC cathodes.

For the first example of half cells directly fabricated with RP-type epitaxial films on single crystal electrolyte material, as shown in **Figure 2.13 (a) and (b)**, Yamada *et al.* [114] successfully deposited the heteroepitaxial SOFC systems prepared by 14nm-thin (110) RP-type $Nd_2NiO_{4+\delta}$ epitaxial films on (100) YSZ single crystal electrolytes. The authors claimed that the K_2NiF_4 structure may possess a certain extent of inherent flexibility enabling epitaxial growth. They discovered $Nd_2NiO_{4+\delta}$ epitaxy can grow along the orientation of (110) plane on (100) YSZ substrates although its lattice mismatch is as large as that of 9.9% with the YSZ substrates. Despite the rather similar value of lattice mismatch along growth directions of (100) or (001), however, it is surprising that they found no orientations of (100) or (001) of $Nd_2NiO_{4+\delta}$ epitaxial films on the (100) YSZ substrates. This might be caused by the different surface energy of crystal planes. Moreover, the authors also found the activation energy for oxide ion conductivity in the series of epitaxial films have a significant influence presumably by the strong compressive strain. In addition to $Nd_2NiO_{4+\delta}$(110)//YSZ(100), the Yamada's group [115] has subsequently performed another configuration of $Nd_2NiO_{4+\delta}$(100)//YSZ(110). Successfully fabricated different orientations of $Nd_2NiO_{4+\delta}$ epitaxial films were achieved by changing the orientation of YSZ substrates. They discovered a new aspect with regard to utilising the advantage of intrinsic anisotropic transport properties of RP-phase materials, and their studies offered the possibility of optimising their oxide ionic transport and catalytic activity by preparing highly oriented samples to align diffusion channels and

surface orientation.

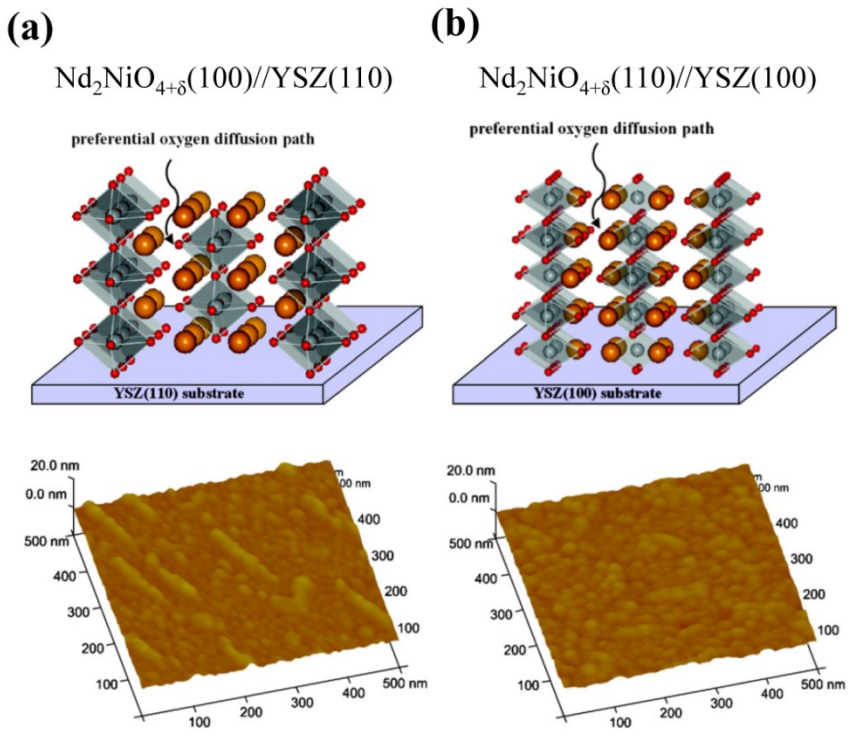


Figure 2.13 Schematic illustration and 3D AFM images of (a) $Nd_2NiO_{4+\delta}$(100)//YSZ(110) (a) and (b) $Nd_2NiO_{4+\delta}$(110)//YSZ(100) hetero-epitaxial films [115].

For subsequent related studies, an investigation into large-grained polycrystalline $La_{0.6}Sr_{0.4}CoO_3$/$(La,Sr)_2CoO_4$ grains was conducted by Sase *et al.* [116] through SIMS and impedance spectroscopy analysis. A remarkable enhancement of the oxygen surface exchange rate was found at the interface of the $La_{0.6}Sr_{0.4}CoO_3$/$(La,Sr)_2CoO_4$ grains (approximately three orders of magnitude larger than single $La_{0.6}Sr_{0.4}CoO_3$ phase). The authors further confirmed the phenomenon through a thin-film structure of $La_{1.5}Sr_{0.5}CoO_4$/$La_{0.6}Sr_{0.4}CoO_3$/CGO fabricated by PLD. After ^{18}O isotope exchange measurements, the observation of SIMS images demonstrated a large amount of ^{18}O incorporation occurs at the hetero-interface of $La_{1.5}Sr_{0.5}CoO_4$/$La_{0.6}Sr_{0.4}CoO_3$ polycrystalline layered-films as can be observed in **Figure 2.14** [117]. This indicates the

importance of hetero-interfaces on oxygen surface exchange kinetics. Further evidence, demonstrated by Crumlin *et al*. [118], is oxygen reduction kinetics enhancement on heterostructured films of $La_{0.8}Sr_{0.2}CoO_{3-\delta}$ (LSC_{113}) decorated by $(La_{0.5}Sr_{0.5})_2CoO_{4\pm\delta}$ (LSC_{214}) deposited on YSZ(001) substrates. The <15nm-thick decoration leads to the formation of nano-islands of LSC_{214} and becomes partial coverage on LSC_{113} while the 15nm-thick LSC_{214} exhibits a full dense surface layer. They also found that a similar enhancement, approximately 3-4 orders of magnitude larger than LSC_{113} for the partial coverage samples. Most recently, an example of multilayer superlattices of $La_{0.8}Sr_{0.2}CoO_3/(La_{0.5}Sr_{0.5})_2CoO_4$ was demonstrated by Chen *et al.* [119]. The authors analysed such multi-heterostructures through a novel combination of in-situ scanning tunnelling microscopy and spectroscopy coupled with sample preparation by grazing incidence focused ion beam milling. Their investigations provided further understanding of local electronic structure of oxide hetero-interfaces at elevated temperature and confirmed the heterostructure to be a key role for the acceleration of oxygen reduction kinetics.

In addition to the fundamental research mentioned above, SOFC research on thin-film technologies includes research into the potential applications. A major field of the application research is the development of micro-SOFCs (μSOFCs) for portable devices such as laptops and mobile phones [106, 109, 110, 120-122]. Beckel *et al.* [110] pointed out that thin-film materials with well-defined structures can be also utilised to improve the performance of μSOFC cathodes.

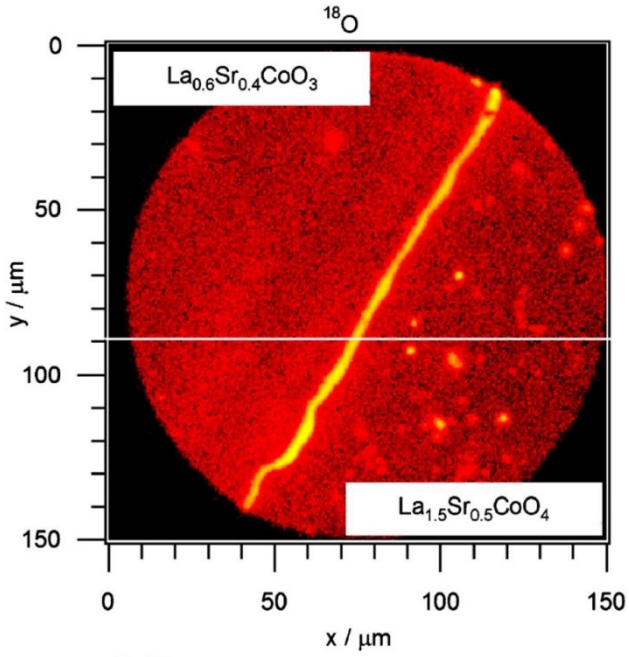


Figure 2.14 SIMS image of ^{18}O intensity at the surface of $La_{1.5}Sr_{0.5}CoO_4/La_{0.6}Sr_{0.4}CoO_3$/CGO, after the diffusion annealing at 773 K for 180 s in 0.2 bar $^{18}O_2$ gas [117].

2.5 Summary

Based on all the reviews, it appears clearly that although layered RP-phases oxides are quite promising for use as SOFC cathodes, their intrinsic diffusion and surface exchange properties have not yet been fully understood due to the influence of non-kinetic factors such as porosity and density, especially in the case of higher order RP-type materials. Moreover, growing well-defined RP-phase epitaxial films makes the possibility of either investigating or controlling their intrinsic anisotropic transport properties. Further application in the series of layered epitaxial films is highly expected for actual SOFC devices. By building on our current knowledge, this thesis will further cover a series of investigations of $La_{n+1}Ni_nO_{3n+1}$ (n = 1, 2 and 3) thin-films, but mainly focus on $La_3Ni_2O_{7-\delta}$ (n = 2) and $La_4Ni_3O_{10-\delta}$ (n = 3) phases.

Chapter 3 Experiments and Characterisation Techniques

The purpose of this chapter is to present an overview of the experiments and the characterisation techniques used for this thesis. The pulsed laser deposition (PLD) technique will be described, including background, principles and the general deposition procedure adopted for the growth of the RP-type lanthanum nickelate films, followed by the synthesis method of PLD targets. Next, a series of material characterisation techniques will be demonstrated. Finally, the functional property characterisation techniques utilised for charactering the obtained RP films.

3.1 Pulsed Laser Deposition (PLD)

The pulsed laser deposition (PLD) technique was utilised to grow the layered RP-type $La_{n+1}Ni_nO_{3n+1}$ (n = 1, 2 and 3) epitaxial films in this work. Prior to describing the experimental procedure, a brief background and basic principles of PLD will be described.

3.1.1 Background of PLD

PLD is a type of physical vapour deposition (PVD) technique. This technique was first introduced by Smith and Turner in 1965 [123], and by Hass and Ramsey in 1969 [124] for growing semiconductor and dielectric films due to the discovery of lasers. Then it was rapidly developed and popularised in the 1980s due to the successful deposition of high-temperature superconducting films (e.g. $YBa_2Cu_3O_{7-\delta}$) [125]. Such great attraction is particularly because of the primary characteristics of the PLD technique – the complex stoichiometric transfer from a single target to deposited films, allowing for precise

stoichiometric control. Since these successful developments, this technique has been widely applied to deposit a very widespread range of materials such as superconductors, semiconductors, insulators, oxides, nitrides, carbides, metals, polymers, and even bio-materials throughout various research fields [126]. In addition, this technique has presented remarkably effective fabrication of epitaxial films, superlattices, and electronic devices in the past few decades [126, 127]. Recently, PLD is also gathering increasing attention in the current development of electrochemical applications [128].

PLD System Setup and Principle

A typical PLD system setup is schematically shown in **Figure 3.1**, which mainly consists of a vacuum chamber, a substrate heater, usually six target holders, and a high energy density UV pulsed laser (pulse duration is in nanosecond range). The distance between target and substrate is approximately 5 cm and a spinning target is usually applied during the deposition in order to obtain a homogeneous film. Several targets can be positioned in the chamber to facilitate the production of multilayer films. The system is normally operated under a high vacuum (typically $\leq 10^{-6}$ Torr) and a controlled gas pressure during the deposition. A number of different gases can be used in the system, including inert gas (e.g. Ar) and reactive gas (e.g. O_2, N_2, etc.). For example, performing PLD in an O_2 background gas aids the maintenance of the oxygen stoichiometry of the deposited oxide films.

The laser is guided via UV transparent mirrors, focused by quartz lenses, passed through a UV transparent quartz window into the high vacuum chamber, and then reached on the target surface. The UV transparent lenses and windows is to minimise the loss of the laser beam. The laser beam is applied to vaporise or ablate materials, forming a plasma plume (including atoms, electrons, molecules, ions, clusters etc.) to transfer the ablated materials onto the substrate surface that desired films are to be grown upon.

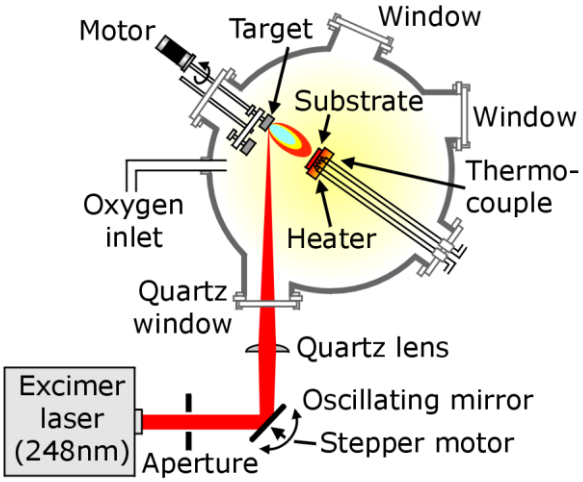


Figure 3.1 Schematic illustration of PLD system setup (adapted from [129])

A schematic illustration with regard to the pulsed laser ablation (PLA) process is conceptually demonstrated and described in **Figure 3.2**, although the laser-target interaction during PLA is a very complicated process and still has not been fully understood [130]. When a high energy, nanosecond pulsed laser beam impinges on the target, the very high energy is immediately absorbed by a very small volume of target materials, resulting in electronic excitation. Since the thermal conductivity of the materials is far too low to dissipate the high energy in the very short period of laser pulse duration, the small volume of materials is instantaneously evaporated via a superheating process, forming a high-temperature plasma plume [131]. Such process is far from thermodynamic equilibrium. Therefore, the melting temperature of the materials is of minor importance, and the stoichiometry of the materials can be preserved from the target to substrate through the plasma plume [132].

However, the rapid heating during ablation of the target materials may cause phase transitions and introduce high amplitude stress waves in the target, leading to the exfoliation phenomenon which can bring the formation of aggregates and particulates on the film surface [130, 133]. The PLD dynamics, therefore, are closely associated with the

laser energy, background gas, and the physical and chemical properties of target materials (such as target density, surface morphology of target, ionisation of species, electronic excitation, etc.) [130, 134], and consequently has significant influence on the quality of the deposited films (e.g. density, surface roughness and stoichiometry of deposited films) [133, 135-137]. Further related discussion in terms of the PLA of RP-phase lanthanum nickelate targets in this work will be investigated in Ch.4.

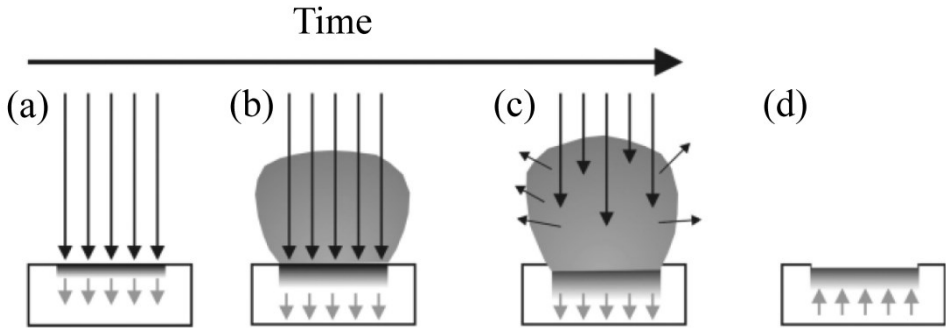


Figure 3.2 Schematic illustration of PLA process: (a) laser pulse is initially absorbed, melting and vaporisation (shaded area indicates melted materials, and the short arrows represent motion of the solid-liquid interface), (b) vaporisation continues, the melt front propagates into the solid target, and laser plume starts to form, (c) absorption of incident beam through the expanding plum leads to plasma formation, (d) the melt front recedes after the laser pulse, resulting re-solidification [130].

There are a number of advantages of using PLD for growing oxide films as follows [132]. As mentioned above, the most admirable merit is stoichiometry transfer from a single target with multi-element materials to deposit complex oxide films. The phase of the targets generally does not need to be exactly identical to the phase of the desired films, but the phase separation has to be smaller than the laser spot, and ensuring the right cation stoichiometry is of importance. In addition, a small target size is acceptable (even $< 1 cm^2$), depending on the adopted spot size of the laser beam. Furthermore, growing high-quality epitaxial oxide films, superlattices, multi-target for multilayer, and even the growth via layer-by-layer deposition is effectively achievable. Other advantages are about precise

thickness control by laser pulses, short deposition time and high growth rate (up to ~10 μm/s). On the other hand, the main drawback for this technique is that it is not yet suitable for large-scale production in industry despite several studies on the scale-up of commercial PLD [138]. Additionally, the issues of particulates [133] is of importance. In terms of ceramic material targets, highly dense targets are favourable for use to reduce or avoid particulate formation during the deposition. Also, placing a cover in front of the target with the target spinning can minimise the issue and increase the homogeneity and quality of the deposited films [132, 133].

3.1.2 Thin-Film Growth

Thin-film growth is governed by thermodynamics and kinetics, covering various nucleation, adsorption and diffusion processes on the surface. When numerous vapour atoms are continuously deposited on the surface, a variety of atomic migration processes can take place on the surface and interface during film growth such as deposition, adsorption, desorption, diffusion on terraces, diffusion along step edges, re-evaporation, nucleation, and coalescence, etc. [136, 139]. These processes may also interact with each other, forming two dimensional (2D) and three dimensional (3D) clusters.

Based on these processes, three common growth modes can occur and are schematically shown in **Figure 3.3**. **Figure 3.3 (a)** shows 2D layer-by-layer growth mode (also called Frank-van der Merwe), which arises because the atoms of the deposited materials are more strongly attracted to the substrate than they are to themselves. This growth mode leads to the best crystallographic structure of the deposited films and hence can form unit cell thick layers. Conversely, 3D island growth mode (Volmer-Weber) is driven from the fact that the deposited atoms are more strongly bound to each other than they are to the substrate (see **Figure 3.3 (c)**). This island mode results in the effects of

more crystallographic disorder and less consummate layers in the films, leading to the formation of defects and grain boundaries. For an intermediate case, the layer-island growth mode (Stranski-Krastanov), the film starts to grow layers initially, followed by growing islands [136, 140].

The growth modes can be significantly influenced through the surface morphology of the substrate as well as the lattice mismatch between film and substrate. These features play important roles to affect the thin-film growth modes, leading to the microstructural variations of the film, covering grains, dislocations or different types of defects. Moreover, the growth conditions also can dramatically alter the microstructure of the deposited film, and consequently influence the quality of the film.

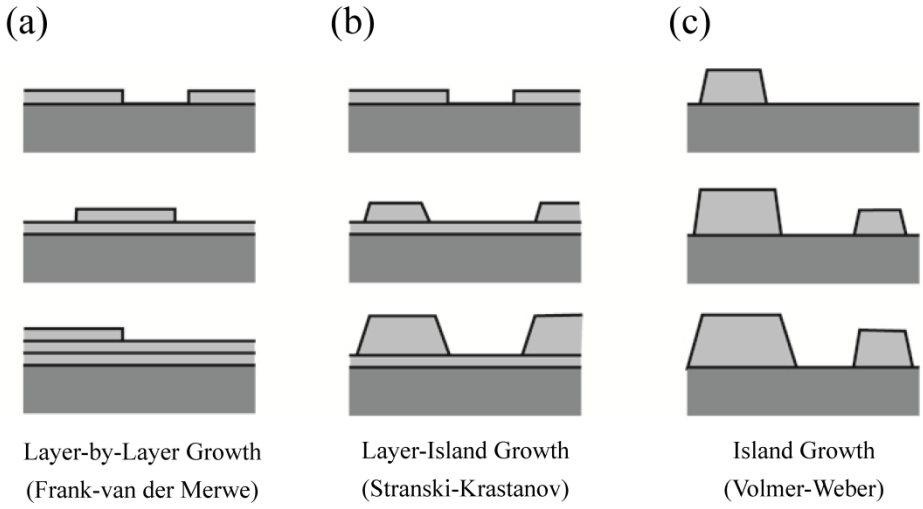


Figure 3.3 Schematic representation of the three typical thin-film growth modes: (a) is layer-by-layer growth mode (Frank-van der Merwe), (b) is layer-island growth mode (Stranski-Krastanov), and (c) island growth mode (Volmer-Weber) (adapted from [140]).

In comparison with other deposition techniques (such as molecular beam epitaxy (MBE) and sputtering), PLD has higher supersaturation, resulting in a very large nucleation density covering on the surface and therefore leading to the formation of continuous layers via a favourable 2D growth (layer-by-layer) instead of 3D growth. Thus

highly uniform and smooth (low roughness) films can be grown [135, 136].

3.1.3 General Deposition Procedure

Prior to deposition, all the bare substrates (i.e. $SrTiO_3$ and $NdGaO_3$) were ultrasonically cleaned with acetone, isopropanol and deionised water for 3 minutes for each solvent and dried with a N_2 gas gun in order to remove contamination (e.g. organics or impurities introduced during substrate preparation) on the sample surface. Furthermore, prior to deposition, a laser calibration process is required in order to ensure that the laser beam is properly aligned on the target with an appropriate spot size and energy. The energy at the target position must be always measured through a laser energy detector.

After the cleaning and laser calibration process, the substrates were mounted on the stage of the heater using conductive silver paste for providing good thermal contact, and masked with a small droplet of the TiO_2 paint at the edge of the substrate surface in order to create a step for the thickness measurement (described in section 3.3.4) after deposition. The working distance between the substrate and the target was 50 mm. The substrates were heated to deposition temperature with 50°C/min under vacuum condition ($3x10^{-5}$ Torr). When reaching the deposition temperature, the oxygen gas filled the chamber to 700 Torr to further burn off the remaining contaminants, and then the oxygen pressure was manipulated to the deposition pressure. Before deposition, with a closed shutter on the substrate, a pre-ablation process with 300 pulses is required to remove any accumulated layers of contamination, followed by the deposition process. During deposition, a spinning movement was applied to the target in order to keep an even ablation, and a homogeneous deposition. After deposition, the sample was cooled down to 200°C with a rate of 10°C/min under a filled O_2 atmosphere of 600 Torr, then followed by natural cooling to room temperature (RT). Having reached RT, the sample was taken out

and cleaned via the cleaning procedure mentioned above.

For the PLD equipment adopted in this work, a KrF excimer laser (λ=248 nm, Lambda Physik COMPex 201) was utilised. The spot size of the laser beam was approximately 0.10-0.13 cm^2, depending on the laser energy used. Further deposition conditions (such as deposition temperature, oxygen partial pressure and laser fluence) for the layered RP-type $La_{n+1}Ni_nO_{3n+1}$ (n = 1, 2 and 3) films will be systematically investigated in Chapters 5 and 6 in detail in order to optimise the growth conditions for these complex materials.

3.2 Synthesis of PLD Targets

The synthesis method used in this work was the modified Pechini sol-gel route [141]. The basic principle of the method is utilizing multifunctional organic acids capable of chelating metal cations to form complex precursor solution (sol), which is then polymerised to form a polymeric network with the incorporated metal cations via polyhydroxy alcohol. The formed organic-polymeric-metal solution is dehydrated to form plastic-like gel, followed by a calcination process to remove organic compounds, resulting in the production of fine powder of the desired metal oxide. The full details of the sol-gel chemistry are beyond the scope of this thesis and therefore interested readers are referred to the comprehensive references [142, 143].

The utilized synthesis conditions for the lanthanum nickelate targets were based on previous literature, reported by Fontaine *et al.* [79, 80] and Amow *et al.* [32, 33]. The essential steps of the synthesis are presented in **Figure 3.4 (a)**. Firstly, lanthanum nitrate ($La(NO_3)_3$) and nickel nitrate ($Ni(NO_3)_2$) solutions were prepared using stoichiometric amounts of the $La(NO_3)_3$•$6H_2O$ (99.999% Aldrich) and $Ni(NO_3)_2$•$6H_2O$ (99.0%, Fluka)

salts, respectively, with the La and Ni molar concentration both of 0.5 mol/L. The molar concentrations of the solutions were confirmed by ICP-AES (inductively-coupled plasma atomic emission spectroscopy), which will be described later.

To make precursor solutions, the $La(NO_3)_3$ and $Ni(NO_3)_2$ starting solutions were mixed in stoichiometric proportions ($La(NO_3)_3$: $Ni(NO_3)_2$ = 2:1 for $La_2NiO_{4+\delta}$, 3:2 for $La_3Ni_2O_{7-\delta}$ and 4:3 for $La_4Ni_3O_{10-\delta}$), stirred on a hot plate with a magnetic stirrer, and heated at ~90°C. With continuous stirring, a 1:1 molar ratio of citric acid (CA) and polyethylene glycol (PEG) was added in order until each was completely dissolved to form an organic-polymeric-metal ions complex solution. The ratios of CA to nickel metal were held at 3:1 for $La_2NiO_{4+\delta}$, 9:2 for $La_3Ni_2O_{7-\delta}$ and 9:3 for $La_4Ni_3O_{10-\delta}$.

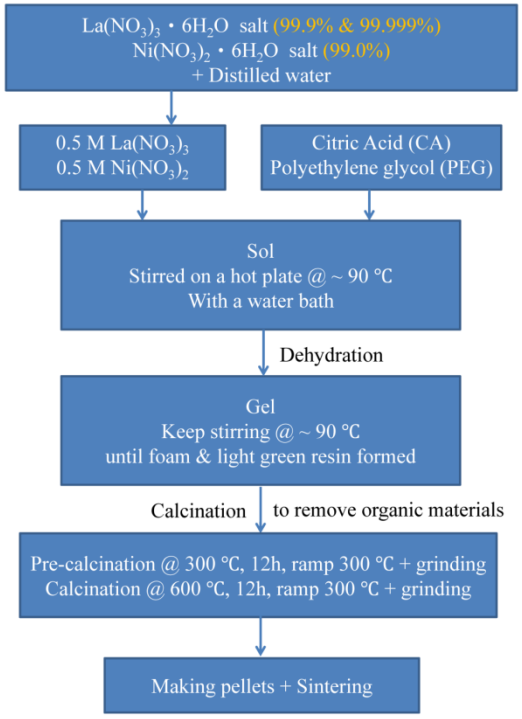
The precursor solutions were dehydrated at approximately 90°C on a hot plate with a water bath and constant stirring (for ~10 h depending on the amount of solutions) until a green gel formed, and the stirrer is needed to be taken out before gel formation, otherwise there is a small loss of the final products. The gel is continuously heated at a constant temperature for 2 h, and then is put into a drying oven with ventilation to leave overnight at ~90°C until the formation of a light-green solid polymeric resin. In the next step, the resin was decomposed in a decomposition furnace at 300°C (ramp: 300°C/h) followed by a grinding step; a subsequent calcination with increasing temperature at 600°C (ramp: 300°C/h) was carried out. The resulting powders were all ground with a mortar and pestle.

To make PLD targets, the precursor powders were pelletized by using the uniaxial press and the pellets were sintered in static air with the conditions for each lanthanum nickelate phase as shown in **Figure 3.4 (b)**.

The density of the final PLD targets ($La_2NiO_{4+\delta}$, $La_3Ni_2O_{7-\delta}$ and $La_4Ni_3O_{10-\delta}$) was determined using the Archimedes principle. Their chemical composition (cation ratio) was determined by means of ICP-AES and EDX (energy-dispersive X-ray spectroscopy)

to confirm the cation stoichiometry for each target. In addition, their phases were verified by using x-ray powder diffraction (XRD). All of these techniques will be described in the following sections.

(a)



(b)

Sintering Conditions

Materials	T (°C)	Ramp (°C/h)	Sintering Time
$La_2NiO_{4+\delta}$	1370	150	24h
$La_3Ni_2O_{7-\delta}$	1100	300	2days
$La_4Ni_3O_{10-\delta}$	1050	300	2+2days* or more*

* With intermediate grindings

Figure 3.4 (a) The flow chart of the synthesis procedure and (b) the table of the sintering conditions for $La_2NiO_{4+\delta}$ (n = 1), (b) $La_3Ni_2O_{7-\delta}$ (n = 2) and (c) $La_4Ni_3O_{10-\delta}$ (n = 3) target preparation

3.3 Material Characterisation

3.3.1 Density Measurement of PLD Targets

The density of the targets was determined through a high-accuracy balance and using Archimedes' Principle:

$$\rho_A = \frac{W(a)\cdot\rho_{fl}}{I(W(a)-W(fl))} \quad (3.1)$$

Where ρ_A represents the measured density of the targets by Archimedes' Principle; ρ_{fl} represents the density of the fluid (i.e. here is distilled water); W(a) represents the weight

of the specimen when it is dry; W(fl) represents the weight of the specimen when it is immersed in a fluid; I represents a correction factor associated with the water displaced by the wires of the weighing assembly.

Note that before measuring the W(fl), immersing the specimens in distilled water with vacuum for 15 minutes is necessary to remove bubbles from the external voids of the samples and ensure they are completely filled with water.

By comparing measured density by Archimedes' Principle (ρ_A) with theoretical density (ρ_{the}), the relative density (ρ_A/ρ_{the}) of a sample can be worked out. The theoretical density of the oxide materials can be determined by the formula:

$$\rho_{\text{the}} = \frac{weight\ of\ ions\ within\ unit\ cell}{volume\ of\ unit\ cell} = \frac{n'(\sum M_A + \sum M_B)}{V_C N_A} \quad (3.2)$$

Where n' represents the number of cation and anion atoms in the unit cell; $\sum M_A$ represents the sum of atomic weights of all cations in the unit cell; $\sum M_B$ represents the sum of atomic weights of all anions in the unit cell; V_C the volume of unit cell; N_A Avogadro constant (i.e. 6.022×10^{23} mol^{-1}).

The related lattice parameters of the materials for calculating their theoretical density can be obtained from crystallographic data, that is, the Inorganic Crystal Structure Database (ICSD) from the Chemical Database Service (CDS).

3.3.2 Inductively-Coupled Plasma Atomic Emission Spectroscopy (ICP-AES)

Inductively coupled plasma - atomic emission spectroscopy (ICP-AES) is a conventional analytical technique to identify the composition (or stoichiometry) of materials through determining concentration of measured elements with a level of parts per million (ppm) to parts per billion (ppb) range and is hence highly sensitive. The technique exploits the fact of stimulating electronic transitions of a particular atom. The process occurs as an inductively coupled plasma stimulates electrons of atoms from the ground state to the

excited state, leading to the emission of electromagnetic radiation at a characteristic emitted wavelength for each particular element when they return to the ground state. Although each element emits energy at multiple wavelengths, the technique is capable of selecting a single wavelength (or a very few) for the measurement of a given element.

For the utilised ICP-AES instrument, argon gas is used to generate the plasma, and the plasma is confined and stabilised by an intense electromagnetic field. To execute the measurements, the tested solid samples are required to be dissolved in nitric acid solution, and introduced as an aqueous mist to the plasma flame through a nebulizer. The samples immediately collide with electrons and charged ions in the Ar plasma, resulting in electronic transitions repeatedly and giving light at specific wavelengths, which permits the identification of elements. The intensity of the light corresponds to the concentration of each particular element within the given sample.

As mentioned above, the instrument is highly sensitive. The preparation of the solution sample with appropriate concentration is therefore of importance; otherwise, the detectors can be saturated if the concentration of tested samples is too high, this will consequently lead to significant experimental errors. For the utilised detector in this instrument, the most accurate concentration signal that can be detected is at approximately 10 ppm. Thus, the tested samples were diluted with distilled water to around this level. Furthermore, to analyse the concentrations of the tested elements (e.g. La and Ni) in a given sample, standard solutions with these elements are required as references. These standard solutions were purchased from commercial sources (MBH Analytical Ltd). For the ICP-AES measurements, these standard solutions were also diluted with distilled water and prepared with the concentration levels of 1, 5 and 20 ppm. A blank solution (distilled water) with 0 ppm was also prepared. Based on these standards, a calibration line can be created. If the tested sample is diluted to the appropriate level, then its concentration should lie on the line, indicating the validity of the measurements.

Based on the obtained concentration (ppm) from tested samples, the cation stoichiometric ratio (La/Ni) of a PLD target can be calculated using the following formula:

$$\frac{La}{Ni} = \frac{moles(La)}{moles(Ni)} = \frac{ppm(La)/M(La)}{ppm(Ni)/M(Ni)} \tag{3.3}$$

where $M(La)$ and $M(Ni)$ represents the atomic weights of La and Ni cations.

The ICP-AES measurements for this thesis were performed using Thermo Scientific iCAP 6300 Duo spectrometer (Thermo Electron Corporation). For more detailed information on ICP-AES, readers are referred to a comprehensive text [144].

3.3.3 X-ray Diffraction (XRD)

X-ray Diffraction (XRD) is a conventional characterisation technique for primarily evaluating the crystallographic structure of a material, and is particularly a non-destructive technique. Thus, it can be applied before, during, and after experiments without any effects or damage to the materials.

This technique is based on incident X-ray beams interacting with a series of crystallographic planes in a crystalline material. It also relies on the fact that the X-ray wavelength is comparable to the atomic spacing of the crystalline material, resulting in diffraction. Then a unique diffraction pattern can be obtained to present the features of a certain structure for the material. This behaviour only takes place when a proper X-ray wavelength is selected, and the diffraction condition is satisfied. This condition is the well known Bragg's law, which is:

$$n\lambda = 2d_{\mathrm{hkl}} \sin\theta \tag{3.4}$$

where n is an integer of the order of the reflection, λ is the wavelength of the incident X-ray (typically Cu Kα radiation (λ = 1.5418Å)), d_{hkl} is the lattice interplanar spacing between Miller planes passing through the crystal structure, h, k, and l are defined by the

Miller indices, and θ is the angle of incidence to the planes.

The fundamental diffraction equation states that constructive interference occurs only if the path difference is an integral of multiple X-ray wavelengths, and the monochromatic X-ray diffraction only takes place at those particular incident angles satisfying Bragg's law. Thus, if λ is known and the intensity of the diffracted beam is obtained by a scan over a range of θ, then the interplanar spacing can be determined as shown in **Figure 3.5**.

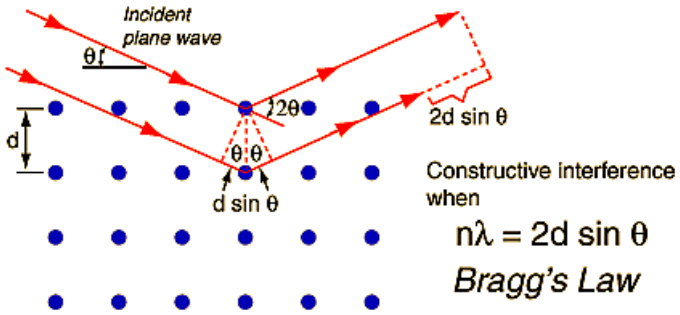


Figure 3.5 An illustrated diagram of Bragg's Law for X-ray diffraction (adapted from [145])

In this work, the XRD technique was applied to identify the crystallographic structure and phase purity of the obtained PLD targets (including powders) and thin-films. The crystallinity and orientation of the films were also characterised. For PLD target materials the measurements were carried out using symmetric θ/2θ geometry PANalytical X'Pert Pro MPD with X'Celerator detector, Ni filtered Cu K_α radiation (λ = 1.5418), and tube voltage/current at 40 kV/40 mA. The diffraction scans were measured between 10° to 80° with a step size of 0.0334° and counting rate of 50 seconds per step.

In the case of characterising the obtained thin-films, different equipment was used. It was a high-resolution X-ray diffractometer (PANalytical X'Pert Pro MRD), utilizing Cu K_α radiation (λ = 1.5418 Å) with graphite monochromator, X'Celerator detector for high-speed data collection, and 4-angle (2θ, ω, φ and Ψ scan axes) goniometer, as

schematically shown in **Figure 3.6**. The equipment was used to analyse the orientations and crystallinity of the epitaxial films through symmetric θ/2θ, rocking curves, and phi (φ) scans, and reciprocal space mapping (RSM) measurements, which will be described as follows.

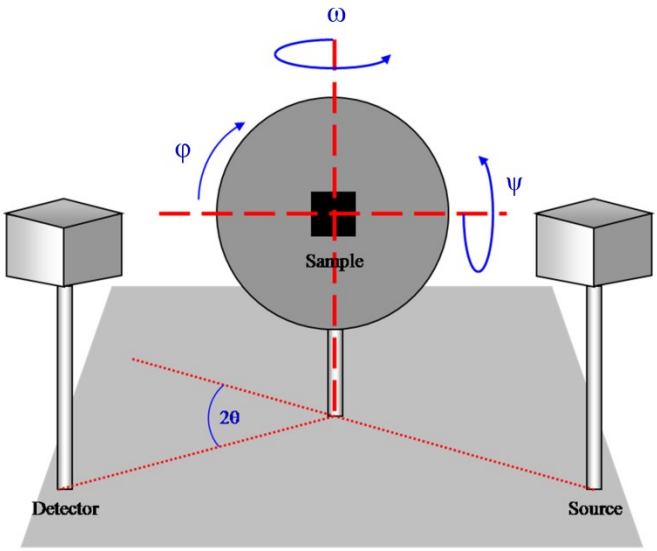


Figure 3.6 Schematic diagram showing the X'pert MRD system, indicating the 2θ, ω, φ and Ψ scan axes (adapted from [146])

Symmetric θ/2θ Scans

The symmetric θ/2θ scans were used to determine the out-of-plane orientations of the films. Prior to the measurements, the film samples must be precisely aligned in order to position the diffraction vector perpendicular to the film surface through a series of alignment calibrations (including Z-scans, ω-scans and Ψ-scans). A 1/16° divergent slit was used for measuring 5×5 mm^2 samples. The diffraction peaks were identified using X'pert Highscore software, and ICSD (Inorganic Crystal Structure Database), provided by the CDS (Chemical Database Service). All 2θ peak positions of every (00L) reflection for each RP material were carefully fitted by the Lorentz method. The out-of-plane (c-axis) parameters of the films were determined using these fitted 2θ angles.

Rocking Curves

Rocking curve measurements were performed to estimate the crystallinity or mosaicity of the films. Mosaicity is created by slight misorientations of different crystals when they nucleate and grow on the substrate during deposition. Before measuring the rocking curves, again the alignment calibration for the sample position is required. Rocking curves were performed such that the detector is fixed at a 2θ position of a Bragg peak (selected from the obtained data of the symmetric θ/2θ scans above); that is, the fixed angle between detector and source is a constant angle. Then the sample is rocked in the vicinity of the Bragg peak around a few degrees along the ω angle. A schematic diagram can be seen in **Figure 3.6**. A FWHM (full width at half maximum) value of the resultant peak can be obtained, which is associated with the crystallinity of the film. The smaller the FWHM of the peak is, the higher the crystallinity of the films, indicating that the film is less misoriented.

Phi (φ) Scans

The orientation alignment between film and substrate was determined by φ-scan measurements. This measurement was performed to investigate a plane which is not normal to the growth direction of the film (i.e. c-axis in this work). Prior to the measurement, again the alignment calibration for the sample position is also required. To carry out this characterisation, an appropriate reflection of the plane is required. Through examining the ICSD data sheet of the material, the selected reflection of the plane is preferable to yield high intensity, and there are no reflections from the substrates close to the 2θ and Ψ(psi) azimuths for this selected reflection. Then the sample was offset to the Ψ angle, and the detector was set at the 2θ position. The measurement proceeded to collect the reflections of the plane as the sample was rotated around the phi (φ) azimuth from 0° to 360°. Considering the RP lanthanum nickelate, they have tetragonal or

orthorhombic symmetry, but the a and b parameters of the orthorhombic structure are very similar. Therefore, the orthorhombic structure can be referred as a distorted tetragonal structure. Based on this, a family of four reflections for the selected plane were observed for the RP films after the φ-scan. Further detailed discussions with regard to φ-scan will be described in the following result chapters.

Reciprocal Space Mapping (RSM)

Reciprocal Space Mapping (RSM) measurements were used in an attempt to determine the in-plane and out-of-plane lattice parameters, understand the distortion of the RP films with substrate, and investigate the influence of strain as a function of thickness through the relative positions of the reciprocal lattice points. Several RSM analyses were performed in the thesis through asymmetric measurements. These measurements were conducted using point-focus mode with a crossed slit collimator (the slit size is 2.5 × 2.5 mm^2) at incident side, and graphite monochromator, X'Celerator detector at diffraction side. After the alignment calibration, the measurements were performed by successive ω-2θ scans over a range of 8° with a step size of 0.0376° around the selected diffraction peaks by varying ω angle over a range of 8° with a step size of 0.0250°. The reciprocal vectors Q_x and Q_y were calculated using the equations through those series of 2θ and ω values:

$$Q_x = \sin\theta \sin(\theta - \omega) \tag{3.5}$$

$$Q_y = \sin\theta \sin(\theta - \omega) \tag{3.6}$$

The in-plane (a- or b-axis) and out-of-plane (c-axis) lattice parameters can then be determined by the following equations:

$$a\ (or\ b) = \frac{\lambda \mathrm{h}}{2Q_x} = \frac{\lambda \mathrm{h}}{2\sin\theta \sin(\theta-\omega)} \tag{3.7}$$

$$c = \frac{\lambda l}{2Q_y} = \frac{\lambda l}{2\sin\theta \sin(\theta-\omega)} \tag{3.8}$$

where λ is Cu K_α wavelength (1.5418 Å), h and l are Miller indexes (h k l) from the selected reflection plane. In this thesis, only two RSM examples of $La_3Ni_2O_{7-\delta}$, $La_4Ni_3O_{10-\delta}$ samples are presented, as can be seen and will be briefly discussed in Ch.6. The RSM measurements were collected in collaboration with Dr. A. Cavallaro in the Department of Materials, Imperial College London.

3.3.4 Film Thickness Measurement

The thickness of films was determined using a contact profilometer (Vecco DekTak 150) with a stylus of 2.5 μm (radius) and a force of 5.00 mg.

As mentioned previously, during PLD experiments, each sample was masked by a droplet of the TiO_2 paint on the substrate. After the deposition, the TiO_2 mask was removed through a standard cleaning process with acetone, isopropanol and deionised water in an ultrasonic bath for 3 minutes each process, leading to the formation of a height difference between the surfaces of the film and substrate. Thus, the film thickness can be measured via this difference after deposition. In the measurements, ten measured readings were taken at various locations and the average values of average step height (ASH) were calculated.

3.3.5 Scanning Electron Microscope with Energy Dispersive X-ray Spectrometer (SEM-EDX)

Scanning Electron Microscopy (SEM) is a typical microscope technique capable of producing high-resolution images through a focused electron beam for examining the morphological, microstructural and chemical composition details of samples. This technique is based on the fact that the wavelength of an electron beam is much smaller than that of visible light. SEM, therefore, possesses a much better resolution and

magnification (up to three orders of magnitude) than an optical microscope [147].

A primary high-energy electron (typically 0.2~40 keV) beam is produced by thermionic emission (usually tungsten or LaB_6 filament) or field emission gun, and accelerated by a typical range of voltage between 0.2 and 40 kV. Through a series of condenser and objective lenses, the beam is focused to a very small spot (typically <10 nm) on the sample surface. When an electron beam interacts with the specimen, a variety of signals will be produced such as secondary electrons (SE), backscattered electrons (BE), characteristic X-rays, Auger Electrons, etc. [148]. Various detectors can be used for analysing different signals. The SEM technique is mainly used to detect SE and BE for the formation of images, while if it is fitted with EDX or WDX, characteristic X-rays can be detected for the compositional analysis of specimens.

SE are low energy electrons (normally < 50 eV). Only the SE formed in the near surface region (approximately 50-500Å) can escape to be detected and the amount of SE is strongly affected by the topography of the specimen surface. Therefore SE image mode is suitable to provide information on surface morphology. On the other hand, BE are high energy electrons (normally > 50 eV). BE stems from the electrons formed by elastic collisions with specimens and are from the near surface region around 5000 Å. The amount of BE is strongly associated with the atomic number of the specimen. In a BE image, the area of the element that has high atomic numbers will be brighter than the other areas with low atomic number. Hence, the BE image is usually used to provide contrast information with regard to the distribution of different chemical compositions in the specimen.

To characterise the chemical composition of the specimen, the energy dispersive X-ray spectrometer (EDX) was used. EDX is commonly accessory equipment installed on a SEM system, allowing qualitative and semi-quantitative analysis of the sample composition for localised surface areas through the detection and determination of energy

distribution of the excited characteristic X-rays. The identification of compositions is achieved since each element has a unique atomic structure emitting characteristic X-rays.

It should be noted that the penetration of the electron beam can strongly influence the penetration depth of the X-ray probe for EDX, typically ~1 μm, which is associated with the energy of the incident electron beam and the composition of samples [149]. Therefore, for a thin-film sample, the information from the substrates can be contained in the EDX spectra, leading to the film-substrate peak overlapping, and consequently certain experimental errors. This influence may significantly occur on the measurements of the very thin-films because more signal is collected from the substrate proportionally and hence there is insufficient signal from the thin-films, making it difficult to distinguish the peaks in the spectra.

The SEM images presented in this thesis were obtained using SE image mode to provide the surface morphology of lanthanum nickelate films. There were two different instruments used for this work: JSM 6400 SEM and LEO Gemini 1525 FEG-SEM (Carl. Zeiss, Oberkochen, Germany) equipped with an Oxford Instruments INCA energy dispersive X-ray spectrometer. Prior to the SEM measurements, all samples were mounted on aluminium stubs using conductive carbon tape, with no need to gold coat the specimen due to the lanthanum nickelate samples being conductive. For more detailed information about SEM-EDX, interested readers are referred to a comprehensive text by Goldstein *et al*. [149].

3.3.6 Atomic Force Microscopy (AFM)

Atomic Force Microscopy (AFM) is utilised to characterise the surface roughness and topography of thin-films. Compared to SEM, the AFM technique can provide more topographical contrast and vertical information of surface features, while it can also

provide three dimensional images without a complex procedure of sample preparation and data processing in comparison with TEM. A high vacuum is not necessary for AFM measurements, and the measurements can be carried out under ambient atmosphere [150].

This technique is based on the measurements of the atomic forces (repulsive and attractive) between the sample surface and a sharp, force-sensing tip, which is mounted at the end of a cantilever. Thus it is non-destructive. Through the tip scanning over the sample surface, the three dimensional images can be obtained with lateral resolution (< 1 nm) and particularly vertical resolution (< 0.1 nm) [150]. The resolution is highly related to the sharpness of the tip (i.e. the radius of tip). When the tip approaches the surface, an interaction force between the tip and surface is varied, resulting in deflections of the cantilever. These deflections are detected via a laser beam and photodiode. Through analysing these deflections, a high-resolution topographic image of the sample surface can be produced by a digital computer system. A schematic illustration of the AFM setup is shown in **Figure 3.7**.

AFM can be typically operated in three different modes: contact, intermittent and non-contact modes, for topographic measurements. In the contact mode, the tip is forced to very gently touch the sample surface, but this mode is capable of obtaining very high-resolution images and usually for hard solid samples. Conversely, the non-contact mode means that the tip does not touch the sample, but is set very close to the sample surface to achieve a high sensitivity. Therefore, non-contact mode relies on the attractive forces. For the intermittent mode, it is also called tapping mode. The tip does not touch the sample in order to avoid any damage of the surface. The cantilever is oscillated, and is typically set close to its resonance frequency. The tapping mode is usually applied to highly sensitive surfaces such as magnetic materials.

To obtain very high-resolution images and accurately determine surface roughness and structure of the films, all the AFM images presented in this thesis were obtained by

contact mode. Although AFM can actually profile the topographic appearance of the samples, a number of artefacts could occur, for example, when the images are produced with a damaged or dirty tip, leading to a blurred image. More information about AFM image artefacts can be found in reference [151]. The AFM analyses were performed using a Veeco Bruker di Dimension 3100 at the London Centre for Nanotechnology, University College London. The WSxM 5.0 Develop 6.4 software was used for further processing the obtained AFM data such as the calculation of surface roughness [152].

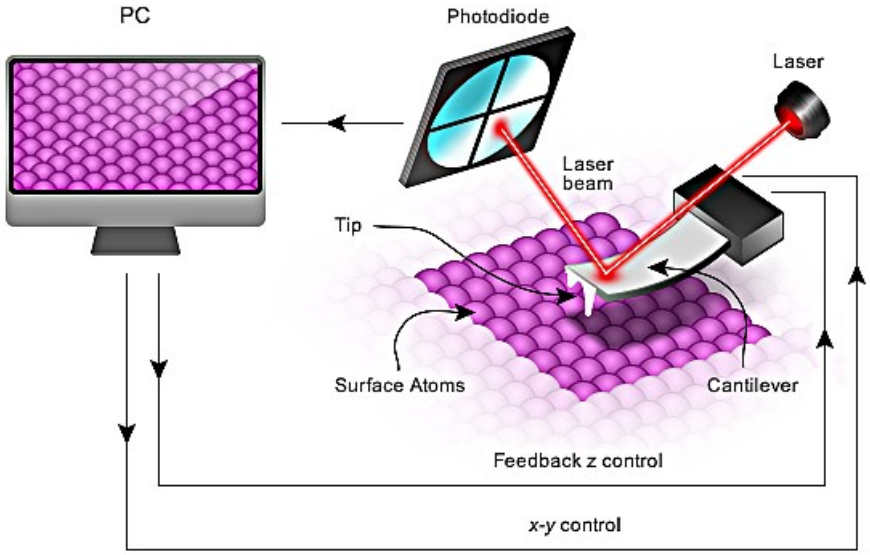


Figure 3.7 Schematic illustration of the operation and setup of the AFM (adapted from [153]).

3.3.7 Transmission Electron Microscopy (TEM)

Transmission Electron Microscopy (TEM) is a good complementary technique to XRD for evaluating the crystallography of materials, and conventionally applied to obtain microstructure of materials using a high-energy electron beam (typically 200 keV). The electron beam is focused on a thin sample (typically < 100 nm) through an electromagnetic field produced by a series of magnetic lenses, and the beam is then passed through the sample, resulting in the formation of a diffraction pattern on the back focus plane, and image on the image device (such as CCD (charged-coupled device)

camera). The resolution of the TEM technique is usually ~ 0.3 nm [154].

In this thesis, to obtain high-resolution atomic images at a localised area of the complex oxide epitaxial film sample, scanning transmission electron microscopy (STEM) with a high angle annular dark field (HAADF) detector was utilised. STEM is a variant of TEM. This technique has better spatial resolution (typically < 0.1 nm) than conventional TEM and allows to position and scan a specific area of the thin sample though a fine, narrow focused beam [155, 156]. The HAADF detector can collect a large number of incoherently scattered electrons and produce an incoherent high-resolution image. The incoherence image directly reflects the actual atomic columns of the epitaxy, and provides strong composition contrast via the intensity of atoms, which is approximately proportional to Z (atomic number). Thus the HAADF image is also called Z-contrast image. Such HAADF-STEM technique not only can obtain the information of the true structure arrangement of atoms, but also the different atoms (particularly cations, e.g. La and Ni) can be visually distinguished. The full detailed information of TEM and STEM is beyond the scope of this thesis, interested readers can referred to references [154, 157].

In this thesis, the HAADF-STEM images were presented for the cross-section of the RP $La_{n+1}Ni_nO_{3n+1}$ (n = 1, 2 and 3) films. These images was analysed from [110] viewing direction as shown in **Figure 3.8**, and the La and Ni/O atomic columns are observed in the obtained HAADF-STEM images. The La atomic columns have higher intensity due to its large atomic number than Ni/O columns. The results will be shown in Ch.6.

All the HAADF-STEM analyses were performed using FEI probe-corrected Titan3^{TM} 80-300 S/TEM (spatial resolution: ~0.07 nm) located at Center for Electron Microscopy and Analysis (CEMAS) in The Ohio State University, and were conducted by Dr. Y. Fan and Professor D. McComb. The TEM samples were prepared to be very thin sections using focused ion beam (FEI Helios NanoLab^{TM} 600 DualBeam) by G Harrington at Department of Materials in Imperial College London and by Dr. Y. Fan at

Department of Materials Science and Engineering in The Ohio State University.

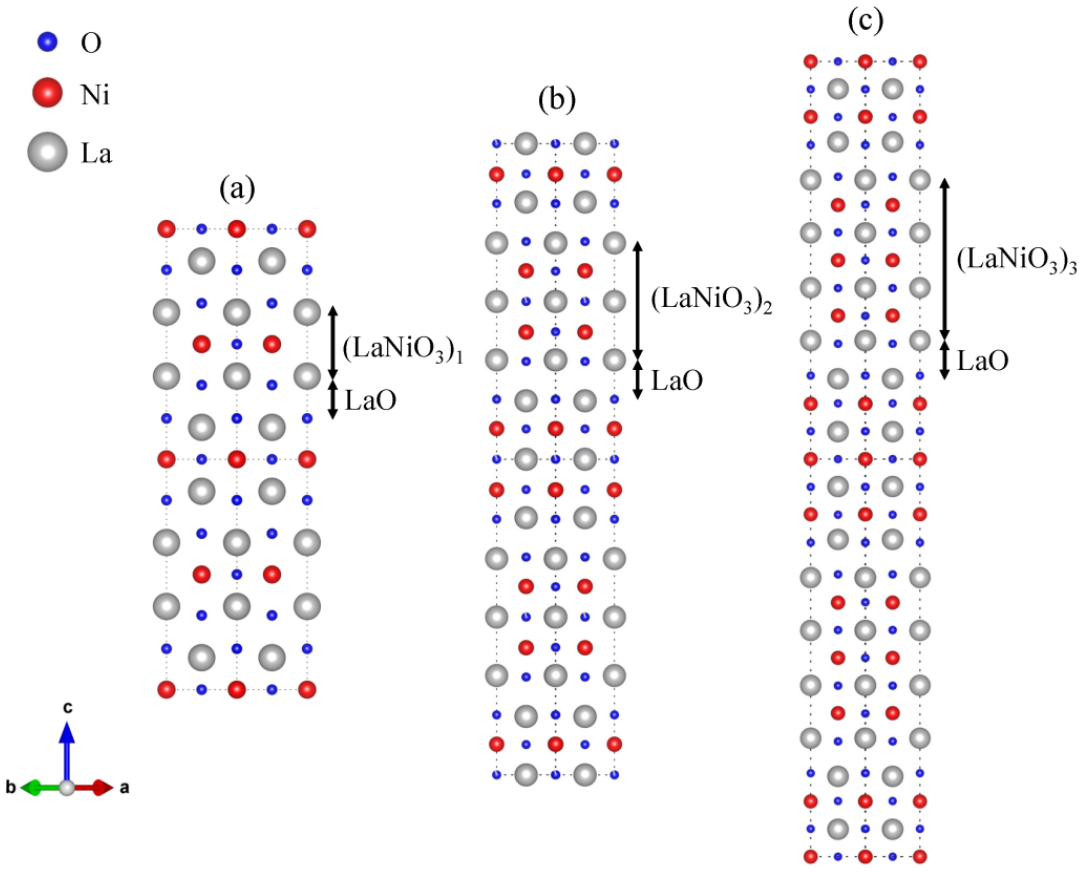


Figure 3.8 [110] viewing direction of layered RP-phases (space group: Fmmm) for (a) La_2NiO_4 (n = 1), $La_3Ni_2O_7$ (n = 2), and $La_4Ni_3O_{10}$ (n = 3).

3.4 Transport Property Characterisation

3.4.1 Electrical Conductivity Measurements

The total planar electrical conductivity of the obtained c-axis oriented RP layered $La_{n+1}Ni_nO_{3n+1}$ (n = 1, 2 and 3) epitaxial films was investigated as a function of temperature using 4-point DC van der Pauw method, proposed by Van der Pauw in 1958 [158, 159]. This method was developed to measure the sheet resistance (and resistivity) of thin and flat semiconductor samples, allowing not only eliminating the electrode contact contribution but also avoiding the issues of sample geometry [158, 159].

The four-point electrode contacts (numbered 1-4) were manually prepared by silver (Ag) pads at the edges of the four sample corners using an injector (0.3 mm in diameter) on a hot plate, and connected with platinum (Pt) wires. After the contacts and wires were bonded, the samples were sintered in a furnace under static air at 700°C for 1 h with a heating/cooling rate of 5°C/min in order to obtain good homogeneous contacts with the wires and sample.

The measurements were conducted via two configurations of electrode contacts, as schematically shown in **Figure 3.9**. When the current is supplied in the sample between contact 1 and 4 ($I_{1,4}$) and the voltage is measured between contact 2 and 3 ($V_{2,3}$). Conversely, as the $I_{1,2}$ is supplied and the $V_{3,4}$ can be obtained. Based on Ohm's law, two sheet resistances R_a and R_b can be obtained as follows:

$$R_a = \frac{V_{2,3}}{I_{1,4}} \tag{3.9}$$

$$R_b = \frac{V_{3,4}}{I_{1,2}} \tag{3.10}$$

According to the van der Pauw equation:

$$\exp\left(\frac{-\pi d}{\rho} R_a\right) + \exp\left(\frac{-\pi d}{\rho} R_b\right) = 1 \tag{3.11}$$

Due to the symmetric shape of the sample, it can be assumed that the R_a and R_b are similar. Therefore, the equation can be simplified and given as:

$$\rho = \frac{\pi d}{ln2} \frac{R_a + R_b}{2} f = \frac{1}{\sigma} \tag{3.12}$$

where d represents the thickness of films, estimated by DekTak 150 Profilometer (see section 3.3.4), and f represents a correction function driven from the ratio of R_a and R_b. The f values are provided from the papers of van der Pauw [158, 159], and were found to be approximately 0.65-0.95 for the films presented in this thesis. The variation of f may correspond to not only the homogeneity of the electrode contact and obtained films, but also the size of electrode contacts and the separation distance of contacts.

According to the papers, the ideal case ($f = 1$) means that the electrode contacts are made perfectly at the edges of the four sample corners, and using the Eq.3.12 is based on an assumption that the contacts are extremely small. It, however, is apparent that the measurements are impossible to be perfect. Hence, relative errors are caused by the non-zero values of the contact size and are approximately the ratio of the diameter of contacts to the separation distance of the contacts. The relative errors therefore may be significantly minimised through reducing the size of contacts and increasing the separation of electrode contacts. Despite such errors, the obtained electrical conductivity data were consistent with the data from literature obtained via AC impedance, indicating the validation of the measurements, which will be shown in the following result chapters.

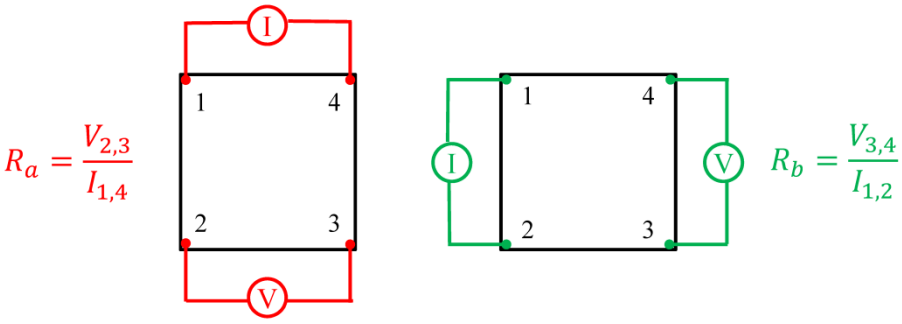


Figure 3.9 Schematic illustration of two configurations of electrode contacts for 4-point DC van der Pauw measurements. I represents current; V represents voltage.

Note that prior to measuring the electrical conductivity of the films, it is of importance to ensure that the substrate is electrically insulating; otherwise, the substrate would provide the electrical paths, hence resulting in experimental errors. For the cases in this thesis, the conductivity of adopted $SrTiO_3$ and $NdGaO_3$ substrates have ~10^{-3} Scm^{-1} and ~10^{-6} Scm^{-1} at 700°C respectively, which are several orders of magnitude lower than the RP lanthanum nickelate films. Hence, an effective measurement can be carried out.

In the electrical measurements, the sample was positioned next to a thermocouple

and in the centre of the tube furnace in order to obtain an accurate sample temperature since generally there is a temperature gradient decaying from the centre to the end of furnace. The temperature variation was estimated to be ~±5°C. Each measurement was conducted from room temperature (RT) to 700°C under static air. The heating/cooling rate was 5°C/min. When reaching each measuring temperature, the sample was set for approximately 1 h to thermally equilibrate. The electrical data were collected using an Agilent 34401A Multimeter.

3.4.2 Oxygen Transport Measurements

The ionic transport properties of an oxide ion conductor are characterised by two parameters – oxygen diffusion and surface exchange coefficients. In this thesis, these parameters were determined by an isotope exchange depth profile (IEDP) method using secondary ion mass spectrometry (SIMS) to analyse the diffusion profile, as developed by Kilner *et al.* since 1984 [160-162]. The method consists of four stages: sample preparation, isotope exchange, determination of the resulting ^{18}O distribution by SIMS, and data processing to extract oxygen tracer coefficient (D^*) and surface exchange coefficient (k^*) from the obtained diffusion profile. Each of these steps will be briefly described in the following, but more comprehensive information with respect to the procedure can be found in, for example, reference [162].

Prior to the isotope exchange annealing, the film samples are ultrasonically cleaned with acetone, isopropanol and deionised water for 5 minutes for each solvent and dried with a N_2 gas gun in order to remove contamination (such as organic contaminants or impurities introduced during sample preparation) on the sample surface. The samples are then ready for oxygen isotope exchange measurements. In order to establish thermodynamic and chemical equilibrium at the exchange conditions, the samples are

usually pre-annealed in research grade (99.9995% pure, BOC Industrial Gases, UK) oxygen of normal isotopic abundance at the temperature and oxygen partial pressure of the following exchange, for a duration approximately one order magnitude greater than that of the ^{18}O tracer anneal [36, 162, 163]. Oxygen gas enriched in the ^{18}O isotopic tracer (~97%, Isotec Inc. USA) is then introduced and the sample annealed at the same temperature for the desired time. The ^{18}O isotopic exchanges reported in this thesis were performed at a pressure of 200 mbar (i.e. a similar pO_2 to air), and temperatures of 400-500°C for around 20-30 min.

Then the samples were measured through the SIMS technique with time-of-flight (ToF) type analyser [162, 164] to determine the distribution of the oxygen isotopes (e.g. ^{18}O and ^{16}O) and other species (e.g. LaO^-, NiO^-, NdO^- and GaO^-) from the samples.

SIMS is a well-known surface analysis technique used to obtain both elemental and molecular information of the surface composition within a typical depth of 1 nm (2-3 nm) [162, 164] by analysing the ionised particles that are emitted as a material surface is bombarded by an energetic (10-40 keV) primary ion beam. This primary beam strikes the sample surface and transfers energy through a series of collisions (collision cascade). As a consequence of this collision cascade, several secondary particles can be emitted from the sample surface, such as electrons, neutral atoms and molecules, and/or ions (both atomic and molecular fragments) [165]. The emitted secondary ions are separated as a function of their *m/z* ratio, providing isotopic information of the elemental and molecular surface composition. The process is schematically illustrated in **Figure 3.10**. Further detailed information about SIMS can be found in reference [165].

The instrument used for the IEDP technique is a Time-of-Flight (ToF)-SIMS apparatus (Tof.SIMS^5, ION-TOF GmbH, Münster, Germany) fitted with a ToF analyser for the separation of the secondary ions according to their flight times that allows quasi-simultaneous detection of the emitted species. The ToF-SIMS^5 works in a dual

beam mode, using two different ion sources that are alternated during depth profiling measurement to decouple the analysis and sample erosion aspects. The analytical beam used to generate the analysed secondary ions is provided by a 25 keV Bi^+ liquid metal ion gun (LMIG) incident at 45°, while the sputtering is performed with a 2 keV Cs^+ beam also incident at 45°. After the isotope exchange experiments, the samples were analysed in the ToF-SIMS[5] to obtain the ^{18}O diffusion depth profiles. By using a solution to Fick's second law of diffusion with appropriate boundary conditions (many of which are given by Crank [166]), the oxygen diffusion and surface exchange coefficients can be extracted from analysing the obtained diffusion depth profile through a series of data processing, which will be further described in Ch.7.2. For further detailed information on the diffusion measurements by the IEDP-SIMS method, several reviews are recommended [162, 167, 168].

Note that all the IEDP and ToF-SIMS measurements and data processing reported in this thesis were conducted by the collaborator, Dr M. Burriel, in the Department of Materials, Imperial College London.

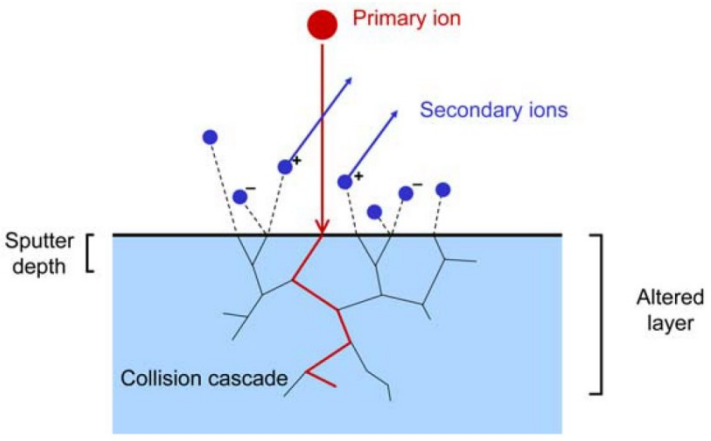


Figure 3.10 Schematic illustration of the SIMS process (adapted from [167]

3.5 Surface and Interface Characterisation

To obtain compositional information from the surface and interface (between film/substrate) regions of the lanthanum nickelate epitaxial samples, both SIMS and low energy ion scattering (LEIS) techniques were adopted. The basic concept of the SIMS technique has been briefly described in the previous section (Ch.3.4.2). In addition to the oxygen isotope fraction depth profiling, the compositional depth profiling of other cluster ions (e.g. LaO^-, NiO^-, NdO^- and GaO^-) characteristic of the lanthanum nickelate film and NGO substrate were obtained through the SIMS measurements.

On the other hand, LEIS is a unique analytical technique that is capable of providing quantitative information on the atomic composition of the **outermost** and near-surface layers of the materials [169]. For comparison, the surface specificity of LEIS, limited to the first single layer of atoms in the surface, is far superior to other conventional surface analysis techniques such as x-ray photoelectron spectroscopy (XPS), Auger electron spectroscopy (AES) and SIMS, where the information comes from approximately 1-10 nm [162]. Thus this extreme sensitivity makes LEIS a powerful tool to probe these oxide-film surfaces of interest for the materials; for example, surface contamination, termination and segregation phenomena [162, 170, 171]. Moreover, it is believed that there is generally no matrix effect in LEIS, in contrast to SIMS [169]. As known SIMS is based on the analysis of secondary ions. When the secondary ions are generated, ionisation of emitted particles occurs at the surface matrix, resulting in participation of charge exchange process. Thus, the yield of secondary ions is strongly affected by the electronic and chemical states of the materials and the analysed surface. The phenomenon is known as the matrix effect [165]. The charge exchange can strongly influence the yield of secondary ions, which consequently complicates analysis of the obtained data. On the contrary, due to no matrix effect in LEIS, quantification of surface compositional data is relatively straightforward [162, 171]. This means that the presence of other species on the

surface does not affect the signal obtained from the measured element.

LEIS is based on fundamental principles: the laws of mechanics. The material surface is targeted by low-energy noble gas ions (typically He^+ and Ne^+ with 0.5-10keV). As the ions collide with surface atoms, a conservative momentum-energy transferring process happens. The energy distribution of the backscattered ions is measured, and is related to the mass of the atoms on the surface and the angle through which the projectile is scattered by the kinematic expression [169, 172]:

$$E_f = \mathrm{k} \times E_i \tag{3.13}$$

$$\mathrm{k} = \left(\frac{\cos\theta + \sqrt{\left(\frac{m2}{m1}\right)^2 - sin^2\,\theta}}{1+\frac{m2}{m1}}\right) \tag{3.14}$$

where k is the kinematic factor, m_1 is the mass of the primary ion, m_2 is the mass of the atom on the surface and E_f and E_i represent the initial and final energies primary noble gas ions, respectively; θ represents the scattering angle.

A schematic illustration is shown in **Figure 3.11**. In an experimental LEIS spectrum, the intensity of a measured peak is proportional to the surface coverage of the measured elements on the surface, as can be schematically seen in **Figure 3.11**. For quantitative information, the obtained surface coverage and concentration of the measured materials is compared to the integrated intensities of the peaks collected from "standard" compounds (for example, high-purity NiO and La_2O_3 powders as calibration reference materials) for quantification of the relative surface coverage of each element. An example of the procedure can be found in a recent paper about the study on the outer surface of Sr doped La_2NiO_4 single crystals, reported by Burriel *et al.* [170]. Such comparison is allowed due to the advantage of no matrix effects in LEIS.

It is of importance that due to the extreme surface sensitivity of LEIS, the samples have been treated and cleaned with great care; otherwise, contaminants such as adsorbed water and hydrocarbons due to atmospheric exposure will cover the sample surface

during storage and transport [162]. For further details and related aspects in compositional analysis by LEIS, readers are referred to the comprehensive review by Brongersma *et al.* [169].

The utilised LEIS apparatus (ION-TOF GmbH Qtac^{100}, Münster, Germany) is equipped with the primary gun at normal incidence, providing a low-energy beam of noble gas ions (usually 3 keV He^+ and 5 keV Ne^+), and an Ar^+ beam (0.5 keV) incident at 59^o for low-energy sputtering. Note that the LEIS measurements (including all data processing) regarding the $La_3Ni_2O_{7-\delta}$ and $La_4Ni_3O_{10-\delta}$ film samples, reported in this thesis were conducted by a collaborator, Dr. H. Téllez, in the Department of Materials, Imperial College London. The $La_2NiO_{4+\delta}$ sample was characterised by the same researcher with a similar type of apparatus at International Institute for Carbon Neutral Research (I^2CNER) in Kyushu University.

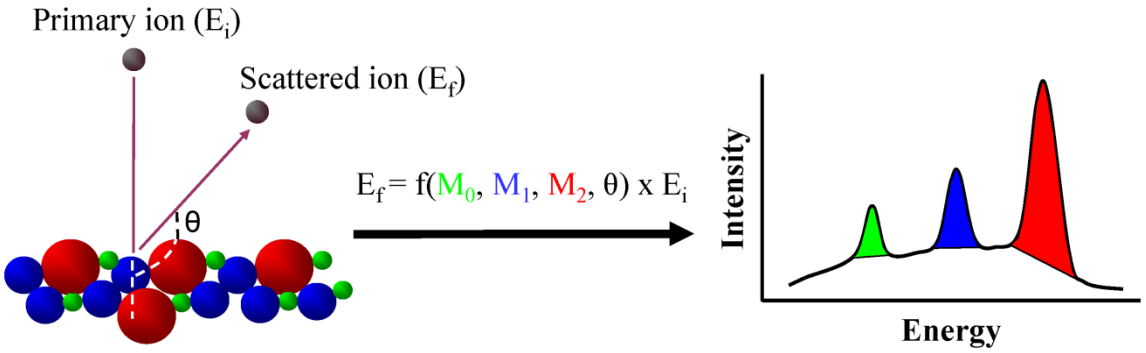


Figure 3.11 an illustrated diagram of LEIS process: incident primary ions (gray colour) collide with surface atoms (green, blue and red) and are scattered back at an angle of θ. The energy of backscattered ions is related to a function of the mass of incident primary ions, surface atoms and the collision angles. The experimental LEIS spectrum is also schematically shown. The red peak represents the energy of a heavy atom whereas the green one represents that of a light atom after collisions.

3.5.1 Crater Depth Measurement

The depths of sputtered craters obtained from SIMS and LEIS measurements were estimated using a white-light optical interferometer (Zygo NewView 200 Profilometer).

This technique measures and maps the topography of the crater in three dimensions through the constructive and destructive interference of light when the light reflects from the sample surface, forming the light and dark fringes. A schematic illustration is shown in **Figure 3.12**. The sample was placed under the optical path. The light source is directed to the objective lens. After the light passes through the lens, the light beam is divided into two separate beams. One is directed towards the sample surface while the other one is reflected to an internal reference surface. Both beams are recombined to be directed to a digital CCD sensor. Then the sensor will detect the difference of intensity driven from the interference on the sample surface, forming a topographic image of the crater [173].

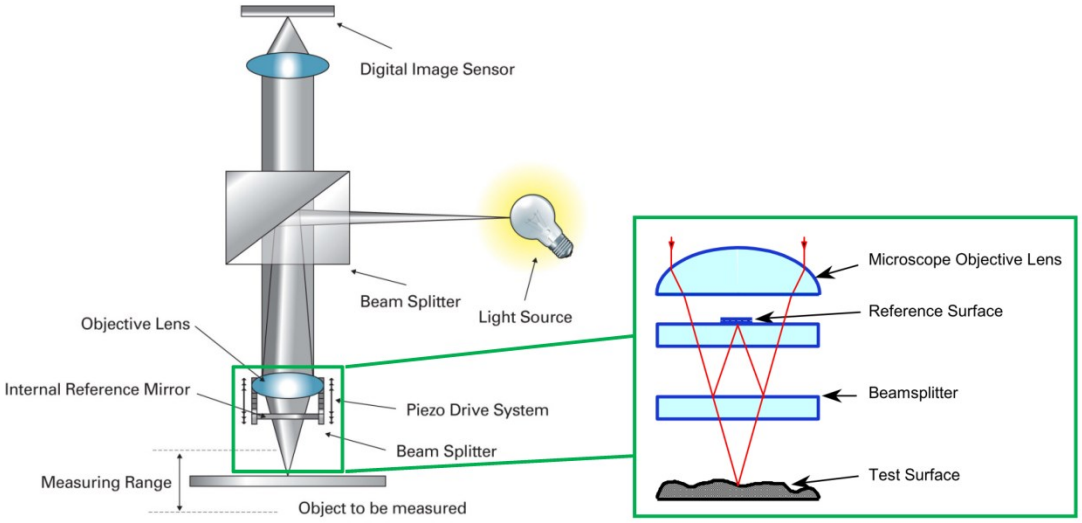


Figure 3.12 Schematic Diagram of the white light optical interferometer (adapted from [173])

Chapter 4 Requirements of PLD Targets and Substrate

The aim of this chapter is to investigate the preparation of PLD targets, followed by the requirement of the selected substrates. Prior to film deposition, the PLD targets have to be confirmed to be close to pure-phase with appropriate cation ratios and overall sample density. In section 4.1, the phase, composition and density of these targets are evaluated. An interesting phenomenon of target degradation is discussed afterwards. Furthermore, the crystal structure parameters, preferential orientation, and mismatch relationship of different composition films and substrates are investigated in section 4.2.

4.1 PLD Targets

The synthesis process used to produce the $La_{n+1}Ni_nO_{3n+1}$ (n = 1, 2 and 3) targets used in this project has been introduced in Chapter 3.2. Appropriate $La_2NiO_{4+\delta}$ (25 mm in diameter), $La_3Ni_2O_{7-\delta}$ and $La_4Ni_3O_{10-\delta}$ targets (13 mm) were achieved via the modified Pechini nitrate-citrate route under various sintering times and temperatures (see **Figure 3.4** in Chapter 3.2).

4.1.1 Phase, Composition and Density Identification

The nickelate targets were verified as nearly single phase compounds with a minor amount of a secondary phase via XRD as shown in **Figure 4.1**. The secondary phase is attributed to NiO, with Bragg peaks located at 2θ=37.0° and 63.5° in **Figure 4.1 (a)**. The obtained patterns were compared with ICSD (Inorganic Crystal Structure Database), provided by the CDS (Chemical Database Service): the codes of 158307 ($La_2NiO_{4.25}$), 91141 ($La_3Ni_2O_7$) and 80279 ($La_4Ni_3O_{10}$) and found to match well. The NiO phase was

compared to a reference pattern from the JCPDS (Joint Committee on Powder Diffraction Standards) database, with the code 00-044-1159. As seen in the XRD patterns of $La_3Ni_2O_{7-\delta}$ and $La_4Ni_3O_{10-\delta}$, **Figure 4.1**, there are some broad peaks observed (especially at high 2θ angles from 60° to 80°), which might be because of poor crystallinity, superstructures or lower crystal symmetry than space group *Fmmm*. [47, 51]

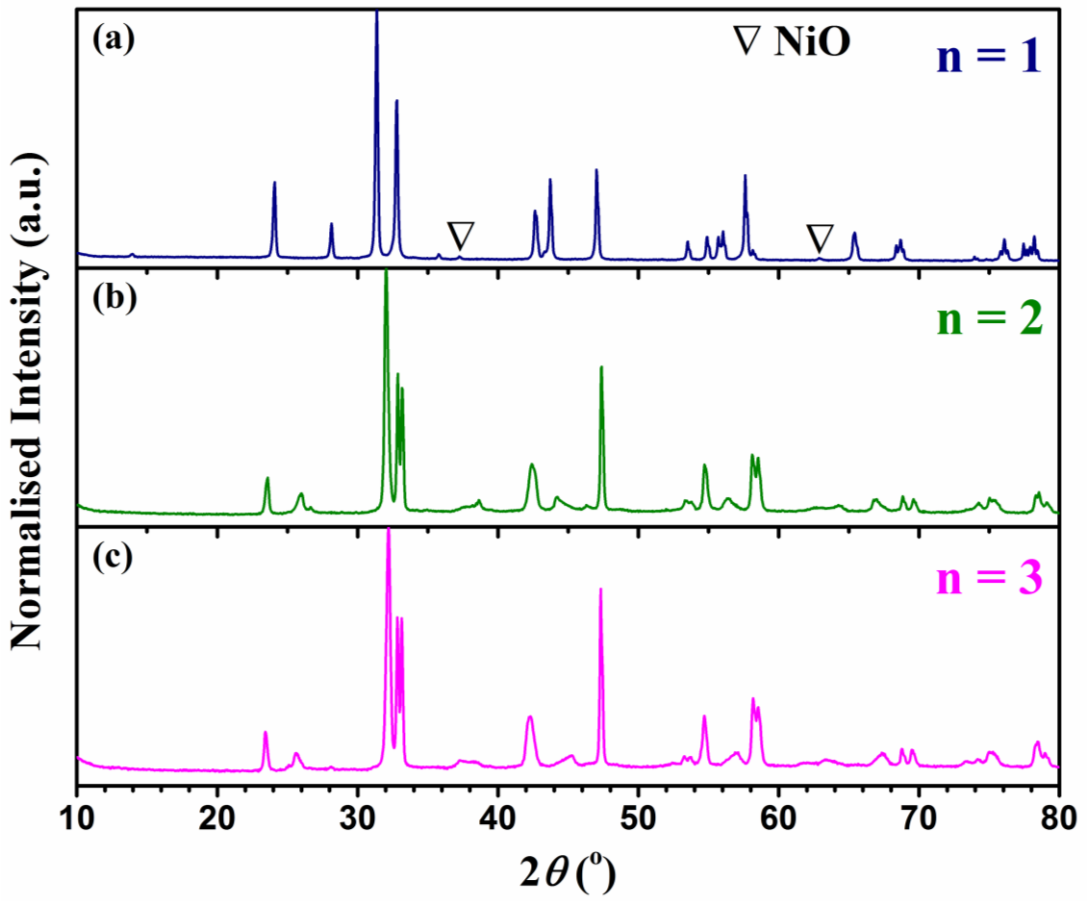


Figure 4.1 θ/2θ X-ray diffraction patterns of (a) $La_2NiO_{4+\delta}$ (n = 1), (b) $La_3Ni_2O_{7-\delta}$ (n = 2) and (c) $La_4Ni_3O_{10-\delta}$ (n = 3) targets show the near pure-phase of these materials with a minority of NiO phase indicated by the symbol (▽).

In spite of the presence of a small extent of the impurity phase NiO in the La_2NiO_4-phase matrix, the target is still acceptable for use in PLD because the materials can be deposited via adjusting various deposition parameters such as deposition temperature and oxygen pressure during the PLD process.

The compositions (La/Ni cation ratios) of the targets were determined by EDX and ICP-AES. EDX can contain information from the target surface to approximately 1µm depth due to the penetration depth of X-ray probe. On the other hand, ICP-AES can give an average stoichiometric composition of these targets. As seen in **Table 4.1**, the results from EDX show that the samples are La-rich on the surface. For the results of ICP-AES, the average cation ratios of the $La_3Ni_2O_{7-\delta}$ and $La_4Ni_3O_{10-\delta}$ targets, apart from the $La_2NiO_{4+\delta}$ targets, show slight La-deficiency, which most likely corresponds to La-segregation to the surface. These findings are in agreement with Woolley and Harrington's work using low energy ion scattering (LEIS) analysis of bulk RP oxides. [174].

The cation ratio of the $La_2NiO_{4+\delta}$ targets was confirmed by EDX and ICP-AES as being close to the expected ratio (see **Table 4.1**). For $La_3Ni_2O_{7-\delta}$ and $La_4Ni_3O_{10-\delta}$ targets, however, it is apparent that the ratios from EDX were significantly less accurate than from ICP-AES, which is probably due to the highly rough surface of the targets. The surface morphology of the targets can be seen in **Figure 4.2** (a) and (b) SEM images, respectively. These images show irregular particle shapes with a large range of particle sizes, varying from 1 to 80 µm. The rough surface is due to the low sample density of the $La_3Ni_2O_{7-\delta}$ and $La_4Ni_3O_{10-\delta}$ targets.

Members	La/Ni (Expected)	La/Ni (EDX)	La/Ni (ICP-AES)	Density
n = 1	2.00	2.07±0.14	2.01±0.02	~90%
n = 2	1.50	1.60±0.06	1.48±0.01	~50%
n = 3	1.33	1.44±0.03	1.31±0.01	~50%

Table 4.1 Cation ratios and density of $La_2NiO_{4+\delta}$ (n = 1), $La_3Ni_2O_{7-\delta}$ (n = 2) and $La_4Ni_3O_{10-\delta}$ (n = 3) targets determined by EDX and ICP-AES.

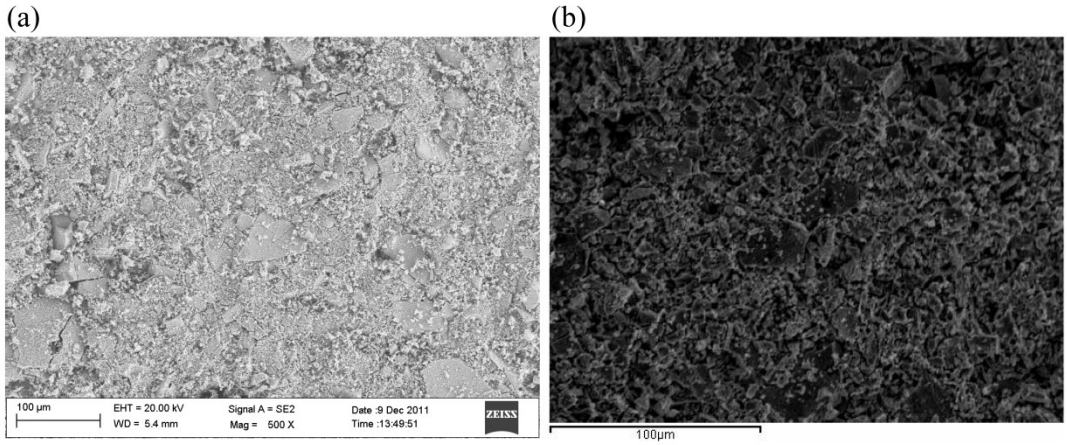


Figure 4.2 SEM secondary electron (SE) images of surface morphology of $La_3Ni_2O_{7-\delta}$ (a) and $La_4Ni_3O_{10-\delta}$ (b) targets prepared by the modified Pechini nitrate-citrate method. Scale marker: 100 µm.

Highly dense targets are favourable for PLD. [132] In earlier studies [32, 33, 70], although attempts and efforts have been made to densify $La_3Ni_2O_{7-\delta}$ and $La_4Ni_3O_{10-\delta}$ materials by conventional ceramic processes (such as solid state and Pechini methods), the sintered density of both materials have only reached 50-65% of theoretical density. For our work presented in **Table 4.1**, only ~50% of the theoretical density was obtained for the $La_3Ni_2O_{7-\delta}$ and $La_4Ni_3O_{10-\delta}$ targets, but approximately 90% of the theoretical density was achieved for the $La_2NiO_{4+\delta}$. The density values are consistent with the density reported by Amow *et al.* [32, 33]. The density of $La_2NiO_{4+\delta}$ target was measured by Archimedes' principle method; density of $La_3Ni_2O_{7-\delta}$ and $La_4Ni_3O_{10-\delta}$ targets was measured by means of geometric density method as used by Carvalho *et al.* [70].

The high surface roughness and low density of targets were considered to be two of the major issues in depositing high quality films of the higher order RP-phase $La_3Ni_2O_{7-\delta}$ and $La_4Ni_3O_{10-\delta}$ material. As PLD targets, normally, above approximately 80% of theoretical density is suggested for the deposition of other materials [175-177], otherwise issues such as target degradation and particulate formation during the pulsed laser ablation (PLA) process (further discussed in section 4.1.2) can occur. These issues can

significantly affect the quality of the deposited films. It is apparent that the density values of the obtained $La_3Ni_2O_{7-\delta}$ and $La_4Ni_3O_{10-\delta}$ targets are much lower than the expected values. These issues, therefore, significantly raised the level of the difficulty of depositing these complex structures.

4.1.2 Target Degradation and Particulate Formation

The pure-phase $La_3Ni_2O_{7-\delta}$ and $La_4Ni_3O_{10-\delta}$ targets were prepared with appropriate cation compositions. We, however, found phase transitions of the targets after PLA. As mentioned in the previous section, the density of targets is considered to be of significance on PLA in earlier studies of other oxide materials [175-177]. The low-density targets can lead to target degradation (including surface modification [137] and composition variation [178, 179]), and particulate formation [133, 175, 177] during the PLA process. In this section, the effects of low-density $La_3Ni_2O_{7-\delta}$ and $La_4Ni_3O_{10-\delta}$ targets during PLA are investigated.

Firstly, the issue of the target degradation is discussed. Laser irradiation severely alters the surface morphology of these targets, leading to physical and chemical changes. In **Figure 4.3**, it is apparent that surface morphological changes of the $La_4Ni_3O_{10-\delta}$ target can be clearly seen after PLA. Similar morphological changes are also seen on the $La_3Ni_2O_{7-\delta}$ target after PLA. The morphological changes imply a compositional change. These targets were further examined via XRD measurements prior to PLA, after the PLA process, and after removing the surface via SiC abrasion in order to examine what the compositional changes are and how the changes might occur.

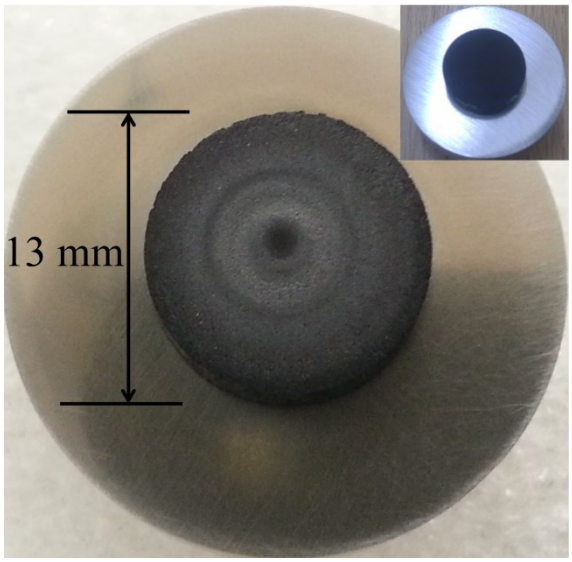


Figure 4.3 Photographs of $La_4Ni_3O_{10-\delta}$ target (13 mm) on a target holder after a pulsed laser ablation process with 3000 pulses of ~0.6 J/cm^2 and before ablation process (upper right)

Before the discussion of the XRD results, we should be aware that the pulsed laser beam only impinged upon a small area of the target surface, and that the information from XRD were not only extracted from the area illuminated by the laser and close to the target surface, but were also extracted from the material underneath the surface-changed area. Due to the geometry of the XRD configuration it is possible to estimate the penetration depth of Cu Kα X-rays for these samples as 10-100 μm, varying with incident angle. [180] Despite this, the XRD measurements enable analysis of the ablated targets qualitatively.

The XRD patterns of the $La_3Ni_2O_{7-\delta}$ and $La_4Ni_3O_{10-\delta}$ targets prior to, after the PLA process, and after removal of the surface layer are shown in **Figure 4.4** and **4.5**, respectively. The intensity of all patterns has been normalised to the most intense peak in order to facilitate meaningful comparisons. Comparing **Figure 4.4 (a) and (b)**, it is clearly observed that the $La_3Ni_2O_{7-\delta}$ phase is reduced to a mixture of La_2NiO_4 + La_2O_3 + NiO (the peaks are marked) after laser ablation. On the other hand, the $La_4Ni_3O_{10-\delta}$ phase is reduced to a mixture of $La_3Ni_2O_7$ + La_2NiO_4 + La_2O_3 + NiO, as can be seen in the comparison of **Figure 4.5 (a) and (b)**. The presence of $La_3Ni_2O_7$ phase can be recognised

by identifying the position of the two peaks between 25°-26° from the inset.

Earlier studies have reported that during laser ablation the stoichiometry-controlled complex oxide targets undergoing repeated thermal (heating-cooling) cycles can lead to an incongruent melting process, followed by a change of target composition (phase separation), and potentially the formation of stoichiometry-deviated films, as proposed by Dam *et al.* in the case of $Yba_2Cu_3O_{7-\delta}$. [178, 179] In terms of our complex $La_3Ni_2O_{7-\delta}$ and $La_4Ni_3O_{10-\delta}$ targets, it is likely that similar effects with the targets could occur during laser ablation. Thus, based on the Dam's studies, a similar investigation was carried out as follows.

To further understand the behaviour of laser-target interactions regarding our case, the calculated ternary phase diagram of the La-Ni-O system is adopted (**Figure 4.6**). [78] In the diagram, the dashed lines represent the stoichiometric La_2NiO_4, $La_3Ni_2O_7$ and $La_4Ni_3O_{10}$ phases. Along all dashed lines, it is clear that La_2NiO_4, $La_3Ni_2O_7$ and $La_4Ni_3O_{10}$ possess incongruent melting behaviour, resulting in a sequence of coexisting phases whilst the temperature is rapidly increased during laser ablation. Take the $La_4Ni_3O_{10}$ target for example (see along the pink dashed line in **Figure 4.6**); in the beginning, $La_4Ni_3O_{10}$ is partially melted and the $La_3Ni_2O_7$ + NiO phases appear whilst the temperature is increased rapidly. As the temperature rises, the La_2NiO_4 + NiO phases progressively appear and also the production of La_2O_3 is a result of the decomposition of La_2NiO_4. [72] Moreover, during laser ablation, a re-solidification process is consecutively preceded, as described in Ch.3.1.1. Thus, once these phases formed, they would stably coexist in the matrix. Such mechanism is presumed to explain the formation of the coexisting phases in our case, and is relatively consistent with the XRD results in **Figure 4.4 (b)** and **4.5 (b)**.

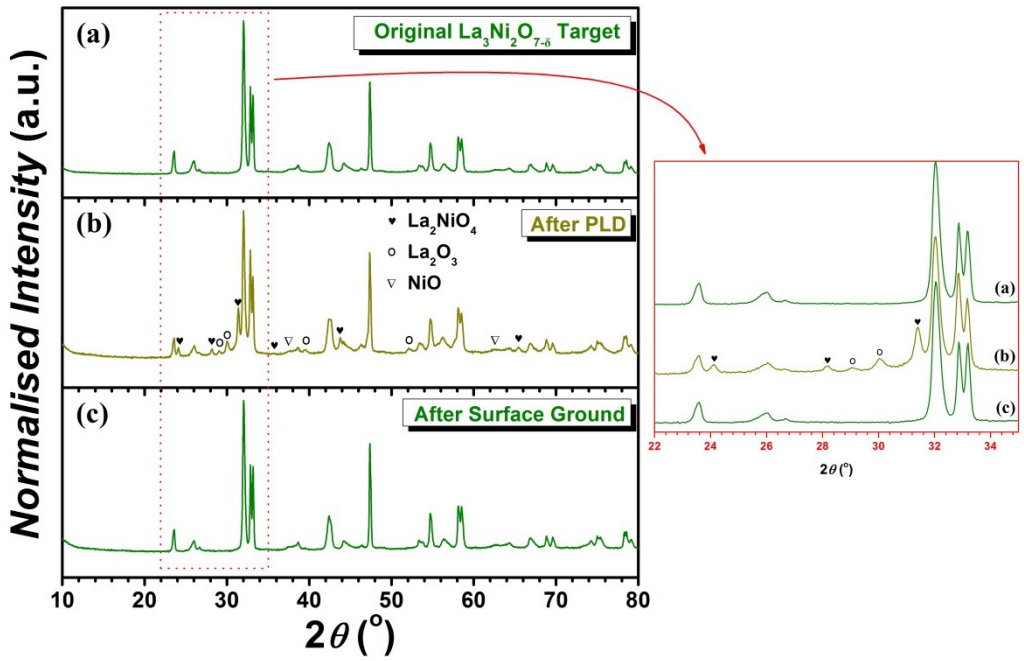


Figure 4.4 Normalised XRD patterns of (a) the original (before PLD) $La_3Ni_2O_{7-\delta}$ target, (b) the target after the use of PLA, and (c) the pellet after grinding the unwanted top-surface. (Inset: zoom of the range of 22-35° to show the impurity phases). ICSD code: 91141 ($La_3Ni_2O_7$), 158830 (La_2NiO_4); JCPDF code: 00-005-0602 (La_2O_3), 00-044-1159 (NiO).

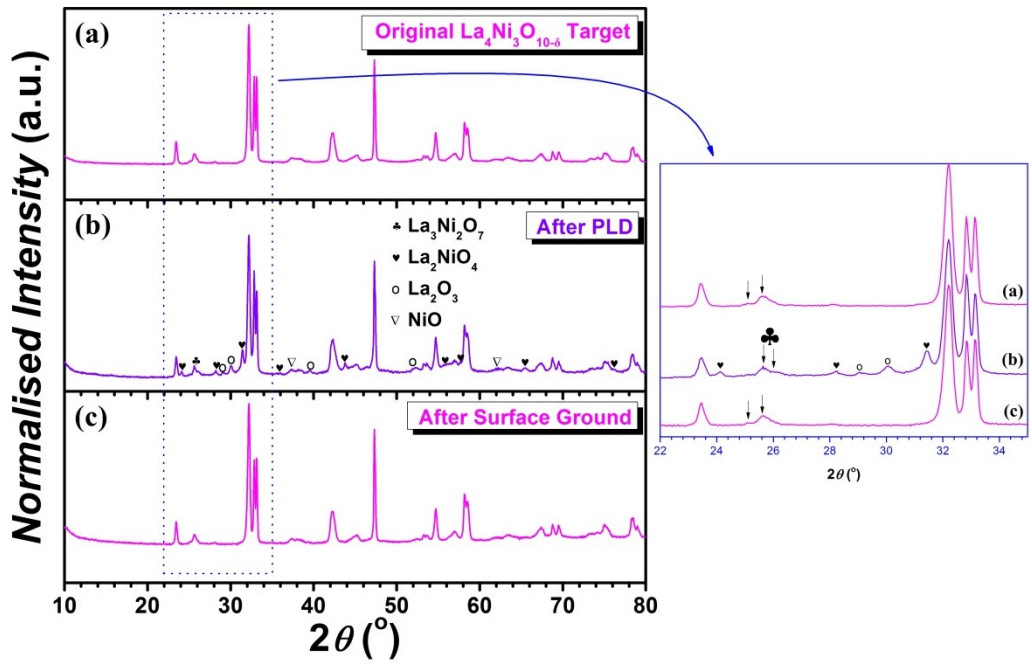


Figure 4.5 Normalised XRD patterns of (a) the original (before PLD) $La_4Ni_3O_{10-\delta}$ target, (b) the target after the use of PLA, and (c) the pellet after grinding the unwanted top-surface. (Inset: zoom of the range of 22-35° to show the impurity phases). ICSD code: 80279 ($La_4Ni_3O_{10}$), 91141 ($La_3Ni_2O_7$), 158830 (La_2NiO_4); JCPDF code: 00-005-0602 (La_2O_3), 00-044-1159 (NiO).

The effects of incongruent melting of the materials may be enhanced by the very low density (~50%) of the targets because the porosity of the low-density target possesses a low thermal conductivity in comparison with a solid phase. The influence would, therefore, further facilitate the occurrence of the target degradation.

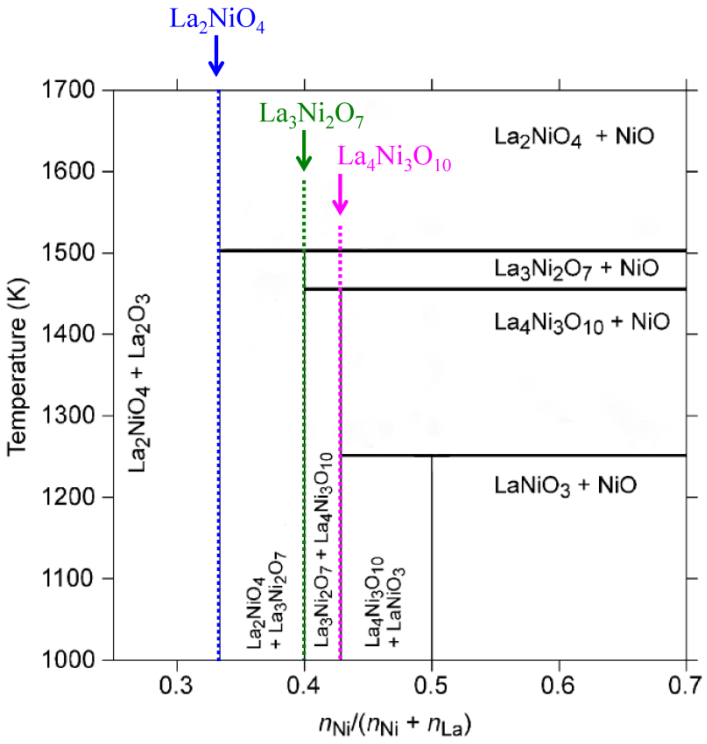


Figure 4.6 La-Ni-O phase diagram (temperature vs composition) in air (pO_2 = ~0.2 atm). The theoretical positions of the stoichiometric La_2NiO_4, $La_3Ni_2O_7$ and $La_4Ni_3O_{10}$ phases are labeled in blue, green and pink colour, respectively (adapted from [78])

The behaviour also indicates the possibility of obtaining non-stoichiometric films. A number of studies have confirmed that the stoichiometry of films is highly associated with the laser fluence dependence for a variety of oxide thin-films. [181-185] An appropriate laser fluence utilised, therefore, to avoid the formation of non-stoichiometric films is critical and is strongly dependent on the nature of the materials. However, if high laser fluence (typically > 1 J/cm^2) is adopted, another issue of particulate formation would occur, as will be discussed in the following text.

The issue of particulate formation has been generally observed in many previous studies [175-177, 186, 187] and is undoubtedly regarded as the greatest obstacle for the growth of high-quality of thin-films. It is commonly believed that the occurrence of particulates can be minimized via the use of high-density targets with smooth surfaces. [133, 186, 188] The reasonable explanation is that low-density targets have a higher density of pores and possess low thermal conductivity, resulting in a locally irregular heating process while the laser impinges on the target surface. It is likely that the concentration of the heat in the local area is unable to be quickly dissipated through the entire bulk and leads to splashing and the formation of particulates. [133, 188]

Unfortunately, the obtained targets of higher-order lanthanum nickelate (n = 2 and 3) bear a very low density (~50%) and high-roughness surface. The formation of particulates has been found with the deposition of lanthanum nickelate. As seen in **Figure 4.7 (a) – (c)**, these show the SEM images of a $La_4Ni_3O_{10-\delta}$ thin-film with the particulate formation. A high density of particulates was formed as the substrate was too close to the centre of the plasma plume. Along point a to c, the number of particulates was significantly reduced when the area of the substrate was distant from the centre of the plume. The average size of the particulates was observed as approximately 160 nm in **Figure 4.7 (a)**.

To minimise the effects of target degradation and particulate formation for thin-film growth, in terms of growth conditions, lower laser fluence (< 1 J/cm^2) was adopted to retard the degradation rate and preserve the deposition of particulate-free thin-films. Also, the target-substrate distance was positioned at 5 cm, the optimal position of the substrate was placed away from the centre of the laser plasma plume (~1 cm off), and a shutter was placed in front of the target with the target spinning in order to avoid the direct exposure to the plasma plume, and to reduce the possibility of particulate formation. Essentially, cleaning, and polishing the unwanted target surface, and confirming the target phases via XRD are required before every deposition in order to ensure there are no particulates in

the plasma plume and the reproducibility of the films. [187] The other optimal deposition conditions will be discussed in the following two chapters.

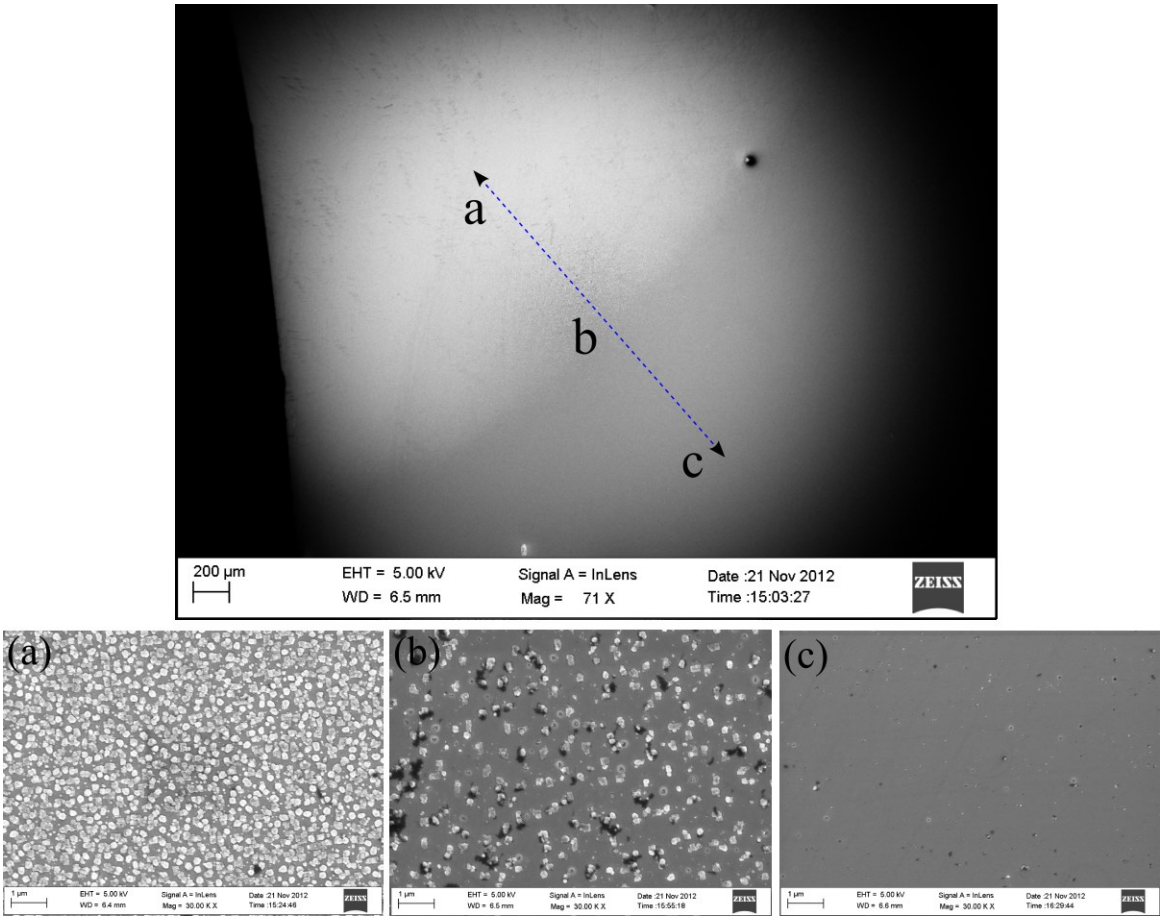


Figure 4.7 SEM images of a $La_4Ni_3O_{10-\delta}$ thin-film to show particulate formation after the PLD. A part of the sample nearly directly exposed the centre of the plasma plume and a reduced evolution of particulate formation can be seen from area a to c, where the microstructure images represent as (a), (b) and (c), respectively. Scale marker: 200 µm (upper); 1 µm (lower three).

4.2 Substrate Requirements

The selection of commercial substrates, the lattice mismatch with lanthanum nickelate (n = 1, 2, and 3), and the relationship of their orientation are all discussed in this section. Moreover, the information of surface roughness of the substrates from different commercial batches is provided.

All thin-films were deposited on well-oriented $SrTiO_3$ (001) or $NdGaO_3$ (110) single crystal substrates (Crystal GmbH, Berlin, Germany), noted as STO and NGO respectively, with a dimension of 5×5×0.5 mm, which were selected due to their low lattice mismatch with the ab-plane of the perovskite blocks (i.e. $LaNiO_3$) in the target materials.

Film-substrate preferential orientation is shown in **Table 4.2**. The data for n = 1, 2 and 3 compounds with orthorhombic structures were selected as standard references for the calculation of mean lattice mismatch. We consider the room-temperature orthorhombic $La_2NiO_{4.25}$, $La_3Ni_2O_7$ and $La_4Ni_3O_{10}$ [45, 47, 189] with their lattice parameters as displayed in **Table 4.2**. The crystal structure of the STO substrate is cubic with a lattice constant of 3.9050 Å (JCPDF: 35-734); that of the NGO is orthorhombic with a=5.4310, b=5.4990, and c=7.7100 Å (JCPDF: 21-0972), possessing pseudo-cubic in-plane parameters of 3.8644 and 3.8550 Å for the (110) plane. The mean lattice mismatch (f) [190] was calculated by using the formula $f = [(a_s-a_p)/a_p]\times100\%$, where a_s represents the lattice parameter of the substrates; i.e. a_s = 3.9050 for STO (001), and 3.8597 Å for NGO (110), which originates from the average of the pseudo-cubic in-plane parameters of 3.8644 and 3.8550 Å for the NGO (110) plane. The term a_p represents the pseudo-cubic lattice parameters of the RP phases (n = 1, 2 and 3), defined as $a_p = \sqrt{a^2 + b^2}/2$ = 3.8606, 3.8331 and 3.8467 Å, respectively. A positive value of f indicates the epitaxial film is stretched by a tensile strain, while a negative f expresses the film is compressed by a compressive strain as shown in the schematic diagram (**Figure 4.8**).

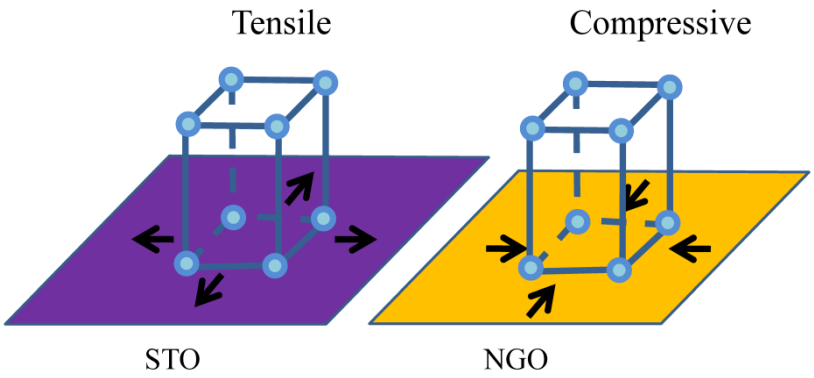


Figure 4.8 A schematic diagram of the epitaxial films oriented under tensile and compressive strain on STO and NGO substrates.

Phase	n	Crystal System	Lattice Parameters (Å)			[Ref.]	Lattice Mismatch	
			a	b	c		STO (001)	NGO (110)
$La_2NiO_{4.25}$	1	Orthorhombic (Fmmm)	5.4563	5.4630	12.7049	[189]	+1.15%	-0.02%
$La_3Ni_2O_7$	2	Orthorhombic (Amam)	5.3928	5.4486	20.5185	[45]	+1.88%	+0.69%
$La_4Ni_3O_{10}$	3	Orthorhombic (Fmmm)	5.4150	5.4650	27.9590	[47]	+1.52%	+0.34%

Table 4.2 Summary of crystal structures, space groups, lattice parameters and mean mismatch with STO (001) and NGO (110) substrates for the layered RP-type $La_{n+1}Ni_nO_{3n+1}$ (n = 1, 2 and 3) compounds based on ICSD (Inorganic Crystal Structure Database) data.

Based on the a and b lattice parameters of the orthorhombic structures in **Table 4.2**, c-axis oriented epitaxial films are expected to grow in 45° geometrically rotated alignment on the basal planes of STO (001) and NGO (110) substrates (illustrated by **Figure 4.9**); along crystallographic c-axis alignment in parallel to the normal directions of the STO and NGO substrates (demonstrated by NGO in **Figure 4.10**).

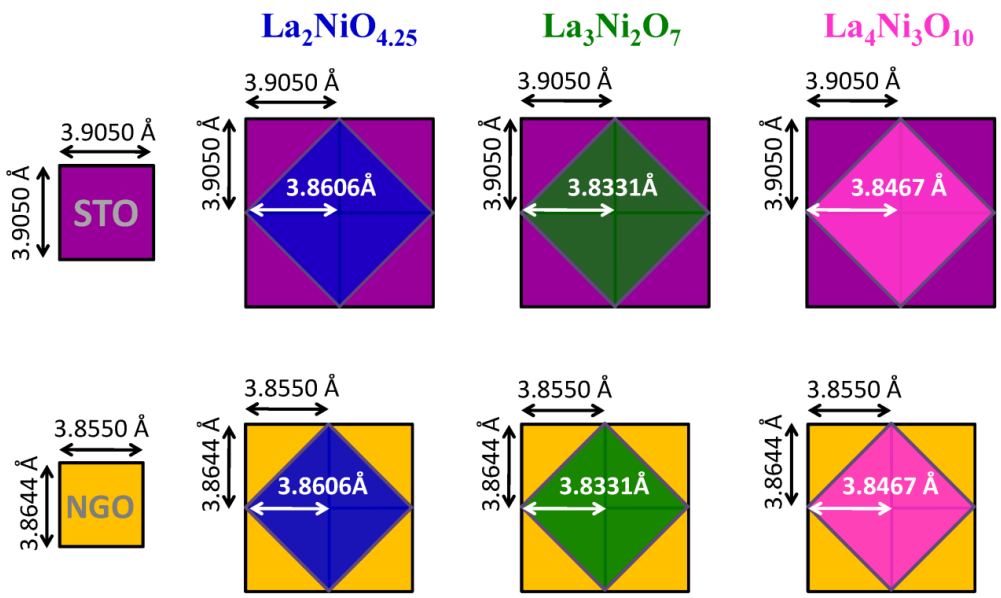


Figure 4.9 A schematic diagram of the basal arrangement of film-substrate orientation with the relevant lattice parameters a_p = 3.8606, 3.8331 and 3.8467 Å for $La_2NiO_{4.25}$, $La_3Ni_2O_7$ and $La_4Ni_3O_{10}$, respectively. Purple and yellow squares represent the basal planes of STO (001) and NGO (110) unit cells, respectively; blue, green and pink squares represent those of lanthanum nickelates.

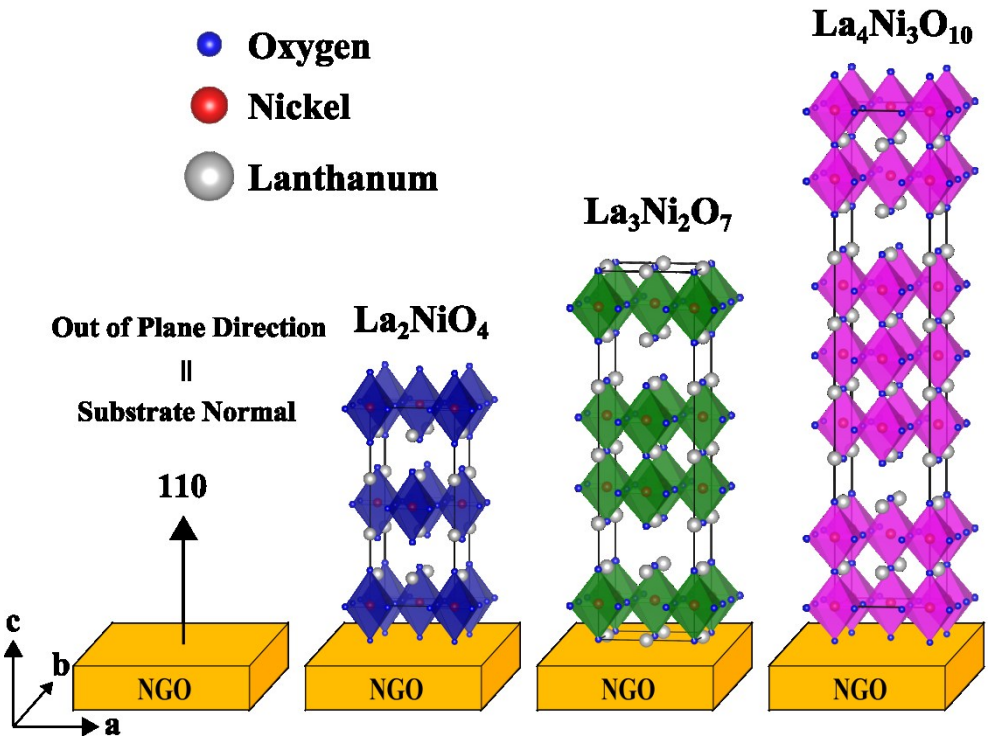


Figure 4.10 Schematic representation of the orientation of the $La_2NiO_{4.25}$, $La_3Ni_2O_7$ and $La_4Ni_3O_{10}$ thin-films in relation to the NGO substrate normal direction [110], which corresponds to out of plane direction [00L] of these films.

To successfully achieve the growth of the complex epitaxial films, especially for the higher-order $La_3Ni_2O_{7-\delta}$ and $La_4Ni_3O_{10-\delta}$ phases, the surface roughness of substrate is considered as an essential parameter for the deposition. Under a series of deposition conditions, we found that the surface roughness of the NGO substrates has an influence on the quality of the obtained epitaxial films. **Table 4.3** summarises the surface parameters of all batches of the adopted NGO substrates. Comparing batch A and B it is apparent that batch A has a markedly lower surface-roughness than batch B. By using batch B, the productivity of the thin-films was significantly decreased. It is worth noticing that batch C was completely fresh-prepared from the commercial company, which is considerably better than batch A, and had the productivity of 100% in the series of depositions for $La_3Ni_2O_{7-\delta}$ and $La_4Ni_3O_{10-\delta}$ phases. As for STO substrates, the substrates were only used for the growth of $La_2NiO_{4+\delta}$ and the influence of the surface roughness from different batches shows less significance.

Table 4.3 Surface roughness parameters of the adopted NGO substrates from different batches provided by Crystal GmbH, Berlin, Germany

Substrate	Batch A	Batch B	Batch C
Purchase Date	Jul. 2010	Jun. 2011	Oct. 2012
PV (nm)	7.539	15.390	5.201
RMS (nm)	0.8542	0.9324	0.8520
Ra (nm)	0.131736	0.184565	0.12798

PV: the height between the lowest and the highest measured point
RMS: the root-mean-square roughness of all measured points
Ra: the average roughness of all measured points

4.3 Summary

The phase, composition and density of $La_2NiO_{4+\delta}$, $La_3Ni_2O_{7-\delta}$ and $La_4Ni_3O_{10-\delta}$ targets have all been confirmed for use in the PLD. $La_2NiO_{4+\delta}$ targets present a reasonable value of 90% theoretical density and an expected cation ratio. Single-phase $La_2NiO_{4+\delta}$ films can be grown on STO (001) and NGO (110) single crystal substrates, as described in Chapter 5. As for $La_3Ni_2O_{7-\delta}$ and $La_4Ni_3O_{10-\delta}$ targets, only ~50% of theoretical density is achieved with appropriate cation ratios.

To minimise the effects of target degradation and particulate formation for thin-film growth, lower laser fluence (< 1 J/cm^2) was adopted to retard the degradation rate and preserve the deposition of particulate-free thin-films. Also, to avoid the direct exposure to the plasma plume, and to reduce the possibility of particulate formation, the target-substrate distance was positioned at 5 cm, the optimal position of the substrate was placed away from the centre of the laser plasma plume (~1 cm off), and a shutter was placed in front of the target with the target spinning. The other optimum deposition conditions (such as oxygen partial pressure, deposition temperature, laser power density (fluence), and number of laser pulses), and the characterisation of the thin-films will be discussed in the next two chapters.

Chapter 5 Growth and Characterisation of $La_{n+1}Ni_nO_{3n+1}$ (n = 1)

Appropriate $La_2NiO_{4+\delta}$ targets were prepared for use in the PLD; a series of depositions were undertaken to achieve high quality of $La_2NiO_{4+\delta}$ (n = 1) epitaxial films. Firstly, the growth conditions of the $La_2NiO_{4+\delta}$ phase on either STO or NGO single crystal substrate were optimized (section 5.1). Additionally, structural and morphological characterisation was conducted to evaluate the quality of the obtained $La_2NiO_{4+\delta}$ epitaxial films (section 5.2). Furthermore, the electrical conductivity properties of the obtained films were investigated in section 5.3. This chapter is predominantly concerned with determining the appropriate deposition conditions and substrate for higher order RP film (n = 2 and 3) growth.

5.1 Optimisation of $La_2NiO_{4+\delta}$ Phase Growth

To seek the optimal growth conditions of the $La_2NiO_{4+\delta}$ films, the effects of different oxygen partial pressure, deposition temperature, laser power density (fluence), and number of laser pulses were systematically investigated. For the selection of the initial deposition conditions, the oxygen partial pressure of 250 mTorr and pulse frequency of 8 Hz, reported by Kim *et al.* [42, 85] was used as a starting point. Also, as described in Chapter 4, a low laser fluence (< 1 J/cm^2) is favorable, and therefore a laser fluence of 0.8 J/cm^2 was adopted for the initial depositions. The target-substrate distance was positioned at 5 cm, the optimal position of the substrate was placed away from the centre of the laser plasma plume (~1 cm off). After the deposition, all the samples were cooled to 200°C with a rate of 10°C/min and then followed by natural cooling to room temperature within

an oxygen atmosphere of 600 Torr.

The influence of oxygen partial pressure on film growth was investigated. **Figure 5.1** shows the θ/2θ XRD scans of a series of $La_2NiO_{4+\delta}$ films deposited on STO (001) as a function of oxygen partial pressure (30-400 mTorr). Mainly (00L) and (H00) reflections recognised by ICSD data of tetragonal $La_2NiO_{4.00}$ (space group I4/mmm) [191] can be seen in the patterns. The intensity of (00L) reflections of $La_2NiO_{4+\delta}$ gradually increased with an increase of the oxygen partial pressure from 30 to 250 mTorr while the (H00) reflections are clearly shown at the oxygen partial pressure of 100 and 400 mTorr. It is apparent that two different orientations, corresponding to c-axis oriented and a-axis oriented grains, exist in a single film, as schematically illustrated in **Figure 5.2**. The findings may indicate an effect of reorientation due to a change of oxygen partial pressure.

The crystallographic reorientation behaviour as a function of oxygen partial pressure has been found in $LaNiO_3$ and $La_{1.875}Sr_{0.125}NiO_4$ thin-films grown by the radiofrequency (RF) magnetron sputtering technique [83, 192]. In our case, due to a high oxygen pressure atmosphere during PLD, oxygen incorporation appears to be an important role for the reorientation behaviour. Varying oxygen partial pressure during deposition can strongly influence the oxidation state of Ni from Ni^{2+} to Ni^{3+} as an increase of oxygen incorporation in the interstitial sites of $La_2NiO_{4+\delta}$. The incorporation of interstitial oxygen can lead to rotations and tilts of the NiO_6 octahedra [38] and consequently yield an additional lattice strain within the films (Note that $La_2NiO_{4+\delta}$ possesses a tensile strain caused by deposition on an STO substrate). Also, excess oxygen results in an expansion of the c-axis and a contraction in the ab-plane [38]. Therefore, the reorientation behaviour may occur as the lattice structure is no longer able to accommodate strain within the film.

According to the XRD results of these $La_2NiO_{4+\delta}$ films deposited at various oxygen partial pressures, it is apparent that 250 mTorr appears to be an appropriate condition with

750°C, 5000 pulses, 0.8 J/cm^2 for the c-axis oriented film growth, although some a-axis orientation is still present.

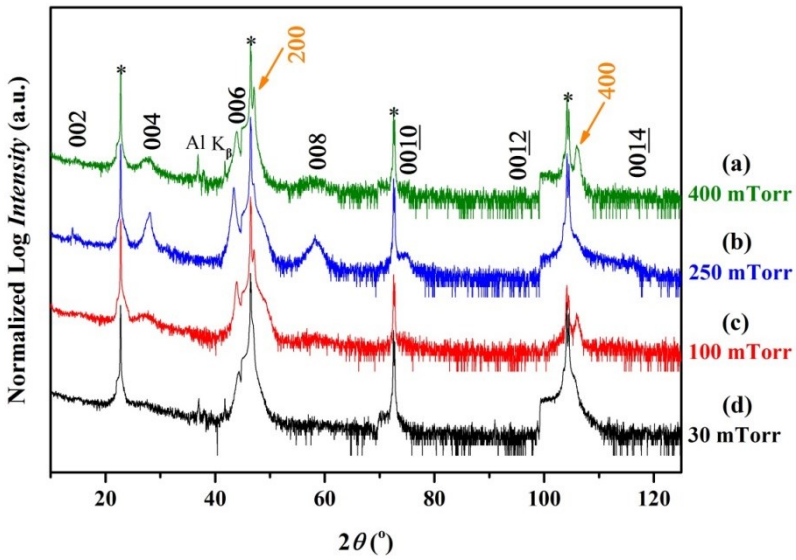


Figure 5.1 θ/2θ XRD patterns of $La_2NiO_{4+\delta}$ films grown on STO (001) single crystal substrate by 750°C, 5000 laser pulses, and power density of 0.8 J/cm^2 with different oxygen pressure 400 mTorr (a), 250 mTorr (b), 100 mTorr (c), and 30 mTorr (d). The STO substrate peaks are indicated by solid circles (*), the c-axis oriented $La_2NiO_{4+\delta}$ film peaks are indexed by (00L), and the extra orientations of (H00) are designated by arrows. Al peaks originate from the aluminium sample cradle of XRD instrument and K_β peaks correspond to XRD background.

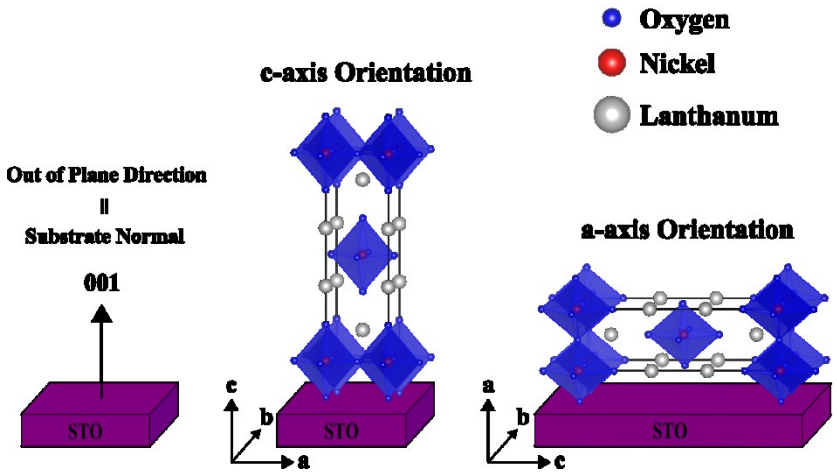


Figure 5.2 Schematic representation of the two orientations of the $La_2NiO_{4+\delta}$ thin-films in relation to the STO substrate normal direction [001], which corresponds to out of plane direction of these films.

Previous oxygen pressure experiments show the oxygen partial pressure of 250 mTorr is appropriate for growing $La_2NiO_{4+\delta}$ films. Taking into account the oxygen partial

pressure, the influence of deposition (substrate) temperatures on film growths has been further investigated. A series of $La_2NiO_{4+\delta}$ films were deposited on STO substrates at various deposition temperatures from 650 to 780°C with 5000 laser pulses and power density of 0.8 J/cm^2, as shown in **Figure 5.3**. The XRD scans of the obtained films mainly show (00L) reflections of $La_2NiO_{4+\delta}$ with a minority of (H00) reflections until the deposition temperature reached 780°C. The crystallinity of the film as evidenced in the (00L) peaks was significantly improved as the deposition temperature increased from 650 to 750°C, becoming sharper and narrower. As the deposition temperature was increased to 780°C, (H00) reflections of the parent phase were clearly shown whilst the (00L) reflections decreased. This indicates a significant reorientation phenomenon occurred at higher deposition temperature.

Generally, the increase of the deposition temperature was expected to improve the crystallinity of the $La_2NiO_{4+\delta}$ films. However, higher temperature may also provide extra thermal energy for the mobility of the in-plane RP layers, resulting in disordered growth [193]. Furthermore, deposition (substrate) temperature, in principle, has a large effect on the mobility of the adatoms (adsorbed atoms) so the adatoms may perform random diffusions, pair with other adatoms and stick to larger clusters or nuclei. Consequently, deposition temperature has a significant influence on the degree of the nucleation density [194]. Early studies have found the nucleation density generally decreases with the increase of deposition temperature [195]. Therefore, a continuous layer needs a longer time to be formed at higher deposition temperature due to the smaller nucleation density. According to this behaviour, if a new layer nucleates before a completed layer is formed, remaining voids (caused by ledges and kinks) are therefore formed and act as a sink, leading to an energetically favorable migration of the adatoms to the sink in order to minimize surface energy. Thus a structural reorientation phenomenon may occur at higher deposition temperature.

The SEM images presented in **Figure 5.4** depict that the evolution of surface morphological change of the $La_2NiO_{4+\delta}$ films is strongly dependent upon the deposition temperature. The image obtained from the films deposited at 650°C displays a uniform and continuous matrix with a small number of crystalline outgrowths at the surface. As the deposition temperature was increased from 650 to 750°C, an increase in the number of small crystallites and a gradual grain growth of the matrix were observed, clearly indicating the nucleation and coalescence of the small crystallites at increasing temperatures. Up to 780°C, the small crystallites became square-like, and were regularly arranged and uniformly covered the base matrix. In comparison with the XRD patterns (**Figure 5.3**), the formation of square-like crystallites shown in **Figure 5.4 (a)** could be speculated to be a result of the a-axis orientation (H00) of $La_2NiO_{4+\delta}$ films. Therefore, this surface morphological change may imply a manifestation of a structural change of the films.

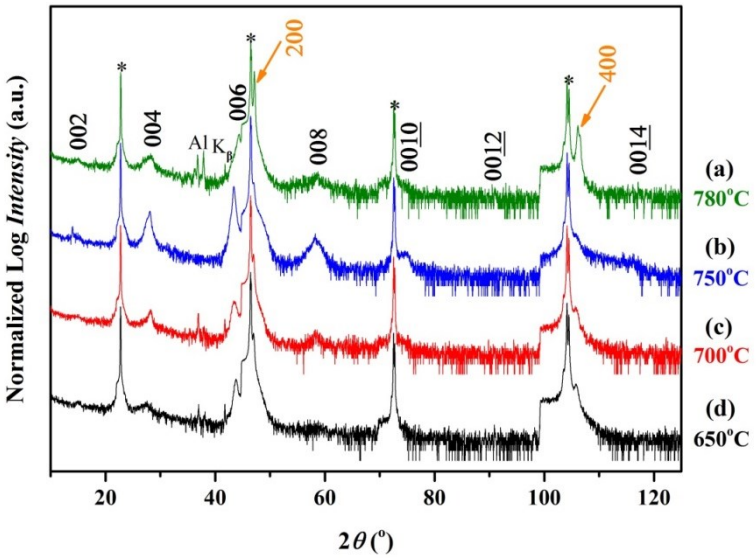


Figure 5.3 θ/2θ XRD patterns of $La_2NiO_{4+\delta}$ films grown on STO (001) single crystal substrate by 250 mTorr, 5000 laser pulses and power density of 0.8 J/cm^2 with various deposition temperatures (a) - (d). The STO substrate peaks are indicated by solid circles (*), the c-axis oriented $La_2NiO_{4+\delta}$ film peaks are indexed by (00L), and the extra orientations of (H00) are designated by arrows. Al peaks originate from the aluminium sample cradle of XRD instrument and K_β peaks correspond to XRD background.

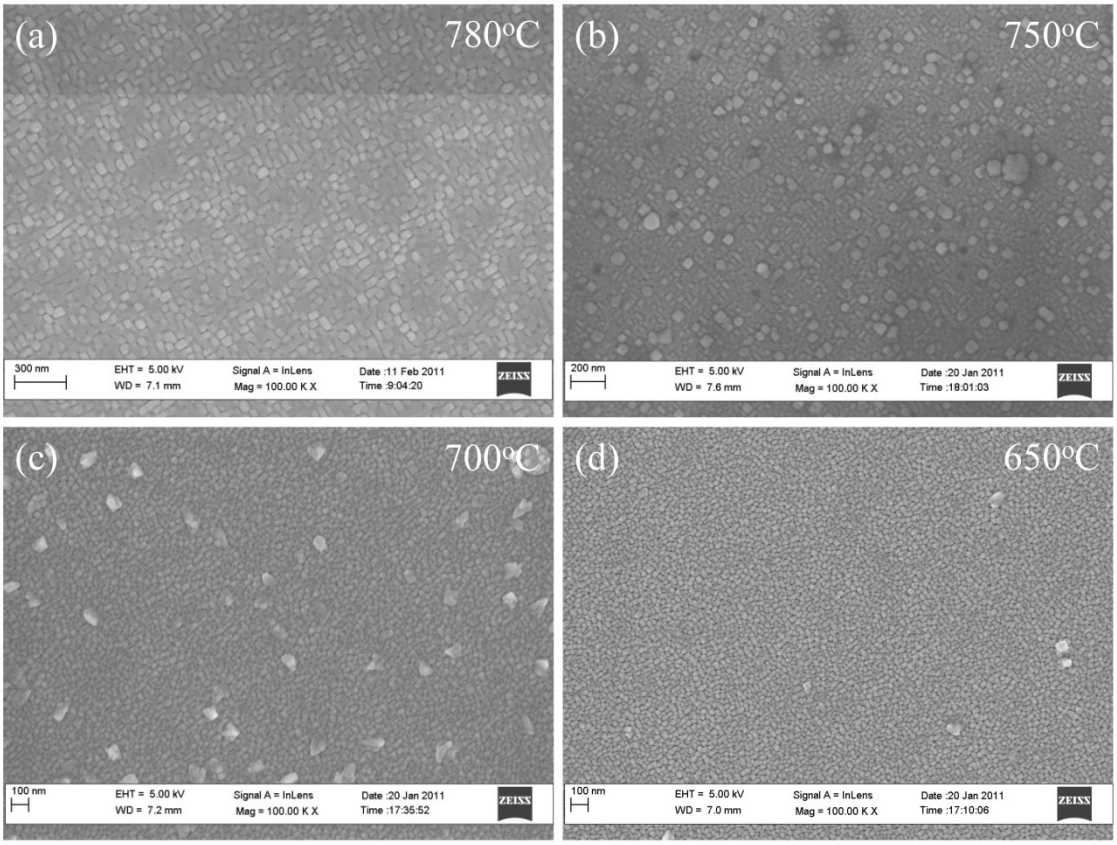


Figure 5.4 SEM morphological images of $La_2NiO_{4+\delta}$ thin-films deposited on STO by 250 mTorr, 5000 laser pulses and power density of 0.8 J/cm^2 with various deposition temperatures of 780°C (a), 750°C (b), 700°C (c) and 650°C. Their scale markers are 300 nm, 200 nm, 100 nm and 100 nm, respectively.

In addition to the effects of oxygen partial pressure and deposition temperature, film thickness was also found to be critical for the formation of reorientation. By reducing the number of laser pulses from 5000 to 3000, (H00) reflections of $La_2NiO_{4+\delta}$ were completely eliminated and only (00L) reflections were observed (see **Figure 5.5**), indicating that the films have a fully c-axis-preferred orientation, within the detection limit of the instrument. Also, the SEM image of films deposited with 3000 pulses (**Figure 5.6 (a)**) exhibits a smoother surface with a smaller crystalline feature than the image of the films deposited with 5000 pulses (**Figure 5.6 (b)**).

The results of the XRD scans and SEM images reveal a structural reorientation as a function of thickness. According to the theoretical studies of surface structure of the La_2NiO_4 system, Read *et al.* has proposed that the (100) plane of the compound has the

lowest surface energy, compared to all other planes [196]. As the films grow thicker, the crystal growths tend to minimise the surface energy, and hence the intensity of the (200) plane becomes enhanced. Similar phenomena of reorientation were also observed by Telesca *et al.* in La_2NiO_4 (grown on STO by PLD) [84] and Podpirka *et al.* in $La_{1.875}Sr_{0.125}NiO_4$ (grown on STO by RF sputtering) [83].

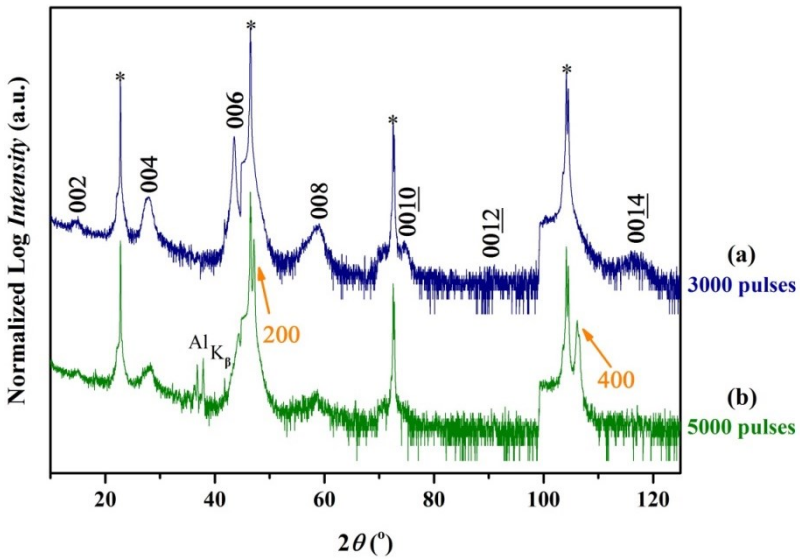


Figure 5.5 θ/2θ XRD patterns of $La_2NiO_{4+\delta}$ films grown on STO (001) single crystal substrate by 780°C, 250 mTorr, and power density of 0.8 J/cm^2 with 3000 (a) and 5000 (d) laser pulses. The STO substrate peaks are indicated by solid circles (*), the c-axis oriented La_2NiO_4 film peaks are indexed by (00L), and the extra orientations of (H00) are designated by arrows. Al peaks originate from the aluminium sample cradle of XRD instrument and K_β peaks correspond to XRD background.

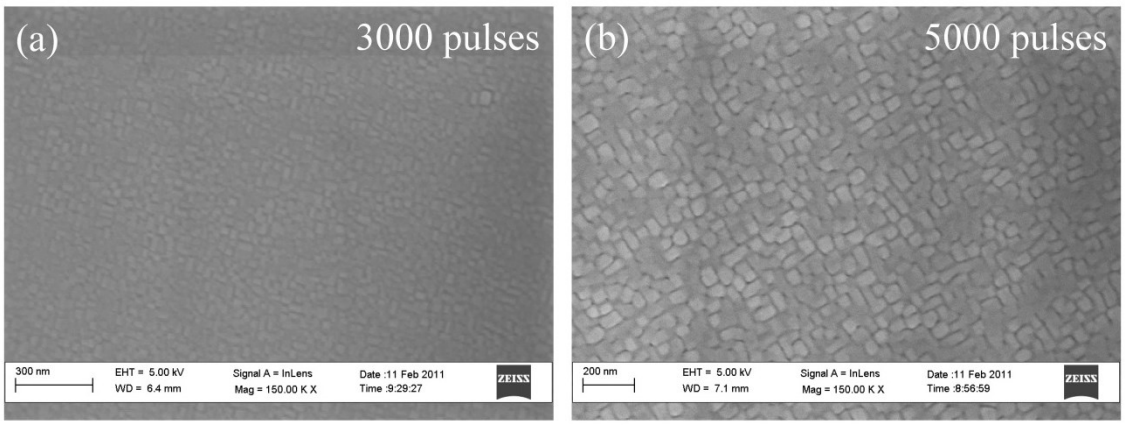


Figure 5.6 SEM morphological images of $La_2NiO_{4+\delta}$ thin-films deposited on STO by 780°C, 250 mTorr and power density of 0.8 J/cm^2 with (a) 3000 and (b) 5000 laser pulses. Their scale markers are 300 nm and 200 nm, respectively.

Presently, c-axis oriented $La_2NiO_{4+\delta}$ films have been obtained at 780°C with an oxygen partial pressure of 250 mTorr, a pulse frequency of 8 Hz, a laser fluence of 0.8 J/cm^2, and 3000 laser pulses, but the obtained films are of low crystallinity (broad peaks) as seen in **Figure 5.5 (a)**. The low crystallinity behaviour indicates the crystal lattices of the films are disordered or misaligned.

To improve the crystallinity of the c-axis oriented $La_2NiO_{4+\delta}$ films, a series of films were deposited as a function of laser fluence (0.6-1.0 J/cm^2) as seen in **Figure 5.7**. **Figure 5.7 (b)** shows the XRD patterns of the films deposited with a laser fluence of 0.8 J/cm^2 as used previously. In general, a high laser fluence can provide a large amount of ablated material from the target, consequently a high degree of supersaturation (dense plasma) and a large nucleation density on the substrate surface, these factors can lead to a favorable 2D growth (layer-by-layer) to fabricate the films [135, 136]. An attempt to increase the laser fluence (from 0.8 to 1.0 J/cm^2) was expected to improve the crystallinity. However, the result produced films with lower crystallinity and even revealed a reorientation phenomenon, as can be seen in **Figure 5.7 (c)**. The consequence of poor-quality $La_2NiO_{4+\delta}$ films might be caused by a target degradation process (described previously in Section 4.1.2) at higher laser fluence. Also, it is likely that the increasing laser fluence would cause an increase in deposition thickness due to a higher ablation rate and a wider thickness distribution profile [197, 198]. Therefore, again, as the thickness is increased, a tendency of crystal growth along (100) planes (possessing lowest surface energy [196]) could occur in order to minimise the surface energy [83, 199], resulting in such reorientation phenomenon.

On the contrary, as the laser fluence was decreased to 0.6 J/cm^2, the intensity and crystallinity of all (00L) peaks of the films were remarkably improved, leading to tremendously sharper and narrower peaks as shown in **Figure 5.7 (a)**. Thus, a laser fluence of 0.6 J/cm^2 is an appropriate energy for the construction of the lattice blocks,

leading to the fabrication of high-quality c-axis oriented $La_2NiO_{4+\delta}$ films.

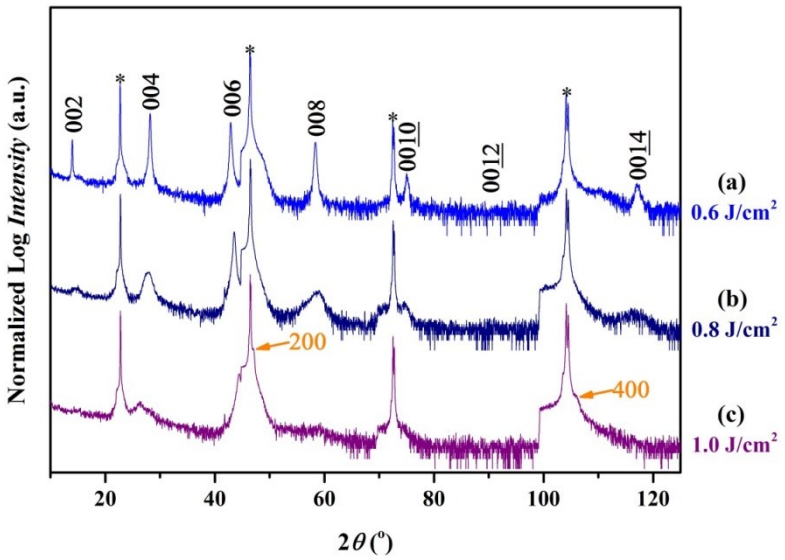


Figure 5.7 θ/2θ XRD patterns of $La_2NiO_{4+\delta}$ films grown on STO (001) single crystal substrate by 780°C, 250 mTorr,, and 3000 laser pulses with various laser fluences of 0.6 J/cm^2 (a), 0.8 J/cm^2 (b) and 1.0 J/cm^2 (c). The STO substrate peaks are indicated by solid circles (*), the c-axis oriented $La_2NiO_{4+\delta}$ film peaks are indexed by (00L), and the extra orientations of (H00) are designated by arrows.

Taking into account the optimal laser fluence of 0.6 J/cm^2, a series of thin-films were deposited as a function of laser pulses or thickness in order to estimate the growth rate of the c-axis oriented $La_2NiO_{4+\delta}$ epitaxial film deposited on STO (001) substrate and briefly investigate the growth mode for this compound.

Figure 5.8 shows the XRD patterns of $La_2NiO_{4+\delta}$ epitaxial films plotted with various number of laser pulses: 1000, 3000 and 5000 pulses, corresponding to ~17 nm, ~52 nm and ~82 nm, respectively. These thickness values were determined by contact profilometer (Vecco DekTak 150). The growth rate of the films is estimated at approximately 0.169±0.005 Å/pulse. All the diffraction peaks can be assigned to the (00L) reflections of the $La_2NiO_{4+\delta}$ phase, which confirms that pure c-axis oriented $La_2NiO_{4+\delta}$ films were obtained. Overall, the intensity of the peaks increased with increasing thickness, although the peaks of the 82 nm film appear to become broader than the ones

of the 52 nm film, which presumably implies that a phenomenon of disordered growth occurred for the 82 nm film (**Figure 5.8 (a) and (b)**). Such phenomenon can be clearly seen in the SEM images of **Figure 5.9 (a)**, showing a number of small crystallites on the surface. These small crystallites could be attributed to the nucleation spots of (H00) orientations for structural reorientations, as stated previously. Therefore, this suggests a critical thickness exists for the deposition of the c-axis oriented $La_2NiO_{4+\delta}$ films, which is in agreement with the previous literature [84]. In the case of the 52 nm film, **Figure 5.9 (b)** exhibits a continuum surface structure, whereas the 17 nm film appears to show a feature of tiny voids or pinholes uniformly distributed on the surface as shown in the SEM image of the **Figure 5.9 (c)**.

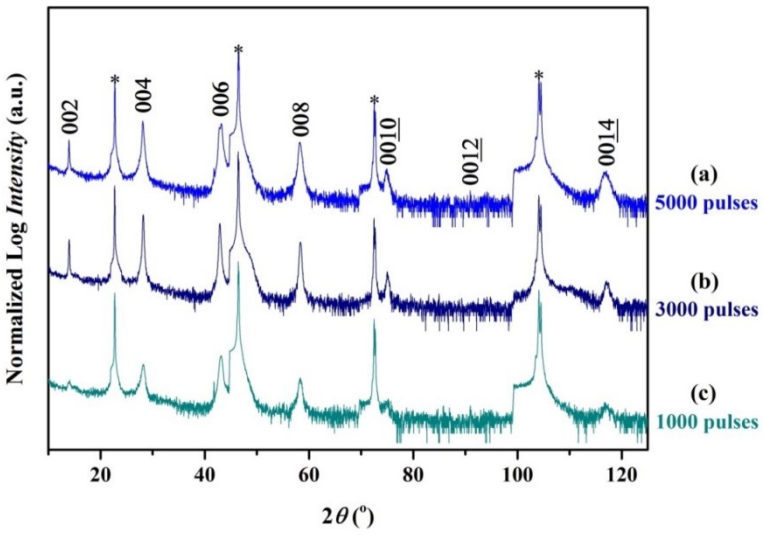


Figure 5.8 XRD patterns of $La_2NiO_{4+\delta}$ films grown on STO (001) single crystal substrate as a function of laser pulses of 5000 (a), 3000 (b) and 1000 (c). The STO substrate peaks are indicated by solid circles (*) and all (00L) reflections shown are attributed to the c-axis oriented $La_2NiO_{4+\delta}$ films.

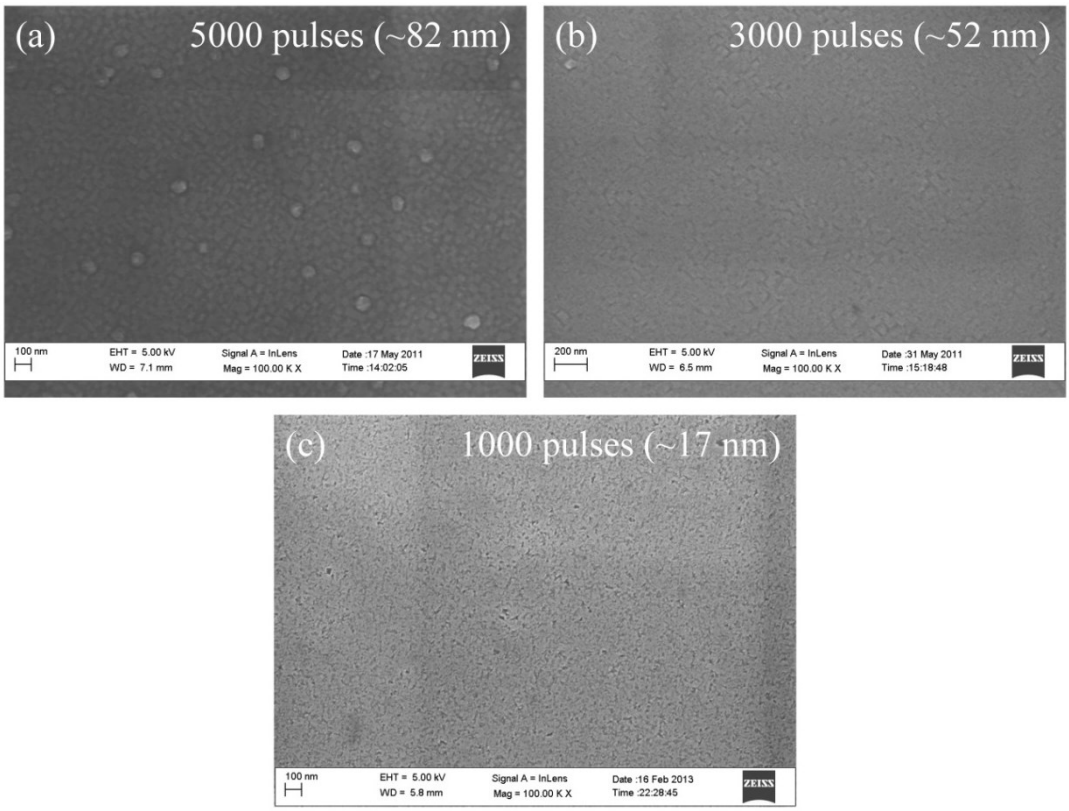


Figure 5.9 SEM morphological images of $La_2NiO_{4+\delta}$ thin-films deposited on STO as a function of laser pulses of 5000 (a), 3000 (b) and 1000 (c). Their scale markers are 100 nm, 200 nm and 100 nm, respectively.

AFM was used to further investigate the evolution of surface morphology as a function of thickness, to estimate the surface roughness, and to demonstrate a possible growth model of the c-axis oriented $La_2NiO_{4+\delta}$ films deposited on STO (001) substrates. **Figure 5.10 (a) - (c)** provide 2D and 3D AFM images of the 17 nm, 52 nm and 82 nm films, respectively. In these figures, distribution histograms of height (Z depth scale) data are also demonstrated in **Figure 5.10 (d) - (f)**.

In the case of the 17 nm film, the features of tiny voids or pinholes observed in the previous SEM image (**Figure 5.9 (c)**) are also exhibited in the AFM images (**Figure 5.10 (a)**). The root-mean-square (RMS) values of the surface roughness was estimated at ~1.3 nm. As the thickness was increased to 52 nm (**Figure 5.10 (b)**), the image apparently shows a spike-like island structure, and the amount of voids or pinholes significantly diminishes due to the coalescence of the spike-like islands, leading to a denser structure and smoother surface with a lower RMS surface roughness of ~1.0 nm, in comparison with the 17 nm film. This suggests grain growth proceeded horizontally with increasing thickness. The smooth surface is further confirmed by a uniform distribution of height demonstrated in **Figure 5.10 (e)**. As the thickness reached 82 nm, the surface structure dramatically changed. The AFM images exhibit strikingly larger spike-shape structures and a strong coalescence of uniform three dimensional spike-like islands, as shown in the 3D image of **Figure 5.10 (c)**. The RMS values of roughness significantly increased to ~3 nm, which can be reflected via a broader distribution histogram of height (**Figure 5.10 (f)**). This indicates the grain growth proceeded not only horizontally but also perpendicular to the substrate with increasing thickness. Therefore, the potential growth mode of the c-axis oriented $La_2NiO_{4+\delta}$ epitaxial films deposited on STO (001) substrate is presumably considered to be the so-called island (Volmer-Weber) growth mode [136, 200]. Such growth mechanism has also been found in layered superconductor $YBa_2Cu_3O_{7-\delta}$ films grown by PLD as function of deposition rate [201].

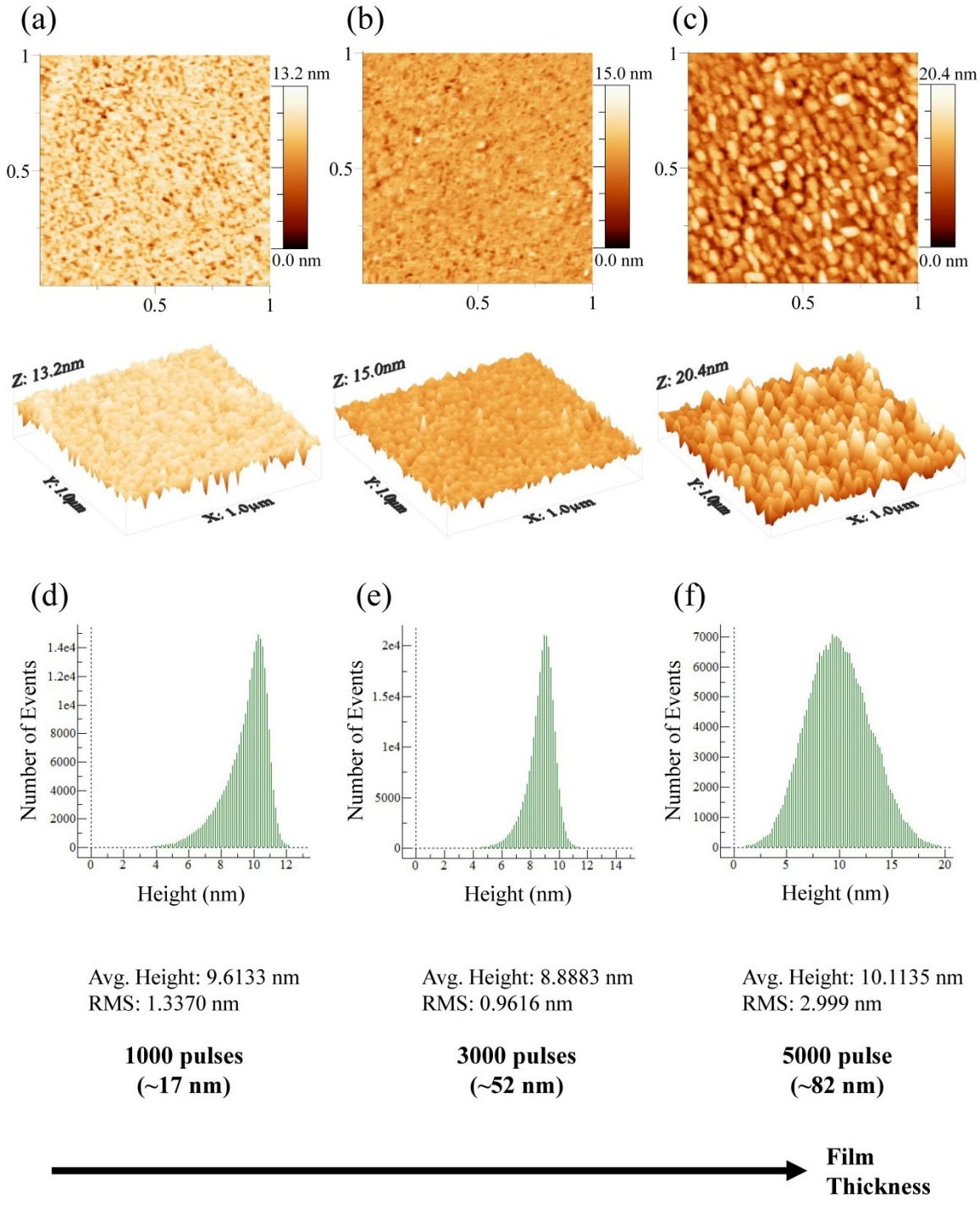


Figure 5.10 AFM images of $La_2NiO_{4+\delta}$ thin-film deposited on STO as a function of laser pulses (or thickness). (a) - (c) show 2D and 3D images of 1000 - 5000 pulses with image size: 1 µm × 1 µm, Z depth scale: (a) 13.2 nm, (b) 15.0 nm and (c) 20.4 nm from dark brown to white. (g) - (i) demonstrate the image distribution histograms of height (Z depth scale) data of each pixel plotted with number of events. The avg, height and RMS values are presented on the bottom of the image group.

After a series of systematic studies of film deposition, the growth conditions were refined via investigating the influence of oxygen partial pressure, deposition temperature, laser pulses (thickness) and laser fluence. These optimal growth conditions to synthesise high quality c-axis oriented layered RP-type epitaxial films of $La_2NiO_{4+\delta}$ can be thereby defined in **Table 5.1**. The conditions were also adopted to successfully prepare the c-axis oriented $La_2NiO_{4+\delta}$ films on NGO (110) substrates, which will be discussed in the next section.

Table 5.1 Optimal Growth Conditions for c-axis oriented $La_2NiO_{4+\delta}$ epitaxial films

Growth conditions	
Laser type	KrF excimer laser (λ=248 nm)
Growth direction	c-axis
Deposition temperature	700~780°C
Oxygen partial pressure	250 mTorr
Laser fluence	~0.6 J/cm^2
Laser pulse frequency	8 Hz
Target-substrate distance	50 mm
Cooling rate	10 °C/min
Oxygen Pressure in Cooling	600 Torr

5.2 Characterisation of $La_2NiO_{4+\delta}$ Epitaxial Films on STO and NGO

By applying the appropriate growth conditions obtained for c-axis $La_2NiO_{4+\delta}$ epitaxial films deposited on STO (001) substrates discussed in section 5.1, high-quality c-axis $La_2NiO_{4+\delta}$ films deposited on NGO (110) were also achieved. In this Section, a series of comparatively structural and morphological investigations for the c-axis $La_2NiO_{4+\delta}$ epitaxial films on STO (001) and NGO (110) are systematically performed, involving X-ray diffraction (θ/2θ, rocking curves, and φ-scans) and AFM characterization, followed by out-of-plane parameter charaterisation. These investigations were carried out to evaluate the quality of the films and to understand the correlation with the effect of strain (tensile and compressive) from the STO and NGO single crystal substrates.

5.2.1 Crystallographic Analysis and Film Quality

Successful deposition of high quality c-axis oriented $La_2NiO_{4+\delta}$ epitaxial films on both STO (001) and NGO (110) substrates was achieved with the correct cation stoichiometry. **Figure 5.11 (a)** shows the θ/2θ XRD scans for epitaxial c-axis oriented $La_2NiO_{4+\delta}$ films deposited on STO (001) at a substrate temperature of 780°C. All the peaks can be assigned to the (00L) reflections of the parent phase. In comparison, $La_2NiO_{4+\delta}$ films grown on NGO (110) substrates at a lower substrate temperature of 750°C show significantly sharper and narrower peaks for all (00L) reflections (**Figure 5.11 (b)**). The lower substrate temperature used for the growth on NGO showing better quality than on STO is likely attributed to a rather low average mismatch of -0.02% (compressive stress) between NGO and $La_2NiO_{4+\delta}$, as seen in **Table 5.2**. Similar to the $La_2NiO_{4+\delta}$ epitaxial films deposited via pulsed injection metal organic chemical vapor deposition [39], it is apparent that in this work single phase epitaxial films were produced. The θ/2θ scans in

this scattering configuration, however, only indicate that the films all have a single orientation normal to the film planes.

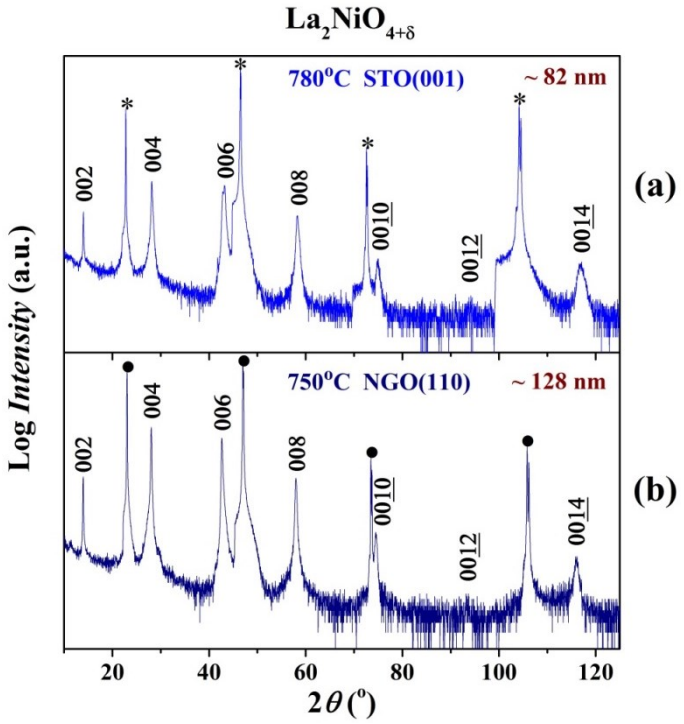


Figure 5.11 θ/2θ XRD patterns of c-axis oriented $La_2NiO_{4-\delta}$ phases grown on STO (001) at 780°C (a) and on NGO (110) single crystal substrates at 750°C (b). The $SrTiO_3$ and $NdGaO_3$ substrate peaks are indicated by star (*) and solid circles (•), respectively. The c-axis oriented film peaks are indexed by (00L). Film thickness determined by Dektak 150 Surface Profiler is shown as an insert in top right of each pattern.

Phase	n	Crystal System	Lattice Parameters (Å)			[Ref.]	Lattice Mismatch	
			a	b	c		STO (001)	NGO (110)
$La_2NiO_{4.25}$	1	Orthorhombic (Fmmm)	5.4563	5.4630	12.7049	[189]	+1.15%	-0.02%

Table 5.2 Summary of crystal structures, space groups, lattice parameters and mean lattice mismatch with STO (001) and NGO (110) substrates for the layered RP-type $La_2NiO_{4-\delta}$ (n = 1) compounds based on ICSD (Inorganic Crystal Structure Database) data.

In order to further ascertain the epitaxial quality of the films, rocking curve measurements were conducted and the full width at half maximum (FWHM) of the (004) peak for the films grown on STO was determined to be 0.55° (**Figure 5.12 (a)**). The $La_2NiO_{4+\delta}$ (n = 1) films deposited on NGO display a significant improvement of FWHM to 0.11° (**Figure 5.12 (b)**), indicating their excellent crystallinity and out-of-plane alignment. The other essential parameters to verify the quality of films are surface morphology and roughness. **Figure 5.13 (a)** and **(b)** show 1×1μm AFM images with ~3.0 nm and ~1.8 nm RMS values of roughness for $La_2NiO_{4+\delta}$ films on STO and NGO substrates, respectively. The AFM image of $La_2NiO_{4+\delta}$ films grown on NGO displays improved surface morphology compared to the films on STO. This is perhaps expected because of the smaller lattice mismatch (only -0.02%) of $La_2NiO_{4+\delta}$ with NGO substrates. As a result of the superior n = 1 film quality and the superior lattice match according to calculation, NGO (110) was decided to be used as substrates for the deposition of all higher-order $La_{n+1}Ni_nO_{3n+1}$ phases (n = 2 and 3), possessing the smaller lattice mismatch with NGO (seen previously in **Table 4.2**).

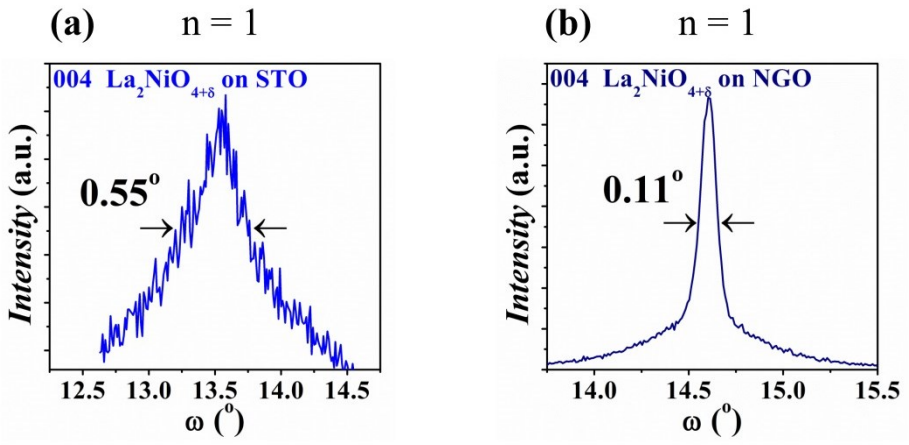


Figure 5.12 X-ray rocking curves of the c-axis oriented $La_2NiO_{4+\delta}$ (n = 1) films: (a) (004) reflection of 82 nm thick $La_2NiO_{4+\delta}$ film on $SrTiO_3$ and (b) (004) reflection of 128 nm thick $La_2NiO_{4+\delta}$ film on $NdGaO_3$.

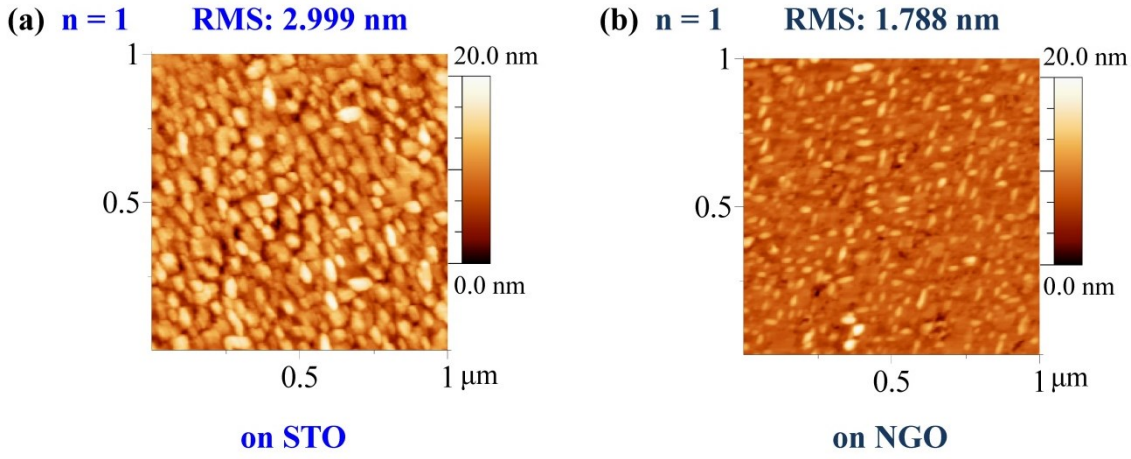


Figure 5.13 AFM images of the c-axis oriented $La_2NiO_{4+\delta}$ (n = 1) films (a) 82 nm thick $La_2NiO_{4+\delta}$ film on $SrTiO_3$, (b) 128 nm thick $La_2NiO_{4+\delta}$ film on $NdGaO_3$. Image size: 1 µm × 1 µm, depth scale: 20 nm from dark brown to white.

5.2.2 Limitation of Identifying Film Crystal Structures

Prior to studying the orientation relationship between films and substrates, it is worth taking account of the limits regarding this case. The possibility of identifying the obtained films was considered with the two different crystal structures that exist in bulk: tetragonal vs. orthorhombic. However, there are several limitations involved in the structural investigation: the nature of the lanthanum nickelates, the resolution of the utilized XRD equipment, and the crystallinity of the films. Firstly, the a and b parameters of the orthorhombic systems have no significant difference (see **Table 4.2**), which indicates the difficulty in distinguishing interplanar distances (d-spacings) along the a and b axes. Additionally, the resolution of the utilized XRD equipment may pose a limit in identifying the structures of the deposited $La_2NiO_{4+\delta}$, $La_3Ni_2O_{7-\delta}$ or $La_4Ni_3O_{10-\delta}$ films. To determine the instrumental contribution to the peak width the resolution of the

diffractometer was determined from the width of the single crystal substrate peaks (~0.04-0.10°).

To investigate the phase deposited two reflections, (101) and (111), were considered. They were selected from the tetragonal and orthorhombic crystal structures of $La_2NiO_{4+\delta}$. The FWHM in 2θ of the (101) and (111) reflections from the XRD results are ~0.35° and ~0.40°, respectively which were determined when Ψ was fixed at 73.05° and 73.09° for (101) and (111) respectively. The peak widths are much broader than the theoretical 2θ difference (~0.01°) of the (101) and (111) reflections for bulk tetragonal and orthorhombic crystal structures. Although, at higher-index planes, the 2θ difference between the tetragonal and orthorhombic structures may increase, the difference is still limited to ~0.5°, making the distinction between tetragonal and orthorhombic structures impossible. It is therefore likely that the peak width is largely attributed to the crystallinity of the film, which leads to no distinguishable difference between the tetragonal and orthorhombic structures in the diffraction patterns. Throughout the rest of the article, we therefore adopt the orthorhombic notation.

5.2.3 Film Orientation Characterisation

Further characterisation through phi(φ) scans of in-plane orientation between film and substrate is necessary to confirm the epitaxial growth. The analyses of the orientation relationship are carried out as follows. For $La_2NiO_{4+\delta}$ films, the (111) reflection was selected for φ-scan characterization since it yields high intensity and there are no reflections from the substrates close to the 2θ and Ψ(psi) azimuths for this reflection. According to the symmetry of an orthorhombic structure with a large difference in a and b lattice parameters, a φ-scan pattern displaying two peaks at intervals of every 180° is expected. However, in **Figure 5.14 (a)** and **(b)**, four peaks were observed in the φ-scans

of (111) reflections from $La_2NiO_{4+\delta}$ with four-fold symmetry at intervals of every 90°, which precisely fit with the φ-scan patterns of (101) and (200) reflections from STO and NGO substrates, respectively. The reason for showing four-fold symmetry is due to the small difference in a and b lattice parameters, the width of the diffraction peaks, and the low resolution of the utilized XRD equipment, as previously discussed. The orientation relationships between $La_2NiO_{4+\delta}$ and the substrates do correspond to the expected geometry as shown previously in **Figure 4.9**.

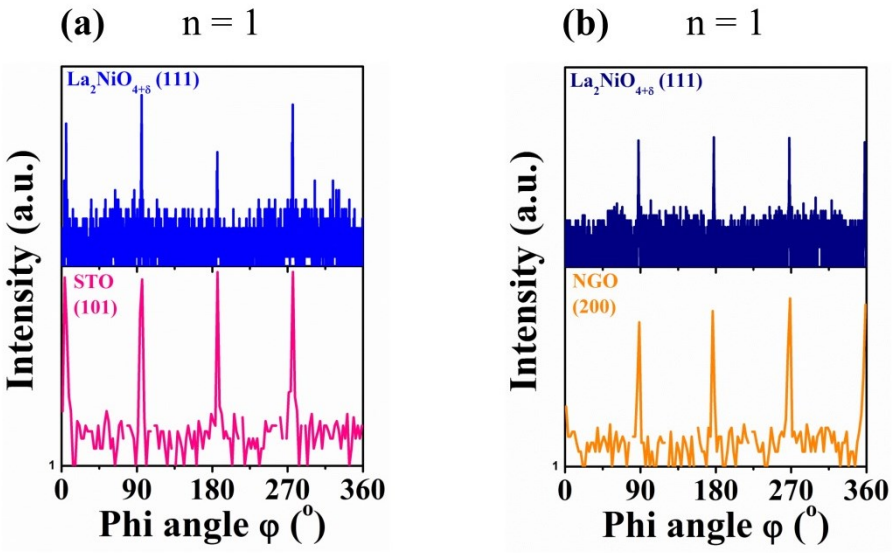


Figure 5.14 Phi(φ)-scan patterns for the c-axis oriented $La_2NiO_{4+\delta}$ (n = 1) films: {111} reflections registered at 2θ=24.093°, Ψ=73.09° for $La_2NiO_{4+\delta}$ films on $SrTiO_3$ and $NdGaO_3$ substrates shown in (a) and (b) respectively.

5.2.4 Out-of-Plane Parameter Characterisation

A detailed analysis of the out-of-plane (c-axis) parameters from θ/2θ XRD patterns of n = 1 films was carried out to compare with the expected c-axis parameters of the bulk

material. Using the Lorentz method, the 2θ peak positions and d-spacings of every (00L) reflection for each sample were carefully fitted. After calculation, the fitted c-axis parameters were plotted as a function of index of (00L) reflections in comparison with the expected parameters from standard orthorhombic and tetragonal bulk references [189, 191]. **Figure 5.15** demonstrates the fitted c-axis parameters of $La_2NiO_{4+\delta}$ films grown on STO and NGO. Although the c-axis parameter of the (006) reflection from the film on STO has a large deviation from that of other reflections due to the splitting of the (006) peak, the rest of the parameters are well fitted with the references from bulk material. Average c-axis parameters of 12.656±0.034 Å and 12.721±0.009 Å were determined for the films grown on STO and NGO respectively. The values reasonably indicate that a compression in the out-of-plane direction can be caused by the in-plane tensile strain (lattice mismatch +1.15%) for films deposited on STO, which contribute to a slight decrease in the c-axis parameter. Conversely, a slight increase in the c lattice parameter can be due to the compressive strain (-0.02%) for films deposited on NGO. Besides lattice strain, the c-axis lattice parameters of films can differ from the bulk values due to non-stoichiometric oxygen content (δ). It is known that the higher the oxygen content, the larger the c-axis parameter in bulk specimens [32, 92, 202]. However, it is challenging to measure the oxygen content of thin-film specimens via typically thermo-gravimetric methods because of the small mass of thin films, and therefore the contribution of oxygen content cannot be assigned to the lattice parameters of our films.

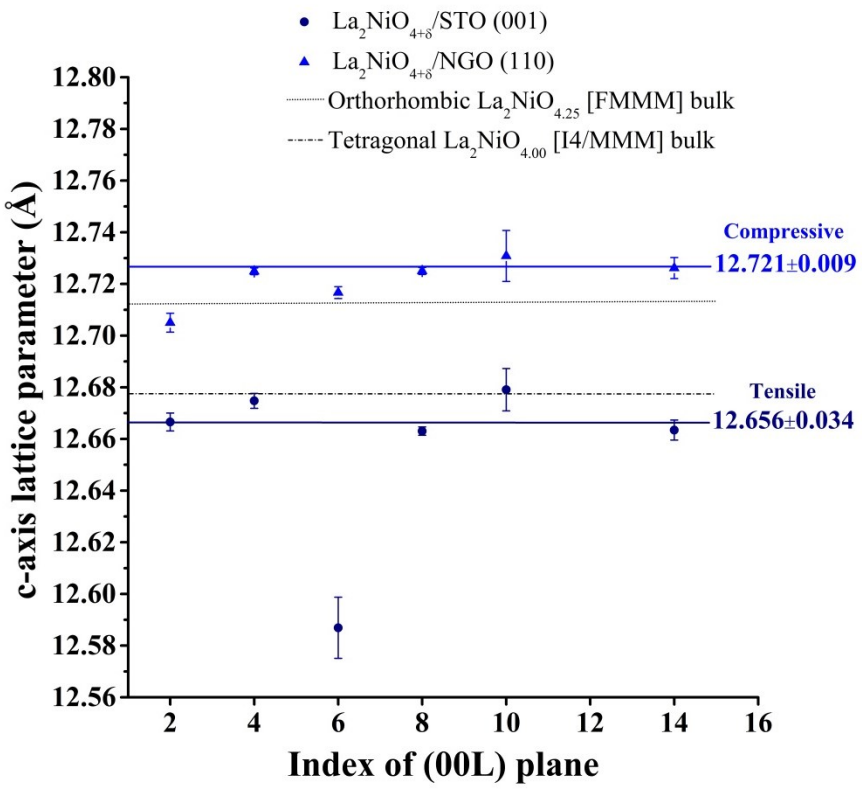


Figure 5.15 c-axis lattice parameter as function of (00L) planes for $La_2NiO_{4+\delta}$ films grown on STO (001) and NGO (110). The $La_2NiO_{4+\delta}$ film on STO is represented by solid circle (●); the film on NGO is represented by solid triangle (▲) with five units of the standard deviation errors from each individual fitted (00L) peak. The measured averages of c-axis parameters are labelled in the diagram. The analyses were based on the compared relationship of measured c-axis lattice parameters of each (00L) plane from the films with the values for the selected standard crystal structures of bulk materials (Orthorhombic [Fmmm]; Tetragonal [I4/mmm]) [189, 191]. The results show the c-axis parameters are influenced by strain from different substrates.

5.3 Electrical Conductivity Characterisation

High quality c-axis oriented $La_2NiO_{4+\delta}$ epitaxial films deposited on STO and NGO substrates have been achieved and structurally and morphologically confirmed in the previous sections. In this section, the functional properties of the films will be investigated. As described previously, the $La_2NiO_{4+\delta}$ naturally possess anisotropic

transport properties (electronic and ionic) due to its layered structure, which has maximum transport along the a-b planes. [37, 41, 87, 111] In the case of the deposited c-axis oriented $La_2NiO_{4+\delta}$ epitaxial films, their total planar electrical conductivity along a-b plane are allowed to be measured via 4-point DC van der Pauw method. With such measurements, in addition to determining their electrical properties, the quality of these $La_2NiO_{4+\delta}$-phase films can be further ascertained via the comparison of their electrical conductivity with literature data.

Prior to the conductivity measurements, it must be noted that the conductivity of STO and NGO substrates have total conductivity of 10^{-3} Scm^{-1} and 10^{-6} Scm^{-1} at 700°C respectively [40], which are several orders of magnitude lower than that of $La_2NiO_{4+\delta}$ and other higher order compounds. Therefore, even for the thinner films (50 nm), the contribution of both substrates (0.5 mm thick) on conductance is anticipated to be negligible during the measurements.

The planar conductivity measurements have been conducted on the films grown on both substrates and performed as a function of temperature from room temperature (RT) to 700°C under static air with a temperature interval of 50°C, as seen in **Figure 5.16 (a)**. The total electrical conductivity exhibits a semiconducting to metallic-like behaviour, with conductivity maxima of 72 Scm^{-1} for the film deposited on STO and 109 Scm^{-1} for the one on NGO, observed at approximately 450-500°C where thermally activated behaviour occurs. Above this temperature, their conductivity gradually decreases due to the loss of oxygen content from the films, leading to a reduction of the Ni^{3+} content and thereby a decrease in the density of hole charge carriers [46, 95, 203]. The conductivity differences between the films grown on STO and NGO could originate from a certain extent of microstructural differences, caused by either the induced strain from the mismatch of the film/substrate or the lattice orientation of the films. Also, the film deposited on NGO exhibits higher conductivity than the film on STO, which is probably

because the film on NGO has better quality than the film on STO. This corresponds to the XRD and crystallinity results (seen previously in **Figure 5.11 and 5.12**). As seen in **Figure 5.16 (a)**, the total electrical conductivity of the film deposited on STO presents anomalies at 250-300°C, which could be attributed to the temperature fluctuation from the tubular furnace.

Previous studies have confirmed, based on the dependence with temperature and oxygen partial pressure, the conductivity of $La_2NiO_{4+\delta}$ exhibits predominantly p-type electronic conductivity and is governed by a small-polaron hopping mechanism [203, 204]. Thus, the Arrhenius equation can be typically defined as:

$$\sigma = \frac{A}{T}\exp(-\frac{E_a}{kT}) \tag{5.1}$$

where σ is the total electrical conductivity, A is a pre-exponential constant, E_a represents the activation energy (eV) for carrier hopping, T is temperature in Kelvin, and k represents Boltzmann's constant (8.617×10^{-5} eVK^{-1}). This equation can be rearranged to Eq. 5.1, which facilitates the determination of activation energy (E_a):

$$\ln(\sigma T) = -\frac{E_a}{kT} + \ln(A) \tag{5.2}$$

According to the equation, a so-called Arrhenius diagram can be plotted with ln(σT) vs reciprocal temperature (1/T), as shown in **Figure 5.16 (b)**. The activation energy for both films on STO and NGO were determined to be ~0.100 eV and ~0.071 eV respectively, which are consistent with the results from previous literature works [40, 87, 111, 203].

In **Figure 5.17** the total electrical conductivity for both c-axis oriented $La_2NiO_{4+\delta}$ epitaxial samples is plotted as a function of temperature, together with literature data for $La_2NiO_{4+\delta}$ polycrystalline bulks [33], single crystals [111], and c-oriented epitaxial films grown by PI-MOCVD [39]. Since the transport properties of the $La_2NiO_{4+\delta}$ are expected to be highly anisotropic, it is apparent that our c-axis oriented epitaxial samples deposited on NGO, except for on STO, exhibit a larger conductivity along a-b plane than the

randomly oriented polycrystalline bulk material. The slightly lower conductivity of the films on STO than that in bulk material might be due to either poor crystallinity or microstructure of the samples (mentioned above). On the contrary, much higher conductivity values of the single crystals than both films and all other samples can be obviously observed in the diagram. Similar electrical behaviour was also observed in the $La_2NiO_{4+\delta}$ epitaxial films deposited by PI-MOCVD from literature data, showing that the films on NGO also presented a higher conductivity than the films on STO. The results could be caused by different deposition techniques, leading to the differences in the quality, crystallinity and thickness of films and hence the variation of the electrical conductivity. However, the conductivity values of both samples, generally, located at a reasonable range, compared to literature data.

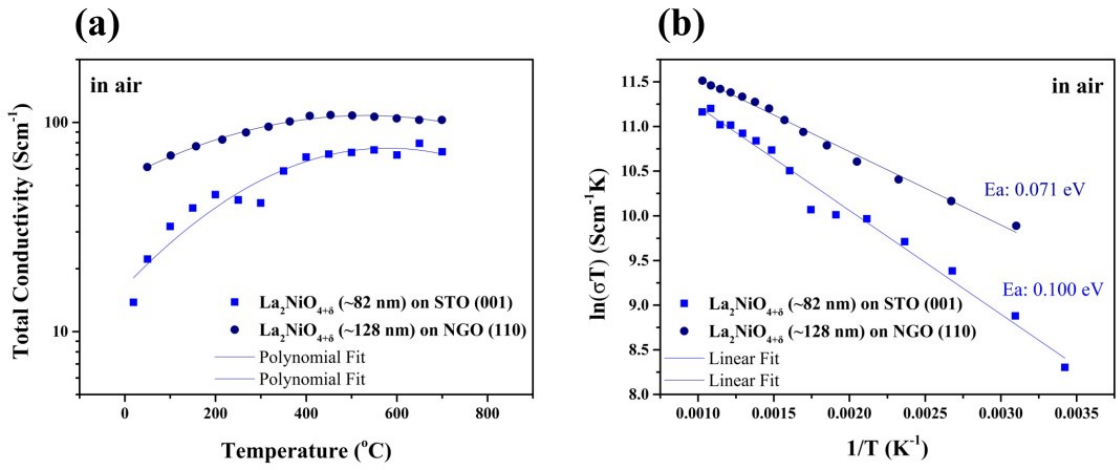


Figure 5.16 Total electrical conductivity of the c-axis oriented $La_2NiO_{4+\delta}$ epitaxial films deposited on STO and NGO substrates as a function of temperature from RT to 700°C in air (a), and Arrhenius plot of the electrical conductivity (b).

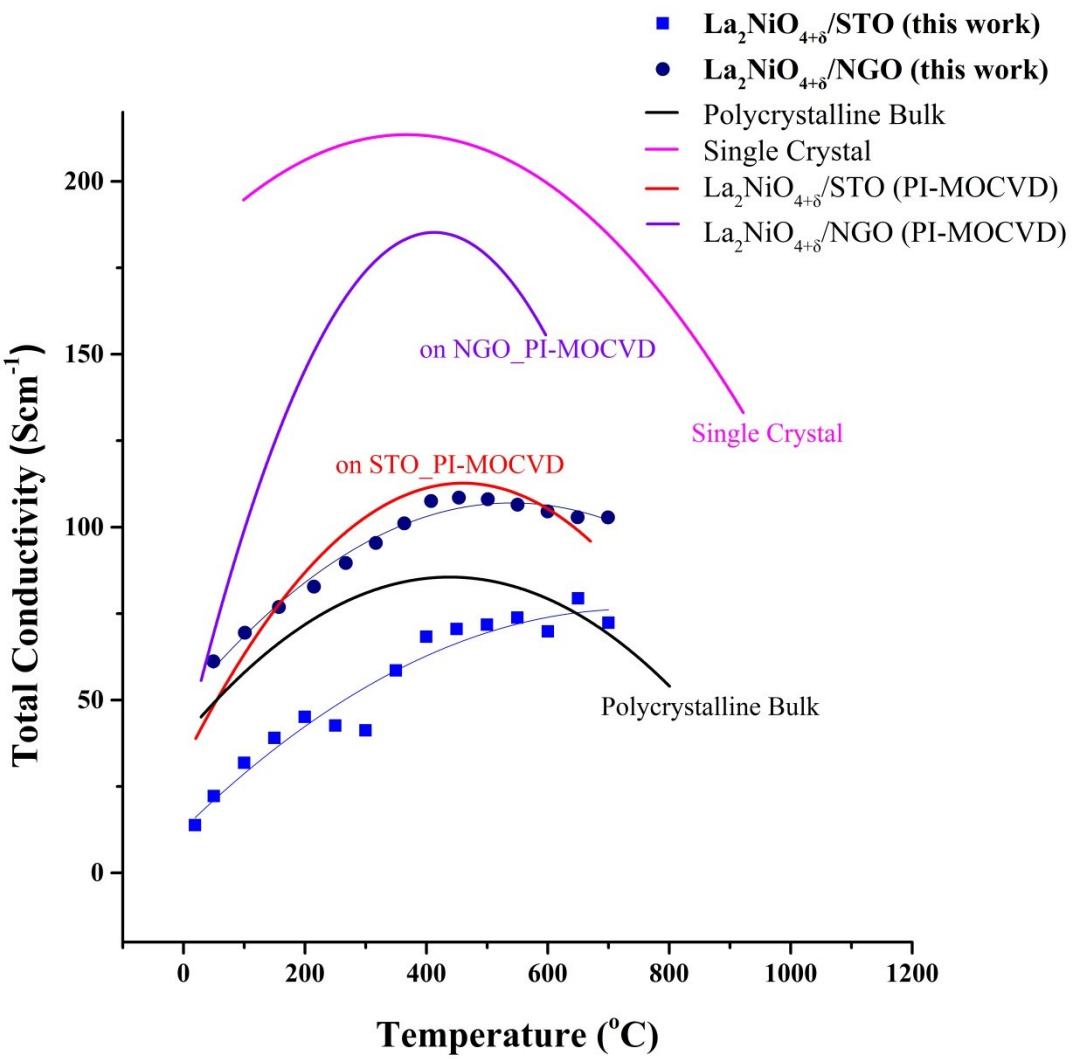


Figure 5.17 Total electrical conductivity of the c-axis oriented $La_2NiO_{4+\delta}$ epitaxial films deposited on STO and NGO substrates as a function of temperature in comparison with literature data from polycrystalline bulk [33], single crystal [111], and thin-films deposited by MOCVD [39].

5.4 Summary

In this chapter, the growth conditions for the $La_2NiO_{4+\delta}$ (n = 1) phase were systematically investigated and the optimal growth conditions have been obtained (**Table 5.1**). These obtained parameters will be undertaken to determine appropriate deposition conditions for higher order RP film growth (n = 2 and 3) in the next chapter. According to the systematic investigations on the growth conditions of La_2NiO_{4+d} films using PLD, in addition to the

influence of thickness (observed in previous literature [84]), the structural reorientation phenomenon of the $La_2NiO_{4+\delta}$ (n = 1) films deposited on STO (001) was found to be strongly related to the influence of oxygen partial pressure, deposition temperature and laser fluence. These findings may reveal the possibility of manipulating film orientations (c- or a-axis oriented) of $La_2NiO_{4+\delta}$ (n = 1) via varying these parameters. A possible growth model for the c-axis oriented $La_2NiO_{4+\delta}$ films deposited on STO (001) substrates was also demonstrated.

A series of structural and morphological characterisation measurements have confirmed the growth of high quality c-axis oriented La_2NiO_4 (n = 1) epitaxial films on STO (100) and NGO (110) substrates. Also, reasonable conductivity values of these films were obtained in agreement with literature data. The films on NGO exhibit higher planar conductivity values than that on STO. Based on these results, it was decided to use NGO (110) as substrates for the deposition of all higher-order $La_{n+1}Ni_nO_{3n+1}$ phases (n = 2 and 3).

Chapter 6 Growth and Characterisation of $La_{n+1}Ni_nO_{3n+1}$ (n = 2 and 3)

As demonstrated in the last chapter, c-axis oriented La_2NiO_4 (n = 1) epitaxial films have been successfully deposited on STO and NGO substrates and appropriate growth conditions have been determined. To date, there is a lack of research on the deposition of the higher order Ruddelsden-Popper (RP)-phase lanthanum nickelate films where n = 2 and 3, by PLD. This chapter focuses on the deposition and characterisation of $La_3Ni_2O_{7-\delta}$ and $La_4Ni_3O_{10-\delta}$ epitaxial thin films. Based on prior experience of depositing the $La_2NiO_{4+\delta}$ phase, a series of depositions have been systematically conducted to finely adjust the growth conditions for both $La_3Ni_2O_{7-\delta}$ and $La_4Ni_3O_{10-\delta}$ phases. It is worth noting again that the obtained $La_3Ni_2O_{7-\delta}$ and $La_4Ni_3O_{10-\delta}$ targets only have ~50% of the theoretical density, which may lead to the target degradation and particulate formation during the ablation process, as mentioned in chapter 4. Therefore, slightly varying these deposition conditions may significantly influence the quality, crystallinity, composition, microstructures, and consequently the functional properties, of the films. These investigations of optimisation for both phases will be firstly discussed in section 6.1. In addition, structural, morphological and cross-sectional image characterisation was conducted to evaluate the quality of the obtained $La_3Ni_2O_{7-\delta}$ and $La_4Ni_3O_{10-\delta}$ epitaxial films (section 6.2). Moreover, the related influences on the variation of microstructure of the obtained films were investigated in section 6.3, including film thickness and post-annealing effects. Finally, the thermal stability of both $La_3Ni_2O_{7-\delta}$ and $La_4Ni_3O_{10-\delta}$ films will be discussed in section 6.4.

6.1 Optimisation of $La_3Ni_2O_{7-\delta}$ and $La_4Ni_3O_{10-\delta}$ Phase Film Growth

To deposit $La_3Ni_2O_{7-\delta}$ and $La_4Ni_3O_{10-\delta}$ epitaxial films, a series of experiments were systematically investigated through fine adjustments of the optimal deposition conditions obtained from the studies of the $La_2NiO_{4+\delta}$ phase as discussed in the previous chapter. These adjustments include the effects of deposition temperature, laser power density (fluence), and laser repetition rate (frequency), as will be investigated in the following sections.

Deposition Temperatures

The influence of deposition temperatures on $La_3Ni_2O_{7-\delta}$ and $La_4Ni_3O_{10-\delta}$ film growth has been firstly investigated. The $La_3Ni_2O_{7-\delta}$ films were deposited on (110) $NdGaO_3$ substrates at various deposition temperatures from 700 to 780°C with oxygen partial pressure of 250 mTorr, 3000 laser pulses and power density of 0.5 J/cm^2. The θ/2θ XRD scans of the obtained films, as can be seen in **Figure 6.1 (a)** and **(b)**, show clear improvements in the intensity of the (00L) reflections of $La_3Ni_2O_{7-\delta}$ as the deposition temperature increased from 700 to 750°C, which indicates a significant improvement of the crystallinity of the films. As the deposition temperature was increased to 780°C, the (00L) peaks became slightly broader, as can be seen especially on the (008), (00$\underline{14}$) and (00$\underline{22}$) reflections. Also some extra undefined peaks can be seen at ~38°, ~41°, ~66° and ~117° two theta in the pattern (**Figure 6.1 (c)**), which may imply decomposition, intergrowth, disorder or misalignment of the film. These results suggest that the 750°C may be an appropriate deposition temperature for the growth of $La_3Ni_2O_{7-\delta}$ films, although the (00$\underline{14}$) peak in the pattern of 750°C (**Figure 6.1 (b)**) presents slightly broad, which indicates that the possibility of the (00$\underline{14}$) peak overlapping with the peaks (i.e. (00$\underline{18}$) and (00$\underline{20}$)) from $La_4Ni_3O_{10-\delta}$ phase (as can be seen in **Figure 6.3** later).

As seen in the AFM images (**Figure 6.2**), the film deposited at 750°C was flat with relatively low RMS roughness; on the contrary, the sample deposited at 700°C exhibits a rather rough surface with a number of small crystallites on the surface. The result is probably associated with the lower thermal energy provided, leading to the low mobility of adatoms (adsorbed atoms) and consequently, island growth. For the sample deposited at 780°C, it also displays a high-RMS-roughness surface, which corresponds to the formation of the extra undefined phases shown in the XRD pattern (**Figure 6.1 (c)**).

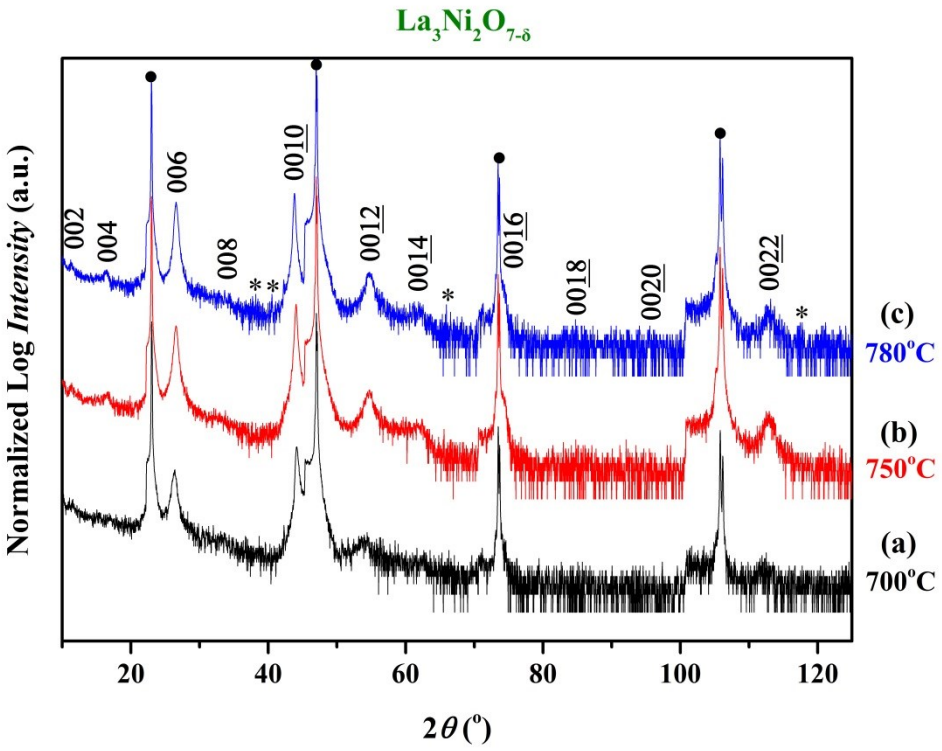


Figure 6.1 θ/2θ XRD patterns of $La_3Ni_2O_{7-\delta}$ films grown on NGO (110) single crystal substrates at 250 mTorr O_2, 3000 laser pulses and power density of 0.5 J/cm^2 with various deposition temperatures (a) - (c). The NGO substrate peaks are indicated by solid circles (•), the c-axis oriented $La_3Ni_2O_{7+\delta}$ film peaks are indexed by (00L) and some extra undefined peaks are indexed by stars (*).

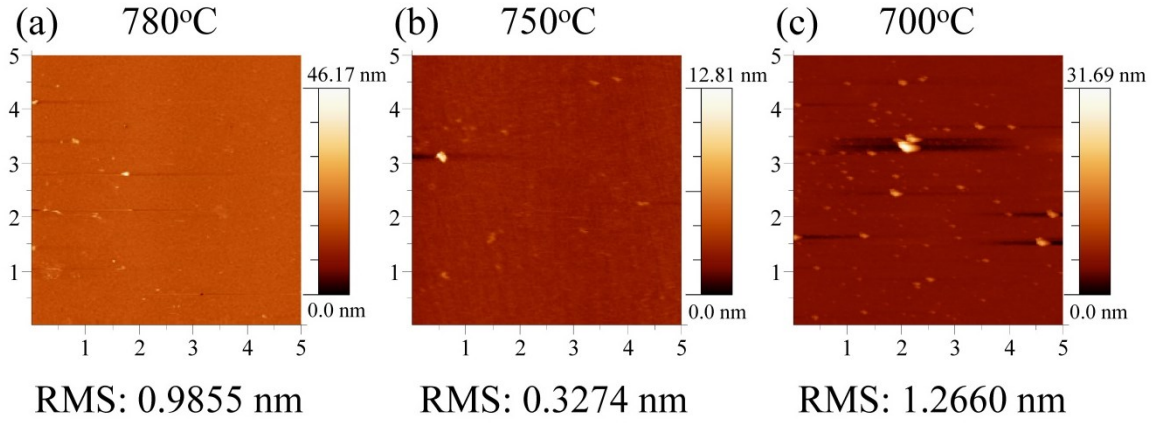


Figure 6.2 AFM images of $La_3Ni_2O_{7-\delta}$ thin-film deposited on NGO as a function of deposition temperature. (a) - (c) show the images of films deposited at nominal temperatures of 780 – 700°C with an image sizes: 5 μm × 5 μm. Z depth scales are indicated from dark brown to white. The avg. RMS values are presented on the bottom of the images.

On the other hand, the $La_4Ni_3O_{10-\delta}$ films were deposited on (110) $NdGaO_3$ at lower deposition temperatures from 650 to 750°C with the same oxygen partial pressure, laser pulses and power density as the previous adoption of the $La_3Ni_2O_{7-\delta}$ films. In **Figure 6.3 (a)** and **(b)**, it is apparent that the obtained film shows low crystallinity at 650°C. The crystallinity of the film as shown evidently in the (00L) peaks was remarkably improved as the deposition temperature reached 700°C, becoming sharper and narrower although there is a sign showing the formation of $La_3Ni_2O_{7-\delta}$ phase at ~35° and ~64°. In an attempt to improve the intensity and crystallinity of the peaks, a higher temperature of 750°C was used for deposition; however, the peaks turn out to be slightly less intense and broadened, as observed in **Figure 6.3 (c)**. This may imply the film crystallinity was no longer able to be improved by a higher deposition temperature (>750°C). Based on these results for the $La_4Ni_3O_{10-\delta}$ films deposited at different deposition temperatures, it seems that the temperature of 700°C could be used for the deposition of $La_4Ni_3O_{10-\delta}$ films although the $La_3Ni_2O_{7-\delta}$ phase was also present at this temperature. The presence of $La_3Ni_2O_{7-\delta}$ phase may be eliminated through adjusting other growth condition (e.g. laser flunence), as will

be described in the next sub-section.

The AFM images of $La_4Ni_3O_{10-\delta}$ deposited at various temperatures (650 to 750°C) are exhibited in **Figure 6.4**. All samples present rather low RMS values of the surface roughness in the range of approximately ~0.2-0.3 nm. However, close inspection of the AFM images obtained from the sample deposited at 650°C shows a feature of tiny voids (dark brown spots) inhomogeneously distributed on the surface, leading to the uneven height of islands. This feature is likely to be associated with the low crystallinity as evidenced by the XRD pattern, as observed in **Figure 6.3 (c)**.

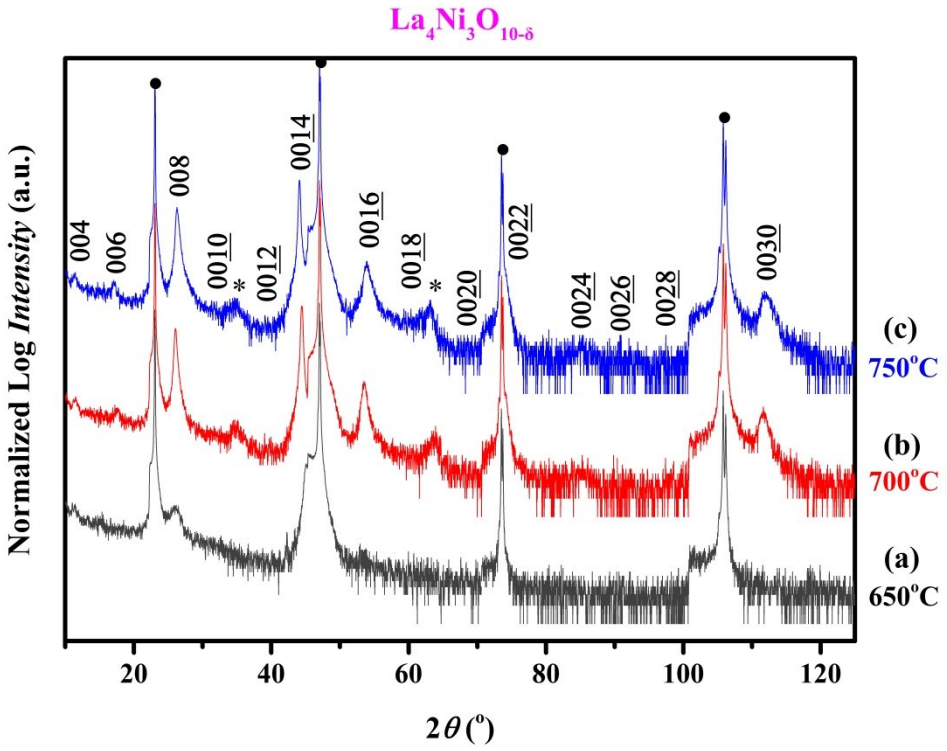


Figure 6.3 θ/2θ XRD patterns of $La_4Ni_3O_{10-\delta}$ films grown on NGO (110) single crystal substrate at 250 mTorr O_2, 3000 laser pulses and power density of 0.5 J/cm^2 with various deposition temperatures (a) - (c). The NGO substrate peaks are indicated by solid circles (•), the c-axis oriented $La_4Ni_3O_{10+\delta}$ film peaks are indexed by (00L). The stars (*) represents the $La_3Ni_2O_{7-\delta}$ phase.

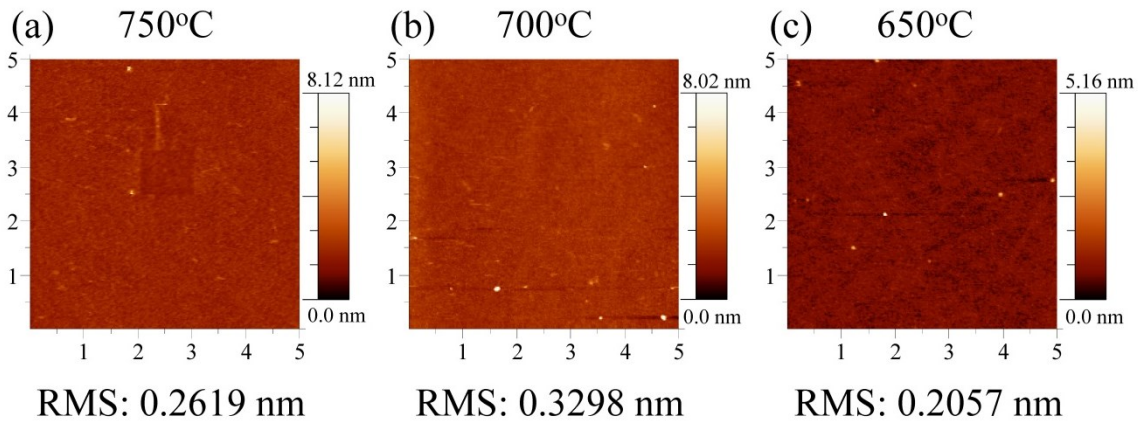


Figure 6.4 AFM images of $La_4Ni_3O_{10-\delta}$ thin-film deposited on NGO as a function of deposition temperature. (a) - (c) show the images of the films deposited at 750, 700 and 650°C with an image sizes: 5 µm × 5 µm. Z depth scales are indicated from dark brown to white. The avg. RMS values are presented on the bottom of the images.

In addition to the structural and morphological analyses discussed above, composition analysis of the series of $La_3Ni_2O_{7-\delta}$ and $La_4Ni_3O_{10-\delta}$ samples was determined by EDX. **Table 6.1** presents the cation (La/Ni) ratios of the obtained films deposited at various temperatures. It is worth noting again that the penetration depth of X-ray probe for EDX is approximately 1 µm. Due to this penetration depth, chemical information from the substrate can also be contained in the obtained EDX spectra, resulting in the substrate peaks overlapping with the film peaks. This may consequently introduce certain errors in the interpretation of these data. In general, EDX spectra can semi-quantitatively provide the compositional information of the thin-films.

In **Table 6.1 (a)**, the La/Ni results with respect to the $La_3Ni_2O_{7-\delta}$ films deposited at 780 and 700°C show a La/Ni ratio close to 1.60, which is higher than the expected value (1.5) presenting a La-rich behaviour, while the film deposited at 750°C exhibits a La/Ni ratio of 1.36 showing a significant La-deficient behaviour, which corresponds to the XRD results showing a broad (0014) peak (see **Figure 6.1 (b)**). Hence, this further indicates the presence of $La_4Ni_3O_{10-\delta}$ in the film deposited at 750°C. On the other hand, as seen in **Table 6.1 (b)**, the findings for the $La_4Ni_3O_{10-\delta}$ films deposited at 750 and 650°C show

considerable deviations from the desired ratio of 1.33; however, the sample deposited at 700°C present a very promising La/Ni ratio, which further indicates that 700°C could be an appropriate deposition temperature for the fabrication of $La_4Ni_3O_{10-\delta}$ films.

(a)

$La_3Ni_2O_{7-\delta}$	
Temperature (°C)	**La/Ni**
780	1.5868±0.22
750	1.3559±0.17
700	1.5806±0.29

(b)

$La_4Ni_3O_{10-\delta}$	
Temperature (°C)	**La/Ni**
750	1.4902±0.20
700	1.3285±0.27
650	1.6924±0.41

Table 6.1 Cation ratios of the deposited $La_3Ni_2O_{7-\delta}$ (a) and $La_4Ni_3O_{10-\delta}$ (b) films with various deposition temperatures were determined by EDX. The theoretical La/Ni ratios for $La_3Ni_2O_{7-\delta}$ and $La_4Ni_3O_{10-\delta}$ are expected to be 1.50 and 1.33, respectively.

According to the XRD and morphological results discussed previously, the $La_3Ni_2O_{7-\delta}$ and $La_4Ni_3O_{10-\delta}$ films deposited at 750 and 700°C respectively exhibit acceptable crystallinity with low surface roughness values. Thus, the two temperatures of 750 and 700°C can be considered as the deposition temperatures for both epitaxial films. However, based on the findings of the composition analyses, further adjustments are required, which will be investigated through the effects of laser power density.

Laser Power Density (Fluence)

Laser fluency is typically considered to be a primary factor in controlling the cation stoichiometry in a variety of oxide thin-films. [181-185] Also, as mentioned in Chapter 4, the behaviour of target degradation and particulate formation could occur due to a very low density (~50%) and high-roughness of the obtained $La_3Ni_2O_{7-\delta}$ and $La_4Ni_3O_{10-\delta}$

targets, and thereby lead to non-stoichiometric films during the PLA and PLD processes. An appropriate utilisation of laser fluence, therefore, is critically required for the fabrication of these complex oxide films with the stoichiometric cation (La/Ni) ratio close to the desired ratio.

(a)

$La_3Ni_2O_{7-\delta}$			
Laser Fluence (J/cm^2)	**La/Ni**	**Compositional Deviation (%)**	**Composition**
0.7	1.76±0.28	17.18	La-excess
0.6	1.54±0.17	2.62	Slight La-excess
0.5	1.36±0.17	-9.61	La-deficient

(b)

$La_4Ni_3O_{10-\delta}$			
Laser Fluence (J/cm^2)	**La/Ni**	**Compositional Deviation (%)**	**Composition**
0.7	1.46±0.21	9.51	La-excess
0.6	1.31±0.20	-1.59	Slight La-deficient
0.5	1.33±0.27	-0.36	Stoichiometric

Table 6.2 Cation ratios and compositional deviation (%) of obtained (a) $La_3Ni_2O_{7-\delta}$ and (b) $La_4Ni_3O_{10-\delta}$ films with various laser fluences from 0.5 to 0.7 J/cm^2 were determined by EDX. The theoretical La/Ni ratios for $La_3Ni_2O_{7-\delta}$ and $La_4Ni_3O_{10-\delta}$ are expected to be 1.50 and 1.33, respectively.

To optimise the stoichiometry of the $La_3Ni_2O_{7-\delta}$ and $La_4Ni_3O_{10-\delta}$ epitaxial thin films, the laser fluence was adjusted in steps from 0.5 to 0.7 J/cm^2. **Table 6.2** exhibits the La/Ni ratio in the fabricated $La_3Ni_2O_{7-\delta}$ and $La_4Ni_3O_{10-\delta}$ epitaxial thin films as a function of the laser fluence. Their compositional deviations were estimated from the expected La/Ni ratio, (experimental ratio – expected ratio)/expected ratio. In the case of the $La_3Ni_2O_{7-\delta}$

films, the La/Ni ratio at high laser fluence of 0.7 J/cm^2 is found to present a large compositional deviation from the stoichiometric ratio, indicating the presence of La-excess in the films, as can be seen in **Table 6.2 (a)**. As the fluence decreased to 0.6 J/cm^2, the deviation of the ratio becomes smaller and the La/Ni ratio closer to the expected stoichiometry (1.50). If the fluence continuously decreases to 0.5 J/cm^2, the deviation becomes larger and negative, leading to La-deficient films. This fluence dependent change in the ratio indicates the high sensitivity of the cation ratio to the utilised laser fluence, which may correspond to the difficulties experienced in attempting to synthesise the $La_3Ni_2O_{7-\delta}$ phase in a pure and stoichiometric state, as reported for bulk materials. [51, 73] For the cation ratio in the $La_4Ni_3O_{10-\delta}$ films, the findings also show a decreasing composition deviation with decreasing laser fluence (see **Table 6.2 (b)**) and very small deviation values were obtained as the fluences were adjusted at 0.5 and 0.6 J/cm^2, resulting in almost stoichiometric La/Ni ratios as being close to 1.33.

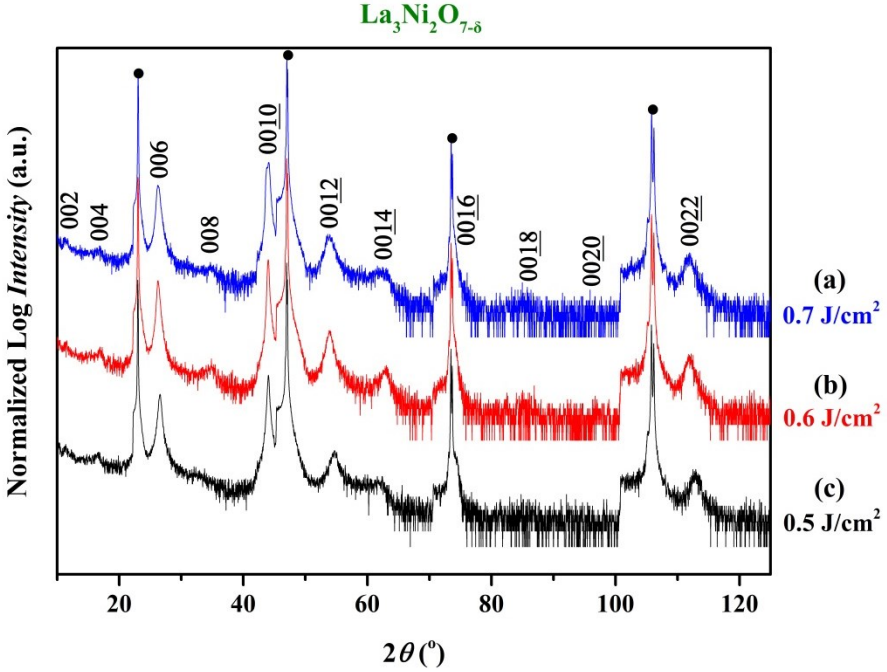


Figure 6.5 θ/2θ XRD patterns of $La_3Ni_2O_{7-\delta}$ films grown on NGO (110) single crystal substrate in 250 mTorr O_2, 3000 laser pulses and deposition temperature of 750°C with various laser fluence (a) - (c). The NGO substrate peaks are indicated by solid circles (•), the c-axis oriented $La_3Ni_2O_{7-\delta}$ film peaks are indexed by (00L).

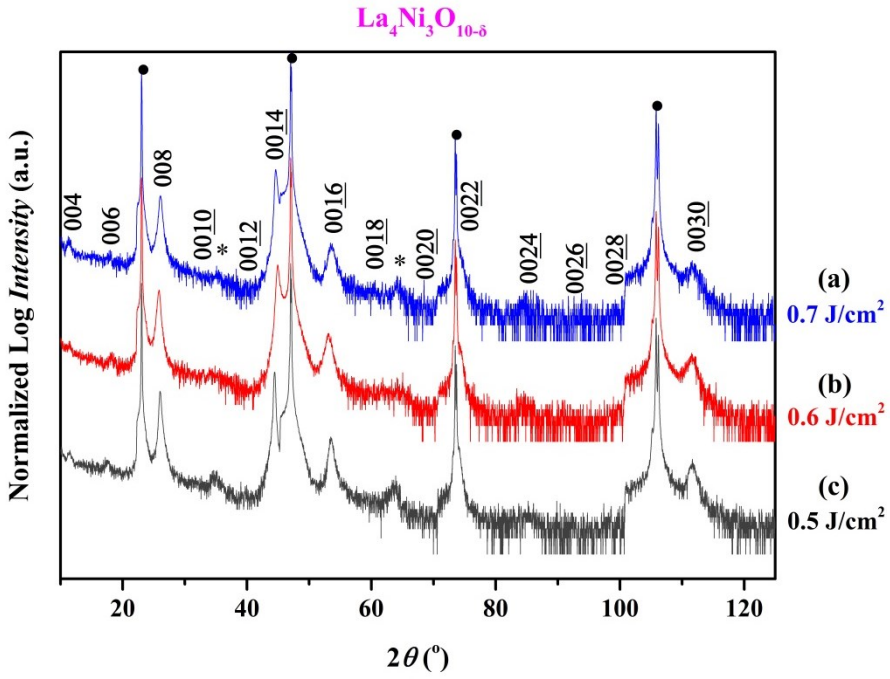


Figure 6.6 θ/2θ XRD patterns of $La_4Ni_3O_{10-\delta}$ films grown on NGO (110) single crystal substrate in 250 mTorr O_2, 3000 laser pulses and deposition temperature of 700°C with various laser fluence (a) - (c). The NGO substrate peaks are indicated by solid circles (•), the c-axis oriented $La_4Ni_3O_{10-\delta}$ film peaks are indexed by (00L). The stars (*) represents the $La_3Ni_2O_{7-\delta}$ phase.

The θ/2θ XRD scans of the fabricated $La_3Ni_2O_{7-\delta}$ and $La_4Ni_3O_{10-\delta}$ films are presented as a function of laser fluence in **Figure 6.5** and **Figure 6.6**, respectively. For $La_3Ni_2O_{7-\delta}$ films, it is apparent that those deposited with a laser fluence of 0.6 J/cm^2 exhibits clearer (00L) reflections with better crystallinity than other two deposited with the laser fluence of 0.7 and 0.5 J/cm^2, which corresponds to the results from the composition analysis (**Table 6.2 (a)**). As seen in **Figure 6.5 (a)**, a slight splitting of (00$\underline{10}$) reflection was observed in the films deposited with a higher laser fluence, which suggests the phenomena of disorder or misalignment within the films. Hence, a laser fluence of 0.6 J/cm^2 was found for the deposition of $La_3Ni_2O_{7-\delta}$ films. In the case of the $La_4Ni_3O_{10-\delta}$ films, the XRD results of the films deposited with the laser fluence of 0.6 J/cm^2 appears a

clearer diffraction pattern than the other two with the laser fluence of 0.5 and 0.7 J/cm^2, showing no significant $La_3Ni_2O_{7-\delta}$ reflections with appropriate crystallinity. Compared to the previous result of deposition temperature (see **Figure 6.3 (b)**), the quality of the film can be improved by increasing laser fluence. Thus, a laser fluence of 0.6 J/cm^2 was adopted for the growth of $La_4Ni_3O_{10-\delta}$ films.

Laser Repetition Rate (Frequency)

Laser repetition rate (frequency) is generally considered to be one of key factors affecting film microstructure. The variation in the laser frequency has significant influence on the kinetics of film growth, and hence the structure and crystallinity of the films. [136] Thus, the influence of laser frequency was investigated in this section in order to seek an appropriate repetition rate for the deposition of the complex oxide films. This series of experiments was conducted only with the deposition of $La_4Ni_3O_{10-\delta}$ films.

Figure 6.7 shows the XRD patterns of the $La_4Ni_3O_{10-\delta}$ films deposited as a function of laser frequency. The intensity of diffraction peaks in the patterns gradually increased with increase of the laser frequency from 3 to 8 Hz while the films deposited with 1 Hz present a lower intensity due to the reduced thickness of the film. The preparation of the thinner films may be attributed to the kinetic effect of the molecules during deposition and therefore a decrease in plasma density; that is, lower amount of the ablated species that reaches the substrate surface. This kinetic behaviour also causes an inhomogeneous surface morphology of the films, as can be observed in **Figure 6.8**. The FWHM values of the (00$\underline{14}$) peaks via rocking curve measurements indicate the quality of the films. The narrower FWHM values generally reveal the better crystallinity of the films, which can be seen in the inset of the **Figure 6.7**. It shows a range of FWHM which increases from ~0.15° to ~0.18° as the laser frequency decreases from 8 to 1 Hz. This behaviour is unusual. Commonly the FWHM values would increase with increasing laser frequency.

The first explanation for this behaviour is likely due to the low laser frequencies adopted for the deposition of the complex oxide films. Secondly, with a decrease in the laser frequency, the interval time between the subsequent ablated species increases; that is, the adatoms on the surface are able to rearrange themselves, and thereby the nuclei have more time to grow as islands. Thus, the island ripening time increases, leading apparently to a larger average size of the formed islands. Conversely, higher laser frequencies can result in the reduced average size of islands and elevated island density. Such high island density is able to facilitate the substrate surface covering with a continuous layer at the initial stage of film growth, and consequently leads to the formation of low-roughness and continuous films. [135, 136, 205]

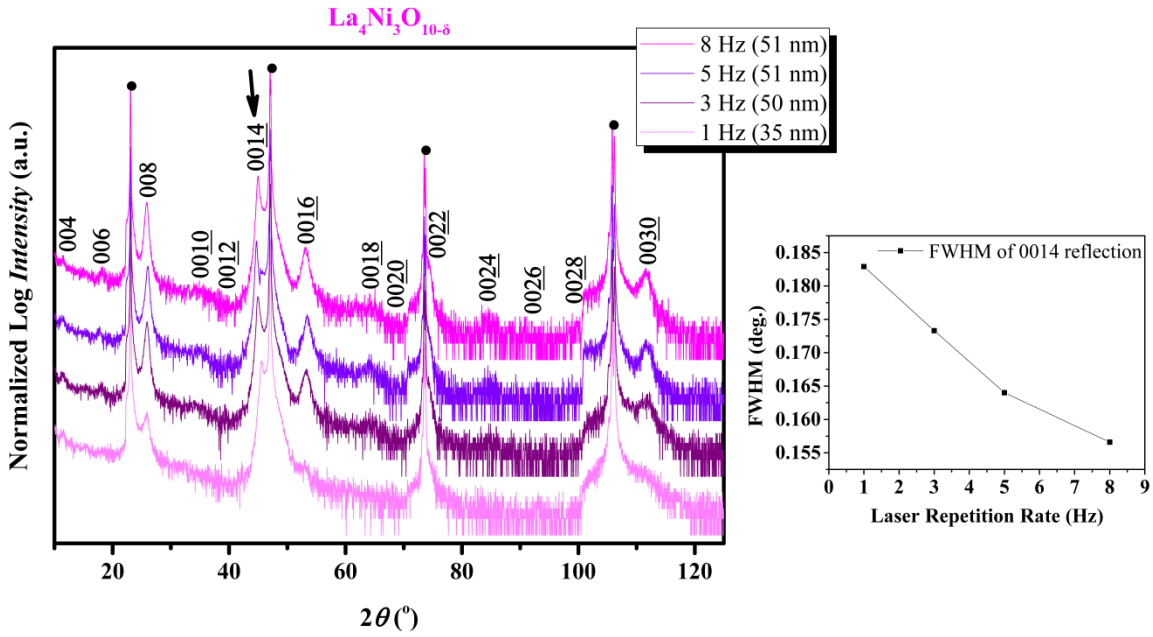


Figure 6.7 θ/2θ XRD patterns of $La_4Ni_3O_{10-\delta}$ films grown on NGO (110) single crystal substrate in 250 mTorr O_2, 3000 laser pulses, deposition temperatures of 700°C, and laser fluence of 0.6 J/cm^2 with various laser repetition rate of 1, 3, 5 and 8 Hz. The NGO substrate peaks are indicated by solid circles (•), the c-axis oriented $La_4Ni_3O_{10-\delta}$ film peaks are indexed by (00L). Inset: the FWHM values as a function of laser repetition rate for the 00$\underline{14}$ reflection.

Surface morphology and roughness determined through 1×1μm AFM images further present the quality of $La_4Ni_3O_{10-\delta}$ epitaxial films. All of the samples show similar surface morphology with ~0.4 nm RMS values of roughness, apart from the 5Hz image, as can be seen in **Figure 6.9**. It is apparent that the AFM image of the material deposited at 5 Hz (**Figure 6.9 (c)**) shows repeating blurred patterns, which is usually caused by a contaminated or damaged tip during the AFM measurements. [206, 207] The similar surface feature may also reflect on the small FWHM difference among the (00$\underline{14}$) peaks of all samples (**Figure 6.7**).

According to the results of the XRD analyses and FWHM values of (00$\underline{14}$) reflections, it is suggested that the laser frequency of 8 Hz was appropriate for the growth of the complex films although a similar surface morphological feature was observed in the AFM images of these films.

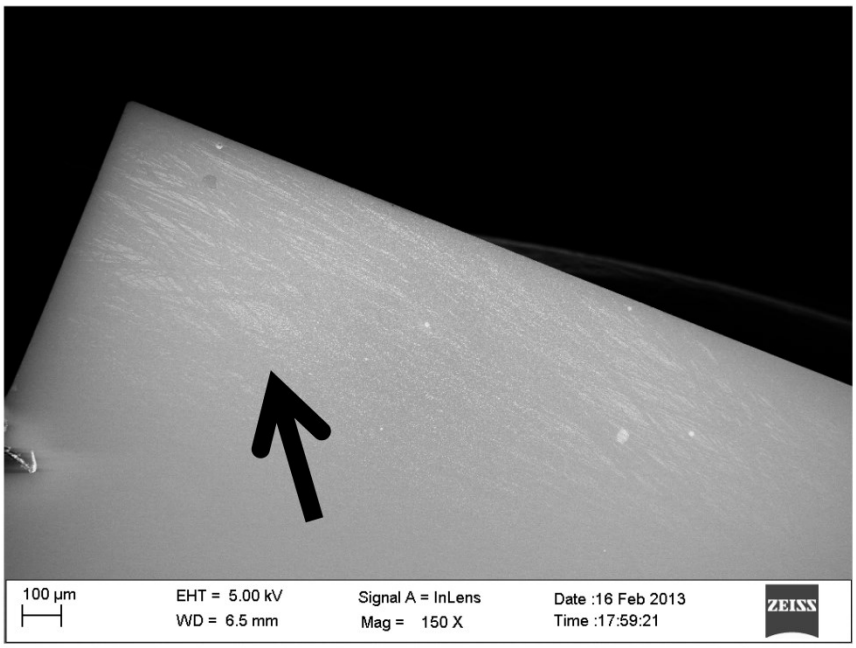


Figure 6.8 A SEM image shows inhomogeneous surface morphology (indexed by black arrow) of $La_4Ni_3O_{10-\delta}$ deposited with the laser frequency of 1 Hz. Scale marker: 100 μm.

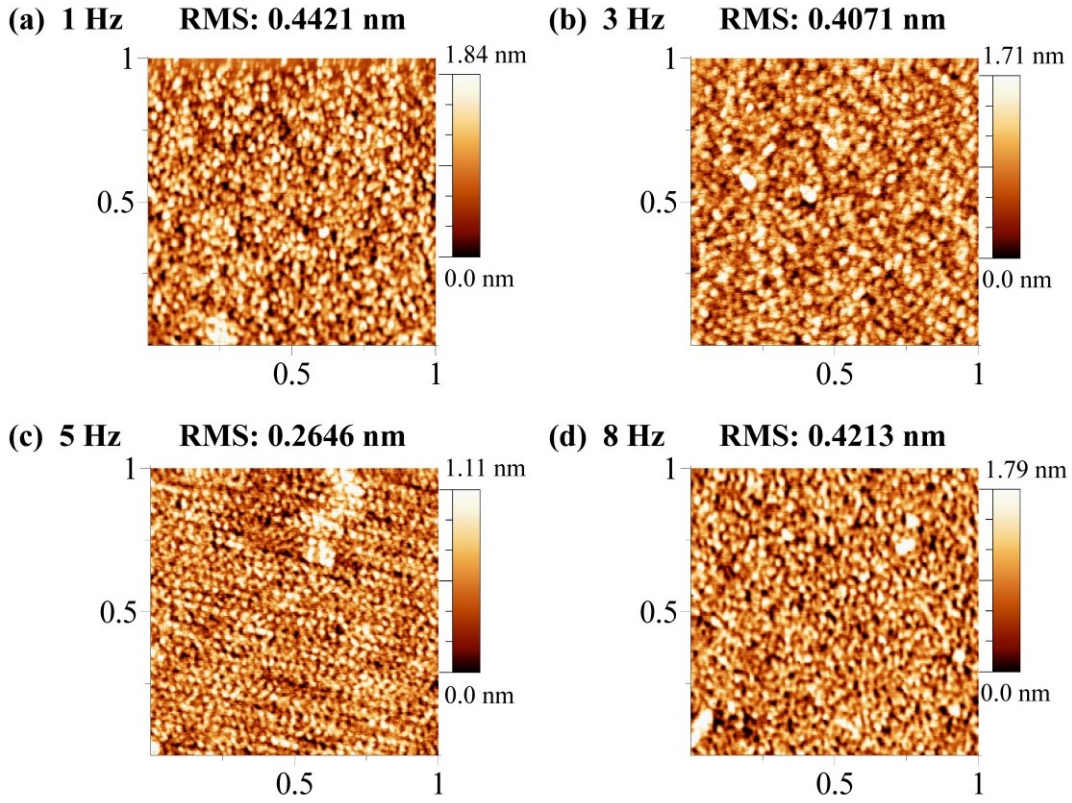


Figure 6.9 AFM images of $La_4Ni_3O_{10-\delta}$ thin-film deposited on NGO as a function of laser repetition rate of 1 Hz (a), 3 Hz (b), 5 Hz (c) and 8 Hz (d) with the image size: 1 μm × 1 μm. Z depth scales are indicated from dark brown to white. The avg, RMS values are presented on the top of the images.

After a series of systematic studies of film deposition, the growth conditions have been obtained. It is worth reiterating that the quality of these complex oxide films is strongly sensitive to the growth conditions utilised and the surface quality of the substrates obtained from the commercial supplier (as mentioned in Ch.4). In addition to ensuring the surface roughness of the adopted substrates, these precise refinements are required through the investigation of deposition temperature, laser power density (fluence), and laser repetition rate (frequency) in the section. Hence, these optimal growth conditions to synthesise high quality c-axis oriented layered RP-type epitaxial films of $La_3Ni_2O_{7-\delta}$ and $La_4Ni_3O_{10-\delta}$ films can be defined as shown in **Table 6.3**.

Table 6.3 Optimal Growth Conditions for c-axis oriented $La_3Ni_2O_{7-\delta}$ and $La_4Ni_3O_{10-\delta}$ epitaxial films

Growth conditions of $La_3Ni_2O_{7-\delta}$	
Laser type	KrF excimer laser (λ=248 nm)
Growth direction	c-axis
Deposition temperature	750°C
Oxygen partial pressure	250 mTorr
Laser fluence	~0.6 J/cm^2
Laser pulse frequency	8 Hz
Target-substrate distance	50 mm
Cooling rate	10 °C/min
Oxygen Pressure in Cooling	600 Torr

Growth conditions of $La_4Ni_3O_{10-\delta}$	
Laser type	KrF excimer laser (λ=248 nm)
Growth direction	c-axis
Deposition temperature	700°C
Oxygen partial pressure	250 mTorr
Laser fluence	~0.5-0.6 J/cm^2
Laser pulse frequency	8 Hz
Target-substrate distance	50 mm
Cooling rate	10 °C/min
Oxygen Pressure in Cooling	600 Torr

6.2 Charaterisation of $La_3Ni_2O_{7-\delta}$ and $La_4Ni_3O_{10-\delta}$ Epitaxial Films on NGO

As discussed in section 6.1, suitable conditions have been determined for growth of c-axis oriented $La_3Ni_2O_{7-\delta}$ and $La_4Ni_3O_{10-\delta}$ epitaxial films deposited on NGO (110) substrates. In this section, first of all, a series of crystallographic and morphological analyses will be investigated in further detail, including X-ray diffraction (θ/2θ, rocking curves, and φ-scans), AFM, cross-section HRTEM and out-of-plane parameter characterization in order to evaluate the quality of the films.

6.2.1 Crystallographic Analysis and Film Quality

The growth of the c-axis oriented $La_3Ni_2O_{7-\delta}$ (~47 nm) and $La_4Ni_3O_{10-\delta}$ (~51 nm) epitaxial films has been achieved with the correct cation stoichiometry on NGO (110) at deposition temperatures of 750 and 700°C respectively. The θ/2θ XRD scans are shown in **Figure 6.10 (a)** and **(b)** where only (00L) type reflections of the n = 2 and 3 films are clearly present although a few weak peaks are observed in the $La_4Ni_3O_{10-\delta}$ pattern (such as (00$\underline{10}$), (00$\underline{12}$), (00$\underline{18}$) and (00$\underline{20}$)), reasonably consistent with the low relative intensity of those peaks from bulk. These scans determined by the θ/2θ scattering configuration essentially indicate that the films all have a single orientation normal to the substrate surface.

To further evaluate the quality of the films, rocking curve measurements and AFM analyses were carried out. In **Figure 6.11 (a)** and **(b)**, the results of rocking curve analysis confirmed the high quality of n = 2 and 3 epitaxial films with FWHM of ~0.18° for the (00$\underline{10}$) and ~0.15° for the (00$\underline{14}$) reflection of the n = 2 and 3 films, respectively. The findings indicate their excellent crystallinity and out-of-plane alignment. In the case of AFM analyses, the surface morphology and roughness of the films, determined through

1×1µm AFM images, further confirmed the excellent surface quality of $La_3Ni_2O_{7-\delta}$ and $La_4Ni_3O_{10-\delta}$ epitaxial films with approximately 0.2-0.3 nm RMS values of roughness for both films as can be seen in **Figure 6.12 (a)** and **(b)**.

As mentioned previously, obtaining a dense and continuous film is one of the main goals for the project. To confirm the density of the obtained film, as an example, a low-magnification HAADF-STEM image of the c-axis oriented $La_4Ni_3O_{10-\delta}$ film deposited on NGO (110) substrate is shown in **Figure 6.13**. A dense and continuous layer can be observed throughout the entire film thickness, which indicates a high quality of the $La_4Ni_3O_{10-\delta}$ film.

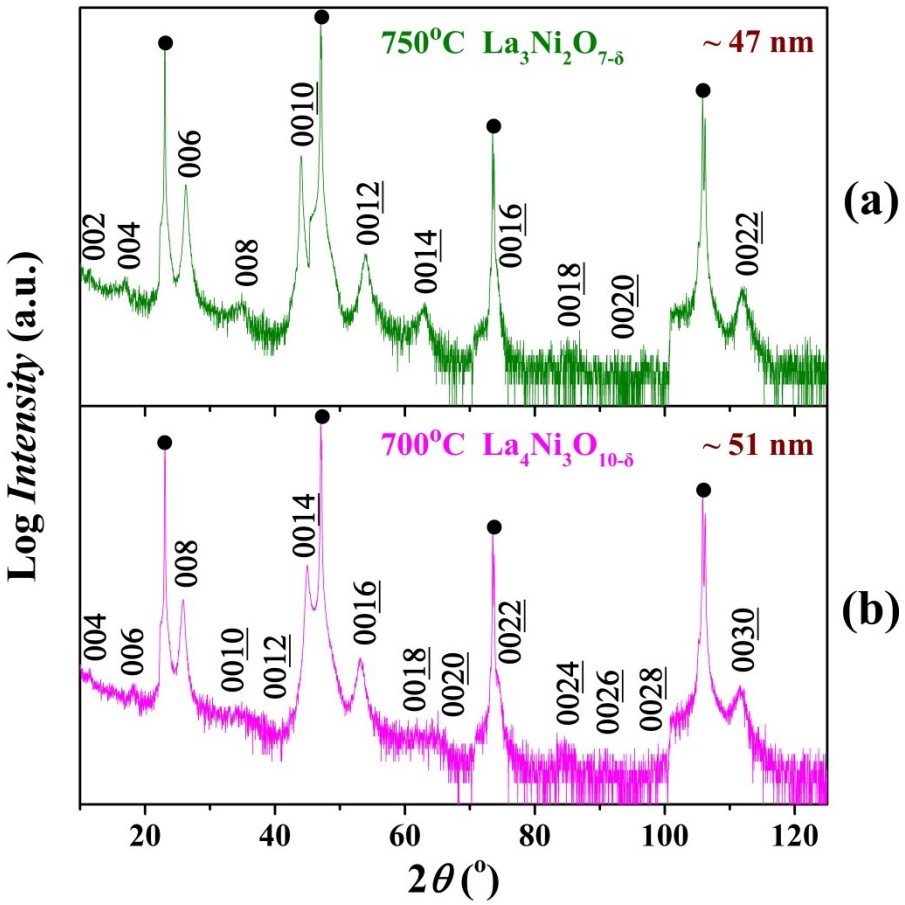


Figure 6.10 θ/2θ XRD patterns of c-axis oriented $La_3Ni_2O_{7-\delta}$ phase at 750°C (a) and $La_4Ni_3O_{10-\delta}$ phases at 700°C (b) grown on NGO (110). The $NdGaO_3$ substrate peaks are indicated by solid circles (•). The c-axis oriented film peaks are indexed by (00L). Film thickness determined by Dektak 150 Surface Profiler is shown as an insert in top right of each pattern.

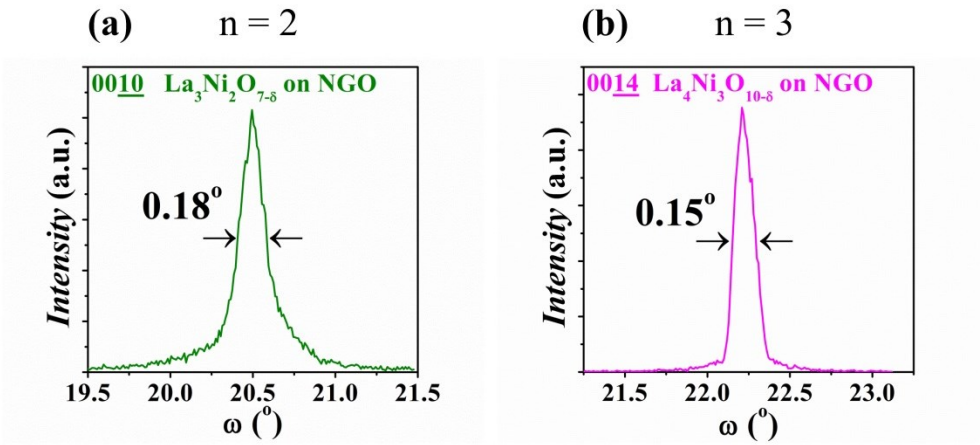


Figure 6.11 X-ray rocking curves: (a) (00<u>1</u>0) reflection of 47 nm thick $La_3Ni_2O_{7-\delta}$ film on $NdGaO_3$; (b) (00<u>1</u>4) reflection of 51 nm thick $La_4Ni_3O_{10-\delta}$ film on $NdGaO_3$.

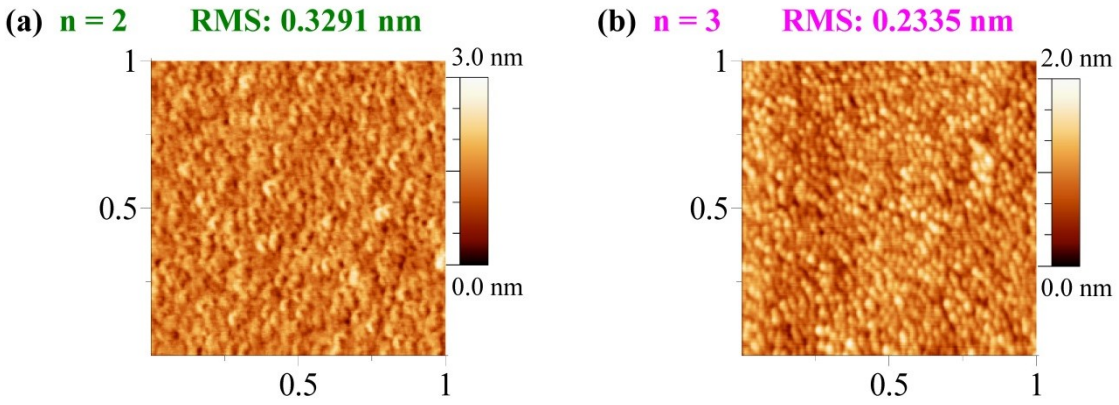


Figure 6.12 AFM images: (a) 47 nm thick $La_3Ni_2O_{7-\delta}$ film on $NdGaO_3$ and (b) 51 nm thick $La_4Ni_3O_{10-\delta}$ film on $NdGaO_3$. Image size: 1 μm × 1 μm, depth scale: both are 2 nm from dark brown to white.

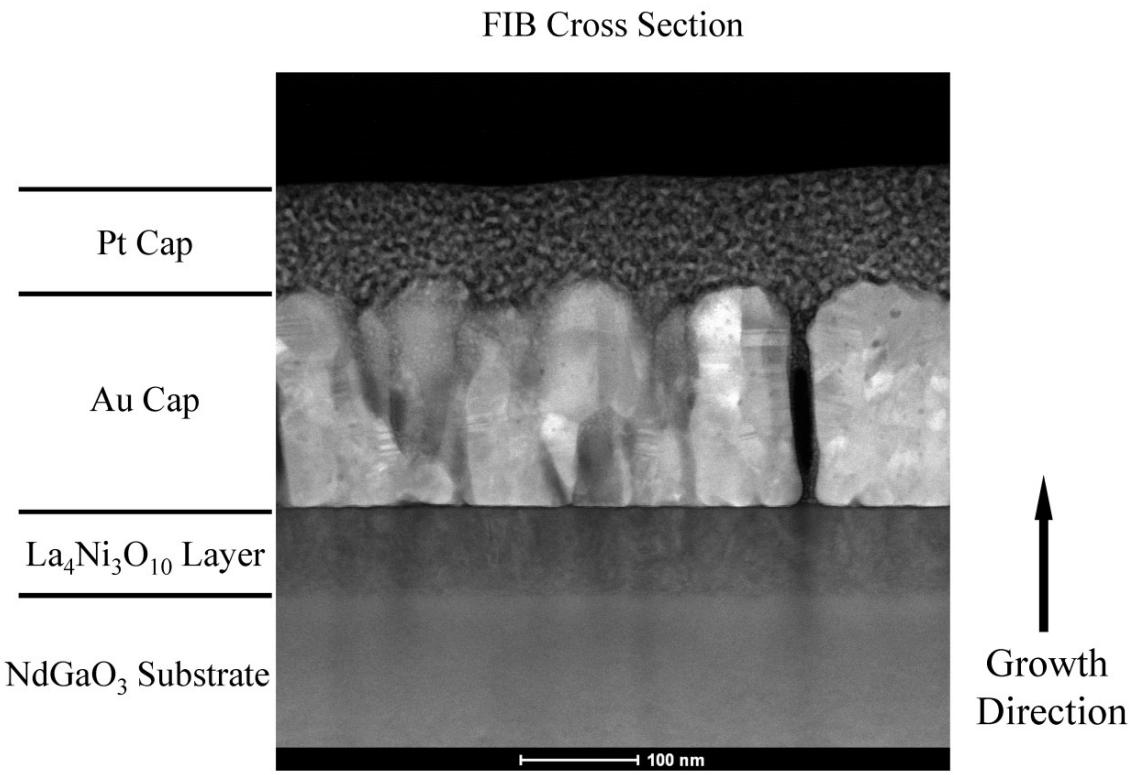


Figure 6.13 Cross-section HAADF-STEM image of c-axis oriented $La_4Ni_3O_{10-\delta}$ film grown on NGO (110) substrate. Pt and Au cap is for the protection of the film under focused ion beam (FIB) preparation process.

6.2.2 Film Orientation Characterisation

The basal-plane-orientation relationship of the $La_3Ni_2O_{7-\delta}$ and $La_4Ni_3O_{10-\delta}$ film with the NGO substrate was characterised via phi(φ) scans of in-plane orientation in order to verify the epitaxial growth. For $La_3Ni_2O_{7-\delta}$ films, the (206) reflection was selected for φ-scan characterization while the (208) reflection was adopted for $La_4Ni_3O_{10-\delta}$ films, since the two reflections yield high intensity and there are no reflections from the substrates close to the 2θ and Ψ(psi) azimuths for these reflections. **Figure 6.14 (a)** and **(b)** show four-fold symmetry of both films rotated by 45° in comparison with the four peaks from NGO substrates, corresponding to the preferential orientation illustrated previously in **Figure 4.9**. Hence, these data provide firm evidence of epitaxial alignments within these films.

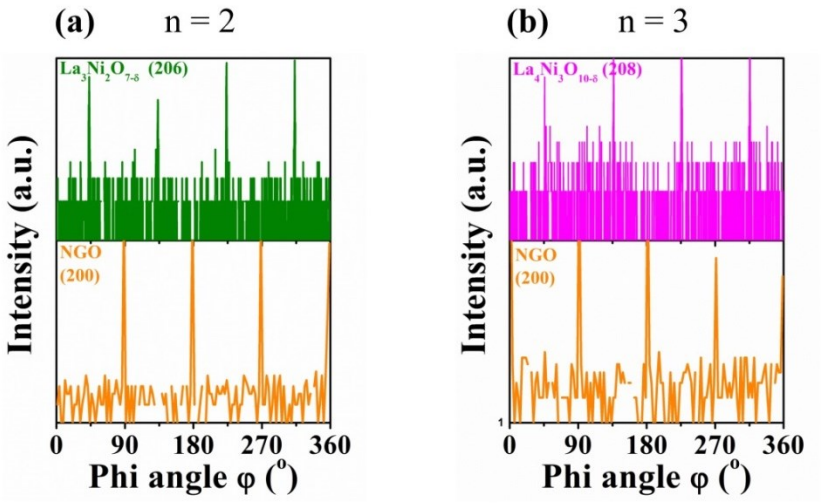


Figure 6.14 Phi(φ)-scan patterns of in-plane diffraction for the c-axis oriented $La_{n+1}Ni_nO_{3n+1}$ (n = 2 and 3) films: (a) {206} reflections registered at 2θ=42.702°, Ψ=51.74° for $La_3Ni_2O_{7-\delta}$ film on $NdGaO_3$ substrate, and (b) {208} reflections registered at 2θ=42.702°, Ψ=51.74° for $La_4Ni_3O_{10-\delta}$ film on $NdGaO_3$ substrate.

6.2.3 Out-of-Plane Parameter Characterisation

The out-of-plane (c-axis) parameters of the $La_3Ni_2O_{7-\delta}$ and $La_4Ni_3O_{10-\delta}$ films were determined from the obtained θ/2θ XRD patterns and were addressed to compare with the expected c-axis parameters in bulk. The same Lorentz method (presented previously in Ch.5) was also applied to carefully fit the 2θ peak positions and d-spacings of the four main reflections: (006), (00$\underline{10}$), (00$\underline{12}$), (00$\underline{22}$) for $La_3Ni_2O_{7-\delta}$ and (008), (00$\underline{14}$), (00$\underline{16}$), (00$\underline{30}$) for $La_4Ni_3O_{10-\delta}$. After calculation, the fitted c-axis parameters were plotted as a function of index of (00L) reflections in comparison with the expected parameters from the selected orthorhombic and tetragonal bulk references.

In **Figure 6.15**, the c-parameters were determined to be 20.29±0.20 Å and 27.80±0.56 Å for $La_3Ni_2O_{7-\delta}$ and $La_4Ni_3O_{10-\delta}$ films, respectively, in agreement with the corresponding standard references. Considering a wide range of oxygen stoichiometry of the $La_3Ni_2O_{7-\delta}$ compounds which has been reported in the range of 7.00 ~ 6.35,[51] orthorhombic and tetragonal crystal structures were selected as the reference data. As shown in **Figure 6.15 (a)**, the average c-axis parameter (20.29±0.20 Å) is located

between the expected c-axis parameters from the two crystal structures. The result firmly indicates the evidence of the growth of $La_3Ni_2O_{7-\delta}$ films. The intermediate value of c parameter, being between the bulk values, may be attributed to two competing effects: lattice strain or oxygen content. In the case of strain, the in-plane tensile strain (+0.69%) on the $La_3Ni_2O_{7-\delta}$ lattice can cause an out-of-plane compression, which might lead to a slight decrease in the c-axis parameter; however, variable oxygen stoichiometry in the films could also be associated with variation of the c-axis parameter. As mentioned earlier, determining the oxygen content is challenging in thin-film materials, and therefore the origin of the intermediate value of the c-axis parameter cannot be clearly assigned to either lattice strain or oxygen content. For the $La_4Ni_3O_{10-\delta}$ films, due to only orthorhombic crystal structures typically present in bulk, only an orthorhombic crystal structure was selected as reference. Again, comparing with the expected parameter from the bulk, a small decrease in the c-axis lattice parameter could be caused by the tensile strain (+0.34%), which yields a reasonable value of 27.80±0.56 Å as can be seen in **Figure 6.15 (b)**.

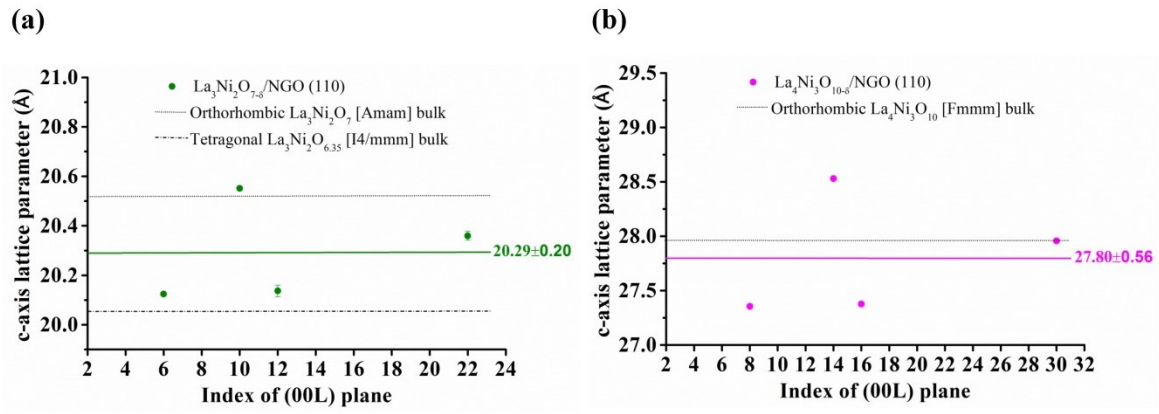


Figure 6.15 c-axis lattice parameter as function of (00L) planes for (a) $La_3Ni_2O_{7-\delta}$ and (b) $La_4Ni_3O_{10-\delta}$ films grown on NGO (110). Four clear peaks from each compound were refined by the Lorentz method. All errors are within the data points to a level of five standard deviations. The reference values as standard correspond to solid and dashed lines in the diagrams. [47, 208, 209] The measured averages of c-axis parameters are labelled by green and pink solid lines.

6.3 Influences on Microstructure

The work reported in section 6.2 confirmed the epitaxial growth of c-axis oriented $La_3Ni_2O_{7-\delta}$ and $La_4Ni_3O_{10-\delta}$ phases through θ/2θ, rocking curves, φ-scans, AFM, cross-sectional HAADF STEM imaging and out-of-plane lattice parameter characterization, showing high quality, dense and continuous $La_3Ni_2O_{7-\delta}$ and $La_4Ni_3O_{10-\delta}$ films with good crystallinity and low surface roughness. However, there potentially exists various RP- and perovskite intergrowths within the matrix of the films. **Figure 6.16** exhibits an offset-plot of θ/2θ scans of $La_2NiO_{4+\delta}$, $La_3Ni_2O_{7-\delta}$ and $La_4Ni_3O_{10-\delta}$ films deposited on NGO (110). It is clearly observed that a significantly overlapping behaviour from the main peaks of each phase can be identified in the inset; particularly for $La_3Ni_2O_{7-\delta}$ and $La_4Ni_3O_{10-\delta}$ phases. Due to such possibility, the aim of this section is to provide a more detailed investigation of the influences correlated with the microstructural variation of $La_3Ni_2O_{7-\delta}$ and $La_4Ni_3O_{10-\delta}$ films through film thickness and post-annealing effects.

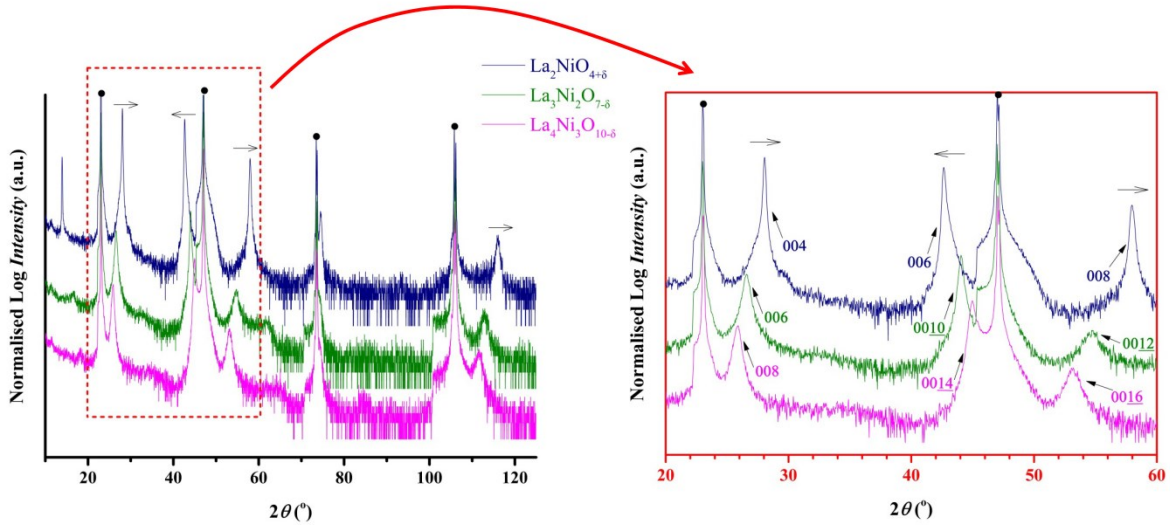


Figure 6.16 θ/2θ XRD scans of $La_2NiO_{4+\delta}$ (n = 1), $La_3Ni_2O_{7-\delta}$ (n = 2) and $La_4Ni_3O_{10-\delta}$ (n = 3) films deposited on NGO (110). The $NdGaO_3$ substrate peaks are indicated by solid circles (•). Inset: zoom of the range of 20-60°, labelled as the dashed square in the whole range pattern. The small arrows indicate the shift direction of the main peaks of each phase varies with n.

6.3.1 Effect of Film Thickness

The correlation of the structure, strain, composition and microstructure of $La_3Ni_2O_{7-\delta}$ and $La_4Ni_3O_{10-\delta}$ epitaxial films will be investigated as a function of film thickness in this section. To address these investigations, a series of c-axis oriented $La_3Ni_2O_{7-\delta}$ and $La_4Ni_3O_{10-\delta}$ epitaxial films of different thickness were prepared on NGO (110) via varying the number of laser pulses. Various film thicknesses were demonstrated as a function of the number of laser pulses in **Figure 6.17** where linear dependence of deposition rate can be apparently observed for both compounds, confirming the reliability of each deposition. The average deposition rates of $La_3Ni_2O_{7-\delta}$ and $La_4Ni_3O_{10-\delta}$ films were estimated at approximately 0.157±0.006 and 0.162±0.008 Å/pulse, respectively. The epitaxial growth of all films has been confirmed to be c-axis oriented alignment via θ/2θ, phi(φ) and rocking curve measurements.

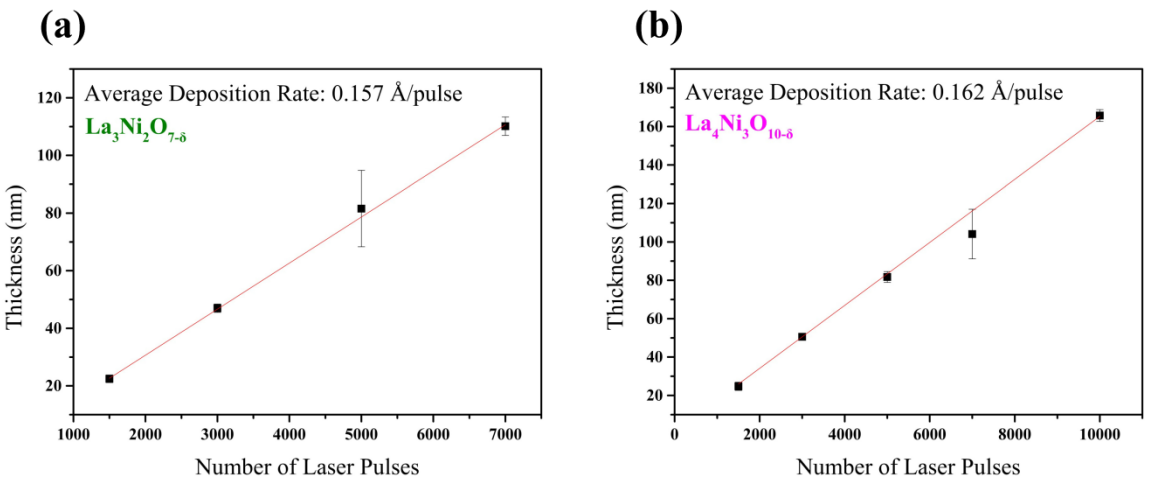


Figure 6.17 Thickness of (a) $La_3Ni_2O_{7-\delta}$ and (b) $La_4Ni_3O_{10-\delta}$ films grown on NGO (110) as a function of the number of laser pulses and their average deposition rates are 0.157±0.006 Å and 0.162±0.008 Å, respectively. The film thickness was determined using Dektak 150 Surface Profiler.

6.3.1.1 Crystallographic Characterisation

The θ/2θ XRD scans of a series of $La_3Ni_2O_{7-\delta}$ films grown on NGO were performed as a function of thickness (23, 47, 82 and 110 nm). To facilitate meaningful comparisons, the intensity of all patterns has been normalised to the most intense peak (220) from NGO substrate; the 2θ positions of all patterns are normalised to the position of the (440) peak from NGO substrate. The high-index 440 reflection was selected as the reference in order to minimise the instrumental errors originating from the configuration geometry and thereby raise the accuracy of the measurements.

In **Figure 6.18 (a)**, clear (00L) reflections with good crystallinity can be observed in all the patterns, indicating the obtainment of c-axis oriented $La_3Ni_2O_{7-\delta}$ films. In particular, the (00$\underline{1}$0) peak of the 23 nm thick film appears to display small oscillation behaviour, the so-called Kiessig fringes. The fringes reveal good crystalline quality of the obtained film (clearly seen in the magnified diagram (**Figure 6.18 (b)**). The Kiessig fringes, in principle, originate from the finite size of the film. [210, 211] In **Figure 6.18 (b)**, it is apparent that the peaks become sharper and narrower as the film thickness increases from 23 to 82 nm, whereas the peaks of the 110nm thick film become slightly broader and less intense, which may imply increasing incorporation of lattice faults within the film. Also, peak shifting can be clearly observed along the bulk position (indexed by dashed line in the figures). As seen at the (006), (00$\underline{1}$0) and (00$\underline{1}$2) peaks, these peaks apparently shift to the position of the bulk oxide as the thickness increases until 82 nm. This behaviour suggests that the c-axis lattice parameters of the thicker films relaxed to the bulk value. However, as thickness continuously increases to 110nm, the peaks shift away from the bulk position again and also become broadened (clearly seen at the (008) reflection), which might imply that the composition changed, and the film started to grow disordered or misaligned.

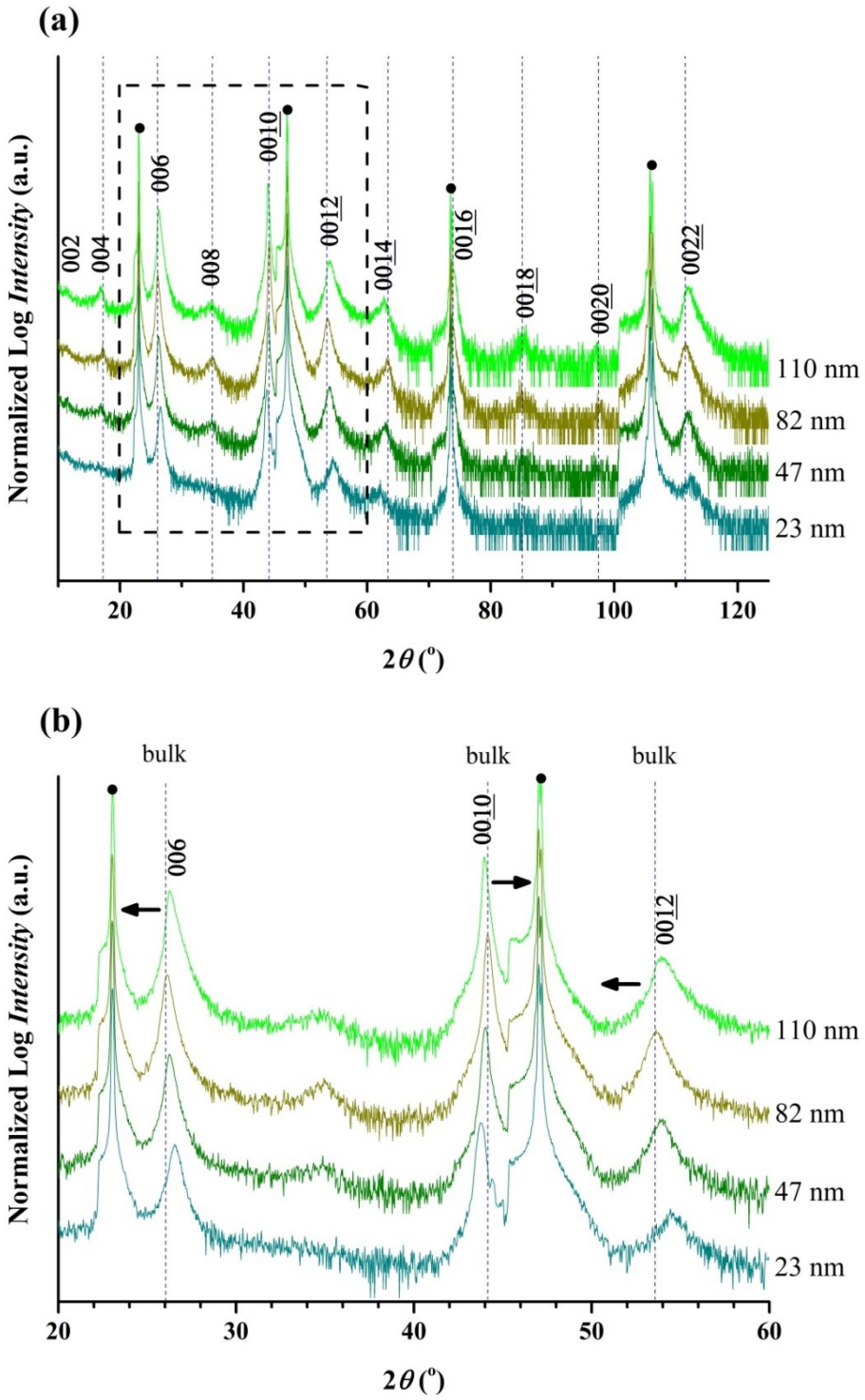


Figure 6.18 (a) θ/2θ XRD scans for $La_3Ni_2O_{7-\delta}$ films with various thicknesses ranging from 23 to 110 nm deposited on NGO (110). The $NdGaO_3$ substrate peaks are indicated by solid circles (•). The c-axis oriented film peaks are indexed by (00L). The dashed lines represent the positions of (00L) reflection from bulk oxide. (b) Zoom of the range of 20-60°, labelled as the dashed square in (a). The arrows indicate the shifting direction of (008), (00$\underline{10}$) and (00$\underline{12}$) peaks.

On the other hand, the same analysis was applied to $La_4Ni_3O_{10-\delta}$ films of different thickness as follows. The θ/2θ XRD results of the series of $La_4Ni_3O_{10-\delta}$ films on NGO with various thicknesses (25, 51, 82, 104, 166 nm) deposited on NGO are shown in **Figure 6.19 (a)**. Sharp and narrow peaks can be observed, indicating a good crystallinity of the films obtained; their intensity generally increased with increasing thickness although the peaks of the 104 nm and 116 nm thick films became slightly broadened.

As seen in **Figure 6.19 (b)**, a significant shifting of the (008), (00$\underline{14}$) and (00$\underline{16}$) peaks can be observed. When the thickness increases, these peaks shifted away from the peak positions of the bulk oxide along the arrowheads; that is, peaks shifted toward the positions of $La_3Ni_2O_{7-\delta}$ phase, potentially resulting in the occurrence of peak overlapping. Evidently, at 2θ position of ~35° (labelled by green solid line) both (00$\underline{10}$) and (00$\underline{12}$) peaks of $La_4Ni_3O_{10-\delta}$ are very close to the (008) peak of $La_3Ni_2O_{7-\delta}$ phase (indexed by green solid line) and both peaks presumably merge into the (008) peak of $La_3Ni_2O_{7-\delta}$. In addition, there likely exists the superstructure of these RP phases due to defect ordering and displacive transitions. The superstructure might also overlap with the peaks of each phase, and thereby cannot be ruled out. Particularly, such phenomena often occurs with thicker films (82 to 116 nm), and suggests that a high possibility of the formation of different RP phases; that is, the presence of RP intergrowths, as the film thickness of $La_4Ni_3O_{10-\delta}$ increases.

Hence, in our case, it can be believed that the deposition of $La_4Ni_3O_{10-\delta}$ films is more challenging than $La_3Ni_2O_{7-\delta}$ ones, based on the θ/2θ results of both phases above. The findings further indicate the possibility for the formation of intergrowths within the matrix of the films as mentioned in Chapter 6.3.

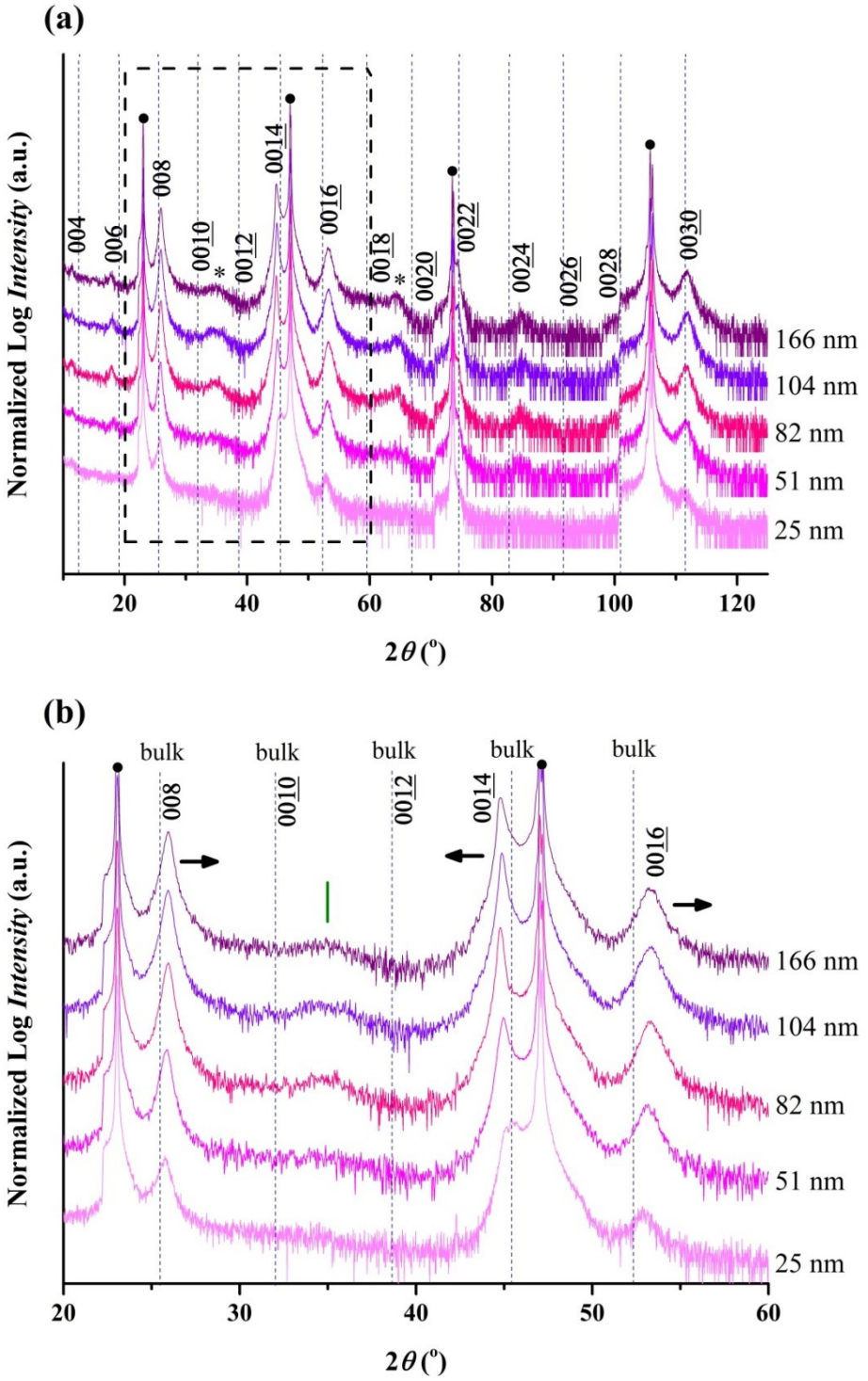


Figure 6.19 (a) θ/2θ XRD scans for $La_4Ni_3O_{10-\delta}$ films with various thicknesses ranging from 25 to 166 nm deposited on NGO (110). The $NdGaO_3$ substrate peaks are indicated by solid circles (•). The c-axis oriented film peaks are indexed by (00L). The star (*) and dashed lines represent the potential alternative phase (intergrowths) and the positions of $La_4Ni_3O_{10-\delta}$ (00L) reflection from bulk, respectively. (b) Zoom of the range of 20-60°, labelled as the dashed square in (a). The arrows display the shifting direction of (008), (00$\underline{14}$) and (00$\underline{16}$) peaks. The short solid green line indicates the (008) position of bulk $La_3Ni_2O_{7-\delta}$ phase.

6.3.1.2 Lattice Parameter and Strain Characterisation

As mentioned previously in Ch.3.3.3, reciprocal space mapping (RSM) analysis was used in an attempt to determine the in-plane (a, b-axis) and out-of-plane (c-axis) lattice parameters, and investigate the influence of strain as a function of thickness through the relative positions of the reciprocal lattice points.

Note that, for the in-plane parameters, only an average value of a, b-axes was selected to present in the following context due to no significant difference between a and b parameters in both $La_3Ni_2O_{7-\delta}$ and $La_4Ni_3O_{10-\delta}$ orthorhombic structures. The average of the c-axis parameter was also calculated from the data obtained by standard θ/2θ measurements (as discussed in Chapter 6.2.3). In principle, the θ/2θ scans were used to extract "average" information along the out-of-plane orientation, while RSM is a typical technique to "selectively" probe the information on the structure and deviation from perfection because the lattice mismatch and the degree of relaxation within the films can be obtained. [211, 212]

Asymmetric measurements, consisting of successive ω-2θ scans around the selected diffraction peaks by varying ω angle as described in detail previously (Chapter 3.3.3) were conducted on the n = 2 and 3 films. In the case of $La_3Ni_2O_{7-\delta}$ phase, the scanned area was set around (11$\underline{7}$) $La_3Ni_2O_{7-\delta}$ and (332) $NdGaO_3$ peaks; for $La_4Ni_3O_{10-\delta}$, it was around (11$\underline{23}$) $La_4Ni_3O_{10-\delta}$ and (332) $NdGaO_3$ peaks. These reflections were selected since they have a high 2θ index with large intensity and thereby can provide precise determination of lattice parameters.

Typical RSM diagrams in Q_x, Q_y coordinates of both phases for the 47 and 51 nm thick films are shown in **Figure 6.20 (a)** and **(b)**, respectively. It is apparent that the (332) spot of the NGO substrate displays a sharp and intense peak with two clear components of $K\alpha_1$ and $K\alpha_2$, as expected in a low-defect single crystal, while the spots of (11$\underline{7}$) $La_3Ni_2O_{7-\delta}$ and (11$\underline{23}$) $La_4Ni_3O_{10-\delta}$ film present more diffuse peaks. Such wide spread of

diffuse spots can cause difficulty in determining the centre of the diffracted spots and result in a certain error in the lattice parameters extracted from the RSM diagrams. The error is likely due to either the intrinsic character of this asymmetric measurement or the nature of the $La_3Ni_2O_{7-\delta}$ and $La_4Ni_3O_{10-\delta}$ phases.

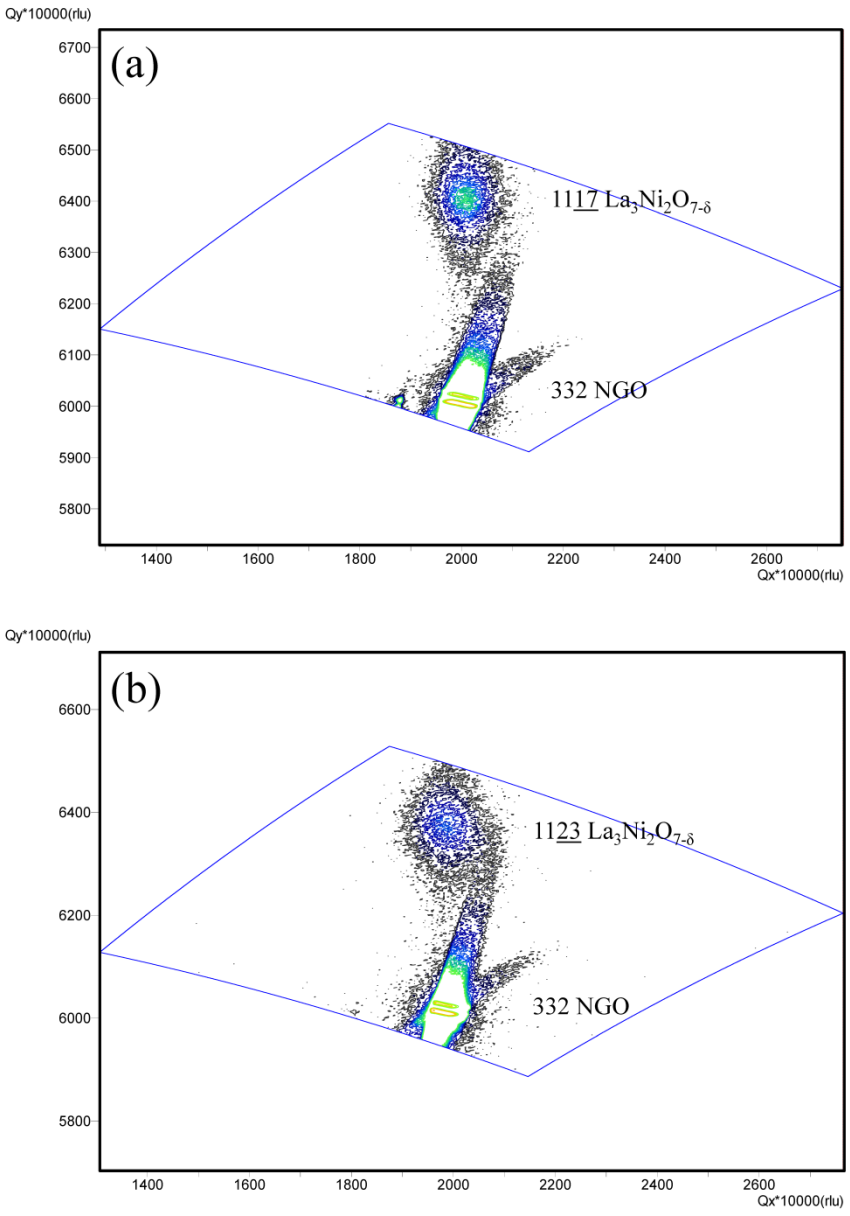


Figure 6.20 Reciprocal space mapping in Q_x, Q_y coordinates with reciprocal lattice unit (rlu) of (11$\underline{7}$) reflection of 47nm-thick $La_3Ni_2O_{7-\delta}$ (a) and (11$\underline{3}$) of 51nm-thick $La_4Ni_3O_{10-\delta}$ (b) around (332) of NGO substrate.

Figure 6.21 (a) exhibits a combined simulation of the theoretical reciprocal lattice points in Q_x, Q_y representation for $La_3Ni_2O_{7-\delta}$, $La_4Ni_3O_{10-\delta}$ and NGO phases together. The geometric path of incident and diffracted beams, and the selected scanning area are schematically illustrated in the diagram. Careful inspection of the enlargement of the scanned area in **Figure 6.21 (b)** shows that the (11$\underline{17}$) reflection of $La_3Ni_2O_{7-\delta}$ and (11$\underline{23}$) of $La_4Ni_3O_{10-\delta}$ obviously appear rather close to each other, suggesting the possibility of overlapping of both peaks. During the measurements, the (11$\underline{17}$) reflection of $La_3Ni_2O_{7-\delta}$ registered at 2θ=81.8518°, ω=23.0998°; the (11$\underline{23}$) of $La_4Ni_3O_{10-\delta}$ registered at 2θ=83.8240°, ω=24.5987°. Such close azimuth angles, unfortunately, could give rise to the difficulty of separating the close peaks and distinguishing their contributions from each phase due to the low resolution of the RSM images, as previously observed in **Figure 6.20 (a)** and **(b)**. Despite the reduced accuracy, after careful fitting of the peaks, the a, b- and c-axis parameters were determined using the reciprocal vector formula (described Chapter 3.3.3), and will be plotted for the following discussion.

In addition to the lattice parameters, the level of lattice strain of the films has also been estimated in different crystallographic orientation as:

$$E_{xx}\ (or\ E_{yy}) = \frac{a - \hat{a}}{\hat{a}} \qquad \text{(Eq.6.1)}$$

$$E_{zz} = \frac{c - \hat{c}}{\hat{c}} \qquad \text{(Eq.6.2)}$$

where E_{xx}, E_{yy} and E_{zz} represent the strain in a, b-axis and c-axis orientations; a and c represent the average lattice constants of obtained films; â and ĉ are the lattice constants of the bulk oxide from the reference, taking into account the stoichiometric $La_3Ni_2O_7$ and $La_4Ni_3O_{10}$ structures reported by Ling *et al.* (ICSD collection code: 91141) and Zhang *et al*. (code: 80279). [45, 47]

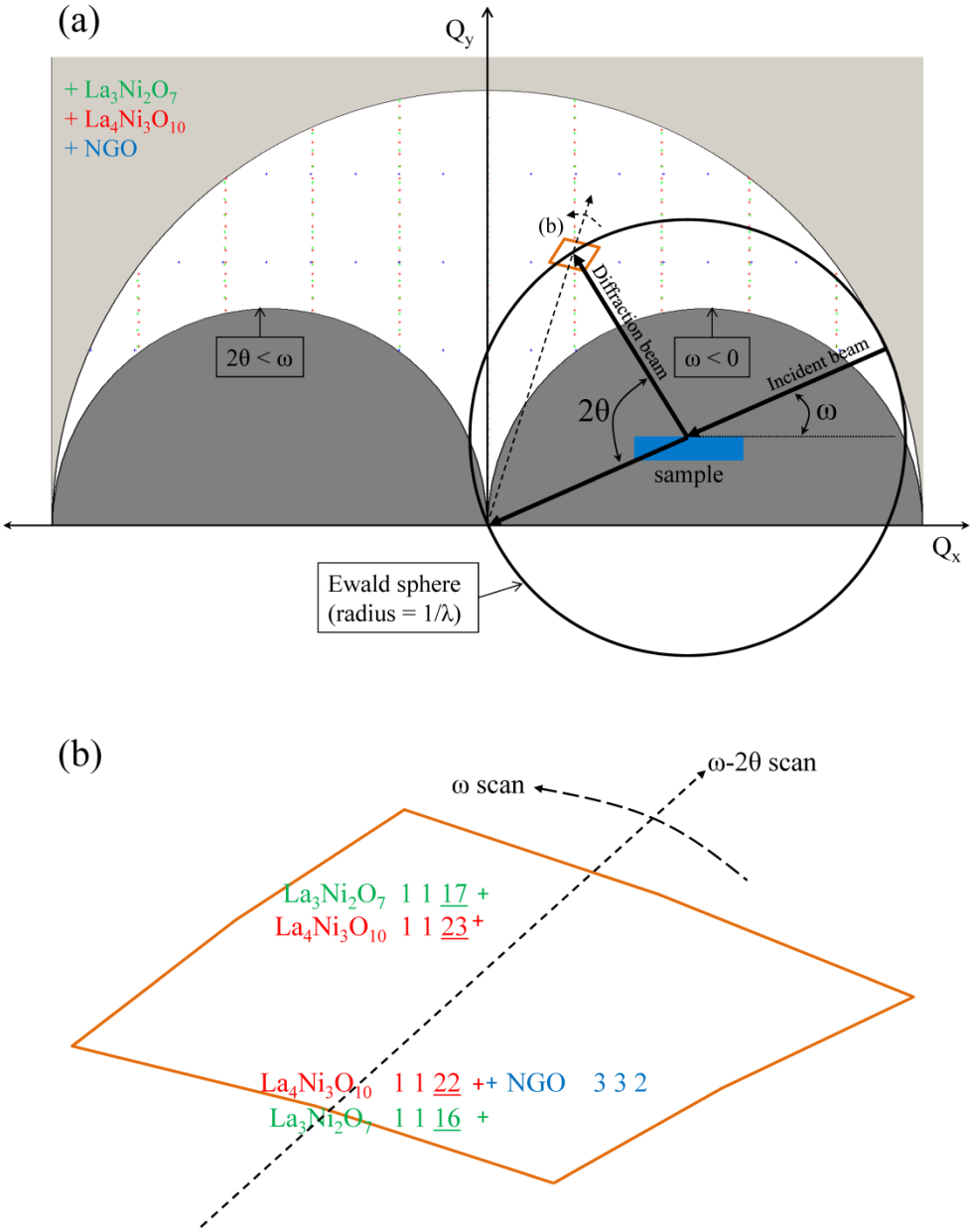


Figure 6.21 (a) A plot of theoretical reciprocal lattice points of the $La_3Ni_2O_7$, $La_4Ni_3O_{10}$ and NGO phases, simulated by PANalytical X'Pert data collector software. The bigger semicircle is defined by the reciprocal lattice coordinates, Q_x and Q_y, with radius of $1/\lambda$ (λ is the X-ray wavelength) and in units of reciprocal lattice units (rlu, 1 rlu = $2/\lambda$). The two grey smaller semicircles represent the Laue zone where diffraction cannot be measured due to the geometric limitation of the equipment configuration. The construction of a Ewald sphere with radius of $1/\lambda$ depicts the relationship of incident and diffracted beams with the selected scan region for (11$\underline{17}$) $La_3Ni_2O_7$, (11$\underline{23}$) $La_4Ni_3O_{10}$ and (332) NGO reflections. (b) the zoom images of the selected scan region are illustrated with the scanning axes of ω and ω-2θ. Two satellites of (11$\underline{16}$) $La_3Ni_2O_7$ and (11$\underline{22}$) $La_4Ni_3O_{10}$ are also shown nearby (332) NGO in the selected region.

Figure 6.22 (a) shows the variation of a, b- and c-axis lattice parameters plotted with various film thicknesses (23, 47, 82 and 110 nm) for $La_3Ni_2O_{7-\delta}$ films; **Figure 6.22 (b)** exhibits a plot of the E_{xx}, E_{yy} and E_{zz} lattice strain of the films as a function of film thickness. In the case of the θ/2θ data, the c-axis parameters gradually increase with thickness from 23 to 82 nm and then decrease at 110nm. Additionally, an absolute lattice strain ranging from 0.26~0.79% can be observed in **Figure 6.22 (b)**. The range is in good agreement with the theoretical lattice mismatch of 0.69% (as calculated previously, **Table 4.2**) between orthorhombic $La_3Ni_2O_{7-\delta}$ and (110)-oriented NGO substrate. For RSM data, a similar trend of c-axis parameters was observed. Such trend from both θ/2θ and RSM data is consistent with the shifting feature of peaks observed in the last section. In general, all c-axis values of the films for both θ/2θ and RSM data appear below the value of bulk material, indicating the existence of compressive strain along the c-axis direction (see **Figure 6.22 (a) and (b)**). On the other hand, the trend of a, b-axis parameters normally should exhibit an opposite behaviour but no opposite trend was observed as the thickness increased. All a, b-axis values of these films are higher than the bulk value, still showing the presence of tensile strain along a, b-axis (**Figure 6.22 (b)**). By careful inspection, the a, b-axis value of the thinnest film (23 nm) closely matches the mean value of NGO substrate (5.4650 Å, JCPDF: 21-0972), suggesting a coherent growth with the substrate. As thickness increases, the a, b-axis parameters also increased, which means the tensile strain increased. This phenomenon might suggest the presence of extra strain due to the formation of microstructural defects along a, b-plane. Moreover, the variation of c-axis parameters with thickness might be associated with the influence on the intergrowths of different RP phases; that is, the thicker films could accumulate larger proportion of RP intergrowths, as discussed in the previous section. It is worth noting that, as seen in **Figure 6.22 (b)**, the 82nm-thick film shows an abnormally high in-plane strain compared to others, which is probably due to the adoption of the high-surface-roughness substrate

(from Batch B, as mentioned in the **Table 4.3** of Chapter 4.2). This further implies that surface roughness of the substrate can significantly affect the quality and lattice strain of films.

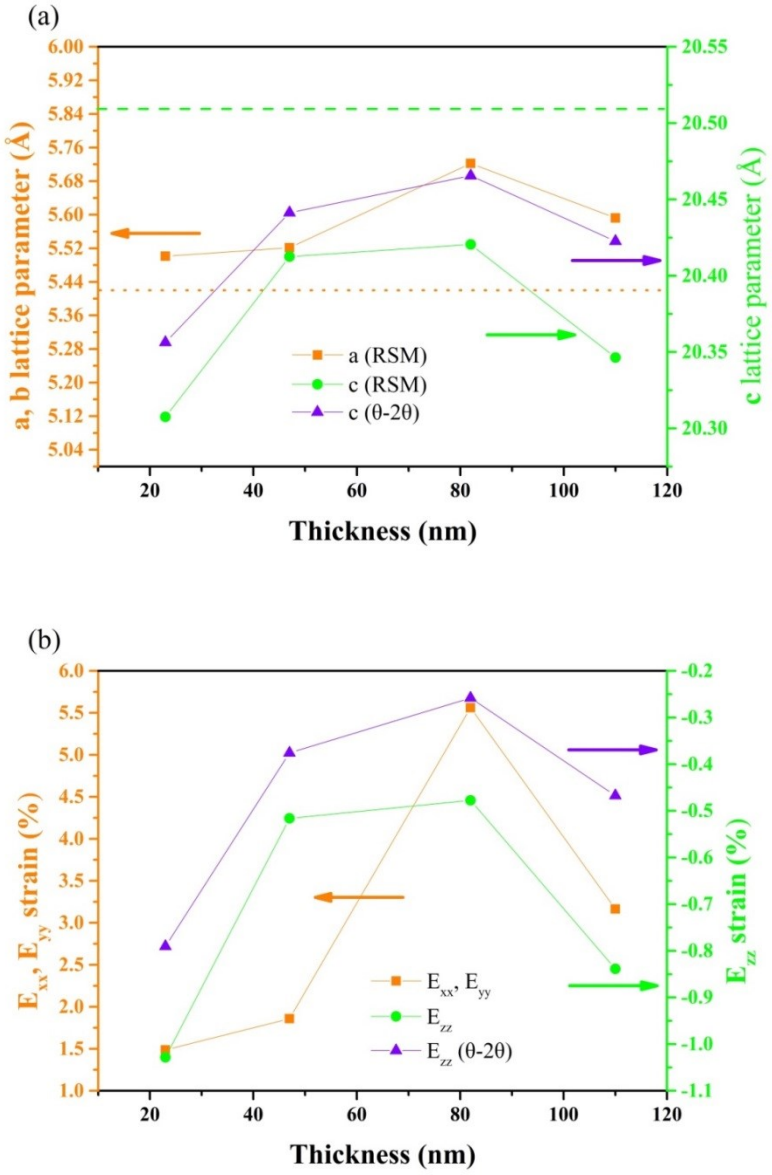


Figure 6.22 (a) Variation of the calculated a,b- and c-axis parameters of $La_3Ni_2O_{7-\delta}$ films with thickness of 23, 47, 82, and 110 nm. The horizontal dotted and dashed lines represent the bulk values of the average a,b-axis and c-axis parameters, respectively. (b) Variation of the estimated E_{xx}, E_{yy} and E_{zz} strains as a function of the film thickness.

To further examine the series of obtained $La_4Ni_3O_{10-\delta}$ films, their in-plane (a, b-axis) and out-of-plane (c-axis) lattice parameters determined by RSM and normal θ/2θ scans is

plotted as a function of film thickness in **Figure 6.23 (a)**. A plot of the E_{xx}, E_{yy} and E_{zz} lattice strain of the films as a function of film thickness is also presented in **Figure 6.23 (b)**.

In **Figure 6.23 (a)**, it can be observed that the c-axis parameters obtained from θ/2θ scans gradually expand until they are close to the bulk value (27.959 Å) with increasing thickness. In **Figure 6.23 (b)**, the results of θ/2θ scans present an absolute value of lattice strain ranging from 0.12~0.25%, which is reasonably consistent with the theoretical lattice mismatch of 0.34% (as calculated previously, **Table 4.2**) between orthorhombic Fmmm $La_4Ni_3O_{10-\delta}$ and (110)-oriented NGO substrate. On the other hand, the c-axis parameters determined from RSM analysis exhibit a completely different behaviour compared to the results of θ/2θ scans.

It is worth noting that, as mentioned above, the analysed reflections in the RSM measurement for both $La_3Ni_2O_{7-\delta}$ and $La_4Ni_3O_{10-\delta}$ phases are rather close to each other and it was difficult to distinguish the respective contributions from each phase due to the low resolution of the obtained RSM images. Thus, these lattice parameters were probably unable to be determined precisely, and thereby an abnormal behaviour is presented. As seen in **Figure 6.23 (a)**, normally, the a, b-axis and c-axis lattice constant should gradually converge on the value of the lattice constant of the bulk material as thickness increased; that is, a cell relaxed along a, b-axis while a cell strained along c-axis with increasing film thickness. However, a clear opposite behaviour was observed instead in that a cell shrinkage along c-axis whilst a cell expansion along a, b-axis with increasing film thickness was observed, which is unusual. The unusual behaviour of the c-axis and a, b-axis constants could be attributed to the formation and relative proportions of different RP phases (e.g.: $La_3Ni_2O_{7-\delta}$); that is, the presence of RP-intergrowths. The shrinkage of the c-axis can be caused when the proportion of $La_3Ni_2O_{7-\delta}$ phase increases, because $La_3Ni_2O_{7-\delta}$ phase apparently possesses a smaller c-axis constant than $La_4Ni_3O_{10-\delta}$. The

expansion of a, b-axis might be explained by a high concentration of microstructural defects (such as stacking faults) accommodated within the films, and thereby a high lattice strain accumulated can be observed (**Figure 6.23 (b)**).

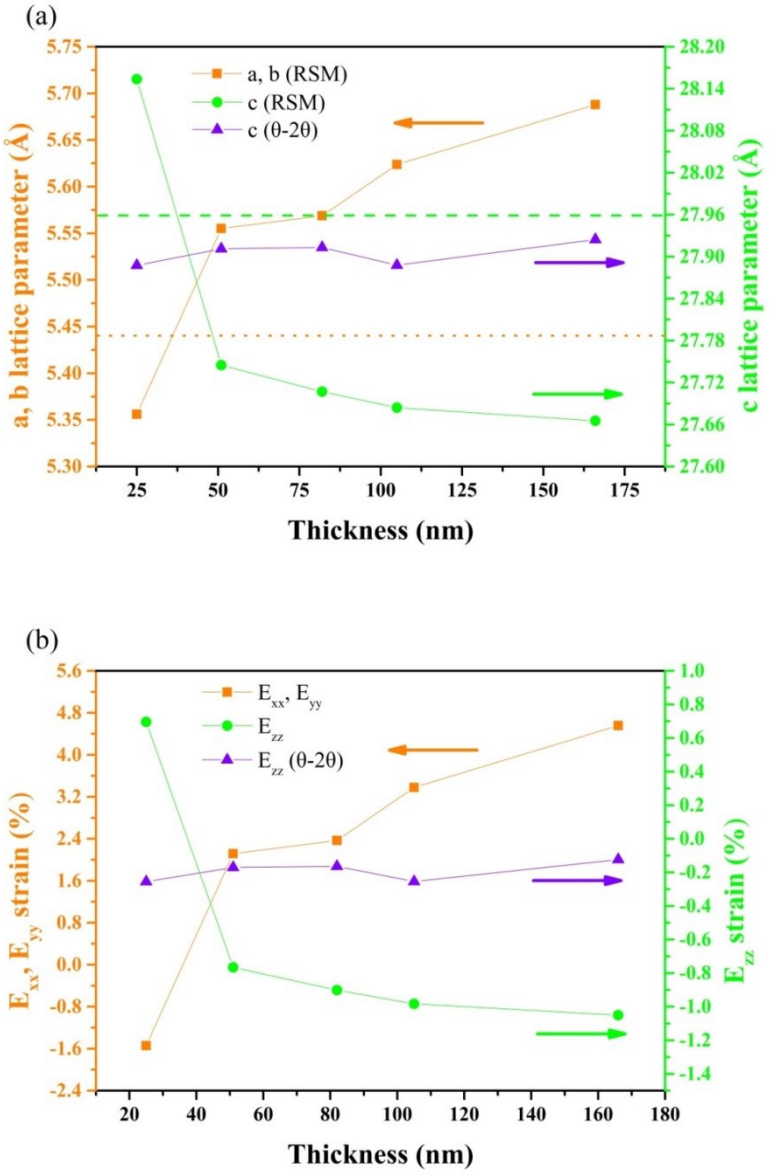


Figure 6.23 (a) Variation of the calculated a,b- and c-axis parameters of $La_4Ni_3O_{10-\delta}$ films with thickness of 25, 51, 82, 104 and 166 nm. The horizontal dotted and dashed lines represent the bulk values of the average a,b-axis and c-axis parameters, respectively. (b) Variation of the estimated E_{xx}, E_{yy} and E_{zz} strain as a function of the thicknesses.

Overall, together with the previous observations of peak shifting in the XRD θ/2θ patterns, these findings of the lattice constant and strain analyses further indicate the possibility for the presence of RP-type intergrowths and the variation of microstructure with an increase in film thickness. These microstructures will be visually investigated through TEM analysis in the following sections.

6.3.1.3 **Compositional Characterisation**

Composition analysis of the series of $La_3Ni_2O_{7-\delta}$ and $La_4Ni_3O_{10-\delta}$ samples was determined by EDX. Again, as mentioned previously, due to the penetration depth of X-ray probe for EDX (~1 μm), information from the substrates can be contained in EDX spectra, leading to the film-substrate peak overlapping, and consequently certain errors. This particularly has a major influence on the measurements of the very thin-films because more signal is collected from the substrate proportionally and hence there is insufficient signal from the thin-films, making it difficult to distinguish the peaks in the spectra.

Despite such errors, useful compositional information is still able to be obtained. **Figure 6.24** shows the cation (La/Ni) ratios of the obtained $La_3Ni_2O_{7-\delta}$ and $La_4Ni_3O_{10-\delta}$ films deposited with various film thicknesses. It is apparent that the thinnest films of both phases display an abnormal ratio due to the penetration issue of the X-ray probe. However, for the rest of $La_3Ni_2O_{7-\delta}$ samples, their measured La/Ni ratios were fairly close to the expected ratio, which corresponds to the deviation of the peaks observed in previous θ/2θ XRD results (shown in **Figure 6.18** previously). For the $La_4Ni_3O_{10-\delta}$ samples, only 51nm-thick film presented a desired La/Ni ratio compared to other samples whereas the rest of the thicker $La_4Ni_3O_{10-\delta}$ films present a similar ratio as the expected ratio of $La_3Ni_2O_{7-\delta}$. For these obtained thicker films, again it is worth noting that, target degradation as laser pulses increase could result in disturbance of the composition of the

thicker films.

Together with the results of crystallographic, lattice parameter and strain characterisation above, the findings of composition analysis are in agreement with the assumption regarding the increasing proportion of $La_3Ni_2O_{7-\delta}$, and further ascertain the possibility of the presence of intergrowths as the film thickness increases. These compositional results may also suggest a critical thickness of ~50 nm for the deposition of $La_4Ni_3O_{10-\delta}$ and even $La_3Ni_2O_{7-\delta}$ phase under the utilised growth conditions. Also the results may imply the change of surface morphological homogeneity and the variation of microstructure, which will be further investigated in the following two characterisations sections.

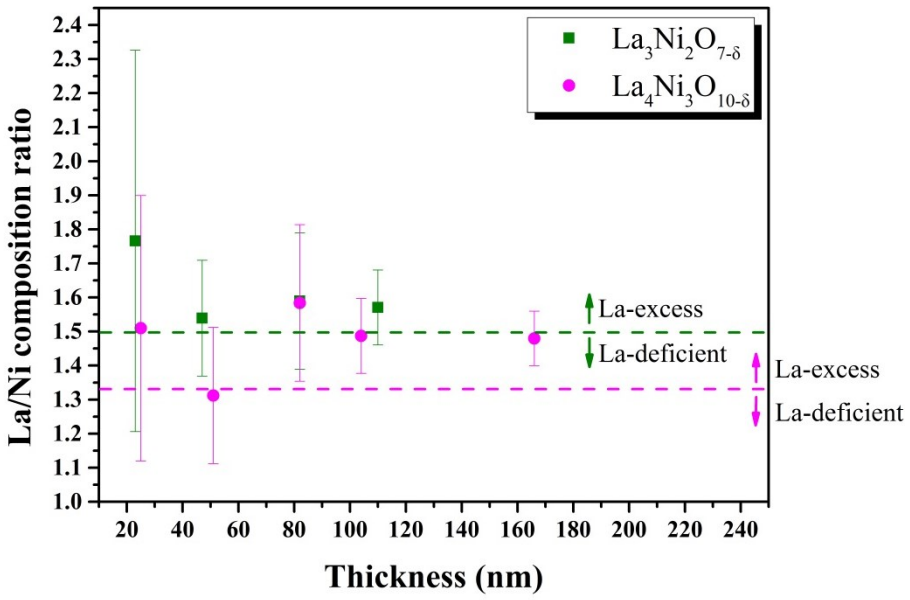


Figure 6.24 The variation of the cation ratio (La/Ni) for $La_3Ni_2O_{7-\delta}$ and $La_4Ni_3O_{10-\delta}$ as a function of film thickness. The horizontal dashed lines at 1.50 and 1.33 represent the expected cation ratio in $La_3Ni_2O_{7-\delta}$ and $La_4Ni_3O_{10-\delta}$, respectively.

6.3.1.4 Surface Morphological Characterisation

The surface morphology of c-axis oriented $La_3Ni_2O_{7-\delta}$ and $La_4Ni_3O_{10-\delta}$ films fabricated with different thickness were characterised using the AFM technique. The scan area was 1 μm × 1 μm. **Figure 6.25 (a)-(d)** presents the AFM images of $La_3Ni_2O_{7-\delta}$ films with various film thicknesses (23, 47, 82 and 110 nm), displaying typically granular morphology with a highly homogeneous grain distribution. Apart from the 82nm-thick film, the RMS roughness of the rest of the films progressively becomes rougher, approximately from 0.24 to 0.47 nm due to the slightly increasing crystallite sizes as the thickness increases. The 82nm-thick film presents the highest RMS value among all films, which may be as a consequence of the film being deposited on a high-surface-roughness substrate (from Batch B, as mentioned in the **Table 4.3** of Chapter 4.2). In general, it is apparent that there is no significant change of the surface morphology for the series of $La_3Ni_2O_{7-\delta}$ films. The results are in accordance with the XRD patterns and compositional analysis previously discussed.

On the other hand, the AFM images of $La_4Ni_3O_{10-\delta}$ films deposited with thickness of 25, 51, 82, 104 and 166 nm are presented in **Figure 6.26 (a)-(e)**. For the films from 25 to 82 nm, a few large particles were observed, which are likely attributed to the typical agglomerates stemming from the plasma plume. Apart from this, a regular granular feature with a crystallite size of ~30 nm and a rather low RMS roughness (< 0.50 nm) was observed in **Figure 6.26 (a)-(c)** while for the thicker films (104 and 166 nm), their crystallite size was remarkably enlarged and an inhomogeneous distribution was observed in **Figure 6.26 (d)** and **(e)**. As a result, the RMS roughness of the 166 nm-thick film rapidly increases to 1.62 nm with a crystallite size of about 40-100 nm, indicating the substantial inhomogeneity of the thickest film. The consequence of surface morphological change of these films varying with thickness is also presumably associated with the existence of different RP phase and thereby the formation of RP intergrowths due to the

consequence of the cation stoichiometric deviation (seen in the compositional characterisation) induced by the degradation of targets with time during the PLA process (described previously in Chapter 4.1.2). These AFM observations are in good agreement with the findings from both the XRD and compositional results in the previous discussions.

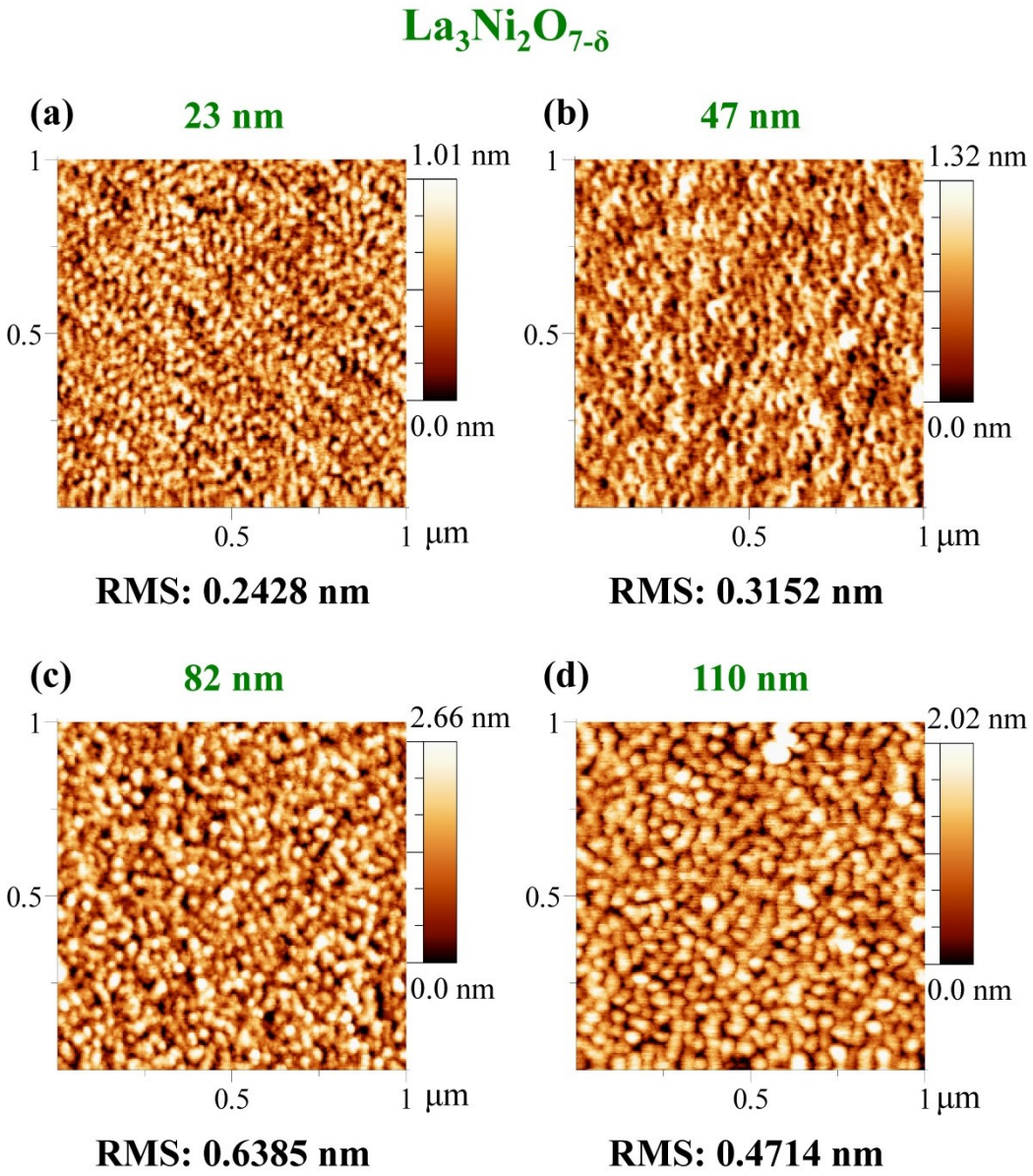


Figure 6.25 AFM images of $La_3Ni_2O_{7-\delta}$ thin film deposited on NGO as a function of film thickness of 23 nm (a), 47 nm (b), 82 nm (c) and 110 nm (d) with the image size: 1 μm × 1 μm. Z depth scales are indicated from dark brown to white. The avg, RMS values are presented on the bottom of the images.

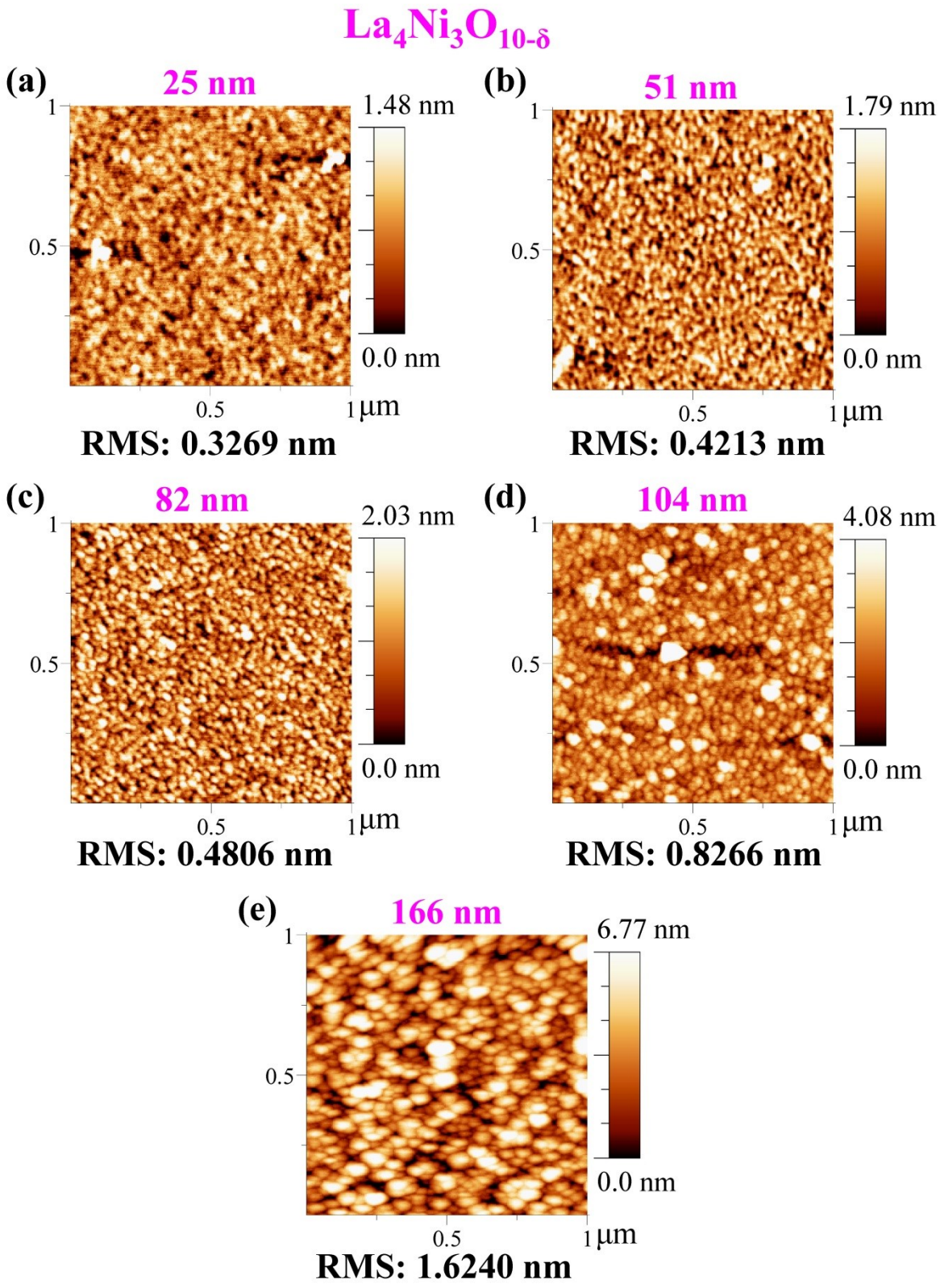


Figure 6.26 AFM images of $La_4Ni_3O_{10-\delta}$ thin film deposited on NGO as a function of film thickness of 25 nm (a), 51 nm (b), 82 nm (c), 104 nm (d) and 166 nm (e) with the image size: 1 µm × 1 µm. Z depth scales are indicated from dark brown to white. The avg, RMS values are presented on the bottom of the images.

6.3.1.5 **Microstructural Analysis**

To assess the microstructure of the films, cross-section high angle annular dark field (HAADF) scanning transmission electron microscopy (STEM) images of the 166 nm thick $La_4Ni_3O_{10-\delta}$ film, as an example (seen in **Figure 6.27**), was performed for high-resolution transmission electron microscopy (HRTEM) analysis. The image was analysed from the [110] viewing direction as described in Ch.3.3.7. Only La and Ni/O mixed atomic columns will be visible in the image. The brightest spots in the image correspond to La atomic columns since the intensity is approximately proportional to Z (atomic number) [213]; the weaker spots are represented as NiO_6 octahedra but basically Ni atomic columns are apparently recognised in the image. Note that all the HRTEM measurements in this thesis were conducted by Dr. Fan and Professor McComb at Department of Materials Science and Engineering, The Ohio State University, USA.

The HAADF image (**Figure 6.27 (a)**) shows the microstructure and planar defects observed in the $La_4Ni_3O_{10-\delta}$ film. It is clearly observed in the image that well-defined RP-phase structures were epitaxially grown along c-axis normal to the substrate surface (schematically shown in **Figure 6.27 (b)**), although a high-density of intergrowth structure of RP-phases parallel to the substrate surface were found. A detailed observation shows that a number of consecutive $LaNiO_3$ (perovskite) layers were sandwiched by LaO (rock-salt) layers within the image, which indicates that the film consisted of intermixed layers with different stacking sequences (primarily n = 2 and 3, occasionally n = 1) along the c-axis growth direction. Such a mixed intergrowth phenomenon has been observed in the series of lanthanum nickelate films deposited by Burriel *et al*. using PI-MOCVD techniques. [91] The consequence of the intermixed n= 2 and 3 intergrowth is in good agreement with the results found from the previous XRD and compositional characterisation.

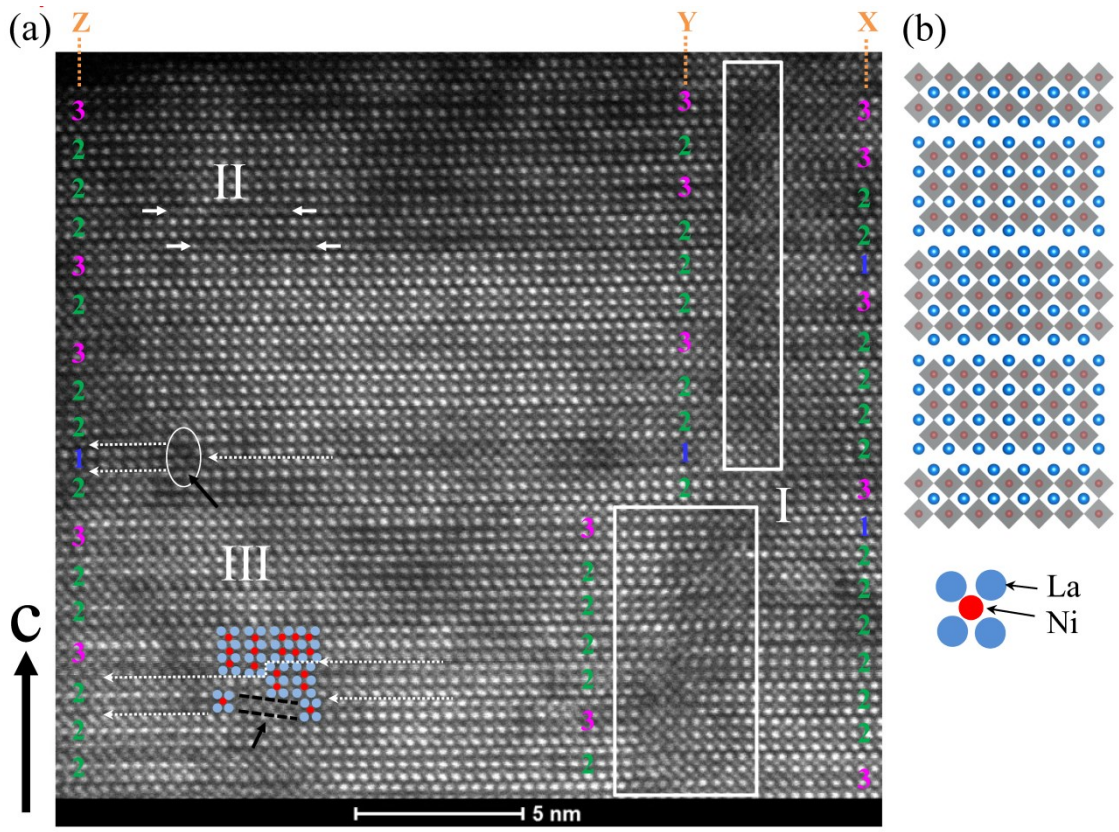


Figure 6.27 Cross-section HAADF STEM image of the 166nm-thick $La_4Ni_3O_{10-\delta}$ film deposited on NGO (110). (a) the film primarily consists of intergrowths of n = 2 and 3 phases, occasionally n = 1 (labelled with different colours at X, Y and Z sections in the image). Three typically observed defects are indexed as domain boundaries (white rectangle), extended faults (solid white arrows) and stacking faults (black arrows), labelled in region I, II and III respectively. The white dotted arrows correspond to the movement of LaO (rock-salt) layers when the propagation of the atomic columns undergoes the extended faults. (b) schematically represents that the film were grown along c-axis even though a variety of imperfection were encountered during deposition. The blue and red circles indicate lanthanum and nickel elements respectively.

A variety of planar defects are also found within the selected area of the image (**Figure 6.27 (a)**). These typically observed defects are categorised into three regions: I, II and III. In region I, two areas delineated by the white rectangle reveal domain boundaries separating the well-defined layered RP structures. Obviously, the layered RP columns effectively propagated through the boundaries. Such boundaries could be associated with either a surface step of the NGO substrate or nucleation interactions of the different intergrowths during deposition, and appear to be one of the origins of the planar defects.

Similar phenomena have been observed typically in layered RP-phase La_2NiO_4 [91], La_2CuO_4 [214], $Sr_{n+1}Ru_nO_{3n+1}$ (n = 1 and 2) [215] and superlattice $LaNiO_3/LaALO_3$ [213] thin-films, and more comprehensive information can be found in these references.

In region II (indicated by solid white arrows), extended faults occurring over a few unit cells are observed. As seen with the extended faults, it seems that the faults are composed of two weaker spots, which can be assigned to a double layer of edge-sharing NiO_6 octahedra connecting each other over several unit cells, a so-called shear structure [216, 217]. The faults may imply the loss of LaO columns, and could result in La deficiency (i.e. Ni excess) at this area. Similar phenomena have been reported in under-stoichiometic $La_{2-x}Sr_xCuO_4$ [216] and Ti-excess $SrTiO_3$ [217] samples. In contrast, in region III, a number of stacking faults were detected. After undergoing these stacking faults, extra LaO rock-salt layers were produced as can be observed along the dotted arrows. The formation of extra LaO layers may indicate La-excess around the faults. Similar faults were also found in previous literature for layered $Sr_{n+1}Ru_nO_{3n+1}$ [215], $Sr_{n+1}Ti_nO_{3n+1}$ [218], and La_2CuO_4 [214] films (typically often observed in n > 1 phase).

In region I, II and III, it generally appears that the composition could be compensated by these observed defects. Interestingly, as seen in the image, all intergrowths of n = 1, 2 and 3 phases are labelled with colour number of 1, 2 and 3, respectively along three different sections of X, Y and Z. A careful inspection shows that from X to Y section, only a single n = 1 layer is annihilated when encountering the domain boundaries; from Y to Z, no change in the total fraction of each member was detected after propagating through the extended and stacking faults. In general, there was no significant variation and only ordering alteration occurred. Moreover, assuming that the n = 1, 2 and 3 members are with ideal La/Ni values, the average La/Ni ratio from X, Y and Z sections can be estimated at 1.51, 1.48 and 1.48, respectively. Their average value is rather consistent with the value of 1.48 obtained by EDX measurements, indicating that

$La_3Ni_2O_{7-\delta}$ phase was prevalent in the obtained film. The results confirmed the possibility of accumulating more $La_3Ni_2O_{7-\delta}$ phase in the thicker $La_4Ni_3O_{10-\delta}$ film.

Overall, these HRTEM results indicate that the 166 nm thick film consists of a mixture of the n = 1, 2 and 3 phases, partially separated by domain boundaries and decorated by extended and stacking fault regions. These imperfections appear to originate from the issue (described previously) that target degradation occurs as the number of laser pulses increases and may lead to the compositional and phase variation of the deposited films during the deposition process, particularly for thicker films because of the longer deposition process. Due to this issue, generally said in our case, it could be inferred therefore that the thicker films were grown, the more defects and intergrowths were accumulated. Such speculation to be proposed here is based on not only the finding through the crystallographic, lattice parameter, compositional, morphological and microstructural characterisation discussed above, but also the electrical transport results, which will demonstrate an evolution of the total electrical conductivity with different film thickness in the next chapter. The behaviour regarding more intergrowths and misalignments accumulated with increasing film thickness has also been reported in $La_{1.2}Sr_{1.8}Mn_2O_7$ [219] and $La_{1.2}Sr_{1.8}Mn_{1.7}Ru_{0.3}O_7$ [220] epitaxial films deposited by PLD. This finding emphasises the difficulties with regard to fabricating defect-free thick films of such complex layered RP oxides.

It is also worth noting that the observed 166 nm thick $La_4Ni_3O_{10-\delta}$ sample was as-deposited without any post-annealing treatment either during a growth process in the PLD chamber or after deposition outside the chamber, followed by a 4-point cycling electrical measurement from RT to 700°C over 2 weeks. Then the HRTEM characterisation was conducted afterwards. It is known that undergoing a cycling electrical measurement is subjecting the sample to a thermal treatment. Under the thermal treatment, the observation of the image (**Figure 6.27**) shows that the RP column ordering

was still aligned along the (00L) orientation in the film in spite of the presence of various defects. It is of interest to investigate whether any significant difference will occur before and after a post-annealing treatment during the growth process in the PLD chamber. A detailed study of this effect is discussed in the following section, followed by an investigation with respect to thermal stability of the film.

6.3.2 Effects of Post-annealing

The influences on the microstructure of $La_3Ni_2O_{7-\delta}$ and $La_4Ni_3O_{10-\delta}$ films through the effect of film thickness has been systematically discussed in the previous sections. In this section, an investigation into the influence on microstructure via the effect of post-annealing will be addressed in order to examine if there is any significant variation before and after a post-annealing treatment during the growth process. Two post-annealed film samples for $La_3Ni_2O_{7-\delta}$ and $La_4Ni_3O_{10-\delta}$ phases were first deposited on NGO (110) single crystal substrates by the optimised growth conditions obtained from Ch.6.1, and followed by a post-annealing process with an atmosphere of *700 Torr* O_2, at 500°C for one hour for the $La_3Ni_2O_{7-\delta}$ sample; *250 mTorr* O_2 (the same as used for deposition), at 500°C for one hour for the $La_4Ni_3O_{10-\delta}$ sample.

The comparative θ/2θ XRD scans of the obtained post-annealed and as-deposited samples are shown in **Figure 6.28 (a)** and **(b)** for $La_3Ni_2O_{7-\delta}$ and $La_4Ni_3O_{10-\delta}$ films, respectively. **Figure 6.28 (a)** shows that the pattern of the as-deposited $La_3Ni_2O_{7-\delta}$ film exhibits clear (00L) reflections with a sharp intensity while that of the post-annealed sample became obscured, presenting significantly broader (00L) peaks with a number of fuzzy peaks associated with a small amount of other orientations, as particularly observed around the (006), (008), (00$\underline{1}$0), (00$\underline{1}$2) and (00$\underline{1}$4) peaks. On the other hand, in **Figure 6.28 (b)**, the pattern of the as-deposited $La_4Ni_3O_{10-\delta}$ film displays appropriate (00L)

reflections. Note that although the $La_4Ni_3O_{10-\delta}$ film might be impure and potentially has the presence of different RP-phase intergrowths as has been described in previous sections already, here the purpose is to use the obtained predominantly as-deposited $La_4Ni_3O_{10-\delta}$ sample as a reference to compare with the post-annealed sample and see their difference. Therefore, the pattern of the post-annealed sample exhibits a slightly less intense (00L) and broader peaks (especially seen at the (00$\underline{14}$) reflection, indexed by a black arrow). Similar fuzzy peaks are also observed and likely contributed by other orientations.

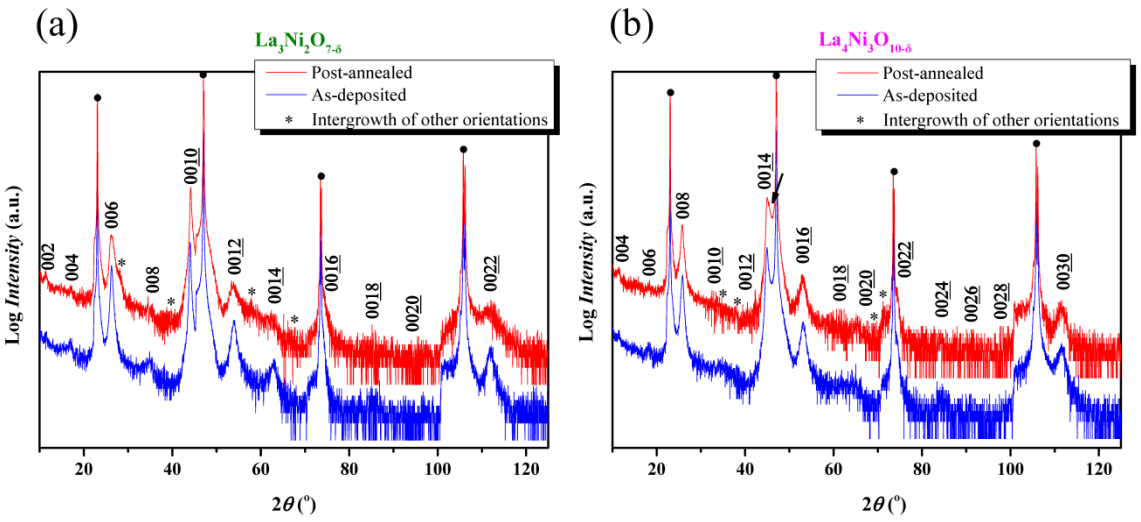


Figure 6.28 θ/2θ XRD patterns of post-annealed and as-deposited films for $La_3Ni_2O_{7-\delta}$ (a) and $La_4Ni_3O_{10-\delta}$ (b) films grown on NGO (110) single crystal substrate. The NGO substrate peaks are indicated by solid circles (•), the c-axis oriented film peaks are indexed by (00L) and some extra peaks are indexed by stars (*) and represented as random intergrowths in the post-annealed films.

When comparing the XRD patterns of both post-annealed $La_3Ni_2O_{7-\delta}$ and $La_4Ni_3O_{10-\delta}$ samples to the ones of both as-deposited samples in **Figure 6.28 (a)** and **(b)**, an interesting finding was observed. It is known that the oxygen partial pressure values of 700 Torr utilised for post-annealing the $La_3Ni_2O_{7-\delta}$ sample was far higher than that of 250 mTorr for the $La_4Ni_3O_{10-\delta}$. Evidently, the diffraction pattern of the post-annealed $La_3Ni_2O_{7-\delta}$ film presents a more fuzzy and broader dataset than that of the $La_4Ni_3O_{10-\delta}$

film. Such behaviour presumably implies that the utilisation of the extremely high oxygen partial pressure atmosphere during the post-annealing process could cause a significant impact upon the orientation or ordering of the RP-type blocks due to a strong influence on the oxidation state of Ni from Ni^{2+} to Ni^{3+} as an increase of oxygen incorporation from the outside of either the $La_3Ni_2O_{7-\delta}$ or $La_4Ni_3O_{10-\delta}$ matrices. In particular, as inserting from the LaO (rock-salt) layers, the insertion of excess oxygen can result in rotations and tilts of the NiO_6 octahedra, then yield an additional lattice strain within the films, and thereby lead to an expansion of the c-axis and a contraction in the ab-plane. As partial lattice structure is no longer able to accommodate strain, a certain proportion of RP segments therefore may randomly distributed within the matrix of the films. The phenomenon is fairly similar to the findings of the investigation into the influence of oxygen partial pressure for film growth of $La_2NiO_{4+\delta}$ (seen in Ch.5.1), but is more moderate under the post-annealing process and even more considerable as a high oxygen partial pressure is used.

The microstructure of the as-deposited and post-annealed $La_4Ni_3O_{10-\delta}$ samples were characterised by HRTEM measurements. **Figure 6.29** exhibits a cross-section HAADF STEM image of the as-deposited $La_4Ni_3O_{10-\delta}$ film as an example. It clearly shows a periodic stacking of $LaNiO_3$ perovskite sequences separated by LaO rock-salt layers. All LaO layers were laid parallel to the substrate surface and regularly ordered along the c-axis oriented growth direction although a number of stacking faults can be observed from the image because the measured film was not optimised. Thus, this film presents c-axis oriented. By contrast, **Figure 6.30 (a)** shows that no regular ordering can be seen, but the LaO layers were randomly distributed along the direction perpendicular and parallel to the growth direction within the film, as can be clearly seen in the magnified image (**Figure 6.30 (b)**) and is schematically demonstrated in **Figure 6.30 (c)**. The random ordering structure has also been observed in a variety of earlier studies with

regard to $SrTiO_3$/SrO superlattices [193, 221], La_2NiO_4 [222], $La_{1.2}Sr_{1.8}Mn_{1.7}Ru_{0.3}O_7$ [220], $Sr_{n+1}Ru_nO_{3n+1}$ [215], $Sr_{n+1}Ti_nO_{3n+1}$ [218, 223] and $Ca_5Mn_4O_{13}$ [224] films grown by a number of typical deposition techniques such as PLD, MOCVD and MBE. These various studies through the different techniques reveal the challenges of growing pure phases of higher order members (typically n > 2) of the RP-series oxide films, in contrast with the far more stable n = 1 phase. In addition, their findings could be simply attributed to several possible reasons for the formation of the random distribution of the RP structure, including thermal stability, compositional fluctuation and nucleation interaction under diverse growth conditions (including post-annealing treatment) for the complex oxide films.

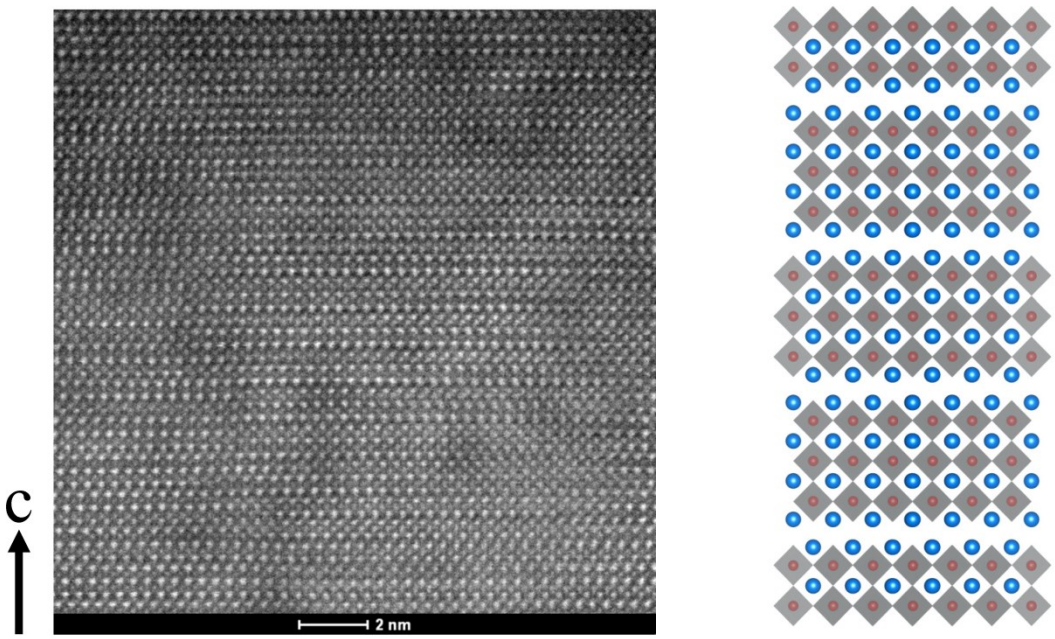


Figure 6.29 Cross-section HAADF STEM image of the as-deposited $La_4Ni_3O_{10-\delta}$ film epitaxially grown on NGO (110) substrate, showing that the c-axis oriented film was observed. A schematic cartoon represents the motif of the observed image. The solid blue circles correspond to lanthanum atoms; the octahedra with solid red circles inside correspond to NiO_6 blocks.

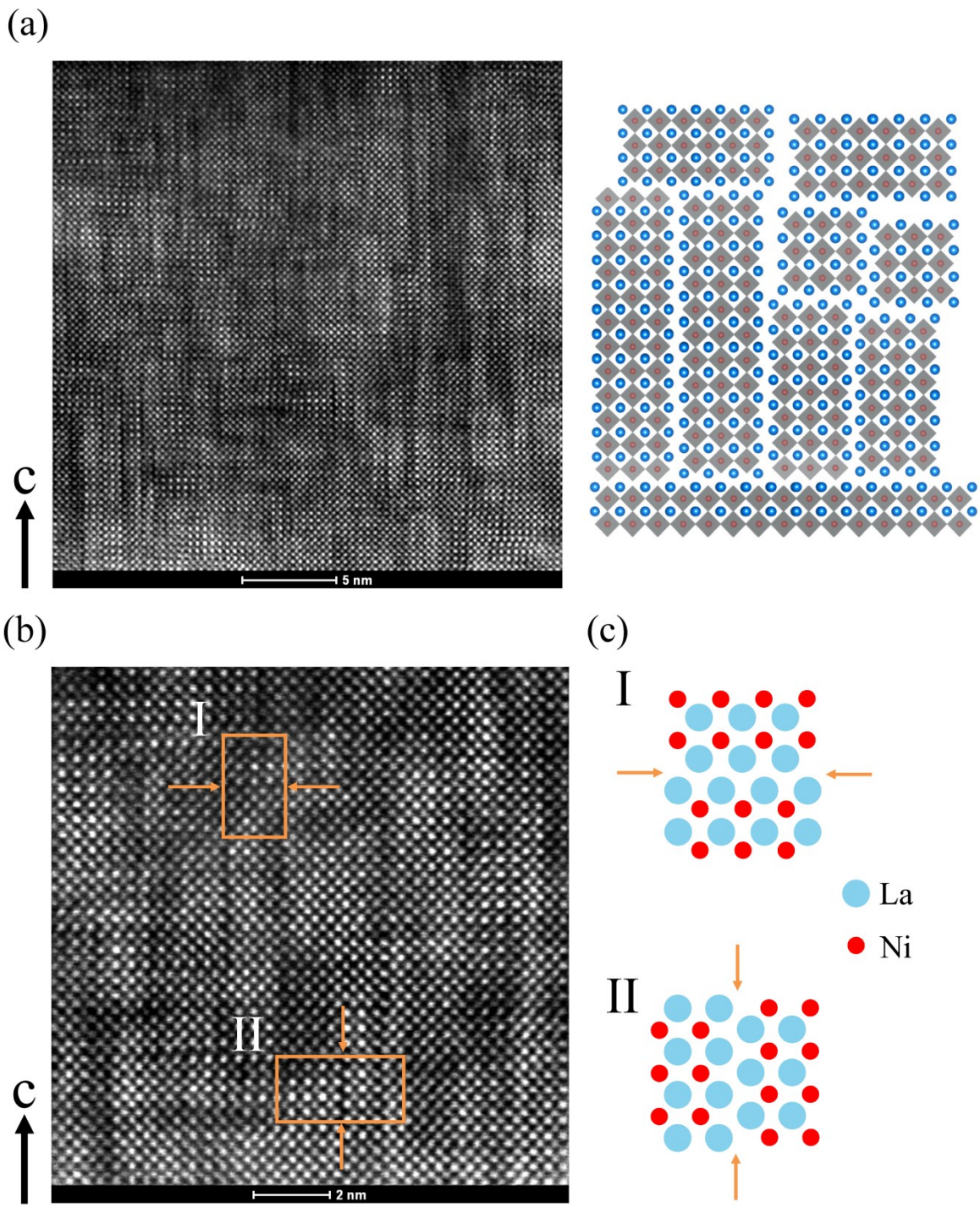


Figure 6.30 Cross-section HAADF STEM image of the post-annealed $La_4Ni_3O_{10-\delta}$ film epitaxially grown on NGO (110) substrate. (a) low-magnification image presents two dimensional planar defects lying perpendicular and parallel to the growth direction (c-axis). A cartoon also schematically represents the motif of the observed image. (b) high-magnification image clearly shows the crystal blocks are randomly distributed in square and rectangular fashion and coherently interleaved with LaO layer along the direction perpendicular and parallel to the growth direction, indexed by region I and II respectively. The two atomic arrangements are schematically exhibited in (c). The arrows correspond to the positions of LaO (rock-salt) layers.

In our case, the observation of the microstructural variation in this section confirmed that the instability can be enhanced when the films were treated with a post-annealing process. Together with the findings in the last sections, the difficulties of obtaining pure phase and defect-free members of each of the RP-type $La_{n+1}Ni_nO_{3n+1}$ (n = 1, 2 and 3) phases are rather in accord with their thermodynamic properties – the enthalpy of formation and stability and of the La-Ni-O family for ceramic bulk: La_2NiO_4 > $La_3Ni_2O_7$ > $La_4Ni_3O_{10}$ phases. [72, 73, 78] Additionally, the instability can be further enhanced when any small fluctuation of the La/Ni composition during deposition occurs (for example, target degradation with time during PLA), and growth conditions are not well-manipulated. These factors can consequently lead to the formation of various defects in the stacking sequence and intergrowths within the matrix.

6.4 Thermal Stability

As described in the previous section, a major impact on the film microstructure has been observed after a post-annealing treatment during the deposition process. These $La_3Ni_2O_{7-\delta}$ and $La_4Ni_3O_{10-\delta}$ materials would be applied as a cathode in electrochemical SOFC devices, underwent to a cycling process, and operated at an oxidising atmosphere for a long period of time. Therefore, in this section, it is also interesting to examine the thermal stability of these $La_3Ni_2O_{7-\delta}$ and $La_4Ni_3O_{10-\delta}$ films after 4-point DC cycling electrical measurements and aging experiments.

The $La_3Ni_2O_{7-\delta}$ and $La_4Ni_3O_{10-\delta}$ films deposited on NGO substrates were treated with 3 thermal cycles from RT to 700°C in air over a period of one month, including an aging treatment at 700°C in air for over 2 weeks (approximately 350 h in total). The cycling electrical and aging effects were characterised through performing XRD

measurements before and after the experiments, as can be seen in **Figure 6.31 (a)** and **(b)** as examples for the $La_3Ni_2O_{7-\delta}$ and $La_4Ni_3O_{10-\delta}$ phases, respectively. After the experiments, a slight broadening and loss of intensity of (00L) reflections for both phases was observed. In general, no major structural variation and only a few Ag peaks were detected after these treatments. The Ag peaks originate from the Ag electrode contacts for the electrical measurements. Of course, there might be a certain amount of defects formed after these treatments, which might be undetectable by XRD measurements. As noted in Ch.6.3.1.5, the HRTEM image was characterised after a 4-point DC cycling electrical measurement, showing the RP column ordering still aligned along (00L) orientation, in contrast with the random ordering of RP columns observed in the previous section (Ch.6.3.2), as well as the existence of various planar defects within the matrix after electrical measurements. Unfortunately, there is not enough evidence assigning whether these defects were formed before or after the electrical measurements. Further investigations by HRTEM analysis will be needed in the future, but will not be covered in this thesis.

Therefore, according to the previous characterisation and the XRD results shown in **Figure 6.31**, it is speculated that the atomic arrangement of the obtained films would not have changed significantly once the film growth was completed although a small concentration of defects might be formed after operating from RT to 700°C. This indicates good thermal stability for the $La_3Ni_2O_{7-\delta}$ and $La_4Ni_3O_{10-\delta}$ films as operated below 700°C, which further confirmed that the two materials are stable at lower operation temperature and could be suitable for use in IT-SOFC devices (500-700°C). The results are consistent with a previous study [33] reported by Amow *et al.* for bulk $La_3Ni_2O_{6.95}$ and $La_4Ni_3O_{9.78}$, showing no deterioration to an impurity were detected at 900°C for 2 weeks in air.

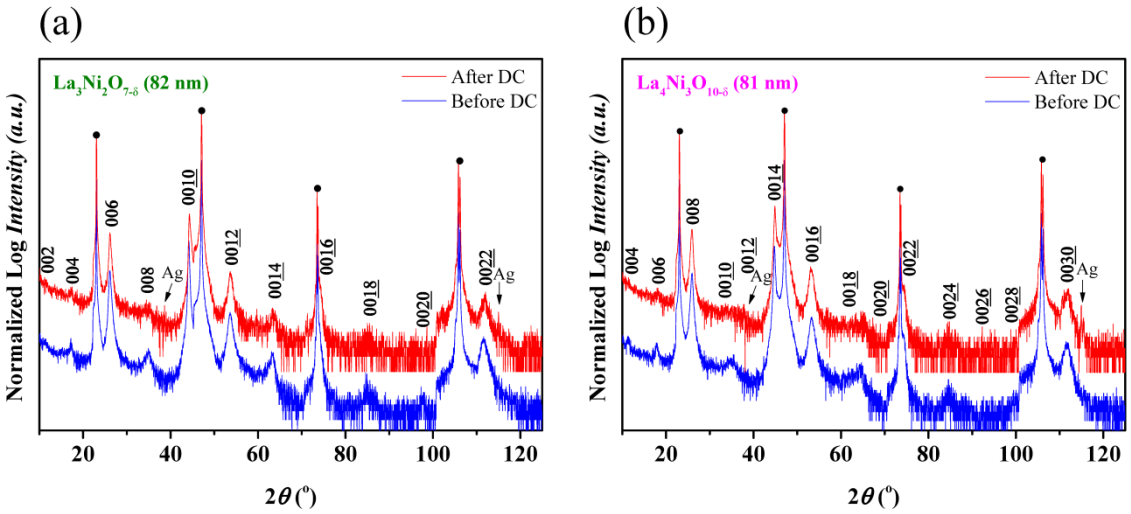


Figure 6.31 comparative XRD patterns of a (a) 82nm-thick $La_3Ni_2O_{7-\delta}$ and (b) 81nm-thick $La_4Ni_3O_{10-\delta}$ film deposited on NGO substrate before and after a 4-point DC cycling electrical measurement from RT to 700°C in air for a month, including an aging treatments at 700°C in air for over 2 weeks (approximately 350 h in total). The Ag peaks originate from the electrode contacts for the electrical measurements.

6.5 Summary

To date there are no reports in the literature with respect to the deposition of the higher order RP-phase lanthanum nickelate films (n = 2 and 3) by PLD. In this chapter, by using the rather low-density targets (50% of theoretical density), successful growth of c-axis oriented layered RP-type $La_3Ni_2O_{7-\delta}$ (n = 2) and $La_4Ni_3O_{10-\delta}$ (n = 3) epitaxial films deposited on NGO (110) substrates with superior crystallinity and low surface roughness values (less than 1 nm) have been confirmed through a series of systematic structure (θ/2θ, rocking curves, and φ-scans) and morphological characterisation. The observation of HRTEM analysis has demonstrated that dense and continuous films were obtained, which was one of crucial goals for the project.

More detailed investigations into the influences on the microstructure variation of $La_3Ni_2O_{7-\delta}$ and $La_4Ni_3O_{10-\delta}$ films through the effects of film thickness and post-annealing have also been discussed. In the investigation into the effect of film thickness, through a

series of crystallographic, lattice strain, compositional, morphological and microstructural characterisations, the obtained $La_3Ni_2O_{7-\delta}$ present fairly well-defined pure-phase films with increasing film thickness while the obtained $La_4Ni_3O_{10-\delta}$ films appear to be a mixture of different phase intergrowths as film thickness increases. In addition, the findings reveal the possibility of accumulating higher level of intergrowths, misalignments and defects with increasing film thickness, particularly since the PLD targets likely have degradation and phase transition behaviours during a relatively high-temperature PLA process (as mentioned in Chapter 4.1.2). Thus, the issue has a marked impact for the thicker films in particular. A critical thickness of ~50 nm was also found for growing both $La_3Ni_2O_{7-\delta}$ and $La_4Ni_3O_{10-\delta}$ epitaxial films under the optimised growth conditions by PLD. On the other hand, a considerable impact upon the effect of post-annealing has been observed, showing a random distribution of LaO layers along the direction perpendicular and parallel to the growth direction within the film matrix. The phenomenon could be enhanced as a high oxygen partial pressure was applied for the treatment.

The thermal stability of the $La_3Ni_2O_{7-\delta}$ and $La_4Ni_3O_{10-\delta}$ films has been examined after 4-point DC cycling electrical measurements and aging experiments through XRD analysis. The results indicates that the $La_3Ni_2O_{7-\delta}$ and $La_4Ni_3O_{10-\delta}$ are stable under operating with 3 cycles from RT to 700°C in air for a month totally, including aging treatments at 700°C in air for over 2 weeks (approximately 350 h in total), and suggests that both materials could be suitable for the use of IT-SOFC devices (500-700°C).

After the series of detailed characterisation for the $La_3Ni_2O_{7-\delta}$ and $La_4Ni_3O_{10-\delta}$ films, the next chapter will focus on their transport properties with regard to electrical and ionic conductivity through Van der Pauw measurements and oxygen isotope exchange analysis, respectively.

Chapter 7 Transport Property of $La_{n+1}Ni_nO_{3n+1}$ (n = 2 and 3)

Like $La_2NiO_{4+\delta}$ (n = 1), higher order RP $La_3Ni_2O_{7-\delta}$ (n = 2) and $La_4Ni_3O_{10-\delta}$ (n = 3) phases are ideally expected to naturally have anisotropic transport properties (electronic and ionic) because of their layered structures although there is still an absence of experimental information about anisotropically electronic and ionic conductions of the higher order phases so far. More importantly, the electronic conductivity of the higher order RP phases should provide better performance than $La_2NiO_{4+\delta}$ due to the larger number of perovskite layers, which naturally offer more conduction pathways and may lead to an enhanced electrical conductivity [47, 51].

In the previous chapter, it was demonstrated that the $La_3Ni_2O_{7-\delta}$ and $La_4Ni_3O_{10-\delta}$ films were successfully grown epitaxially along the c-axis perpendicular to the surface of an insulating NGO substrate. Their electrical and ionic conductivity, in principle, can be characterised anisotropically, and likely further lead to a significant enhancement in comparison with bulk materials. Moreover, a series of detailed investigations into the influence on the film microstructure through the effects of film thickness and post-annealing have also been discussed. Particularly, microstructural observation reveals the presence of a considerable proportion of intergrowths and stacking faults within the films. These imperfections may have a remarkable impact on the transport properties of the films.

In this chapter, the electrical properties of the $La_3Ni_2O_{7-\delta}$ and $La_4Ni_3O_{10-\delta}$ films will be investigated in section 7.1 through the 4-point DC van der Pauw method; the oxygen transport properties of these materials will be demonstrated in section 7.2 via oxygen isotope exchange analysis. With such measurements, the electrical and ionic transport

properties of these materials will be examined and compared with literature data.

7.1 Electrical Conductivity Analysis

The planar electrical conductivity of the obtained c-axis oriented $La_3Ni_2O_{7-\delta}$ and $La_4Ni_3O_{10-\delta}$ epitaxial films deposited on NGO substrate will be systematically investigated through a series of 4-point DC van der Pauw experiments. These investigations, involving the influence of film thickness and cycling measurement, followed by comparative studies of the electrical property data with literature will be performed in the following sub-sections. Before the investigation, again, it must be noted that the conductivity of NGO substrates have conductivity of approximately 10^{-6} Scm^{-1} at 700°C [40], which is over seven orders of magnitude lower than that of $La_3Ni_2O_{7-\delta}$ and $La_4Ni_3O_{10-\delta}$ compounds. Due to the low conductivity values, the contribution of the substrate (0.5 mm thick) on conductance is anticipated to be negligible during the measurements.

7.1.1 Influence of Film Thickness

The temperature dependence of the total electrical conductivity of $La_3Ni_2O_{7-\delta}$ films of different thickness (47, 82 and 110 nm) deposited on NGO is performed from 100 to 700°C under static air atmosphere, as demonstrated in **Figure 7.1 (a)**. These films possess total electrical conductivity values in the range of approximately 300-1100 Scm^{-1} over the whole measured temperature region. As measured temperature increases, their conductivity exhibits a drastic increase at around 200-300°C when the elevated temperature approaches transition temperature point in conductivity. At this point clear semiconducting-to-metallic transition behaviour can be seen for all the measured samples,

which is consistent with the observation for $La_3Ni_2O_{7-\delta}$ polycrystalline materials in earlier literature. [31-33, 49] Such behaviour has been proposed to be primarily due to Mott-Hubbard-type electron localisation at the low-temperature region [31, 49, 225, 226], generally below approximately 280°C, which is reasonably in agreement with our observations. The transition points for the 47nm-, 82nm- and 110nm-thick films can be identified with conductivity maxima of 855, 1123 and 1072 Scm^{-1} at approximately 362, 458 and 410°C respectively, which are much higher than the values of bulk materials (~60 Scm^{-1}) [33, 49, 104]. The values of transition temperatures are rather related to the phase transition from orthorhombic to tetragonal through structural analysis [32, 33, 225], and the weight change via thermogravimetric analysis [33, 51] found in previous studies in polycrystalline materials. There is a slight difference between the transition temperature points of polycrystalline and film materials. Such difference could be attributed to several possibilities such as the influence of oxygen content, cation (La/Ni) composition, and lattice strain derived from the microstructural variation within the films. These possibilities will be discussed further in the following content.

Above the transition temperatures, the conductivity values start to gradually decrease because of the depletion of oxygen content from the lattice of the films, resulting in a reduction of the Ni^{3+} content and therefore a decrease in the concentration of hole charge carriers [49]. Thus, the level of oxygen content of the films may be considered to be crucial for their electrical conductivity behaviour, which might be associated with the wide range of oxygen stoichiometry (7.00 ~ 6.35), reported in the polycrystalline $La_3Ni_2O_{7-\delta}$ [49-51] Unfortunately, as mentioned previously, determining the oxygen content is challenging in thin-film materials. Therefore, the contribution of oxygen content cannot be assigned to the electrical conductivity of the films.

It is of interest that the 82nm-thick $La_3Ni_2O_{7-\delta}$ film displays a slightly higher average

electrical conductivity than the other two films. As remembered in **Figure 6.22 (b)** of Chapter 6.3.1.2, the 82nm-thick $La_3Ni_2O_{7-\delta}$ film shows an abnormally high in-plane strain compared to the other films, which is probably a result of the adoption of the high-surface-roughness substrate (from Batch B, as described in the **Table 4.3** of Chapter 4.2). It could therefore be inferred that in-plane strain could play another key role in the influence of planar electrical conductivity behaviour for such layered structure films.

Additionally, compared to the other two samples, a careful inspection at the transition temperature point reveals an apparent shift to a higher temperature (458°C). The temperature coincides with the observed transition temperature of 450-500°C for $La_2NiO_{4+\delta}$ films (seen in Chapter 5.3). This might suggest the possibility of accumulating a certain proportion of $La_2NiO_{4+\delta}$ intergrowths within the 82nm-thick film. Therefore, it could be speculated that the abnormal trend of the 82nm-thick sample may be attributed to somewhat microstructural differences in comparison with the other two samples. Furthermore, the effect of microstructural variation may be also associated with the cation (La/Ni) compositional variation, and lead to the electrical conductivity variation of these films. Such effect corresponds to the findings observed in non-stoichiometric $La_{2-x}NiO_{4-\delta}$ and $Nd_{2-x}NiO_{4-\delta}$ polycrystalline systems [95, 203], showing that the electrical conductivity values changed with the cation (La/Ni) stoichiometry. As known from the results presented in the previous chapter, the phenomena of microstructural and cation (La/Ni) compositional variations could significantly occur particularly when film thickness increases since the PLD targets likely have degradation and phase transition behaviour during a relatively high-temperature PLA process (as mentioned in Chapter 4.1.2). Consequently, these influences of microstructural variation on the electrical conductivity could become considerable.

In general, apart from the curve of the 82nm-thick sample, the other two $La_3Ni_2O_{7-\delta}$

samples (47nm- and 110nm-thick films) present similar shaped curves for the electrical conductivity, and the trend generally increases with increasing film thickness.

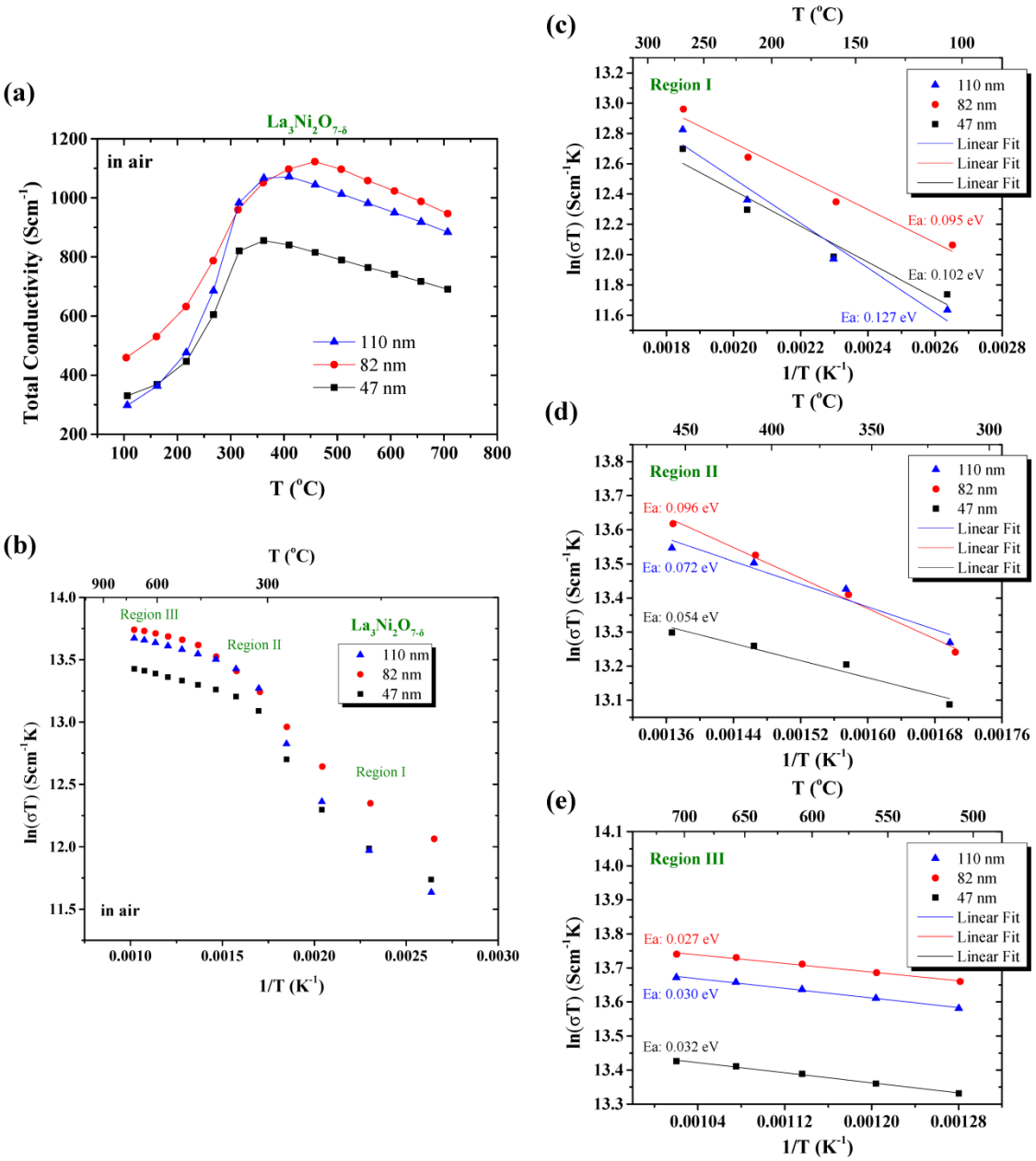


Figure 7.1 Total electrical conductivity of the c-axis oriented $La_3Ni_2O_{7-\delta}$ epitaxial films with various thicknesses of 47, 82 and 110 nm deposited on NGO substrates as a function of temperature from RT to 700°C in air (a), Arrhenius plot of the electrical conductivity showing that the curves can be assigned to three region I, II and III (b), and fit of the curves at (c) region I (100-300°C), (d) II (300-500°C) and (e) III (500-700°C) are presented with calculated activation energy (E_a) values.

Since $La_3Ni_2O_{7-\delta}$ and $La_4Ni_3O_{10-\delta}$ phases are predominantly oxygen-deficient compounds, oxygen vacancies and electron holes are dominant in these materials. Concerning the predominantly p-type electronic conduction for both phases [71, 227, 228], their electrical behaviour could be attributed to the mixed valence state of Ni (Ni^{2+}/Ni^{3+}), vacancy migration and oxygen ion diffusivity, leading to a strong interaction presumably involving the occurrence of considerable deformation of the surrounding structure.

Using the Arrehinus equation (eq. 5.1) as described in Chapter 5.3, the Arrhenius diagram for $La_3Ni_2O_{7-\delta}$ is plotted with $\ln(\sigma T)$ vs reciprocal temperature (1/T) in **Figure 7.1 (b)**. The diagram exhibits a partially non-linear relationship of temperature dependence over the entire temperature range. To address the data in a more tractable way, the total conductivity can be defined as three different regions as a function of temperature: low-temperature area (Region I, ~100-300°C), transition area (Region II, ~300-500°C) and high-temperature area (Region III, ~500-700°C). At Region I and II, the curves still present non-linearity, resulting in the difficulty to appropriately fit with a linear function (as can be seen in **Figure 7.1 (c)** and **(d)**). However, at Region III, a series of clear linear fits can be observed in **Figure 7.1 (e)**. Comparative activation energy (E_a) values for the 47nm-, 82nm- and 110nm-thick films were estimated at each region (I, II and III) and can be observed in **Figure 7.1 (c), (d)** and **(e)** respectively.

Based on the measured data at Region I and II (**Figure 7.1 (c)** and **(d)**), more precise measurements with respect to systematic measurements of oxygen pressure dependence with smaller heating/cooling step size are experimentally required in order to obtain meaningful activation energy values. Also, a more appropriate model is needed for theoretical studies of the transport mechanism either above room temperature or at even higher temperatures based on defect chemistry theory, in particular, involving the

localisation and delocalisation of charge carriers, migration of oxygen vacancies and diffusion of oxygen ions [229, 230] for such complex oxide materials. More importantly, compared to polycrystalline materials epitaxial film-type materials may bring extra factors such as strain [36, 40, 113, 231], orientation [36, 84, 232] and incorporated defect [233-235] effects for consideration [36, 84, 232]. These detailed studies are imperative for further investigation in the future in order to understand the transport properties of such complex oxide films and improve their electrical performance for application. Here. the main purpose is only focused on the basic investigation into the temperature dependence of the total electrical properties for the $La_3Ni_2O_{7-\delta}$ and $La_4Ni_3O_{10-\delta}$ films with different thickness.

On the other hand, the same analysis was also applied to $La_4Ni_3O_{10-\delta}$ films of different thickness. The temperature dependence of the total electrical conductivity for $La_4Ni_3O_{10-\delta}$ films of different thickness (51, 82 and 166 nm) deposited on NGO was performed from approximately RT to 700°C under static air atmosphere. In the measured temperature region, these films present the total electrical conductivity approximately ranging from 800 to 1600 Scm^{-1}, as expected, which is much higher than that of the obtained $La_2NiO_{4+\delta}$ and $La_3Ni_2O_{7-\delta}$ films, as seen in **Figure 7.2 (a)**. It is of interest to observe that the electrical behaviour exhibited an evolution of electrical conductivity with increasing film thickness, which is completely different from the phenomenon observed above in the case of $La_3Ni_2O_{7-\delta}$ films.

The 51nm-thick $La_4Ni_3O_{10-\delta}$ film exhibits a metallic behaviour whose electrical conductivity monotonically decreases with increasing temperature. A metallic-to-metallic transition was observed with an anomaly around 250-300°C, which is consistent with the previous thermogravimetric data, showing a weight change around this temperature, found in polycrystalline $La_4Ni_3O_{10-\delta}$ bulk material [33, 47]. Similar conductivity

behaviour was also observed in previous literature for polycrystalline samples [31, 33, 49] and intermixed nanostructured epitaxial films (n = 2, 3 and 4 domains) deposited by the PI-MOCVD technique [91]. In terms of the comparative studies, these will be further discussed in Ch.7.1.3.

As film thickness increased to 82 nm, a significant change of the electrical conductivity behaviour was observed, showing a steep plateau with a clear semiconducting-to-metallic behaviour. It is of interest that the electrical conductivity of the film remained steady around 300-400°C, presenting an independence of temperature and indicating that the concentration of charge carriers becomes constant at this range of temperature. The phenomenon might imply that the contributions of electron holes, oxygen vacancies, oxygen ions and defects within the film was compensated and reached a balance over this range of temperature.

For the thickest film (166 nm), a more drastic curve was observed, presenting a remarkably steeper and much sharper step than the 82nm-thick film. There was no steady phenomenon observed. It could be speculated that both 82nm- and 166nm-thick films appear to exhibit apparently $La_3Ni_2O_{7-\delta}$-like behaviour of electrical conductivity, which may imply the presence of intergrowths of $La_3Ni_2O_{7-\delta}$ and even other phases when film thickness increased. The phenomena essentially correspond to the findings observed in a previous Chapter 6.3.1 through a series of crystallographic, compositional, surface morphological and microstructural analyses. Hence, the results of electrical conductivity with different thickness further confirmed that the obtained $La_4Ni_3O_{10-\delta}$ films presumably have the possibility of accumulating higher level of intergrowths, misalignments and defects with increasing film thickness. Again, this may be as a result of the degradation and phase transition issues of PLD targets during PLA process (as described previously).

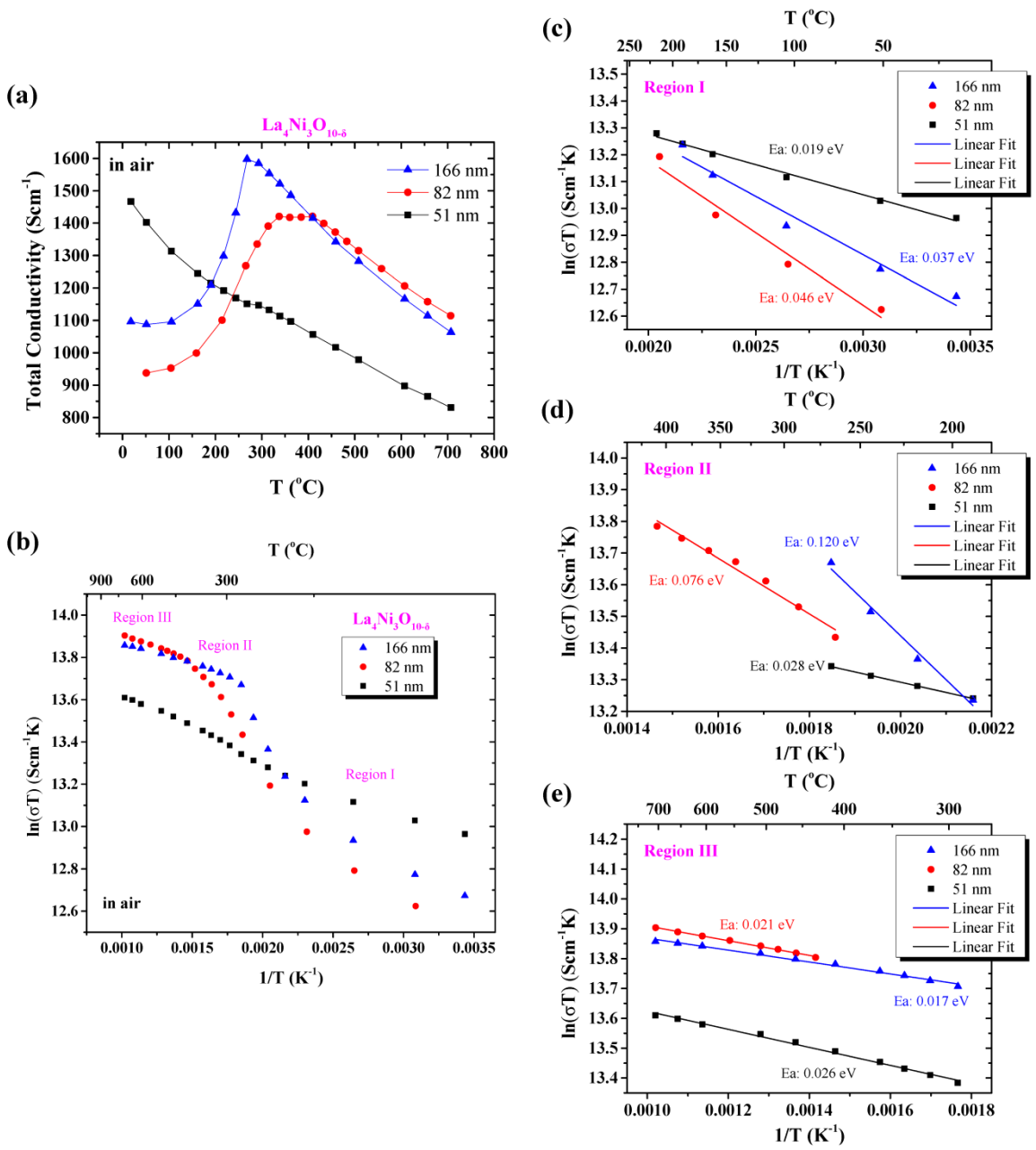


Figure 7.2 Total electrical conductivity of the c-axis oriented $La_4Ni_3O_{10-\delta}$ epitaxial films with various thicknesses of 51, 82 and 166 nm deposited on NGO substrates as a function of temperature from RT to 700°C in air (a), Arrhenius plot of the electrical conductivity showing that the curves can be assigned to three region I, II and III (b), and fit of the curves at (c) region I (RT-250°C), (d) II (200-400°C) and (e) III (300-700°C) are presented with calculated activation energy (E_a) values.

The Arrhenius diagram for $La_4Ni_3O_{10-\delta}$ plotted with ln(σT) vs reciprocal temperature (1/T) is shown in **Figure 7.2 (b)**. In the diagram, except for the entire curve of the 51nm-thick film, the remaining films present a partially non-linear relationship of temperature dependence as observed with the data obtained from $La_3Ni_2O_{7-\delta}$ described above. Therefore, three different regions in terms of low-temperature area (Region I), transition area (Region II) and high-temperature area (Region III) were also considered to address the analysis. As with the treatment for the $La_3Ni_2O_{7-\delta}$ data above, the comparative activation energy (E_a) values for the 51nm-, 82nm- and 166nm-thick $La_4Ni_3O_{10-\delta}$ films were also estimated at each region (I, II and III), as seen in **Figure 7.2 (c), (d)** and **(e)** respectively.

Overall, the observations of electrical conductivity as a function of film thickness for the obtained $La_3Ni_2O_{7-\delta}$ and $La_4Ni_3O_{10-\delta}$ films exhibit good agreement with the results shown in the earlier Chapter 6.3.1 through a series of crystallographic, lattice strain, compositional, surface morphologic and microstructural characterisation. Together with these demonstrated results from the previous chapter, these findings of electrical conductivity behaviour firmly confirmed that the microstructural variation such as different phase intergrowths, misalignments and defects, are likely to be a remarkable influence on the electrical properties of the films since these disordered structures or discontinuous arrangements (for example, as previously seen in **Figure 6.27**) could block and trap the charge carriers along the migration path. Also, the cation (La/Ni) compositional deviation driven from the degradation of PLD targets may have a huge impact on the variation of oxygen content, average Ni oxidation state (Ni^{3+}/Ni^{2+} proportion), and consequently electrical properties for the obtained $La_3Ni_2O_{7-\delta}$ and $La_4Ni_3O_{10-\delta}$ films. Similar findings were observed in layered RP-type $La_2NiO_{4+\delta}$ [233] and other layered systems such as $La_{1.2}Sr_{1.8}Mn_2O_7$ [235, 236] and double-perovskite-type

$GdBaCo_2O_{5+\delta}$ epitaxial films. [233, 234]

7.1.2 Cycling Measurement

A series of heating-cooling cycle measurements of electrical conductivity were conducted on the $La_3Ni_2O_{7-\delta}$ and $La_4Ni_3O_{10-\delta}$ samples of different thickness deposited on NGO substrates. In the case of $La_3Ni_2O_{7-\delta}$, the 47nm- and 110nm-thick films were characterised by two cycling measurements from RT to 700°C under static air over a period of over two weeks (**Figure 7.3 (a)** and **(b)**), whilst the 82nm-thick film was treated with three cycles including an aging treatment at 700°C in air for over 2 weeks (approximately 350 h in total), shown in **Figure 7.3 (c)**.

During the first heating cycle shown in **Figure 7.3 (a)**, **(b)** and **(c)**, slightly low but strongly thermal activated conductivity behaviour was presented. These first heating curves exhibit abnormal behaviour in comparison with the subsequent cycles. This unusual phenomenon might be due to poor contact between silver (Ag) electrodes and the thin films, the connectivity of the Ag/Pt(platinum) wires to measured equipment, or the inhomogeneity of Ag contact on the films at the beginning of the measurements. Similar phenomenon on first heating was also observed in polycrystalline $LaNiO_{3-\delta}$ and $La_4Ni_3O_{10-\delta}$ films deposited by spray pyrolysis [90], and bulk $La_3Ni_2O_{7-\delta}$ and $La_4Ni_3O_{10-\delta}$ ceramics [49]. After the first heating treatment, these Ag contacts and wires became well-connected and homogeneous, as can be seen from the reversibly electrical conductivity cycles in the figures. Thus, the first curves can be disregarded in the following discussions.

In **Figure 7.3 (a)** and **(b)**, the sequence of cycles of 47nm- and 110nm-thick $La_3Ni_2O_{7-\delta}$ samples show clearly reversible semiconducting-to-metallic behaviour with a drastically steep rise at around 200-300°C when the elevated temperature approaches the

phase transition temperature. Additionally, hysteresis behaviour was observed during the transition area (~300-350°C), where the movement of oxygen could start taking place due to the phase transition of $La_3Ni_2O_{7-\delta}$ from orthorhombic to tetragonal structure [32, 33, 225]. It is believed that as temperature increased, the loss of oxygen gradually increased, and may occur dramatically at high temperature (> 550°C). The behaviour of the oxygen gain/loss is reversible, as evidenced by the cycling results of electrical conductivity.

A careful inspection of both **Figure 7.3 (a)** and **(b)** reveals that at the low temperature region (RT-300°C), fairly reversible behaviour was observed. In contrast, up to high temperature region (~550-700°C), the sequence of cycles did not coincide with one another and even shows that the average conductivity gradually decreases for the thinnest film (47 nm), and slightly increases for the thickest film (110 nm) after every heating cycle. The increase in conductivity was also observed in the 82nm-thick film (**Figure 7.3 (c)**) which will be discussed in detail later. Hence, such conductivity variation could be speculated to be related to several possibilities, including the drastic variation of oxygen content of the films taking place at high temperature, and the contributions of lattice variation, and microstructural defects. That is to say, for the thinnest film (47 nm), the drastic loss of oxygen content at high temperature potentially leads to an increase in the rotation and tilt of the NiO_6 octahedra, the bending of Ni-O-Ni bonds, the distortion of perovskite blocks, the discontinuity of hole carrier pathways, and consequently the trapping of the carriers and a decrease in conductivity, as can be seen in **Figure 7.3 (a)**. On the contrary, for thicker films (82 and 110 nm), as discussed in a previous chapter, the thicker the film, the more the microstructural disorder or defects within the films may be accumulated. These defects could cause a high strain (seen in Ch.6.3.1), but would be relaxed via the high temperature treatments, which might lead to a slight increase in the conductivity, as observed in **Figure 7.3 (b)** and **(c)**. Additionally, it has to be noted that

the measurements were executed under air atmosphere, where the electrical conductivity could be influenced dramatically, particularly at high temperature. Similar cycling phenomena were found in polycrystalline $La_3Ni_2O_{7-\delta}$ ceramics, reported by Kobayashi *et al.* [49].

The 82 nm-thick $La_3Ni_2O_{7-\delta}$ sample seen in **Figure 7.3 (c)** exhibits a larger fluctuation (i.e. irreversibility) for the sequence of cycles than the 47nm- and 110 nm-thick samples. As remembered previously, the 82 nm-thick film was deposited on a higher surface-roughness substrate than the other two samples, suggesting the presence of a certain microstructural difference, and probably leading to less coherent lattice structure of the film than the other two films. At the high temperature region, the sequence of cycles of the 82 nm-thick film also present a gradual increasing trend in the electrical conductivity after every heating cycle, similar to the observation in the case of the 110 nm-thick film (**Figure 7.3 (b)**), as already discussed in the previous paragraph. More interestingly, as seen in the heating-cooling cycle 3, an aging treatment was carried out at 700°C in air for over 2 weeks after the third cycle (Heating 3). During the treatment, it is clear to observe that the conductivity values increased with aging time for a period of ~7 days and decreased afterwards, followed by a different track in Cooling 3. The proposed possibilities to explain such abnormal electrical behaviour are discussed in the following paragraph.

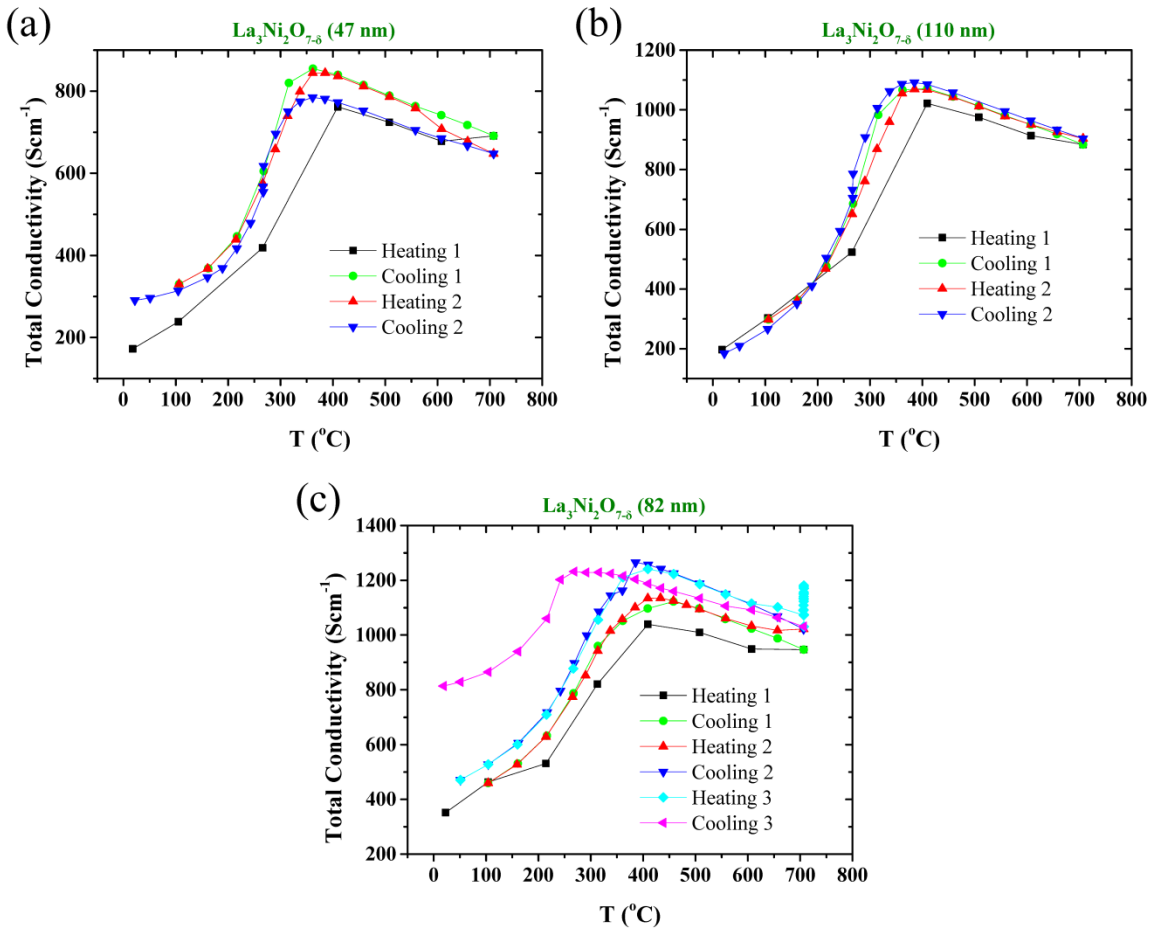


Figure 7.3 Total electrical conductivity of the c-axis oriented $La_3Ni_2O_{7-\delta}$ epitaxial films with various thicknesses of 47 nm (a), 110 nm (b) under two heating-cooling cycle measurements, and 82 nm (c) under three cycling measurements are shown as a function of temperature from RT to 700°C in air. Note that in (c), an aging treatment at 700°C in air for over two weeks (approximately 350 h in total) was carried out between Heating 3 and Cooling 3.

Firstly, considering the previous literature [237, 238], Ag naturally possesses high mobility at high temperature (> 500°C). In terms of our case, at the beginning of the aging treatment, the high-temperature aging process (700°C) can give rise to a very high mobility for the Ag atoms of the electrode contacts. Then, the aging process may give the highly mobile Ag atoms enough time to diffuse into grain boundaries of the films, consequently resulting in a significant influence on the electrical conductivity; that is, an increasing conductivity at the beginning of the aging process (seen in the Heating 3 curve in **Figure 7.3 (c)**). Furthermore, a reorientation or rearrangement behaviour of the

RP-structure columns could occur after aging the sample for a period of ~7 days at the same temperature. Therefore, a phenomenon of decreasing conductivity was observed. The scenario to be considered is based on the findings regarding the occurrence of reorientation of as-deposited films after post-annealing observed in Ch.6.3.2. After the aging process, a different conductivity track was presented in Cooling 3. According to the XRD result of the 82 nm-thick sample shown in Ch.6.4, it revealed that no major structure variation was found. Despite this, considering the detection limit of the XRD technique, we have to leave the question open of whether there is the formation of any reorientation after the conductivity measurement. Further investigations by HRTEM analysis will be needed in the future, but will not be covered in this thesis. Overall, although the electrical conductivity of the 82 nm-thick film was changed after the aging treatment due to several possible influences, its semiconducting-to-metallic behaviour was still retained, suggesting good stability of the film.

On the other hand, the same cycling measurements were also executed for $La_4Ni_3O_{10-\delta}$ films of different thickness (the 51 nm, 82 nm and 110 nm). In all **Figure 7.4 (a)**, **(b)** and **(c)**, abnormal first heating tracks followed by a series of similar subsequent cycles were also observed, as was the case with $La_3Ni_2O_{7-\delta}$, above. As seen in the sequence of cycles, it is apparent that the 51 nm-thick film shows a clearly reversible metallic-to-metallic behaviour (**Figure 7.4 (a)**) whilst the 82 nm- and 166 nm-thick films exhibited a semiconducting-to-metallic transition (**Figure 7.4 (b)** and **(c)**).

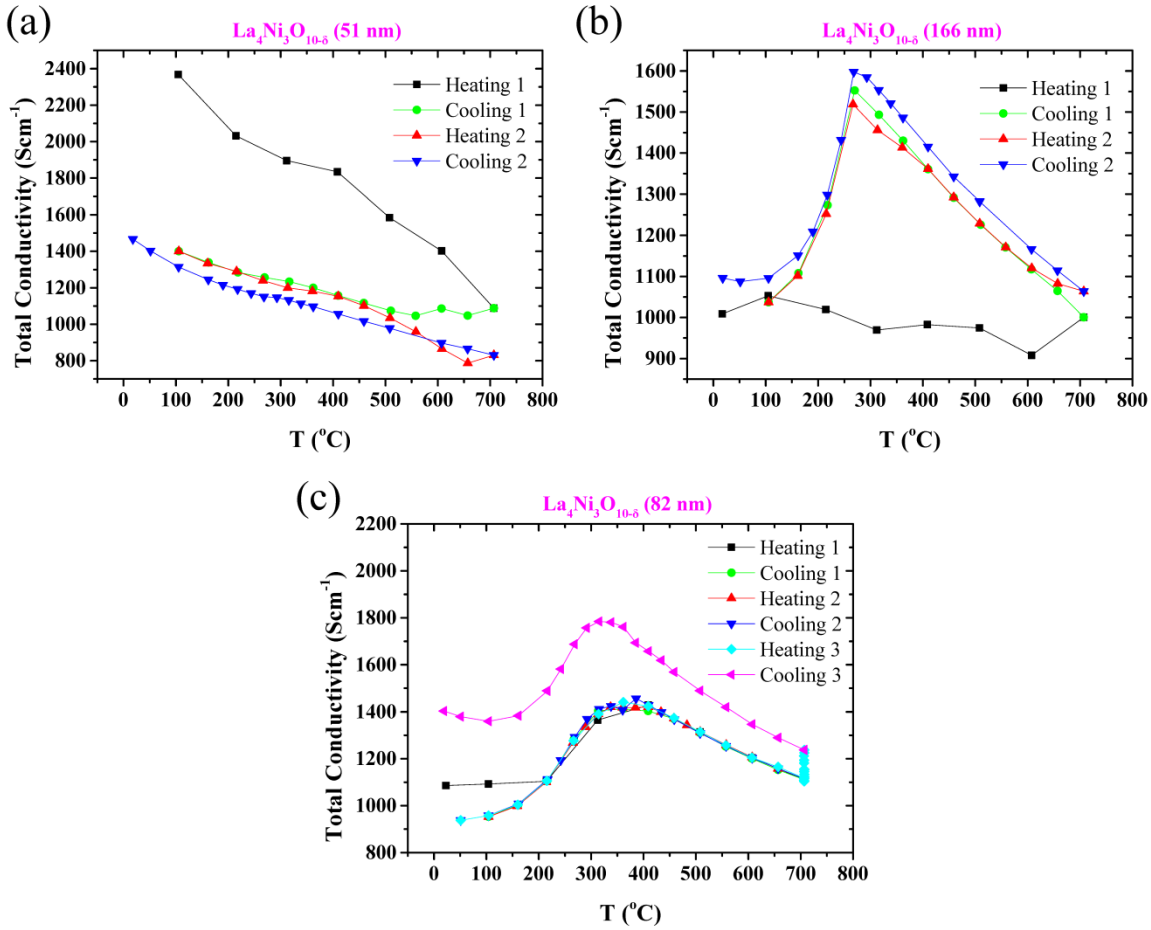


Figure 7.4 Total electrical conductivity of the c-axis oriented $La_4Ni_3O_{10-\delta}$ epitaxial films with various thicknesses of 51 nm (a), 166 nm (b) under two heating-cooling cycling measurements, and 82 nm (c) under three cycling measurements are shown as a function of temperature from RT to 700°C in air. Note that in (c), an aging treatment at 700°C in air for over two weeks (approximately 350 h in total) was carried out between Heating 3 and Cooling 3.

In the high temperature region (500-700°C), a decrease in conductivity for the 51 nm-film but an increase for the 166 nm-film after every heating cycle was also observed in **Figure 7.4 (a)** and **(b)** respectively. However, of interest is that the subsequent cycles of the 82 nm-thick film presents a rather coincident track except for the Cooling 3, in comparison with the other two films. This indicates the presence of stable electrical conductivity and a stable lattice structure of the 82 nm-thick film. In addition, the same aging treatment was also conducted for the 82 nm-thick film (seen at the Heating-Cooling 3). The result shows a continuously increasing conductivity behaviour with aging time,

but no decrease was observed during the entire treatment (over 2 weeks), followed by a higher conductivity behaviour as can be seen in the Cooling 3 data. It can be speculated that the assumption with respect to the influence of Ag contacts on the increase of conductivity at high temperature cannot be ruled out for consideration.

In general, it is clear that the findings through the series of cycling measurements exhibit reversible cycling behaviour, indicating the prominent stability of the obtained $La_3Ni_2O_{7-\delta}$ and $La_4Ni_3O_{10-\delta}$ epitaxial films, even though the actual mechanism to explain the electrical conductivity variation is still unclear. To understand the mechanism, further investigations can be suggested for the future, for example, using a stable electrode material as contacts and wires (e.g. Pt) to minimise their contributions, measuring in pure oxygen and nitrogen atmosphere to investigate the influence of oxygen content, and characterising the microstructure of these films to understand the correlations with electrical behaviour in every cycle.

7.1.3 Comparative Study

A series of comparative studies of electrical conductivity for the obtained c-axis oriented $La_{n+1}Ni_nO_{3n+1}$ (n = 1, 2 and 3) epitaxial films are systematically discussed with the previous literature data from polycrystalline bulks reported by Amow *et al.*[33], and the epitaxial films deposited via PI-MOCVD reported by Burriel *et al.* [91]. They are shown in **Figure 7.5 (a)** and **(b)**.

From **Figure 7.5 (a)**, it is clear that the shape of the conductivity data for each $La_2NiO_{4+\delta}$ (n = 1), $La_3Ni_2O_{7-\delta}$ (n = 2) and $La_4Ni_3O_{10-\delta}$ (n = 3) film appears to be in exceptional agreement with the data of the polycrystalline bulk ceramic. Since the transport properties of these c-axis oriented epitaxial films are expected to be highly anisotropic, our samples exhibit a larger conductivity along the a-b plane than the

randomly oriented polycrystalline bulk samples, as expected. In addition, the obtained films strongly exhibit a systematic enhancement of electrical conductivity when the "n" value increases although the data obtained by Amow *et al*. does not completely present the increasing trend with "n" value, which might be due to the adoption of low-density bulk samples (54-58%) [32, 33]. The results for the systematic enhancement with "n" are primarily attributed to the following reasons: an increasing number of adjacent NiO_6 octahedra of the perovskite layers responsible for the electronic transport pathways, an enhancement of the Ni-O-Ni overlap along the crystallographic c direction (i.e. an increase in the overlap between the $Ni^{2+/3+}$: 3d and O^{2-}: 2p orbitals and the bandwidth (W)), and thereby an increase in charge carrier density, leading to the observed enhanced electrical conductivity [33, 47, 51, 71, 239-242]. Moreover, as seen in the figure at 500~700°C corresponding to the intermediate temperature for IT-SOFC, the total planar electrical conductivity for the c-axis oriented $La_3Ni_2O_{7-\delta}$ and $La_4Ni_3O_{10-\delta}$ films exhibits an order of magnitude improvement over the $La_2NiO_{4+\delta}$ film, showing a promising conductivity value of approximately 700-1000 Scm^{-1}. This conductivity value is potentially suitable for application in an IT-SOFC [20, 33, 243]. Also, the relationship of transition temperature for obtained n = 1, 2 and 3 films can be apparently observed to be $La_2NiO_{4+\delta}$ (~400°C) > $La_3Ni_2O_{7-\delta}$ (~350°C) > $La_4Ni_3O_{10-\delta}$ (~300°C), which corresponds again to their thermodynamic properties (the enthalpy of formation) and stability found in ceramic bulk materials [72, 73, 78], reported by Zinkevich *et al.* and Bannikov. This finding indicates a strong structural relationship for the electrical conductivity behaviour of the RP-phase films.

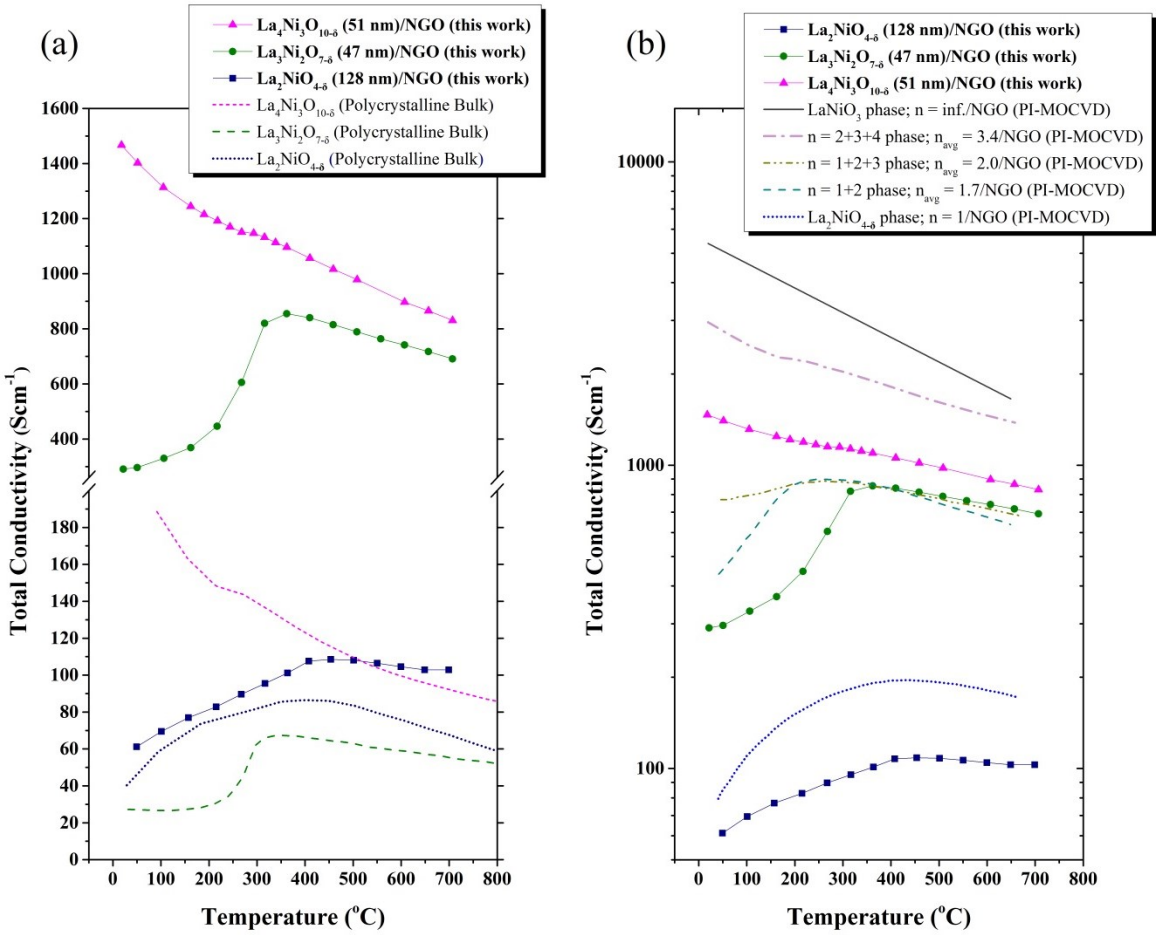


Figure 7.5 Total electrical conductivity of the c-axis oriented $La_2NiO_{4+\delta}$, $La_3Ni_2O_{7-\delta}$ and $La_4Ni_3O_{10-\delta}$ epitaxial films deposited on NGO substrates as a function of temperature in air plotted together with literature data from (a) polycrystalline bulk measured through van der Pauw method in air [33] and (b) epitaxial film of different phases deposited by PI-MOCVD characterised using AC impedance in O_2 atmosphere [91]. Note that for the literature data in (b), only $LaNiO_3$ and $La_2NiO_{4+\delta}$ are pure single phases and others are mixed, reported by the authors.

Figure 7.5 (b) shows that the planar total electrical conductivity of our films plotted together with that of the different RP phase films deposited by PI-MOCVD, reported by Burriel *et al.* [91]. A progressive variation from semiconducting to metallic character can be observed with increasing "n" value. Form the literature data, the authors found that, except for their $LaNiO_3$ and $La_2NiO_{4+\delta}$ films, others exhibited mixed-phase microstructures consisting of intricate intergrowths with different "n" values even though the correct measured cation (La/Ni) ratio was controlled. The comparative relationship

reveals that promising electrical conductivity values of our films were located inside the reasonable range, confirming these $La_2NiO_{4+\delta}$, $La_3Ni_2O_{7-\delta}$ and $La_4Ni_3O_{10-\delta}$ films obtained despite the potential presence of mixed intergrowths within the films. It is worth noting that the Burriel *et al* measurements were carried out under O_2 atmosphere whereas the current work was performed in air. Different measurement atmosphere could cause a considerable variation of electrical conductivity. In our case, there is presently not enough information to assign whether any significant difference of conductivity can be influenced by atmosphere. A further series of electrical measurements under different atmospheres (e.g. O_2 and N_2) will be needed, along with microstructural investigations via HRTEM characterisation in the future, to fully resolve these issues.

7.2 Oxygen Exchange and Transport Analysis

In addition to electrical transport properties, knowledge of the ionic transport properties for the higher order RP-typed $La_3Ni_2O_{7-\delta}$ (n = 2) and $La_4Ni_3O_{10-\delta}$ (n = 3) cathode materials is of fundamental importance for application in IT-SOFCs [30]. It is thus imperative to intrinsically investigate related ionic transport and surface exchange parameters (i.e. oxygen diffusion coefficient D^* and surface exchange coefficient k^*). To date, there is an absence of information with respect to these *intrinsic* ionic transport parameters for both $La_3Ni_2O_{7-\delta}$ and $La_4Ni_3O_{10-\delta}$ compounds. This could be attributed to the difficulty in synthesising dense, continuous polycrystalline samples via conventional ceramic processes (e.g. solid state and sol-gel methods), which are required for diffusion measurements using the IEDP technique [33, 36]. Therefore, dense and continuous $La_3Ni_2O_{7-\delta}$ and $La_4Ni_3O_{10-\delta}$ samples are required for investigation of solid state ionic diffusion.

Producing such highly dense and continuous films was one of the main goals of the project, as described previously. According to the results demonstrated in previous chapter, dense and continuous c-axis oriented $La_3Ni_2O_{7-\delta}$ and $La_4Ni_3O_{10-\delta}$ epitaxial films have been obtained by PLD and may allow investigation of the anisotropic ionic conductivity and surface exchange behaviour.

In this section, several investigations of oxygen diffusion and surface exchange coefficients (D^* and k^* respectively) will be performed through isotope exchange depth profiling with the secondary ion mass spectrometry technique (so called IEDP-SIMS method), as described in Ch.3.4.2. The samples adopted for the IEDP-SIMS measurements were grown using the optimal deposition conditions, as described in a previous chapter, and their structure, composition, and morphology have already been confirmed.

In an earlier study, Burriel *et al.* [41] pioneered an effective approach to extract both oxygen diffusion and surface exchange data along a,b-plane and c-axis directions from c-axis oriented $La_2NiO_{4+\delta}$ epitaxial films deposited on STO and NGO substrates, which has been discussed previously in Ch.2.4. For the data reported in this thesis, due to the limitations of the technique for measuring slow diffusion profiles in the in-plane direction, the $La_3Ni_2O_{7-\delta}$ and $La_4Ni_3O_{10-\delta}$ samples deposited on NGO were only measured along c-axis (out-of-plane direction); that is, only c-axis oxygen diffusion and surface exchange coefficients were obtained. Note that the IEDP and SIMS measurements in this thesis were conducted by Dr. M. Burriel in the Department of Materials in Imperial College London while I was directly involved in the data processing interpretation and discussion.

Before investigating the obtained IEDP-SIMS data, the basic concepts of the data processing have to be understood. As previously explained, the secondary ions depth profile was obtained from the samples via ToF-SIMS. For each depth point the ^{18}O

isotope concentration ratio was directly calculated from the intensities of the measured ^{18}O and ^{16}O ions in the samples:

$$C(\mathrm{x,t}) = \frac{I(^{18}O)}{I(^{18}O) + I(^{16}O)} \tag{7.1}$$

The isotopic fraction for each point was normalised to the gas concentration:

$$\mathrm{C}'(x,t) = \frac{C(x,t) - C_{bg}}{C_g - C_{bg}} \tag{7.2}$$

where C_{bg} represents the natural isotopic background of ^{18}O (=0.002) and C_g represents the isotope fraction of ^{18}O in the gas during the exchange process.

The experimental data can be fitted to the plane sheet solution to the diffusion equation, as described in [162, 163]:

$$\begin{aligned}\mathrm{C}'(x,t) &= \frac{C(x,t) - C_{bg}}{C_g - C_{bg}} \\ &= 1 - \sum_{n=1}^{\infty} \frac{2L \cdot \cos\left(\beta_n \cdot \frac{l-x}{l}\right) \cdot \exp\left(\frac{-\beta_n^2 \cdot D^* \cdot t}{l^2}\right)}{(-\beta_n^2 + L^2 + L) \cdot \cos\beta_n}\end{aligned} \tag{7.3}$$

where l is the total thickness of the film and $\mathrm{L} = l \cdot \mathrm{k}^*/\mathrm{D}^*$, β_n(n = 1, 2, …) are the nonnegative roots of $\beta \cdot \tan\beta = L$, x is the distance from surface of the film sample, t is the time of the isotope exchange, D^* is the oxygen tracer diffusion coefficient and k^* is the tracer surface exchange coefficient. In particular, the obtained oxygen diffusion coefficient (D^*) is directly proportional to the oxygen ionic conductivity of the material. Consequently, the oxygen ionic conductivity can be estimated through the Nernst-Einstein relationship between diffusion coefficient and conductivity. Further information in terms of the relation can be found in references [162, 230], but the present section will only focus on the investigation of D^* and k^*.

Three IEDP-SIMS experiments were performed as follows; in the first experiment, a 44nm-thick $La_4Ni_3O_{10-\delta}$ film deposited on a NGO substrate was subjected to oxygen isotopic exchange at approximately 400°C for 1733 s (~29 min). **Figure 7.6** shows the

obtained normalised isotope fraction ^{18}O depth profile obtained by SIMS from the top film surface into NGO substrate. A compositional depth profile of the sample is placed aside on the top of the normalised isotope fraction ^{18}O depth profile for convenient observation in order to distinguish the diffusion position within the sample. It is clear that the oxygen diffusion profile can be divided into four regions: (I) top surface region of the $La_4Ni_3O_{10-\delta}$ film, (II) $La_4Ni_3O_{10-\delta}$ film, (III) interface region between $La_4Ni_3O_{10-\delta}$ film/NGO substrate and (IV) NGO substrate. In region I, a steeper decay than the rest of the profile was observed at first ~5.0 nm, indicating a lower oxygen diffusion coefficient. This could be due to surface contamination or to surface segregation of one of the constituent elements of the film, which will be further discussed in the following chapter. Due to this, the normalised concentration values in this region will not be taken into account for reliable fitting. In region II, it is observed that the ^{18}O concentration remains constantly decreases throughout the film following a typical diffusion profile. Region III can be regarded as the interface region between the film and the substrate (approximately 8.4 nm). When reaching region III (at approximately 35.4 nm), a change in the slope of the diffusion profile is observed, followed by an abrupt decay as the substrate is reached. It can be observed that the change in slope of the ^{18}O occurs simultaneously to a slight increase in the GaO^- number of counts, meaning that the ion beam is reaching the substrate in some small areas, probably due to small differences in film thickness between different regions. The decrease in ^{18}O concentration can be therefore regarded as an interface effect, and hence, the data at region III was also discarded for the fitting. For region IV, the normalised fraction of ^{18}O was obviously down to zero, with no observable diffusion occurring through the NGO substrate. The normalised oxygen concentration data for region II was selected to fit to the plane sheet solution (Eq.7.3) for a total thickness of 44 nm. As a result, the D^* and k^* parameters of the $La_4Ni_3O_{10-\delta}$ film at 400°C

can be obtained as 1.45 x 10^{-14} cm^2/s and 2.80 x 10^{-10} cm/s, respectively.

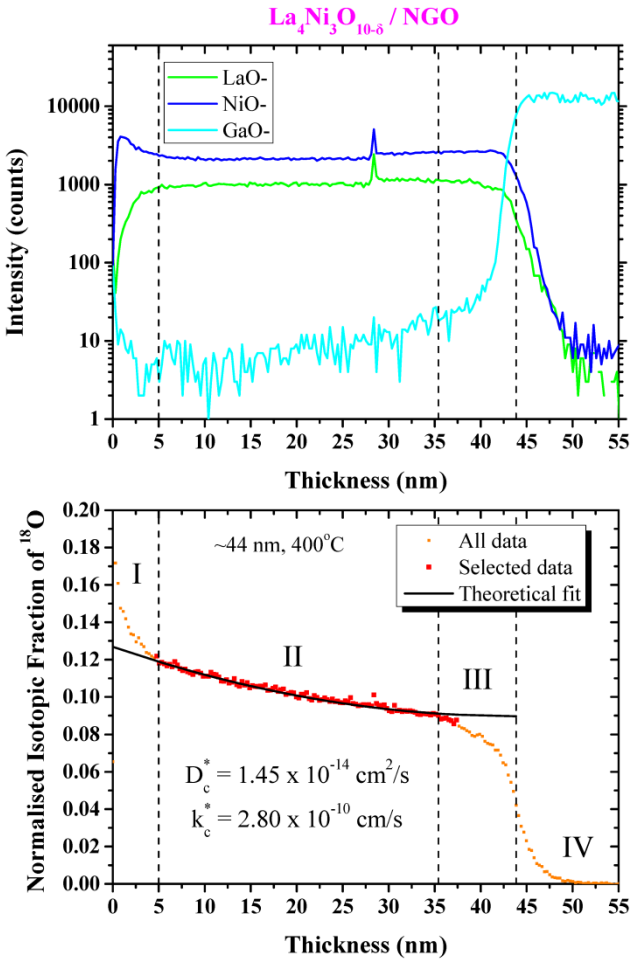


Figure 7.6 Diffusion profile showing the normalised isotope fraction (C') of ^{18}O along the c-axis direction of the 44nm-thick $La_4Ni_3O_{10-\delta}$ / NGO sample exchanged at 400°C for ~29 min.. Note that the data (red solid dot) in region II selected to fit with the Eq.7.3, and then to extract the diffusion and surface exchange coefficients (D^* and k^* respectively) shown in the bottom figure. Top figure: a compositional depth profile (including Lao^-, NiO^- and GaO^-) of the sample for convenient observation in order to distinguish the diffusion position within the sample.

In the cases of the other two experiments, individual 24nm-thick $La_4Ni_3O_{10-\delta}$ and 33nm-thick $La_3Ni_2O_{7-\delta}$ samples deposited on NGO substrates were exchanged simultaneously at approximately 500°C for 1266 s (~21 min). As seen in **Figure 7.7**, the normalised ^{18}O isotope fraction depth profile for the 24nm-thick $La_4Ni_3O_{10-\delta}$ sample also exhibits four apparently different regions. A slight increase in ^{18}O concentration with depth was observed at top surface region (region I), approximately 2.5 nm in width. The behaviour might be attributed to a back-exchange phenomenon (i.e. outward diffusion) at room temperature occurring during the time between the exchange anneal and the SIMS measurement. A close to flat diffusion profile was observed in the majority of the film (region II), while an abnormally slight increase in the ^{18}O fraction was found at the interface in region III. This phenomenon might be attributed to the presence of cracks or pinholes inside the film. The close-to-flat profile observed for region II due to a fast diffusion and very thin thickness of the film (~24 nm), precludes the determination of a value for D^*, but still allowed to obtain the k^* value for the film, as explained in reference [163].

On the other hand, a clear ^{18}O isotope fraction depth profile was obtained for the 33nm-thick $La_3Ni_2O_{7-\delta}$ sample (**Figure 7.8**). The obtained diffusion profile can be fitted to the plane-sheet solution to the diffusion equation as observed in the bottom diagram of **Figure 7.8**. Different ^{18}O isotope diffusion profiles were obtained from the $La_3Ni_2O_{7-\delta}$ and $La_4Ni_3O_{10-\delta}$ samples exchanged at the same temperature (500°C). The measured $La_3Ni_2O_{7-\delta}$ sample exhibited an oxygen diffusion profile which could be appropriately fitted to the plane sheet solution to the diffusion equation, which was not the case for the $La_4Ni_3O_{10-\delta}$ one. This is likely related to the higher quality of the $La_3Ni_2O_{7-\delta}$ sample than the $La_4Ni_3O_{10-\delta}$ sample, corresponding to results from previous chapter.

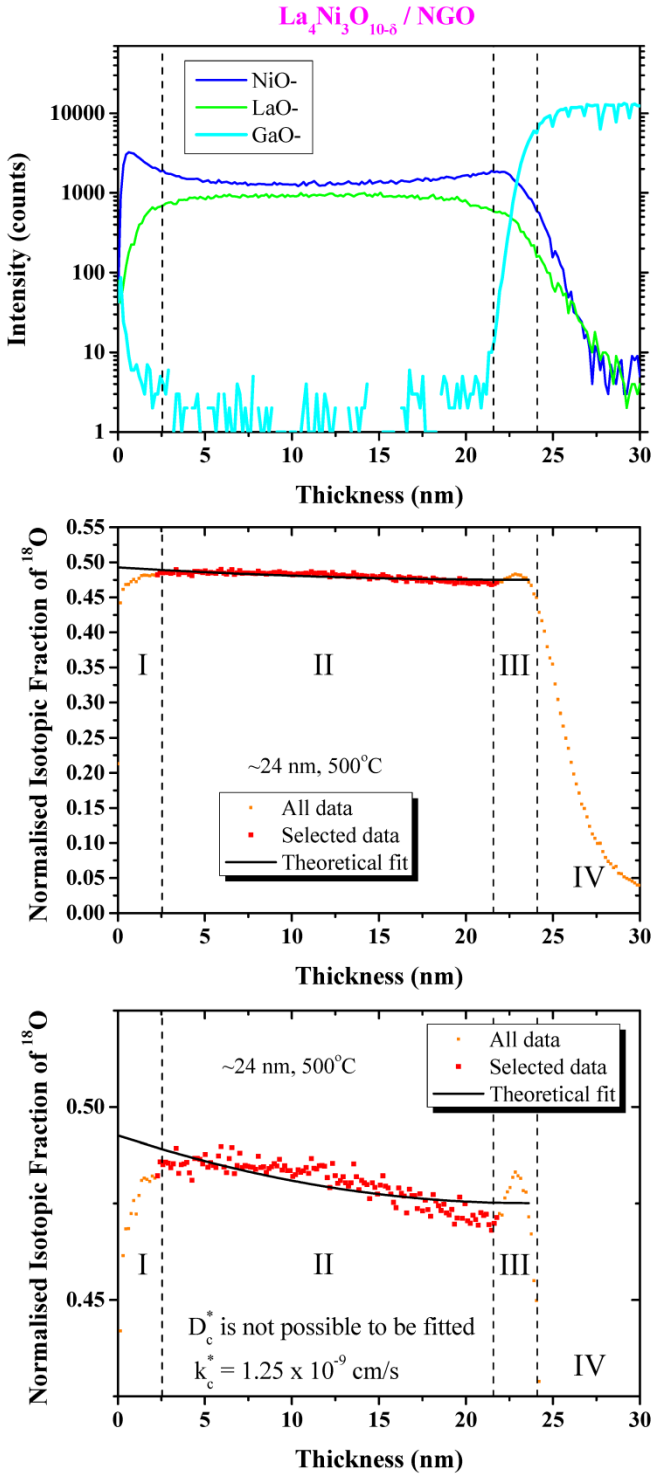


Figure 7.7 Diffusion profile showing the normalised isotope fraction (C') of ^{18}O along the c-axis direction of the 24nm-thick $La_4Ni_3O_{10-\delta}$ / NGO sample exchanged at 500°C for ~21 min. Note that the data (red solid dot) in region II selected to fit with the Eq.7.3, and then to extract the k^* shown in the bottom diagram, but D^* is unable to be fitted. Top diagram: a compositional depth profile (including Lao^-, NiO^- and GaO^-) of the sample for convenient observation in order to distinguish the diffusion position from film surface to substrate. Middle diagram: the normalised ^{18}O isotope fraction depth profile. Bottom diagram: a zoom diagram of the middle one.

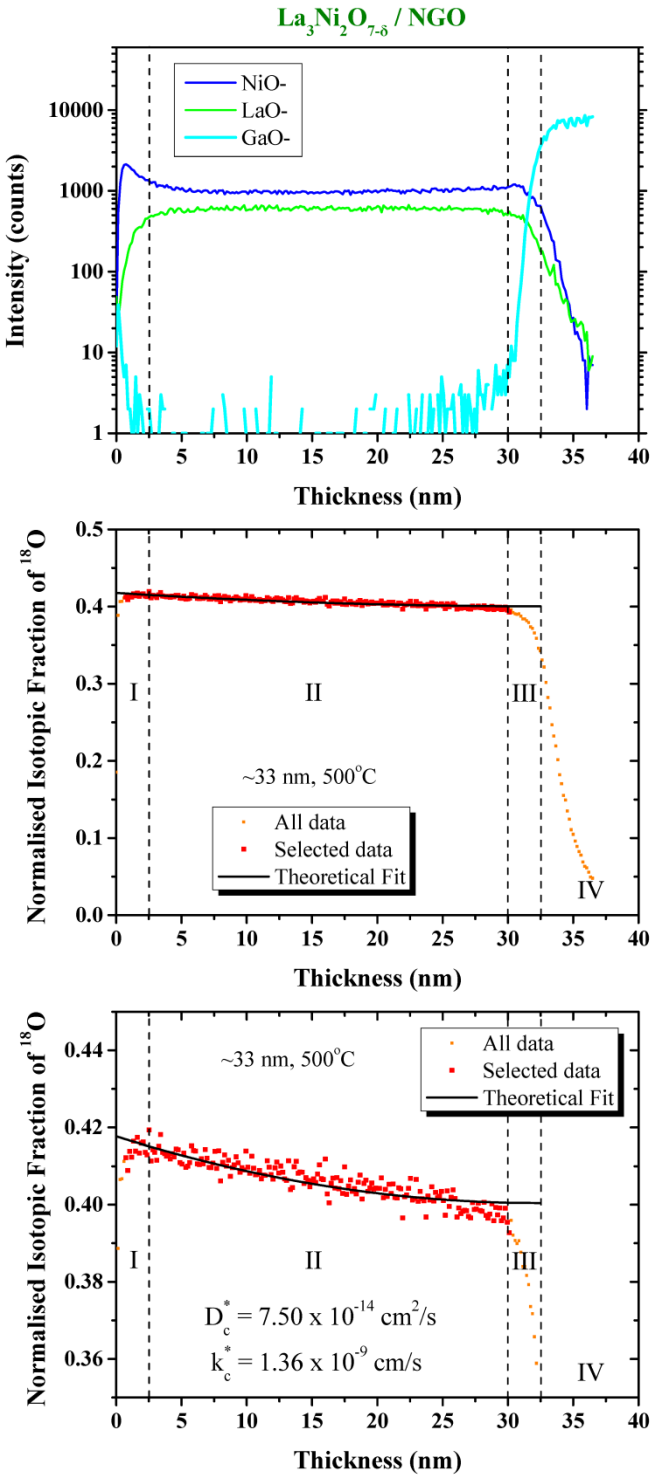


Figure 7.8 Diffusion profile showing the normalised isotope fraction (C') of ^{18}O along the c-axis direction of the 33nm-thick $La_4Ni_3O_{10-\delta}$ / NGO sample exchanged at 500°C for ~21 min. Note that the data (red solid dot) do fit well with the Eq.7.3. The k^* and D^* shown in the bottom diagram. Top diagram: a compositional depth profile (including Lao^-, NiO^- and GaO^-) of the sample for convenient observation in order to distinguish the diffusion position from film surface to substrate. Middle diagram: normalised ^{18}O isotope fraction depth profile. Bottom diagram: a zoom diagram of the middle one.

All the measured D^* and k^* values along c-axis at 500°C for both $La_3Ni_2O_{7-\delta}$ and $La_4Ni_3O_{10-\delta}$ films are summarised in **Table 7.1** and compared to the literature data of the $La_2NiO_{4+\delta}$ epitaxial films deposited by PI-MOCVD, reported by Burriel *et al.* [41]. It is apparent that the D^* value of the $La_3Ni_2O_{7-\delta}$ film is approximately two orders of magnitude lower than the value of $La_2NiO_{4+\delta}$ film. The difference might be related to the oxygen stoichiometry and diffusion mechanism. It is known that $La_2NiO_{4+\delta}$ is a predominant oxygen-excess compound, has oxygen hypersoichiometry, and the oxygen migrates through the interstitials [34, 37, 41, 99, 244, 245]. However, $La_3Ni_2O_{7-\delta}$ and even $La_4Ni_3O_{10-\delta}$ are predominant oxygen-deficient compounds, but their diffusion mechanisms (through interstitials or vacancies) are still unclear. Thus so far it cannot be concluded what the reasons are to cause such difference of oxygen diffusion along the c-axis for these two cases. Further experimental and theoretical studies are required in the future. For example, it would be interesting to systematically investigate the oxygen diffusion along the c-axis and a,b-direction of these c-axis oriented higher order RP epitaxial films under various temperature. Also, combining with microstructural analysis via HRTEM, it would help to understand the oxygen diffusion mechanism of the high order RP materials. On the other hand, the k^* values of $La_3Ni_2O_{7-\delta}$ and $La_4Ni_3O_{10-\delta}$ films appear to exhibit similar values to those of the $La_2NiO_{4+\delta}$ from the literature. The k* values may be associated with the surface structure and composition of these films. Thus it is of interest to examine the surface information of the measured films such as the cation (La/Ni) compositions, which will be discussed in the next chapter.

This section has presented several studies on oxygen diffusion and surface exchange coefficients along the c-axis in these films. These results confirmed that the deposited $La_3Ni_2O_{7-\delta}$ and $La_4Ni_3O_{10-\delta}$ films are dense and continuous enough for IEDP-SIMS measurements. However, according to the crystallographic and microstructural analyses

in the previous chapter, the findings revealed the possibility of the presence of various planar defects, such as stacking faults, mis-orientation of RP blocks, and particularly RP intergrowths of different phases. These imperfections may have a large impact on the ionic transport properties of the complex oxide films. Hence, further systematic investigations of the anisotropic oxygen diffusion along c-axis and also the a,b-directions under a series of different exchange temperatures should be addressed, in conjunction with microstructural investigations via HRTEM characterisation, in the future. Such investigations may permit the determination of the activation energy of oxygen migration for the higher order RP $La_3Ni_2O_{7-\delta}$ and $La_4Ni_3O_{10-\delta}$ epitaxial films. It would be of great interest if strong anisotropic ionic transport properties exist in both high order phases like the behaviour observed in $La_2NiO_{4+\delta}$ single crystals [34] and epitaxial films [41].

Table 7.1 Summary of diffusion coefficient (D^*) and surface exchange coefficient (k^*) along c-axis of $La_3Ni_2O_{7-\delta}$ and $La_4Ni_3O_{10-\delta}$ films at ~400 and ~500°C, compared to the literature values of $La_2NiO_{4+\delta}$ film.

Temp. (°C)	Films on NGO	D* (c-axis) / cm^2s^{-1}	k* (c-axis) / cms^{-1}	Ref.
~500	$La_2NiO_{4+\delta}$	~$4.50x10^{-12}$	~$6.70x10^{-9}$	[41]
	$La_3Ni_2O_{7-\delta}$	$7.50x10^{-14}$	$1.36x10^{-9}$	This work
	$La_4Ni_3O_{10-\delta}$	N/A	$1.25x10^{-9}$	This work
~400	$La_4Ni_3O_{10-\delta}$	$1.45x10^{-14}$	$2.80x10^{-10}$	This work

7.3 Summary

In summary, the planar electrical conductivity properties for the obtained c-axis oriented $La_3Ni_2O_{7-\delta}$ and $La_4Ni_3O_{10-\delta}$ epitaxial films deposited on NGO substrates have been systematically studied as a function of temperature through a series of investigations including influence of film thickness, cycling measurement and comparative study. In the

influence of film thickness, the investigation found that all the obtained $La_3Ni_2O_{7-\delta}$ films displayed semiconducting-to-metallic behaviour and generally increased with increasing film thickness, whilst $La_4Ni_3O_{10-\delta}$ films exhibited a clear evolution of electrical conductivity with increasing film thickness. The evolution strongly suggests the influence of microstructural variation on electrical conductivity behaviour. These findings consistently support the results from the previous chapter, indicating that obtained $La_3Ni_2O_{7-\delta}$ films showed a better quality than the $La_4Ni_3O_{10-\delta}$ films and even the $La_4Ni_3O_{10-\delta}$ films likely have a strong effect of accumulating higher level of intergrowths, misalignments and defects with increasing film thickness.

In the cycling measurements, these $La_3Ni_2O_{7-\delta}$ and $La_4Ni_3O_{10-\delta}$ epitaxial films of different thicknesses showed reversible electrical behaviour, which indicates the good stability of these films during the measurement.

In the comparative study with the literature data, the planar electrical conductivity results of the obtained c-axis oriented $La_2NiO_{4+\delta}$ (n = 1), $La_3Ni_2O_{7-\delta}$ (n = 2) and $La_4Ni_3O_{10-\delta}$ (n = 3) epitaxial films exhibited a systematic enhancement with increasing n value, and showed much larger conductivity than the randomly oriented polycrystalline samples, as expected. This can be attributed to the layered structure of the films and driven from the increasing number of adjacent NiO_6 octahedra of the perovskite layers responsible for the electronic transport pathways. However, by comparing the data with previous literature of the epitaxial films grown by PI-MOCVD, the results indicate the possibility of the presence of mixed intergrowths within these films. Despite this, the electrical conductivities of our films were fairly located at reasonable ranges with promising values. Particularly, the higher order $La_3Ni_2O_{7-\delta}$ and $La_4Ni_3O_{10-\delta}$ films exhibit promising electrical conductivity values of approximately 700-1000 Scm^{-1} along the a,b-direction in comparison with the $La_2NiO_{4+\delta}$ film. This conductivity value is

potentially suitable for use in IT-SOFCs.

It is worth noting that there is still an absence of information regarding the electrical conductivity along the c-direction. It would be of interest to investigate if a highly anisotropic electrical conduction exists in the higher order phases in the future. Additionally, to further understand the influence of the electrical conductivity behaviour with oxygen and microstructural variations, further studies should be conducted with the measurements under different atmospheres (e.g. O_2 and N_2) and with HRTEM characterisation in the future.

Finally, based on the oxygen exchange and transport analysis performed in Ch.7.2, these investigations were clearly preliminary studies. Although the results did not exhibit better D* and k* values along c-axis compared to literature, the findings not only indicated the feasibility of the deposited $La_3Ni_2O_{7-\delta}$ and $La_4Ni_3O_{10-\delta}$ films, but also provides the first information with respect to the diffusion and surface exchange coefficients of these films through the IEDP-SIMS approach. To determine the activation energies of oxygen diffusion and surface exchange behaviour for the $La_3Ni_2O_{7-\delta}$ and $La_4Ni_3O_{10-\delta}$ phases, further systematic investigations into the anisotropic oxygen diffusion measurements along the c-axis and particularly a,b-directions under various temperatures should be conducted in the future. Moreover, these investigations should also be along with microstructural analysis through HRTEM in order to understand the influence of film microstructure on the ionic transport properties. It would help to understand the oxygen diffusion mechanism of the higher order RP films.

Chapter 8 Surface and Interface Characterisation of La-Ni-O Films

The oxygen reduction reaction (ORR) is considered to be limited by the oxygen surface exchange activity at MIEC cathodes particularly at low operation temperature and is thus a crucial factor for implementation of IT-SOFCs (500-700°C) [13, 17]. Therefore, developing MIEC materials with a high ORR rate (i.e. a high oxygen surface exchange coefficient, k^*) at such operating temperatures is imperative. The oxygen surface exchange activity is strongly influenced by the surface composition and atomic surface structure where the adsorption and dissociation of molecular oxygen take place. These effects may further influence the rate determining step [17]; and consequently the ultimate efficiency of the SOFC device. More importantly, compared to bulk samples, the oxygen transport kinetics for thin-film samples is significantly dominated by the surface process [42]. It is therefore of great importance to study the surface compositions and structure (or termination) of the obtained films. These investigations will aid in the understanding of the electrochemical properties of lanthanum nickelate cathode materials in surface regions [162].

In this chapter, the compositional depth profiles of $La_3Ni_2O_{7-\delta}$ and $La_4Ni_3O_{10-\delta}$ films obtained via SIMS analysis will be presented in section 8.1. Through the SIMS depth profiles, the cation compositional variation of film and substrate at surface and film-substrate interface regions will be observed. To further investigate the information at the near-surface and even very outermost atomic surface of these films, a series of low energy ion scattering (LEIS) measurements were conducted on as-deposited and after-heat-treatment samples in section 8.2. The investigations will discuss surface contamination, termination of the outermost surface, and variation in cation concentration

in the sub-surface region.

8.1 Compositional Depth Profiling by SIMS

In the previous chapter (Ch.7.2), the oxygen diffusion and surface exchange coefficients (along c-axis) of the $La_3Ni_2O_{7-\delta}$ and $La_4Ni_3O_{10-\delta}$ epitaxial films have been extracted from the IEDP-SIMS measurements. As previously described, in addition to the ^{18}O isotope fraction depth profile, compositional depth profiles of LaO^-, NiO^-, NdO^- and GaO^- species from the film surface to the film-substrate interface were simultaneously obtained by ToF-SIMS. Therefore the investigation of the compositional depth profiles correspond to the same samples (and same region) used for the oxygen diffusion analysis previously described: the 24 nm-thick $La_4Ni_3O_{10-\delta}$ and 33 nm-thick $La_3Ni_2O_{7-\delta}$ films deposited on NGO substrates. Both samples were annealed in natural oxygen for 16 hours and exchanged for ~21 min together at approximately 500°C (seen in previous **Figure 7.7** and **Figure 7.8**).

The compositional depth profiles of both 24nm-thick $La_4Ni_3O_{10-\delta}$ and 33nm-thick $La_3Ni_2O_{7-\delta}$ samples are shown in **Figure 8.1 (a)** and **(b)**, respectively. The measured species include LaO^- and NiO^- from the films and NdO^- and GaO^- from the NGO substrates. Both depth profiles can be broadly divided into four regions: (I) surface of film, (II) film, (III) film-substrate interface and (IV) substrate. It should be pointed out that for the first data points transient-effects characteristic in SIMS will occur until the steady state is reached (e.g. equilibrium within sputtered-implanted species), which can lead changes in the sputter yields for the different elements). Therefore the first 0.5 nm (approximate depth until the steady state for the total number of O^- secondary ions ($^{16}O^- + {}^{18}O^-$) is treated as a transient region from which no conclusions will be extracted. In

addition in order to carefully take into account all the processes occurring during the SIMS analysis, it should be pointed out that the depth profiles will be affected by a sputter intermixing effect due to the penetration depth of the incident Cs^+ sputter ions. For the beam conditions used: Cs^+ beam at 2 keV and angle of incidence of 45º, the longitudinal straggle ion range has been estimated to be 21 Å for both $La_4Ni_3O_{10-\delta}$ and $La_3Ni_2O_{7-\delta}$ according to simulations using the SRIM (The Stopping and Range of Ions in Matter) software [246].

In the surface region (region I) of both figures, a large variation of both the NiO^- and LaO^- signals is observed until relatively constant values at a depth of approximately 4 nm are reached. A steep decay of NiO^- intensity was observed together with a marked rise of LaO^- intensity in the first ~4 nm, which seems to suggest differences in composition in the top surface. These surface compositional differences are in good agreement with the LEIS observations, which will be described in detail in section 8.2.2. Throughout the LNO film (regions I and II) a negligible number of counts of NdO^- and GaO^- were detected, as expected. In region II, the intensities of LaO^- and NiO^- remain relatively constant in depth, which would constitute the "bulk" of the film. In the interface region (region III), the intensity of NiO^- starts increasing gradually, followed by a rapid drop when the interface is reached whilst that of LaO^- gradually decreases. Although changes in the useful secondary ions yield can occur at the interface region, region III of the $La_4Ni_3O_{10-\delta}$ film (**Figure 8.1 (a)**) seems to have a different composition to the rest of the film (Ni-rich La-poor), while for the $La_3Ni_2O_{7-\delta}$ film no major differences between film and interface are observed. The film-substrate interface is defined as the point at which a 50% of the decrease in the number of NiO^- counts is reached. It should be noted that once the NGO insulating substrate is reached the measurement becomes very noisy, related to charging effects (insulating substrate). Note that the low useful yield of NdO^- makes the

signal difficult to observe in the linear plots, but careful inspection does reveal this increase.

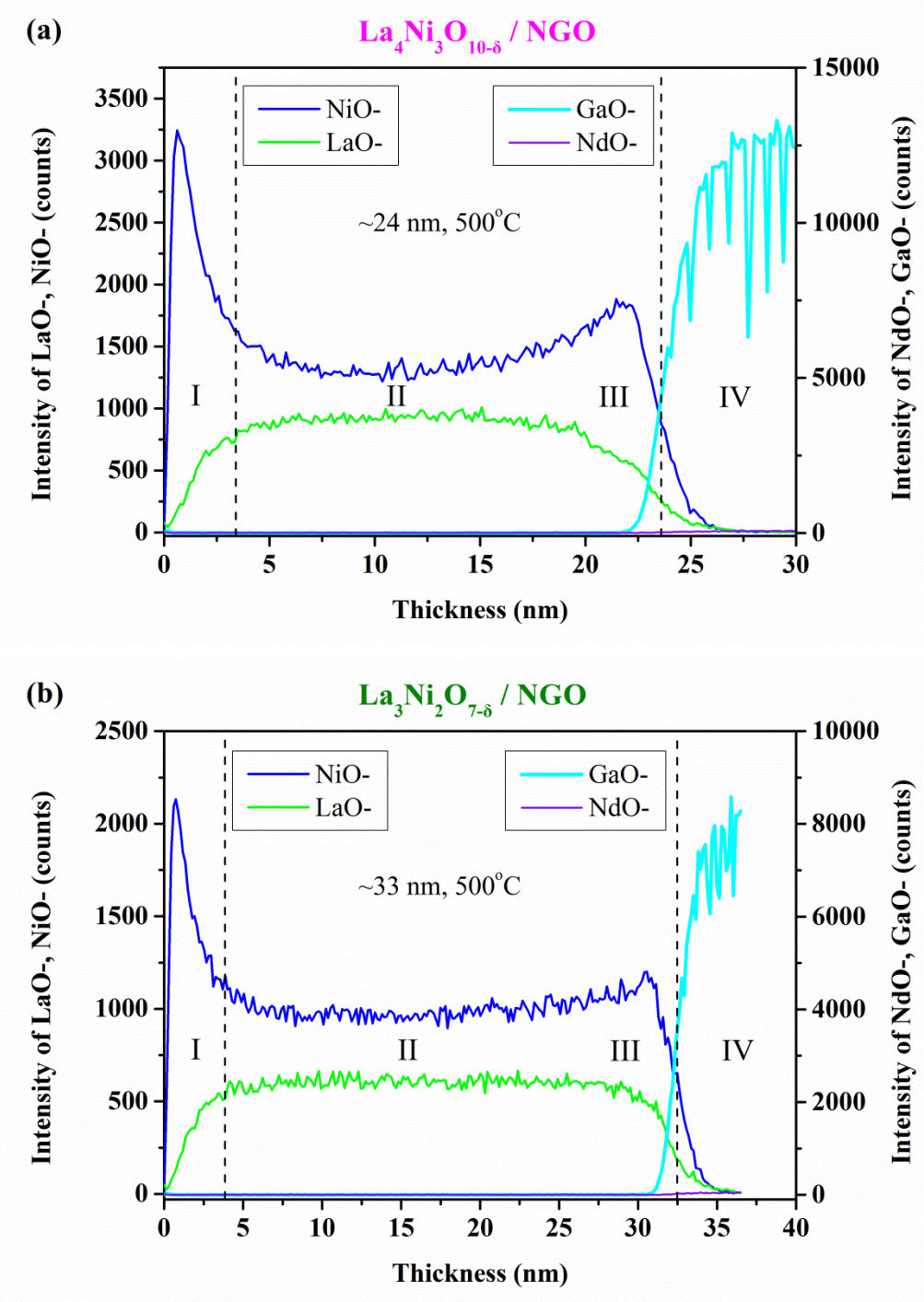


Figure 8.1 Compositional depth profiles for LaO^-, NiO^-, NdO^- and GaO^- secondary ion species in (a) 24nm-thick $La_4Ni_3O_{10-\delta}$ and (b) 33nm-thick $La_3Ni_2O_{7-\delta}$ films deposited on NGO after an oxygen isotope exchange at approximately 500°C. Region I, II, III and IV represent surface of film, film, film-substrate interface and substrate. The dashed lines identify the middle area between surface of film (I) and film (II); the middle interface area between film (III) and substrate (IV).

Overall, the significant variations in LaO^- and NiO^- signals at the surface region (I) for both compositions, also confirmed by LEIS (as explained in section 8.2.2), and at the interface region (III) for the $La_4Ni_3O_{10-\delta}$ film is of interest, as it probably suggests some compositional variation within both films. Additionally, the interface region could have different cation ratio, oxygen content or strain, due to the mismatch in cell parameters between the film and the substrate. The absence of GaO^- signals until close to the interface probably indicates there are no cracks or pinholes within the film; in other words, the films are dense and continuous.

It should be noted that although only the results obtained from the samples exchanged at 500°C are presented here as examples, the sample exchanged at 400°C also exhibits very similar behaviour in cation compositional variation: Ni-enriched at the surface and film-substrate interface (see Appendix III). According to these similar depth profiles, it seems that the different treatment temperature had little effect on the significant cation variations. It would be of interest to investigate whether as-deposited films also exhibit such significantly cation variations. However, as previously described in Ch.3.5, SIMS is based on the analysis of secondary ions, and the secondary ions are emitted from the 2-3 first atomic layers of the sample. Hence, SIMS technique has a large information depth that the surface information cannot be distinguished between from the outermost or the sub-surface region; i.e. the signals from the two regions were integrated. Also the matrix effect of SIMS may complicate analysis of the obtained data, leading to the difficulty of surface quantitative investigations**.** Hence, if we are interested in the outermost surface termination more surface specificity technique is required for further investigations, which will be conducted by LEIS techniques in next section.

8.2 Surface Analysis by LEIS

To further investigate the outer-surface chemical information of the films, the LEIS technique was applied. LEIS is considered to be a very powerful tool for the analysis of atomic composition of the near-surface and particularly of the *outermost* monoatomic layers of materials [169]. The outer-surface information includes, for example, surface contamination, termination and segregation [162, 170, 171]. LEIS is therefore being increasingly utilised to examine the surfaces of SOFC materials [162] such as $La_{2-x}Sr_xNiO_{4+\delta}$ [170], $La_{0.6}Sr_{0.4}Co_{0.2}Fe_{0.8}O_{3-\delta}$ [171] and $Pr_1La_1NiO_{4+\delta}$ [171]. For a detailed description with respect to the basic principle and other useful references for further information on LEIS, please refer to Ch.3.5.

The measurements were performed on two sets of as-deposited and after-exchanged (annealing (16 h) and exchange (~21 min), at 500°C) samples of $La_3Ni_2O_{7-\delta}$ and $La_4Ni_3O_{10-\delta}$ films. The as-deposited $La_3Ni_2O_{7-\delta}$ and $La_4Ni_3O_{10-\delta}$ samples were deposited using the same conditions as the isotopically exchanged films. The after-exchanged samples used for the LEIS analysis were the same $La_3Ni_2O_{7-\delta}$ and $La_4Ni_3O_{10-\delta}$ samples used for the previous SIMS measurements. The analysis of as-deposited $La_3Ni_2O_{7-\delta}$ and $La_4Ni_3O_{10-\delta}$ samples will be discussed in section 8.2.1 and after-exchanged samples in section 8.2.2. For comparison, a $La_2NiO_{4+\delta}$ sample was also analysed, which will be presented in section 8.2.3. Note that the series of LEIS measurements will focus only on the outer surface and outermost regions, excluding the film-substrate region, and the measurements (including all data processing) were executed by Dr. H. Téllez at the Department of Materials in Imperial College London.

Under normal laboratory conditions in the open atmosphere, the sample surface is covered with a range of contaminants including adsorbed water and hydrocarbons.

Appropriate cleaning is therefore necessary for the measured samples [162]. Prior to the LEIS analysis, the as-deposited samples were successively cleaned with acetone, isopropanol, and deionised water for 10 min each in an ultrasonic bath whilst the exchanged samples were analysed without any pre-cleaning after IEDP-SIMS measurements and directly held for LEIS measurements. Then both sets of samples were also cleaned by exposing the surface to the atomic oxygen plasma for a period of time (~10 min), which is a standard surface-cleaning method [247]. To check the effectiveness of the *in-situ* cleaning procedure, a light primary ion beam of 3 keV He^+ was utilised to detect the presence of a surface carbon peak as an indicator of surface contamination by hydrocarbons. This procedure was repeated until there were no noticeable changes between two successive spectra and the peak for carbon has disappeared. The sample was then deemed clean, and ready for depth profiling measurements. However, the light primary ion beam is not ideal for analysing compounds containing heavy elements such as La and Ni in the current work. For the analysis of metals and rare earth elements, a noble gas ion beam of 5 keV Ne^+ was adopted to enhance the signals of these heavier elements. The depth profiles were performed in a dual-beam mode, using a 0.5 keV Ar^+ ion beam for low-energy sputtering and a 5 keV Ne^+ beam for the analysis.

8.2.1 Surface Analysis of As-Deposited $La_3Ni_2O_{7-\delta}$ and $La_4Ni_3O_{10-\delta}$ Films

The He^+ and Ne^+ LEIS spectra for the outer surface of the as-deposited $La_4Ni_3O_{10-\delta}$ film shown side by side in **Figure 8.2 (a)** and **(b)**. Note that the LEIS yield (y-axis) in the figures is defined as the unit of "counts/nC". This is because the obtained signal is related to the intensity of utilised primary ion beam and the analysis time; i.e. depends on the current of primary ion beam. Thus, through the LEIS instrument, the obtained signals is normalised to the intensity of primary ion beam such that the unit is defined as counts/nC.

The spectra clearly show a surface with both La and Ni elements present, and no significant contaminations for the as-deposited $La_4Ni_3O_{10-\delta}$ film. The ^{16}O peak is present only in the He^+ spectrum (**Figure 8.2 (a)**) is because He^+ has smaller scattering cross-section, which is better for probing light elements. In the Ne^+ spectrum (**Figure 8.2 (b)**), there is a broad background below 1000 eV. This corresponds to the secondary ion background such as H^+, OH^+, Na^+, K^+, etc [169]. The background is because the heavier Ne^+ beams with higher energy may lead to the increased sputtering (i.e. the increased production of secondary ions). Both spectra showed mixed cations (i.e. both La and Ni) on the outer surface of the as-deposited $La_4Ni_3O_{10-\delta}$ film. For the as-deposited $La_3Ni_2O_{7-\delta}$ film, the He^+ and Ne^+ LEIS spectra are shown in **Figure 8.3 (a)** and **(b)**, respectively. Again, both cations were also observed on the outer surface of the as-deposited $La_3Ni_2O_{7-\delta}$ sample.

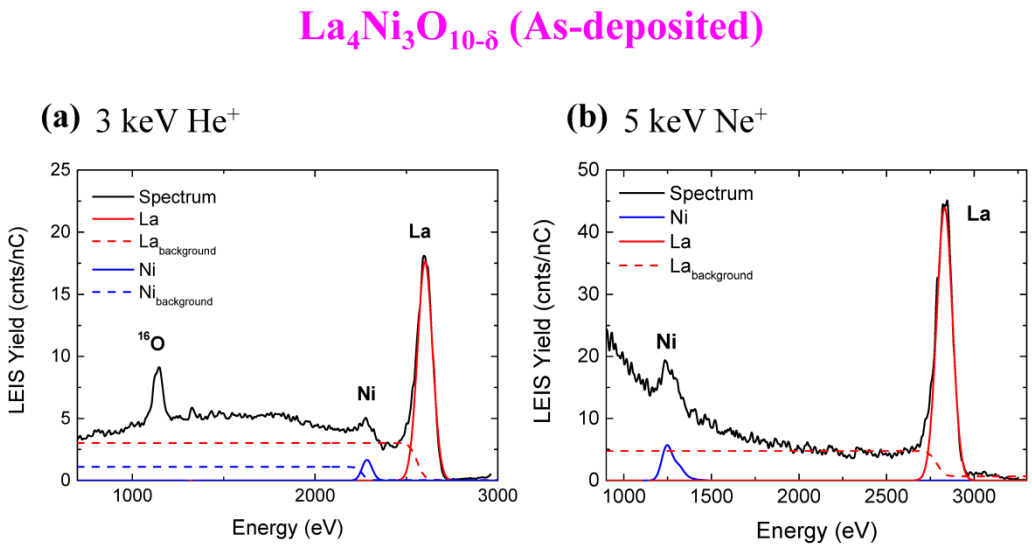


Figure 8.2 LEIS energy spectra of as-deposited $La_4Ni_3O_{10-\delta}$ film performed on the outer surface by (a) 3 keV He^+ and (b) 5 keV Ne^+ ion beams.

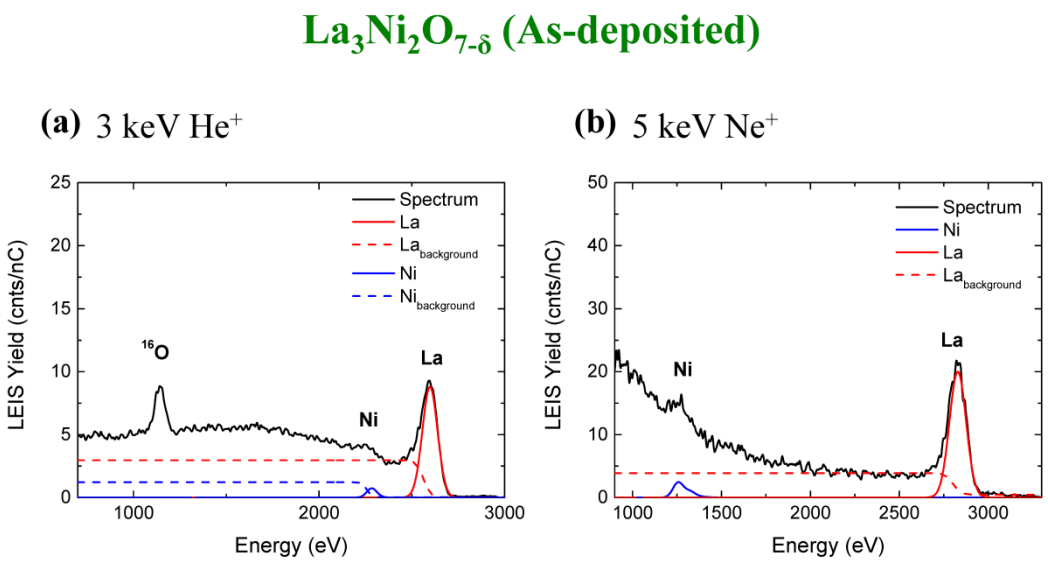


Figure 8.3 LEIS energy spectra of as-deposited $La_3Ni_2O_{7-\delta}$ film performed on the outer surface by (a) 3 keV He^+ and (b) 5 keV Ne^+ ion beams.

In the depth profiling analyses, a series of energy spectra were collected using a 5 keV Ne^+ primary ion beam as successive low-energy sputtering steps were conducted by a 0.5 keV Ar^+ beam for 30 s each step. Through such an iterative process, depth profiles were obtained for the as-deposited samples. The measurements were stopped when a constant intensity of La and Ni signals was reached; that is, no further changes were seen in the spectrum. The depth profile permits the examination of cation composition variation from the outermost surface, through the sub-surface to the bulk of the film.

Figure 8.4 (a), **(b)** and **(c)** shows the depth profile analysis of the as-deposited $La_4Ni_3O_{10-\delta}$ sample. The raw yields of La and Ni signals were plotted in **Figure 8.4 (a)** against Ar^+ ion fluence and estimated depth. Due to the absence of matrix effects, the intensity of a peak in the LEIS spectrum directly reflects the coverage of the corresponding cation on the measured surface during every LEIS scan [169]. Thus, the quantification of the surface coverage of cations can be performed by assuming that the plateau signals in the depth profiles corresponds to the bulk composition of the film, assuming an ideal stoichiometry of the materials (e.g. La/Ni: 4 to 3 for $La_4Ni_3O_{10-\delta}$).

Therefore, these data can be further normalised to the obtained La and Ni plateau signals from the bulk region of the film, and plotted as an apparent cation coverage diagram, as shown in **Figure 8.4 (b)**. Note that the term of apparent cation coverage is used to reference only the fractional cation abundance on the surface.

It should be noted that such data processing assumes no preferential sputtering of the cations. According to simulations using the SRIM (The Stopping and Range of Ions in Matter) software [246], in the case of lanthanum nickelate materials, the sputtering rate using 0.5 keV Ar^+ at an incident angle of 59^o is La: 0.60 atoms/Ar^+ ion, Ni: 0.39 atoms/Ar^+ ion, and O: 2.38 atoms/Ar^+ ion. From the simulation results, although the sputtering yields of La and Ni are different, they are still much lower than the yields of oxygen, meaning that the oxygen is sputtered much faster than the La and Ni cations. Thus, compared to oxygen, the effect of preferential sputtering between both cations is negligible and, further, we can assume that the plateau signals at bulk correspond to the ideal stoichiometry of the materials. Similar data processing has been also reported in lanthanum nickelate powders [174] and other oxide powder materials [248].

As seen in **Figure 8.4 (b)**, the first data point of the apparent cation coverage profile (i.e. at the very outer surface) does not add up to unity. This is because the coverages are normalised to the plateau signals, as mentioned above. These plateau signals are assumed to correspond to the bulk stoichiometry although after a long sputtering time the oxygen has been preferentially sputtered, so the bulk composition has been depleted in oxygen. Therefore, the first point in the profile is oxygen-enriched, compared to the bulk region, leading to the total cation coverage below 1 at the surface. As seen at the end of the depth profile in **Figure 8.4 (b)**, the constant La and Ni plateau signals are outlined by dashed lines, indicating the values of apparent cation coverage for La and Ni to be approximately 0.57 (57%) and 0.43 (43%) respectively. The values correspond to the La 4 and Ni 3 out

of 7 (total stoichiometry) ratios. In this figure, a significant cation variation can be clearly identified at the sub-surface region of the film. From the ratio of the apparent cation coverages of Ni and La, shown in **Figure 8.4 (c)**, a Ni-enriched sub-surface region (~2.0 nm) is apparent for the as-deposited sample, compared to the horizontal dashed line corresponding to the expected Ni/La ratio of 0.75 for the bulk stoichiometry. In careful inspection, the higher Ni/La ratio (>0.75) at the sub-surface seems to suggest that another phase could be formed. According to the cation stoichiometry of the series of RP $La_2NiO_{4+\delta}$ (n = 1), $La_3Ni_2O_{7-\delta}$ (n = 2) and $La_4Ni_3O_{10-\delta}$ (n = 3) compounds, the higher the index is, the higher the Ni/La ratio. Thus, this seems to suggest that there is an increase in the number of perovskite layers in this region. This reconstruction of the near-surface region is likely due to the segregation of La ions to the surface. However, there is no enough evidence to make a conclusion. Further investigation by HRTEM is required in the future.

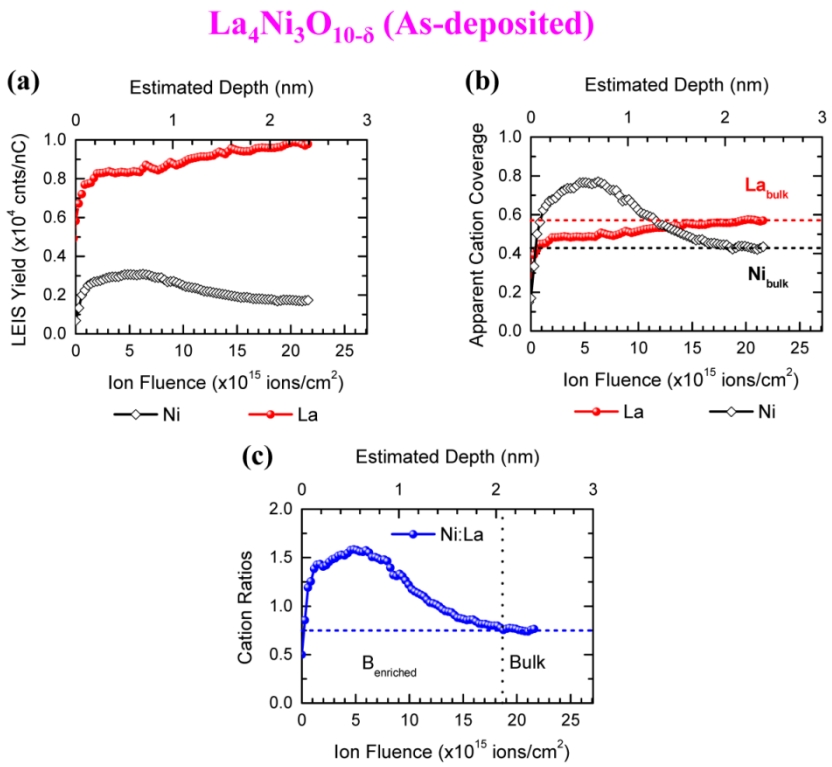


Figure 8.4 Normalised depth profiles of as-deposited $La_4Ni_3O_{10-\delta}$ film from Ne^+ spectra obtained after successive sputtering steps, showing (a) the raw yields of La and Ni, (b) apparent cation coverage and (c) cation (Ni:La) ratios plotted with ion fluence, i.e. Ar^+ ion sputtering rate.

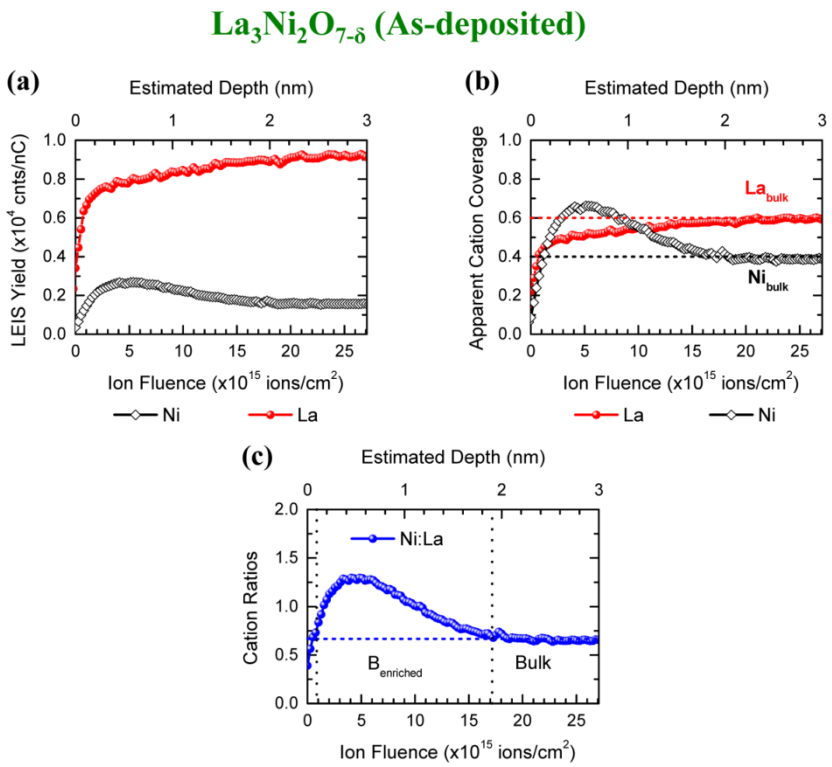


Figure 8.5 Normalised cation depth profiles of as-deposited $La_3Ni_2O_{7-\delta}$ film from Ne^+ spectra obtained after successive sputtering steps, showing (a) the raw yield of La and Ni, (b) apparent cation coverage and (c) cation (Ni:La) ratios plotted with ion fluence, i.e. Ar^+ ion sputtering rate.

The depth profiles for the as-deposited $La_3Ni_2O_{7-\delta}$ sample were processed via the same method described above. The results (measured with Ne^+) are shown in **Figure 8.5 (a)-(c)**. Similar variations in distribution both cations, and the phenomenon of Ni-enrichment were also observed on the sub-surface region of the as-deposited sample with a thickness of around 1.9 nm.

8.2.2 Surface Analysis of After-Exchanged $La_3Ni_2O_{7-\delta}$ and $La_4Ni_3O_{10-\delta}$ Films

In the case of the after-exchanged samples, a series of LEIS analyses were performed as follows. Firstly the He^+ LEIS spectra of the after-exchanged $La_4Ni_3O_{10-\delta}$ film are shown in **Figure 8.6 (a)** and **(b)** for outer surface and depth profile, respectively. In **Figure 8.6 (a)**, the spectrum exhibits a clear La peak with ^{16}O and ^{18}O, but barely the presence of Ni,

suggesting the presence of a LaO-terminated surface after exchange process and presumably the occurrence of reconstruction after exchange process (*cf.* **Figure 8.2 (b)**). Additionally, the significant amount of contamination (Na, K, Ca, P, and S) seen on the surface of the sample is no surprise, because as mentioned previously the samples were not cleaned with acetone, isopropanol, and deionised water in an ultrasonic bath after the IEDP-SIMS measurement. The findings could imply that the sample was probably contaminated during exchange process in the exchange rig, SIMS measurement or the storage and transport. Therefore, attention with great care has to be paid during these processes. Despite this, these absorbed contaminants were only present in the first monoatomic layer (approximately 0.2 nm), as can be observed in **Figure 8.6 (b)**.

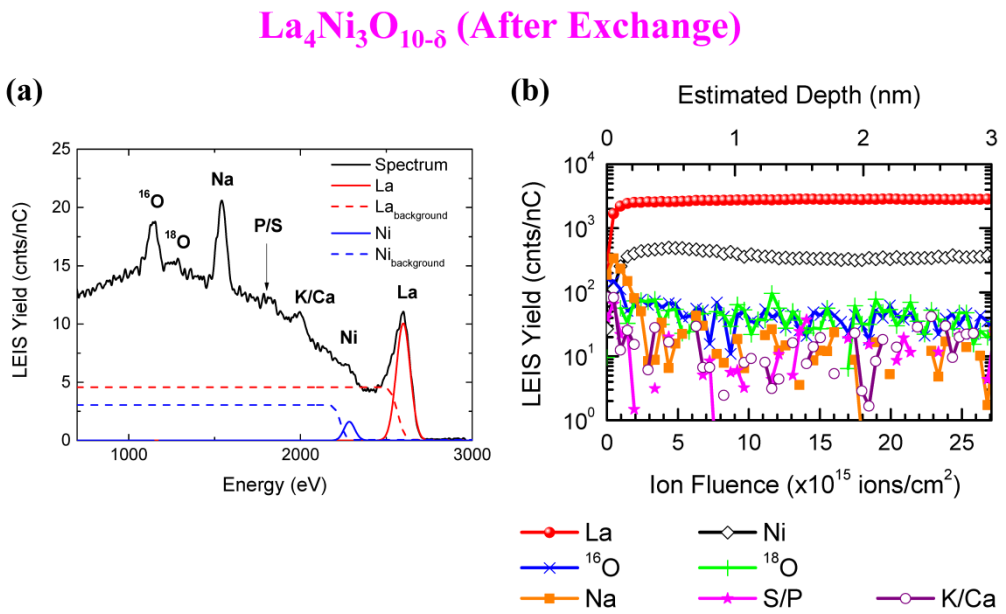


Figure 8.6 LEIS energy spectrum on the outer surface (a) and depth profile (b) of the after-exchanged $La_4Ni_3O_{10-\delta}$ film performed by a 3 keV He^+ ion beam.

Through the analysis of the He^+ surface spectrum and depth profile, the after-exchanged $La_3Ni_2O_{7-\delta}$ sample also exhibited similar findings as the $La_4Ni_3O_{10-\delta}$ sample observed above. In **Figure 8.7 (a)**, the surface spectrum also shows a

LaO-terminated surface after exchange process, and further indicated the presence of contaminations (Na, K, Ca, P, and S) from the exchange process, SIMS measurement or the storage and transport. These contaminants were also only present in the first monoatomic layer (~0.2-0.3 thick), as can be seen in **Figure 8.7 (b)**.

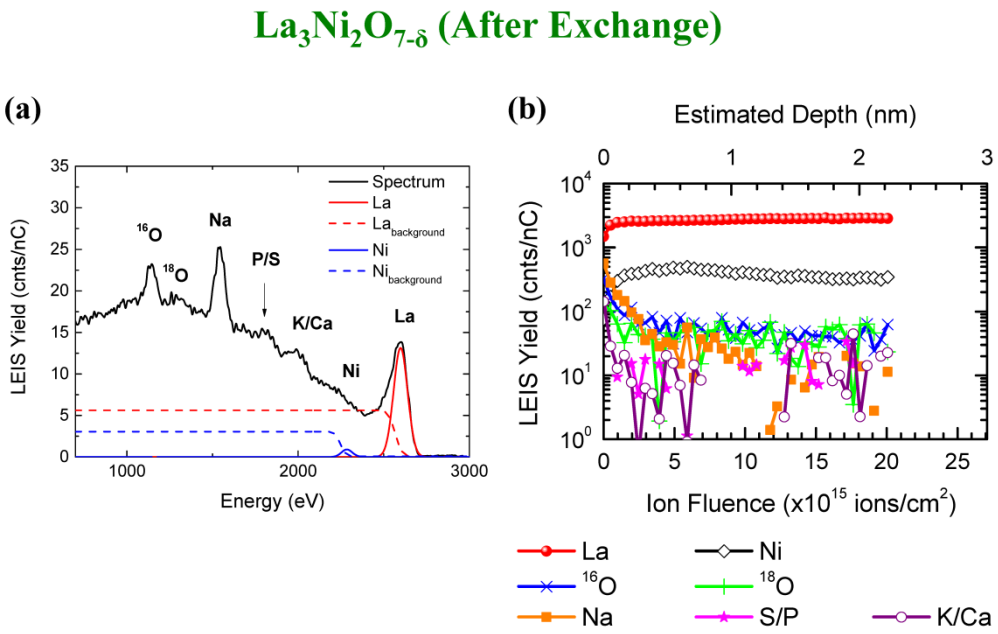


Figure 8.7 LEIS energy spectrum on the outer surface (a) and depth profile (b) of the after-exchanged $La_3Ni_2O_{7-\delta}$ film performed by a 3 keV He^+ ion beam.

A series of analyses of the outer surface composition and depth profiles for after-exchanged samples was also performed using Ne^+ primary ions. Results for the $La_4Ni_3O_{10-\delta}$ film are shown in **Figure 8.8 (a)-(d)**. In **Figure 8.8 (a)**, the contaminants observed in He^+ spectrum above were not detected in the Ne^+ spectrum, as expected, because they are lighter than the Ne primary projectile. **Figures 8.8 (b)-(d)** show the results of the same data treatments described for the as-deposited samples above. A Ni-enriched sub-surface region for the after-exchanged sample was also observed, as can be seen along the horizontal dashed line where the expected Ni/La ratio of 0.75 is indicated in the **Figure 8.8 (d)**. This observation is consistent with the compositional

depth profiles done by SIMS (**Figure 8.1**). Also, as seen at the first data points, it also appears to imply the possibility of the presence of another phase. Again, similar results were also found in the after-exchanged $La_3Ni_2O_{7-\delta}$ sample through analysis using Ne^+, as shown in **Figure 8.9 (a)-(d)**. Again, these observations are consistent with the surface region I observed by SIMS, for which the larger thickness (approximately 4 nm) can be directly related by ion sputter intermixing effects (region of approximately 2.1 nm estimated by SRIM).

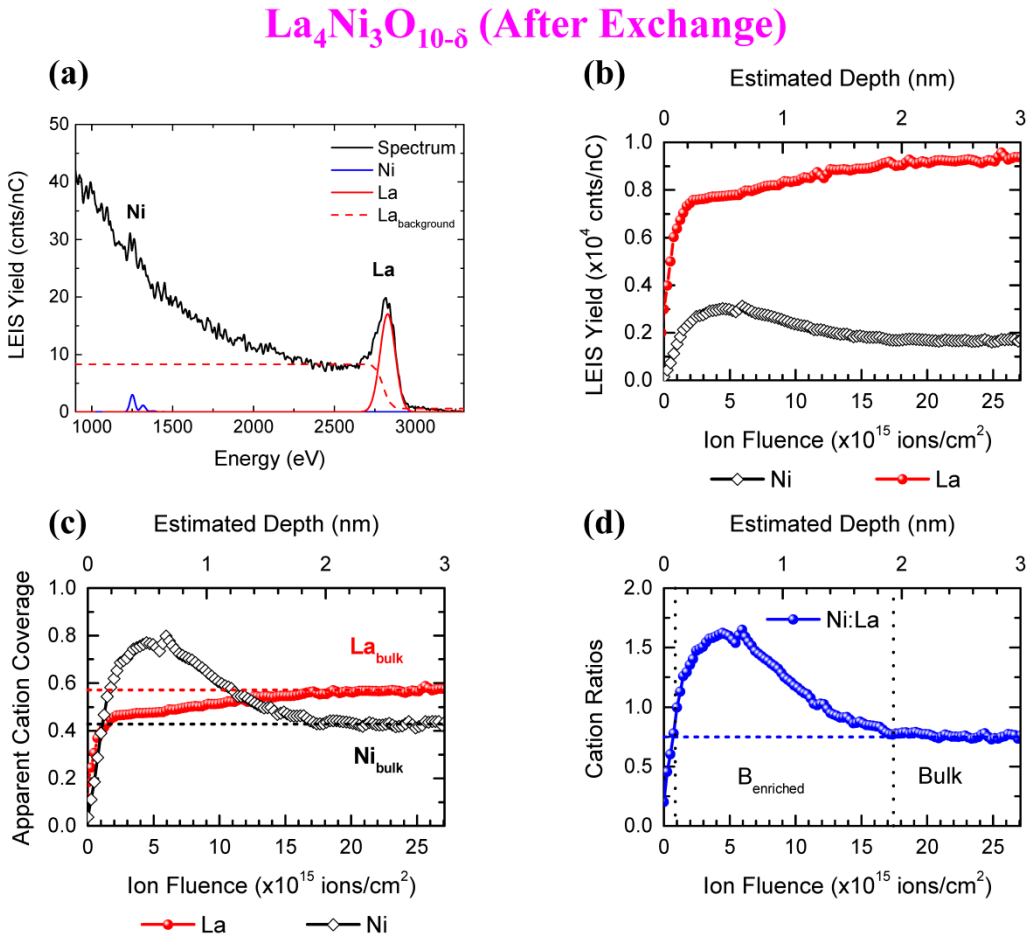


Figure 8.8 (a) LEIS energy spectra of after-exchanged $La_4Ni_3O_{10-\delta}$ film performed on the outer surface by 5 keV Ne^+ ion beams. Normalised cation depth profiles from LEIS spectra obtained after successive sputtering steps, showing (b) the raw yield of La and Ni, (c) apparent cation coverage and (d) cation (Ni:La) ratios plotted with ion fluence, i.e. Ar^+ ion sputtering rate.

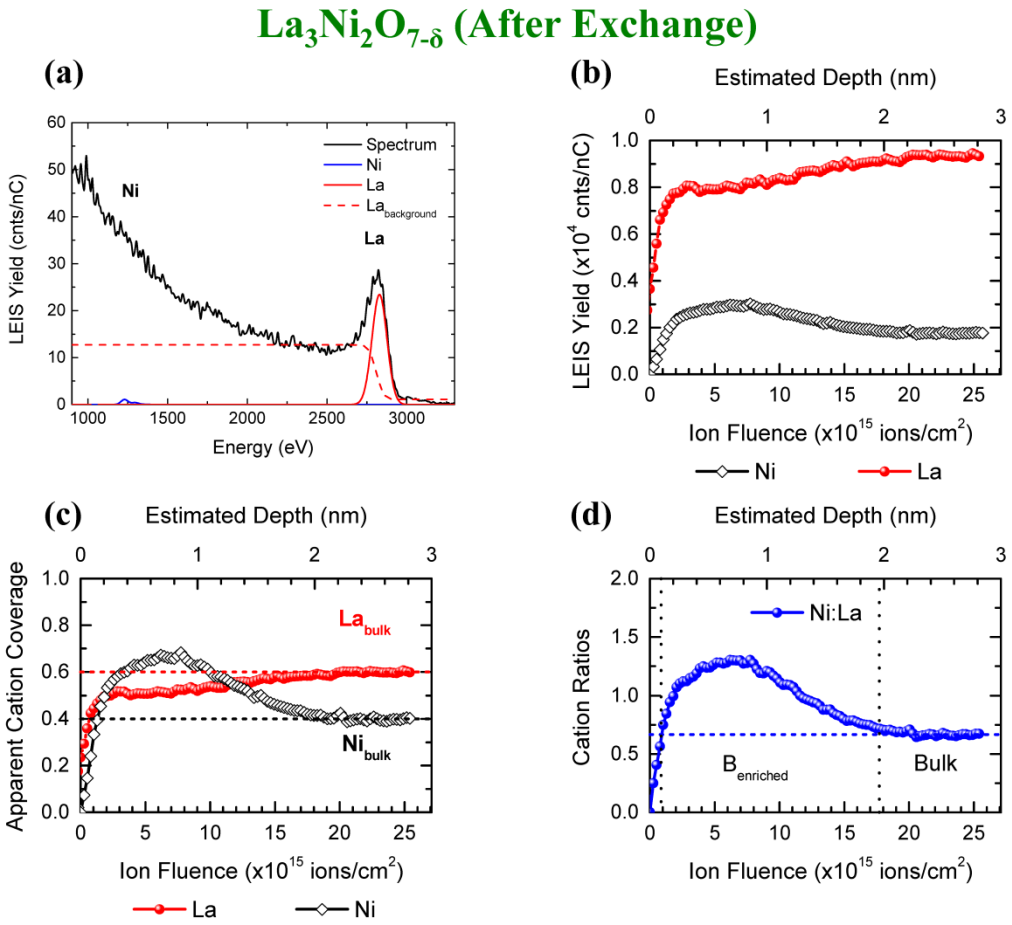


Figure 8.9 (a) LEIS energy spectra of after-exchanged $La_3Ni_2O_{7-\delta}$ film performed on the outer surface by 5 keV Ne^+ ion beams. Normalised cation depth profiles from LEIS spectra obtained after successive sputtering steps, showing (b) the raw yield of La and Ni, (c) apparent cation coverage and (d) cation (Ni:La) ratios plotted with ion fluence, i.e. Ar^+ ion sputtering rate.

Figure 8.10 shows a comparison of the depth profiling cation (Ni:La) ratios of $La_4Ni_3O_{10-\delta}$ films before and after exchange. The Ni-enriched regions of both samples seem to match relatively well. On the other hand, the results of the $La_3Ni_2O_{7-\delta}$ samples before and after exchange are plotted in **Figure 8.11**. Interestingly, in the case of the $La_3Ni_2O_{7-\delta}$ samples, the Ni-enriched region is slightly thicker after exchange. However, it is not possible to determine whether the exchange resulted in the small variation because the two analysed results were not obtained from the same sample (although identical deposition conditions were adopted to produce both samples). Further investigation

should be conducted by HRTEM to visually characterise the atomic structure of these samples on the surface region and correlate these results with the findings found in the effects of post-annealing (seen in Ch.6.3.2).

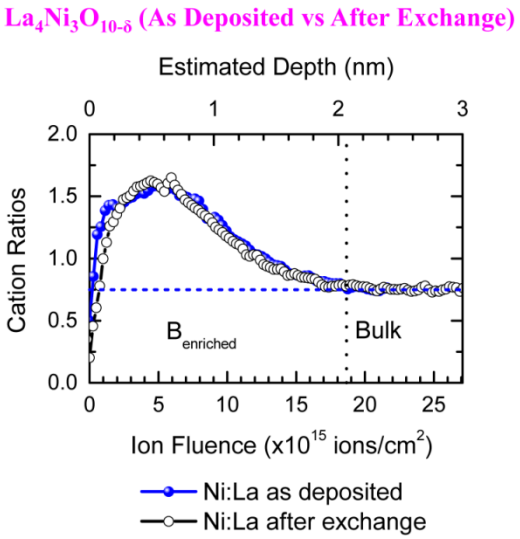


Figure 8.10 Comparison of cation (Ni:La) ratios as a function of depth for as-deposited and after-exchanged $La_4Ni_3O_{10-\delta}$ samples.

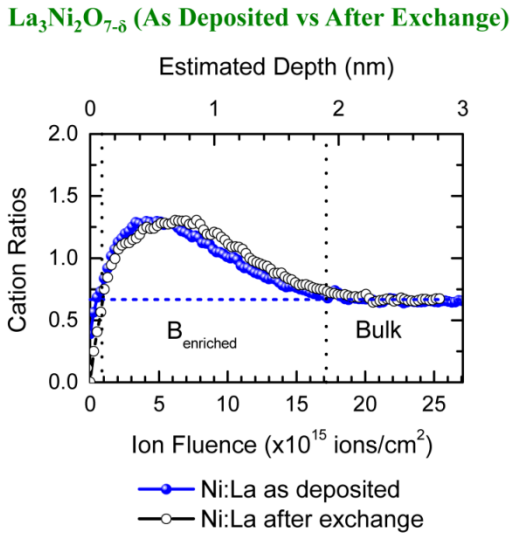


Figure 8.11 Comparison of cation (Ni:La) ratios as a function of depth for as-deposited and after-exchanged $La_3Ni_2O_{7-\delta}$ samples.

8.2.3 Surface Analysis of As-Deposited and Annealed $La_2NiO_{4+\delta}$ Films

For compare with the results presented for $La_3Ni_2O_{7-\delta}$ and $La_4Ni_3O_{10-\delta}$ in previous sections, LEIS experiments were also performed on a $La_2NiO_{4+\delta}$/NGO film sample. The film was deposited by the optimal condition described in Ch.5.1 and 5.2. However, the $La_2NiO_{4+\delta}$ sample was not treated in an ^{18}O isotopic exchange process, but it was annealed in oxygen of normal isotopic abundance with the same period of time (16 h and 21 min) and temperature (500°C) as used for the previous $La_3Ni_2O_{7-\delta}$ and $La_4Ni_3O_{10-\delta}$ samples. It should be noted that all the measurements (including annealing and LEIS experiments) for $La_2NiO_{4+\delta}$ were executed at the International Institute for Carbon Neutral Research (I^2CNER) in Kyushu University, but by the same researcher, Dr. H. Téllez, with a similar type of LEIS equipment.

In the case of the as-deposited sample, **Figure 8.12 (a)** and **(b)** show the He^+ and Ne^+ LEIS spectra for the as-deposited $La_2NiO_{4+\delta}$ film on the outer surface, respectively. It is clear to observe in the He^+ spectrum that the surface of the as-deposited sample has La and ^{16}O elements with only very small amount of the light elements Na and K/Ca, which commonly exist in open atmosphere. From both He^+ and Ne^+ spectra, a LaO-terminated surface was identified for the as-deposited sample. For the annealed sample, no significant change was observed in the He^+ spectrum after annealing, as can be seen in **Figure 8.13 (a)**. This indicated that no significant contamination occurred in the annealing rig, or either storage and transport process. As mentioned above, the annealing rig was different from that used for the measurements of $La_3Ni_2O_{7-\delta}$ and $La_4Ni_3O_{10-\delta}$. Based on such finding, it could be inferred that the serious contaminations on the after-exchanged $La_3Ni_2O_{7-\delta}$ and $La_4Ni_3O_{10-\delta}$ samples (*cf.* **Figure 8.6** and **8.7**) seem to be from the exchange rig. However, as seen in **Figure 8.13 (b)**, it is of interest that an unknown peak was found from the annealed sample via the Ne^+ analysis. According to

the scattering energy, the peak could be Ag or Pd, although it is difficult to assign the peak without a comparison with appropriate reference materials. Also, the unknown element appears to segregate from the film after annealing, as can be observed from the depth profile of elemental signals in **Figure 8.13 (c)**. Such impurity could be originated from the deposition process. As remembered during deposition, the substrate was stick on the heater by Ag paste. After deposition, the Ag paste might remain on the edge of the sample even though a standard cleaning process with acetone, isopropanol and deionised water in an ultrasonic bath for 3 minutes each process was carried out. There might be still the possibility of a small amount remaining on or within the film, which is hard to detect by a XRD measurement.

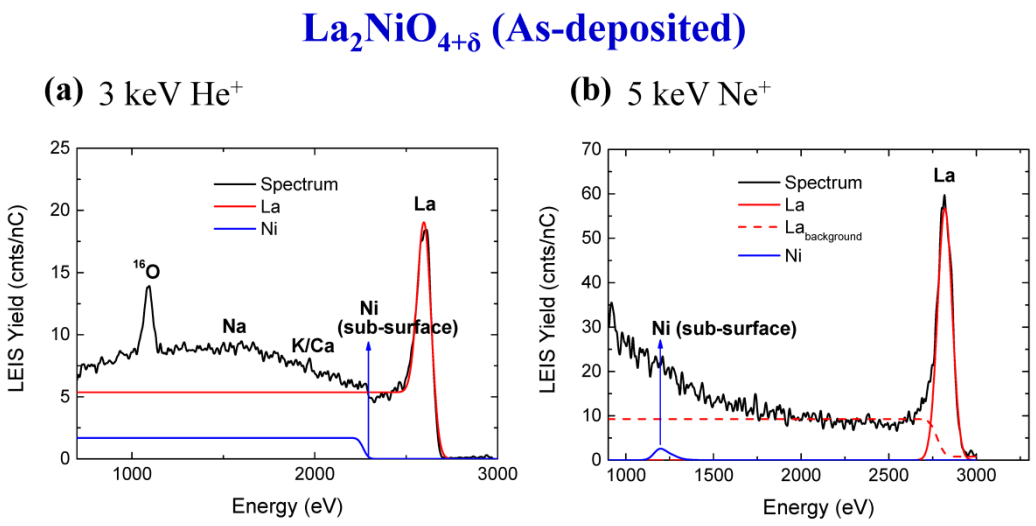


Figure 8.12 LEIS energy spectra of as-deposited $La_2NiO_{4+\delta}$ film performed on the outer surface by (a) 3 keV He^+ and (b) 5 keV Ne^+ ion beams.

Figure 8.14 shows a depth profile of cation (Ni:La) ratios of the $La_2NiO_{4+\delta}$ film before and after annealing. A Ni-enrichment phenomenon (approximately 2.2nm-thick) in the sub-surface region was not only found after annealing, but also after deposition, similar to the observation from the cases of $La_3Ni_2O_{7-\delta}$ and $La_4Ni_3O_{10-\delta}$. This further indicated that the Ni-enrichment likely stemmed from the PLD process. As remembered,

a high temperature treatment (over 700°C) was undertaken during the deposition for the $La_2NiO_{4+\delta}$ film. The results are in good agreement with the previous literature, reported by Gauquelin *et al.* [249]. The authors found nick-rich RP phases at $La_2NiO_{4+\delta}$ single crystal surfaces after a long-term annealing treatment at 1000°C for 13 days. For surface structure of the $La_2NiO_{4+\delta}$ film, a LaO-termination was exhibited either before or after annealing, but no NiO-termination was detected, which may be because the Ni signals was below the detection limit.

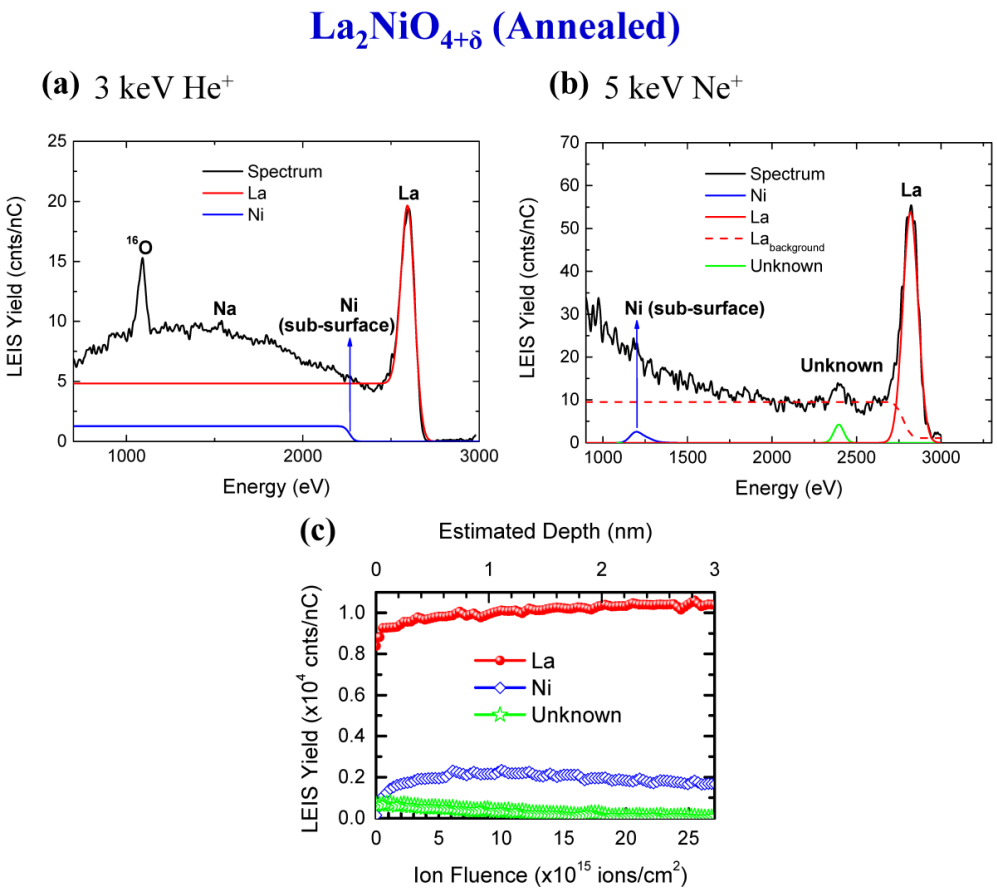


Figure 8.13 LEIS energy spectra of annealed $La_2NiO_{4+\delta}$ film performed on the outer surface by (a) 3 keV He^+ and (b) 5 keV Ne^+ ion beams. (c) depth profile of LEIS yield for La, Ni and a unknown elements analysed by 5 keV Ne^+ ion beams and obtained after successive sputtering steps plotted with ion fluence, i.e. Ar^+ ion sputtering rate.

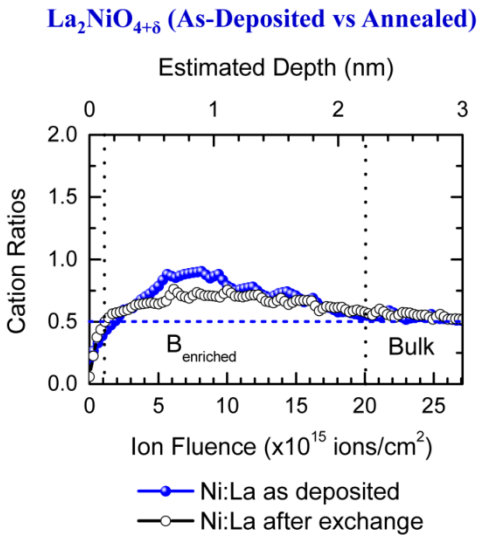


Figure 8.14 Comparison of cation (Ni:La) ratios as a function of depth for as-deposited and annealed $La_2NiO_{4+\delta}$ samples.

8.3 Discussion

To date, only few studies regarding the outermost surface structure and surface chemistry have been experimentally explored through LEIS analysis in RP-type compounds of $La_{n+1}Ni_nO_{3n+1}$ (n = 1, 2 and 3) powder [174], $La_{2-x}Sr_xNiO_{4+\delta}$ single crystal [170], and $Pr_1La_1NiO_{4+\delta}$ polycrystalline bulk [171]. Several examples of perovskite include $LaNiO_3$, $La_{0.6}Sr_{0.4}Co_{0.2}Fe_{0.8}O_{3-\delta}$ [171], $Sm_{1-x}Sr_xCoO_{3-\delta}$ [250]. These experiments all exhibit a AO-termination. In these results, the series of the LEIS analyses above reveal that the outermost surfaces structure of as-deposited $La_3Ni_2O_{7-\delta}$ and $La_4Ni_3O_{10-\delta}$ films shows mixed LaO-NiO terminations. After heat treatment (including exchange and annealing), the surfaces become clearly LaO-terminated, and not NiO-terminated. This implies the presence of reconstruction. The phenomena of reconstruction before and after heat treatments on the outermost surface of the $La_3Ni_2O_{7-\delta}$ and $La_4Ni_3O_{10-\delta}$ films could be not only driven by the segregation of La ions to the surface, but also attributed to other numerous possibilities such as strain effects, various defects, re-orientation, and mixed

intergrowths of the films, as discussed previously in Ch.6.3. In general, AO-terminations dominate the outermost surface in all the measured films, in a good agreement with the experimental literature mentioned above.

In the sub-surface region, it was found that the depth profiling results of LEIS analysis present Ni-enrichments with a thickness of ~2 nm in either as-deposited or after-heat-treatment samples for all $La_2NiO_{4+\delta}$, $La_3Ni_2O_{7-\delta}$, and $La_4Ni_3O_{10-\delta}$ samples. Such finding is perfectly consistent with the compositional depth profiling results obtained by SIMS (see section 8.1), showing that a Ni-enriched region is roughly ~4 nm at surface. This larger thickness region can be directly attributed to the larger projected range of the sputtered beams for SIMS (estimated to be 2.1 nm under the measured conditions).

The significant findings of AO-termination and Ni-enrichment are relevant to the catalytic and electrochemical properties of the series of RP phases. The oxygen reduction reaction is generally assumed to take place at the site of transition metals (i.e. BO-termination) [196, 251]. The result of LaO-termination obtained by LEIS seems to be in conflict with these theoretical aspects, but is in good agreement with observations in other RP phases, as previously explained. It should be noted that the LaO-termination just take place at outermost surface, followed by a Ni-enriched region. According to thermodynamics, entropy dictates that the real surface of materials will not exhibit a perfect structure and a certain content of defects must exist. Read *et al*. found that the formation of oxygen vacancies has lower energy at the surface than in the bulk for the $La_2NiO_{4+\delta}$-related family. This means that these oxygen vacancies on the surface could provide oxygen molecules the opportunity to contact the NiO-sites, which facilitates the occurrence of the oxygen reduction reaction due to charge transfer between the mixed valence state of Ni (Ni^{2+}/Ni^{3+}).

The surface exchange mechanism is still particularly unclear in $La_3Ni_2O_{7-\delta}$ and

$La_4Ni_3O_{10-\delta}$. Unlike the interstitial $La_2NiO_{4+\delta}$, the $La_3Ni_2O_{7-\delta}$ and $La_4Ni_3O_{10-\delta}$ phases are regarded as predominantly oxygen-deficient compounds. In the present work, it is the first time to investigate the outermost and sub-surface information for the the RP-type $La_{n+1}Ni_nO_{3n+1}$ (n = 1, 2 and 3) epitaxial films. These investigations were preliminary studies. To complement the investigations in the future, further investigation by HRTEM analysis will be needed in order to visually observe the surface structure variation before and after heat treatment. Also X-ray photoelectron spectroscopy (XPS) analysis may be conducted to investigate variations in oxidation state near the surface region, which will help to understand the mechanism of electrochemical reaction in the series of epitaxial films [170].

8.4 Summary

Significant cation variations (i.e. Ni-enrichment) of $La_3Ni_2O_{7-\delta}$ and $La_4Ni_3O_{10-\delta}$ films were observed in SIMS depth profiles of surface and film-substrate interface regions. Through the following LEIS analysis on the outer surface, the results of surface cation coverage were totally consistent with the observations in the SIMS measurements.

A systematic LEIS investigation has probed the outermost and sub-surface composition for the RP-type $La_{n+1}Ni_nO_{3n+1}$ (n = 1, 2 and 3) epitaxial films for the first time. During the LEIS investigations, the presence of surface contaminations (Na, K, Ca, P, and S) after isotopic exchange was found. Thus, extra attention has to be paid during the exchange process, to the cleanliness of the rig, as well as during storage and transport in order to avoid cross-contamination. In addition, a clear outermost surface structure of LaO-termination, followed by a Ni-enrichment at sub-surface region was generally found for all epitaxial films after heat treatment. For both $La_3Ni_2O_{7-\delta}$ and $La_4Ni_3O_{10-\delta}$, a mixed

termination of LaO- and NiO-planes was observed in as-deposited samples, whilst only LaO-termination was found after anneal and isotope exchange. This suggests the possibility of the occurrence of reconstruction (absence of Ni) after the heat treatment process for the $La_3Ni_2O_{7-\delta}$ and $La_4Ni_3O_{10-\delta}$ films. Finally, a brief discussion was conducted with literature with regard to the surface information of different SOFC materials. It should be noted that the investigations were clearly preliminary studies. Further studies will be required in order to thoroughly understand these electrochemical mechanisms of oxygen reduction reaction for the series of RP-type lanthanum nickelate epitaxial films.

Chapter 9 Conclusion and Future Work

9.1 Conclusion

Layered RP-type $La_{n+1}Ni_nO_{3n+1}$ (n = 1, 2 and 3) have been considered as promising candidates for SOFC cathodes, in particular the higher order $La_3Ni_2O_{7-\delta}$ and $La_4Ni_3O_{10-\delta}$.phases. The principal aim of this work was to achieve dense, continuous or ideally epitaxial $La_3Ni_2O_{7-\delta}$ and $La_4Ni_3O_{10-\delta}$ films using the PLD technique in order to fundamentally investigate their anisotropic properties and understand their intrinsic functional properties for SOFC applications.

To achieve these studies, the essential prerequisite for PLD target and adopted substrates were discussed in Ch.4. A series of $La_2NiO_{4+\delta}$, $La_3Ni_2O_{7-\delta}$ and $La_4Ni_3O_{10-\delta}$ PLD targets were successfully synthesised using a modified Pechini nitrate-citrate approach. These PLD targets were confirmed to be with appropriate single phase, cation ratio and density for the PLD deposition. Through composition analysis of these PLD targets, a La-segregation phenomenon was found using EDX and ICP. In addition, target degradation and particulate issues for $La_3Ni_2O_{7-\delta}$ and $La_4Ni_3O_{10-\delta}$ during PLA and PLD processes were highlighted. These issues were evaluated to be likely due to the low density of the targets of $La_3Ni_2O_{7-\delta}$ (~50%) and $La_4Ni_3O_{10-\delta}$ (~50%), and are highly associated with the adopted growth conditions (such as laser fluence). Therefore, these issues raised the level of the difficulty of depositing these complex materials. Furthermore, in order to grow c-axis oriented films for these RP phases, two different well-defined single crystals of STO (001) and NGO (110) were selected as the substrates. Different surface roughness of these substrates from different commercial batches was carefully taken into account because they have significantly influenced the productivity of these RP

films, particularly for higher order phases.

To date, there is an absence of research on the deposition of the higher order RP lanthanum nickelate (n = 2 and 3) using PLD. Therefore, a series of depositions and charaterisations for $La_2NiO_{4+\delta}$ (n = 1) were first investigated in Ch.5 in order to determine appropriate deposition conditions and substrate for the higher order $La_3Ni_2O_{7-\delta}$ and $La_4Ni_3O_{10-\delta}$ film growth. During these depositions, reorientation phenomena of the c-axis oriented $La_2NiO_{4+\delta}$ films deposited on STO (001) were observed. These reorientation phenomena were driven by various growth conditions, covering different oxygen pressures, deposition temperatures, number of laser pulses and laser fluence. Additionally, an island (Volmer-Weber) growth mode was proposed for the $La_2NiO_{4+\delta}$ films through the studies of the influence of laser pulses. Finally, the optimal growth conditions were determined for the growth of high quality c-axis oriented layered RP-type $La_2NiO_{4+\delta}$ epitaxial films deposited on STO and NGO substrates.

The high quality growth of these $La_2NiO_{4+\delta}$ films was verified through a series of structure characterisation and AFM analysis. However, the film deposited on NGO shows much better crystallinity (FWHM: 0.11°) and lower surface roughness (RMS: ~1.8 nm) than the films deposited on STO (FWHM: 0.55°, RMS: ~3 nm). Thus, the NGO substrate was decided as the substrate for the deposition of the higher order RP phases. Furthermore, the results of total planar electrical conductivity for the $La_2NiO_{4+\delta}$ films deposited on STO and NGO were in good agreement with literature data through 4-point DC van der Pauw measurements, indicating the validation of the growth of $La_2NiO_{4+\delta}$.

Using the growth conditions determined from $La_2NiO_{4+\delta}$, a series of depositions were systematically conducted to finely adjust the growth conditions for both $La_3Ni_2O_{7-\delta}$ and $La_4Ni_3O_{10-\delta}$ films, including deposition temperature, laser fluence and laser repetition rate (Ch.6.1). Eventually, good quality of high order c-axis oriented films has been

achieved with good crystallinity and very low surface roughness for $La_3Ni_2O_{7-\delta}$ (FWHM: 0.18°, RMS: ~0.2 nm) and $La_4Ni_3O_{10-\delta}$ (FWHM: 0.15°, RMS: ~0.2 nm). In particular, epitaxial growth by PLD of the higher order phases (n = 2 and 3) of lanthanum nickelate has been demonstrated for the first time. The dense and continuous features of the $La_4Ni_3O_{10-\delta}$ film were confirmed by the observation of low-magnification cross-section HAADF-STEM images, which was one of the main goals for the research.

The influences of microstructural variation of the $La_3Ni_2O_{7-\delta}$ and $La_4Ni_3O_{10-\delta}$ epitaxial films were further investigated through film thickness and post-annealing effects (Ch.6.3). In the investigation of film thickness effect, the obtained $La_3Ni_2O_{7-\delta}$ showed fairly well-defined pure-phase films with increasing film thickness while the $La_4Ni_3O_{10-\delta}$ films seemed to have a mixture of different phase intergrowths as film thickness increased. Such conclusion was based on a series of systematic crystallographic, compositional, and surface morphological analyses. The findings from the microstructural observation also revealed the possibilities of accumulating higher level of intergrowths, misalignment and defects with increasing film thickness. These results strongly corresponded to the influence of the target degradation during the rather high-temperature PLA process, as found from the previous studies (Ch.4). Also, a critical thickness of ~50 nm was found for growing both higher order epitaxial films. For the post-annealing effect (i.e. post-anneal after deposition in the deposition chamber), a remarkable impact was observed, showing a random distribution of LaO layers along the direction perpendicular and parallel to the growth direction within the film matrix. The phenomenon could be enhanced as a high oxygen pressure was applied for the treatment.

The obtained $La_3Ni_2O_{7-\delta}$ and $La_4Ni_3O_{10-\delta}$ films also showed good thermal stability behaviour after a three-cycle electrical measurement from RT to 700°C in air for a month in total, including an aging treatment at 700°C in air for over 2 weeks (approximately 350

h in total). This finding suggested that both films could be suitable for the potential SOFC applications.

The total planar electrical conductivity of c-axis oriented $La_3Ni_2O_{7-\delta}$ and $La_4Ni_3O_{10-\delta}$ films were investigated using the 4-point DC van der Pauw method (Ch.7.1). The electrical measurements were performed as a function of temperature through the influence of film thickness, cycling measurement and comparative study. For the influence of film thickness, all the $La_3Ni_2O_{7-\delta}$ films presented semiconducting-to-metallic behaviour and generally increased with increasing film thickness, while $La_4Ni_3O_{10-\delta}$ films exhibited a clear evolution of electrical conductivity from metallic to semiconducting-to-metallic behaviour with increasing film thickness. This strongly suggested the influence of microstructural variation; i.e. $La_4Ni_3O_{10-\delta}$ films likely have a strong effect of accumulating higher level of intergrowths, misalignments and defects with increasing film thickness. These findings also corresponded to the results obtained from the previous crystallographic, compositional, surface morphology and microstructural analyses, indicating the obtained $La_3Ni_2O_{7-\delta}$ films showed a better quality than the $La_4Ni_3O_{10-\delta}$ films.

In the cycling measurements, all the $La_3Ni_2O_{7-\delta}$ and $La_4Ni_3O_{10-\delta}$ films of different thicknesses generally exhibited reversible electrical conductivity, indicating the good stability of these films. For comparison, the planar electrical conductivity results of these obtained c-axis oriented $La_2NiO_{4+\delta}$ (n = 1), $La_3Ni_2O_{7-\delta}$ (n = 2) and $La_4Ni_3O_{10-\delta}$ (n = 3) films presented a systematic enhancement with increasing “n” value, and showed much larger conductivity than the randomly oriented polycrystalline samples. In particular, the higher order $La_3Ni_2O_{7-\delta}$ and $La_4Ni_3O_{10-\delta}$ films exhibit promising electrical conductivity values of approximately 700-1000 Scm^{-1}, which is potentially suitable for IT-SOFC applications.

Several studies on oxygen diffusion coefficient (D^*) and surface exchange coefficient (k^*) along c-axis in the $La_3Ni_2O_{7-\delta}$ and $La_4Ni_3O_{10-\delta}$ films were performed by IEDP-SIMS measurements (Ch.7.2). These results not only confirmed the deposited $La_3Ni_2O_{7-\delta}$ and $La_4Ni_3O_{10-\delta}$ films are dense and continuous enough for the measurements, but also provides the first information with respect to the oxygen diffusion and surface exchange coefficients of these higher order RP films.

Through SIMS depth profiles analysis, significant cation variations (i.e. Ni-enrichment) of $La_3Ni_2O_{7-\delta}$ and $La_4Ni_3O_{10-\delta}$ films were observed at surface and film-interface regions (Ch.8.1). The LEIS analysis on the outer surface further supported the phenomenon of cation segregation (Ch.8.2). In addition, a clear outermost surface structure of LaO-termination, followed by a Ni-enrichment in the sub-surface region was generally found for all $La_{n+1}Ni_nO_{3n+1}$ (n = 1, 2 and 3) epitaxial films after heat treatment. For both $La_3Ni_2O_{7-\delta}$ and $La_4Ni_3O_{10-\delta}$, a mixed termination of LaO- and NiO-planes was observed in as-deposited samples, whilst only LaO-termination was found after the anneal and isotope exchange. This implied the possibility of the occurrence of reconstruction (absence of Ni) after the heat treatment process for the $La_3Ni_2O_{7-\delta}$ and $La_4Ni_3O_{10-\delta}$ films. These findings also provide the first information of the outer surface of the c-axis oriented $La_{n+1}Ni_nO_{3n+1}$ (n = 1, 2 and 3) epitaxial films through LEIS analysis.

9.2 Future Work

Based on the fundamental research of these layered RP lanthanum nickelate materials throughout the work, a number of proposed studies would be further investigated in the future. For example, RP-phases possess natural heterostructures with alternating blocks of perovskite and rock-salt. Perhaps utilising the PLD with the in-situ reflection high-energy

electron diffraction (RHEED) monitoring technique it would be possible to grow the RP-type films layer-by-layer (i.e. perovskite and rock-salt layers), and may further improve the film quality.

Measuring the electrical conductivity of these RP $La_3Ni_2O_{7-\delta}$ and $La_4Ni_3O_{10-\delta}$ epitaxial films under different atmospheres (e.g. O_2 and N_2) would be of interest in order to figure out whether any significant difference of conductivity can be influenced by atmosphere.

To determine the activation energies of oxygen diffusion and surface exchange behaviour for the $La_3Ni_2O_{7-\delta}$ and $La_4Ni_3O_{10-\delta}$ phases, the anisotropic oxygen diffusion measurements along the c-axis and particularly a,b-directions under various temperatures should be further systematically investigated in the future. Moreover, these investigations should also be along with microstructural analysis through HRTEM in order to understand the influence of film microstructure on the ionic transport properties. Also, the HRTEM would help to understand the oxygen diffusion mechanism of the higher order RP films.

To complement the surface and interface analyses via SIMS and LEIS, further HRTEM analyses will be also required. It would be interesting to visually observe the microstructure of the films before and after isotopic exchange in order to evaluate whether there is any segregation, compositional variation, and reconstruction at the surface and the interface of these RP films.

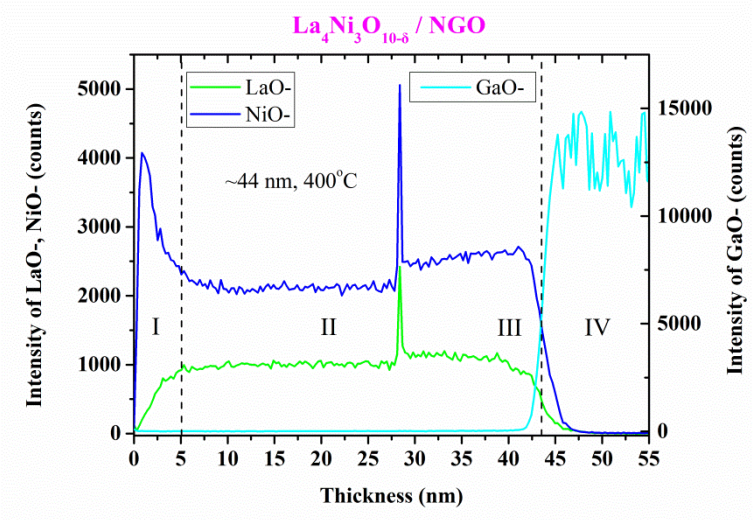
It is of interest to investigate whether growing heteroepitaxial films of these oxides will enhance electrical and electrochemical properties in SOFC cathodes. It would be beneficial to study the correlation of strain effect with electrical conductivity, oxygen diffusion and surface exchange properties for the high order RP epitaxial films through growing these films on different substrates. The studies on the other related higher order

RP-type Pr- and Nd-substituted nickelate films are also of interest.

In addition to the fundamental research, the layered RP films could be applied for the potential micro-SOFCs (μSOFCs) applications for portable devices such as laptop and mobile phones. Once suitable RP-type thin-film materials have been identified and well-understood, they would be used to fabricate devices and to evaluate the performance of these devices.

Appendices

Appendix I



Compositional depth profiles for LaO^-, NiO^-, and GaO^- secondary ion species in 44nm-thick $La_4Ni_3O_{10-\delta}$ films deposited on NGO after an oxygen isotope exchange at approximately 400°C. Region I, II, III and IV represent surface of film, film, film-substrate interface and substrate. The dashed lines identify the middle area between surface of film (I) and film (II); the middle interface area between film (III) and substrate (IV). Note that the sharp peaks observed from the depth profiles of LaO^- and NiO^- were caused by an unstable beam current supply during the SIMS measurement.

Bibliography

1. Tanaka, N., *World Energy Outlook*, N. Tanaka, Editor 2009. p. 58.
2. Dudley, B., *BP Energy Outlook 2030*, 2011. p. 8.
3. Tanaka, N., *World Energy Outlook*, N. Tanaka, Editor 2009. p. 74-75.
4. Stambouli, A.B. and E. Traversa, *Solid oxide fuel cells (SOFCs): a review of an environmentally clean and efficient source of energy.* Renewable and Sustainable Energy Reviews, 2002. **6**(5): p. 433-455.
5. Züttel, A., et al., *Hydrogen: the future energy carrier.* Philosophical Transactions of the Royal Society A: Mathematical, Physical and Engineering Sciences, 2010. **368**(1923): p. 3329-3342.
6. Marquis, M. and P. Tans, *A primer on climate change*, in *Fundamentals of Materials for Energy and Environmental Sustainability*, D.S. Ginley and D. Cahen, Editors. 2012, MRS, Cambridge University Press. p. 2-25.
7. Larminie, J., A. Dicks, and Knovel, *Fuel cell systems explained*. 2003: Wiley New York.
8. O'Hayre, R., et al., *Fuel Cell Fundamentals*. 2nd ed. 2009.
9. Steele, B.C.H. and A. Heinzel, *Materials for fuel-cell technologies.* Nature, 2001. **414**(6861): p. 345-352.
10. Wachsman, E.D. and K.T. Lee, *Lowering the Temperature of Solid Oxide Fuel Cells.* Science, 2011. **334**(6058): p. 935-939.
11. Brett, D.J.L., et al., *Intermediate temperature solid oxide fuel cells.* Chemical Society Reviews, 2008. **37**(8): p. 1568-1578.
12. Kreuer, K.-D., *Fuel Cells, Introduction*, in *Fuel Cells: Selected Entries from the Encyclopedia of Sustainability Science and Technology*, K.-D. Kreuer, Editor. 2013, Springer. p. 3.
13. Brandon, N.P., S. Skinner, and B.C.H. Steele, *Recent advances in materials for fuel cells.* Annual Review of Materials Research, 2003. **33**: p. 183-213.
14. Weber, A. *Transport and reaction mechanism in a SOFC*. [cited 2013 12/25]; Available from: http://www.iwe.kit.edu/english/mitarbeiter_sofc.php.
15. Jiang, S.P. and S.H. Chan, *A review of anode materials development in solid oxide fuel cells.* Journal of Materials Science, 2004. **39**(14): p. 4405-4439.
16. Jacobson, A.J., *Materials for Solid Oxide Fuel Cells.* Chemistry of Materials, 2010. **22**(3): p. 660-674.
17. Adler, S.B., *Factors governing oxygen reduction in solid oxide fuel cell cathodes.* Chemical Reviews, 2004. **104**(10): p. 4791-4843.

18. Goodenough, J.B., *Review Lecture: Fast Ionic Conduction in Solids.* Proceedings of the Royal Society of London. Series A, Mathematical and Physical Sciences, 1984. **393**(1805): p. 215-234.
19. Orera, A. and P.R. Slater, *New Chemical Systems for Solid Oxide Fuel Cells.* Chemistry of Materials, 2009.
20. Aguadero, A., et al., *Materials development for intermediate-temperature solid oxide electrochemical devices.* Journal of Materials Science, 2012. **47**(9): p. 3925-3948.
21. Yokokawa, H. and T. Horita, *Cathodes*, in *High Temperature Solid Oxide Fuel Cells: Fundamentals, Design and Applications*, S.C. Singhal and K. Kendall, Editors. 2003, Elsevier. p. 119-147.
22. Kawada, T., *Peroskite Oxide for Cathode of SOFCs*, in *Perovskite Oxide for Solid Oxide Fuel Cells*, T. Ishihara, Editor. 2009, Springer. p. 147-166.
23. Sun, C., R. Hui, and J. Roller, *Cathode materials for solid oxide fuel cells: a review.* Journal of Solid State Electrochemistry, 2010. **14**(7): p. 1125-1144.
24. Singhal, S.C. and K. Kendall, *High Temperature Solid Oxide Fuel Cells: Fundamentals, Design and Applications*. 2003: Elsevier.
25. Singhal, S.C., *Advances in solid oxide fuel cell technology.* Solid State Ionics, 2000. **135**(1-4): p. 305-313.
26. Skinner, S.J., *Recent advances in Perovskite-type materials for solid oxide fuel cell cathodes.* International Journal of Inorganic Materials, 2001. **3**(2): p. 113-121.
27. Skinner, S.J. and J.A. Kilner, *Oxygen ion conductors.* Materials Today, 2003. **6**(3): p. 30-37.
28. Istomin, S.Y. and E.V. Antipov, *Cathode materials based on perovskite-like transition metal oxides for intermediate temperature solid oxide fuel cells.* Russian Chemical Reviews, 2013. **82**(7): p. 686.
29. Tsipis, E.V. and V.V. Kharton, *Electrode materials and reaction mechanisms in solid oxide fuel cells: a brief review I. Performance-determining factors* Journal of Solid State Electrochemistry, 2007. **12**(9): p. 1039-1060.
30. Tarancon, A., et al., *Advances in layered oxide cathodes for intermediate temperature solid oxide fuel cells.* Journal of Materials Chemistry, 2010. **20**(19): p. 3799-3813.
31. Takahashi, S., et al., *Electrode Properties of the Ruddlesden–Popper Series, $La_{n+1}Ni_nO_{3n+1}$ (n=1, 2, and 3), as Intermediate-Temperature Solid Oxide Fuel Cells.* Journal of the American Ceramic Society, 2010. **93**(8): p. 2329-2333.
32. Amow, G. and S.J. Skinner, *Recent developments in Ruddlesden-Popper nickelate systems for solid oxide fuel cell cathodes.* Journal of Solid State Electrochemistry, 2006. **10**(8): p. 538-546.

33. Amow, G., I.J. Davidson, and S.J. Skinner, *A comparative study of the Ruddlesden-Popper series, $La_{n+1}Ni_nO_{3n+1}$ (n=1, 2 and 3), for solid-oxide fuel-cell cathode applications.* Solid State Ionics, 2006. **177**(13-14): p. 1205-1210.
34. Bassat, J.M., et al., *Anisotropic ionic transport properties in $La_2NiO_{4+\delta}$ single crystals.* Solid State Ionics, 2004. **167**(3-4): p. 341-347.
35. Tsipis, E.V. and V.V. Kharton, *Electrode materials and reaction mechanisms in solid oxide fuel cells: a brief review II. Electrochemical behavior vs. materials science aspects.* Journal of Solid State Electrochemistry, 2008. **12**(11): p. 1367-1391.
36. Santiso, J. and M. Burriel, *Deposition and characterisation of epitaxial oxide thin films for SOFCs.* Journal of Solid State Electrochemistry, 2010: p. 1-22.
37. Chroneos, A., et al., *Anisotropic oxygen diffusion in tetragonal $La_2NiO_{4+\delta}$: molecular dynamics calculations.* Journal of Materials Chemistry, 2010. **20**(2): p. 266-270.
38. Frayret, C., A. Villesuzanne, and M. Pouchard, *Application of density functional theory to the modeling of the mixed ionic and electronic conductor $La_2NiO_{4+\delta}$: Lattice relaxation, oxygen mobility, and energetics of Frenkel defects.* Chemistry of Materials, 2005. **17**(26): p. 6538-6544.
39. Garcia, G., et al., *Electrical conductivity and oxygen exchange kinetics of $La_2NiO_{4+\delta}$ thin films grown by chemical vapor deposition.* Journal of the Electrochemical Society, 2008. **155**(3): p. P28-P32.
40. Burriel, M., et al., *Enhancing total conductivity of $La_2NiO_{4+\delta}$ epitaxial thin films by reducing thickness.* Journal of Physical Chemistry C, 2008. **112**(29): p. 10982-10987.
41. Burriel, M., et al., *Anisotropic oxygen diffusion properties in epitaxial thin films of $La_2NiO_{4+\delta}$.* Journal of Materials Chemistry, 2008. **18**(4): p. 416-422.
42. Kim, G., et al., *Measurement of oxygen transport kinetics in epitaxial $La_2NiO_{4+\delta}$ thin films by electrical conductivity relaxation.* Solid State Ionics, 2006. **177**(17-18): p. 1461-1467.
43. Ruddlesden, S. and P. Popper, *The compound $Sr_3Ti_2O_7$ and its structure.* Acta Crystallographica, 1958. **11**(1): p. 54-55.
44. Voronin, V.I., et al., *Neutron diffraction, synchrotron radiation and EXAFS spectroscopy study of crystal structure peculiarities of the lanthanum nickelates $La_{n+1}Ni_nO_y$ (n=1,2,3).* Nuclear Instruments & Methods in Physics Research Section a-Accelerators Spectrometers Detectors and Associated Equipment, 2001. **470**(1-2): p. 202-209.
45. Ling, C.D., et al., *Neutron diffraction study of $La_3Ni_2O_7$: Structural relationships among n=1, 2, and 3 phases $La_{n+1}Ni_nO_{3n+1}$.* Journal of Solid State Chemistry,

2000. **152**(2): p. 517-525.

46. Greenblatt, M., *Ruddlesden-Popper $Ln_{n+1}Ni_nO_{3n+1}$ nickelates: structure and properties.* Current Opinion in Solid State & Materials Science, 1997. **2**(2): p. 174-183.
47. Zhang, Z. and M. Greenblatt, *Synthesis, Structure, and Properties of $Ln_4Ni_3O_{10-\delta}$ (Ln = La, Pr, and Nd).* Journal of Solid State Chemistry, 1995. **117**(2): p. 236-246.
48. Greenblatt, M., Z. Zhang, and M.H. Whangbo, *Electronic properties of $La_3Ni_2O_7$ and $Ln_4Ni_3O_{10}$, Ln=La, Pr and Nd* Synthetic Metals, 1997. **85**(1-3): p. 1451-1452.
49. Kobayashi, Y., et al., *Transport and magnetic properties of $La_3Ni_2O_{7-\delta}$ and $La_4Ni_3O_{10-\delta}$.* Journal of the Physical Society of Japan, 1996. **65**(12): p. 3978-3982.
50. Taniguchi, S., et al., *Transport, Magnetic and Thermal Properties of $La_3Ni_2O_{7-\delta}$.* Journal of the Physical Society of Japan, 1995. **64**(5): p. 1644-1650.
51. Zhang, Z., M. Greenblatt, and J.B. Goodenough, *Synthesis, Structure, and Properties of the Layered Perovskite $La_3Ni_2O_{7-\delta}$.* Journal of Solid State Chemistry, 1994. **108**(2): p. 402-409.
52. Perez-Coll, D., et al., *Effect of DC current polarization on the electrochemical behaviour of $La_2NiO_{4+\delta}$ and $La_3Ni_2O_{7+\delta}$-based systems.* Journal of Power Sources, 2009. **192**(1): p. 2-13.
53. Carvalho, M.D., et al., *Influence of oxygen stoichiometry on the electronic properties of $La_4Ni_3O_{10\pm\delta}$.* Journal of Applied Physics, 2000. **88**(1): p. 544-549.
54. Amow, G., J. Au, and I. Davidson, *Synthesis and characterization of $La_4Ni_{3-x}Co_xO_{10\pm\delta}$ ($0.0 \leq x \leq 3.0$, $\Delta x=0.2$) for solid oxide fuel cell cathodes.* Solid State Ionics, 2006. **177**(19-25): p. 1837-1841.
55. Nedilko, S.A., et al., *Oxygen nonstoichiometry and properties of lanthanum nickelates $La_{3-x}Ca_xNi_2O_{7-\delta}$ ($0 \leq x \leq 2.0$)* Journal of Alloys and Compounds, 2004. **367**(1-2): p. 251-254.
56. Zhang, Z. and M. Greenblatt, *Synthesis, Structure, and Physical Properties of $La_{3-x}MxNi_2O_{7-\delta}$ ($M = Ca^{2+}, Sr^{2+}, Ba^{2+}$; $0 < x \leq 0.075$)* Journal of Solid State Chemistry, 1994. **111**(1): p. 141-146.
57. Bassat, J.-M., et al., *Anisotropic Oxygen Diffusion Properties in $Pr_2NiO_{4+\delta}$ and $Nd_2NiO_{4+\delta}$ Single Crystals.* The Journal of Physical Chemistry C, 2013. **117**(50): p. 26466-26472.
58. Jorgensen, J.D., et al., *Superconducting Phase of $La_2CuO_{4+\delta}$: a Superconducting Composition Resulting from Phase-Separation.* Physical Review B, 1988. **38**(16): p. 11337-11345.
59. Spalek, J., Z. Kakol, and J.M. Honig, *Onset of superconductivity, antiferromagnetism, and exchange-mediated pairing in $La_{2-x}Sr_xNiO_4$* Solid State Communications, 1989. **71**(6): p. 511-515.

60. Kakol, Z., J. Spalek, and J.M. Honig, *Superconductivity and antiferromagnetism in $La_{2-x}Sr_xNiO_4$.* Journal of Solid State Chemistry, 1989. **79**(2): p. 288-292.
61. Kakol, Z., J. Spalek, and J.M. Honig, *Onset of Superconductivity in Antiferromagnetic La_2NiO_4.* Solid State Communications, 1989. **71**(4): p. 283-286.
62. Hücker, M., et al., *Oxygen and strontium codoping of La_2NiO_4: Room-temperature phase.* Physical Review B, 2004. **70**(6): p. 064105.
63. Skinner, S.J., *Characterisation of $La_2NiO_{4+\delta}$ using in-situ high temperature neutron powder diffraction.* Solid State Sciences, 2003. **5**(3): p. 419-426.
64. Paulus, W., et al., *Neutron diffraction studies of stoichiometric and oxygen intercalated La_2NiO_4 single crystals.* Solid State Sciences, 2002. **4**(5): p. 565-573.
65. Burns, G., et al., *Low-temperature structural phase transition in $La_2NiO_{4+\delta}$.* Physical Review B, 1990. **42**(16): p. 10777.
66. Rodriguez-Carvajal, J., M.T. Fernandezdiaz, and J.L. Martinez, *Neutron-Diffraction Study on Structural and Magnetic-Properties of La_2NiO_4.* Journal of Physics-Condensed Matter, 1991. **3**(19): p. 3215-3234.
67. Demourgues, A., et al., *Electrochemical Preparation and Structural Characterization of $La_2NiO_{4+\delta}$ Phases ($0 \leq \delta \leq 0.25$).* Journal of Solid State Chemistry, 1993. **105**(2): p. 458-468.
68. Boehm, E., et al., *Oxygen transport properties of $La_2Ni_{1-x}Cu_xO_{4+\delta}$ mixed conducting oxides.* Solid State Sciences, 2003. **5**(7): p. 973-981.
69. Naumovich, E.N., et al., *Oxygen nonstoichiometry in $La_2Ni(M)O_{4+\delta}$ (M = Cu, Co) under oxidizing conditions.* Solid State Sciences, 2005. **7**(11): p. 1353-1362.
70. Carvalho, M.D., et al., *Electrochemical oxidation and reduction of $La_4Ni_3O_{10}$ in alkaline media.* Journal of Solid State Electrochemistry, 2003. **7**(10): p. 700-705.
71. Yoo, S., et al., *Electrical properties, thermodynamic behavior, and defect analysis of $La_{n+1}Ni_nO_{3n+1+\delta}$ infiltrated into YSZ scaffolds as cathodes for intermediate-temperature SOFCs.* RSC Advances, 2012. **2**(11): p. 4648-4655.
72. Bannikov, D.O. and V.A. Cherepanov, *Thermodynamic properties of complex oxides in the La-Ni-O system.* Journal of Solid State Chemistry, 2006. **179**(8): p. 2721-2727.
73. Zinkevich, M., et al., *Stability and thermodynamic functions of lanthanum nickelates.* Journal of Alloys and Compounds, 2007. **438**(1-2): p. 92-99.
74. Rao, C.N.R., A.K. Ganguli, and R. Nagarajan, *Superconductivity in Layered Nickel Oxides.* Pramana, 1989. **32**(2): p. L177-L179.
75. Ram, R.A.M., et al., *Evolution of three-dimensional character across the $La_{n+1}NinO_{3n+1}$ homologous series with increase in n.* Journal of Solid State Chemistry, 1986. **63**(2): p. 139-147.

76. Drennan, J., C.P. Tavares, and B.C.H. Steele, *An Electron-Microscope Investigation of Phases in the System La-Ni-O.* Materials Research Bulletin, 1982. **17**(5): p. 621-626.
77. Carvalho, M.D., et al., *New preparation method of $La_{n+1}Ni_nO_{3n+1-\delta}$ (n = 2, 3).* Journal of Materials Chemistry, 1997. **7**(10): p. 2107-2111.
78. Zinkevich, M. and F. Aldinger, *Thermodynamic analysis of the ternary La-Ni-O system.* Journal of Alloys and Compounds, 2004. **375**(1-2): p. 147-161.
79. Fontaine, M.L., et al., *Synthesis of $La_2NiO_{4+\delta}$ oxides by sol–gel process: Structural and microstructural evolution from amorphous to nanocrystallized powders* Materials Research Bulletin, 2006. **41**(9): p. 1747-1753.
80. Fontaine, M.L., et al., *Synthesis of $La_{2-x}NiO_{4+\delta}$ oxides by polymeric route: non-stoichoimetry control.* Ceramics International, 2004. **30**(8): p. 2087-2098.
81. Fontaine, M.L., et al., *Elaboration and characterization of $La_2NiO_{4+\delta}$ powders and thin films via a modified sol–gel process* Journal of Solid State Chemistry, 2004. **177**(4-5): p. 1471-1479.
82. Faucheux, V., S. Pignard, and M. Audier, *Growth of La_2NiO_4 thin films by chemical vapor deposition.* Journal of Crystal Growth, 2005. **275**(1-2): p. e947-e951.
83. Podpirka, A., V. Balakrishnan, and S. Ramanathan, *Heteroepitaxy and crystallographic orientation transition in $La_{1.875}Sr_{0.125}NiO_4$ thin films on single crystal $SrTiO_3$.* Journal of Materials Research, 2013. **28**(11): p. 1420-1431.
84. Telesca, D., B.O. Wells, and B. Sinkovic, *Structural reorientation of PLD grown La_2NiO_4 thin films.* Surface Science, 2012. **606**(9–10): p. 865-871.
85. Kim, G.T., et al., *Impedance studies of dense polycrystalline thin films of $La_2NiO_{4+\delta}$.* Journal of Materials Chemistry, 2007. **17**(13): p. 1316-1320.
86. Jang, W.J., et al., *Growth and structure of $La_2NiO_{4+\delta}$ ($0.19 \geq \delta \geq 0.12$) single crystals* Journal of Crystal Growth, 1995. **152**(3): p. 158-168.
87. Bassat, J.M., et al., *Anisotropic transport properties of La_2NiO_4 single crystals.* Materials Science and Engineering: B, 1989. **3**(4): p. 507-514.
88. Weng, X., et al., *Direct syntheses of $La_{n+1}Ni_nO_{3n+1}$ phases (n=1, 2, 3 and ∞) from nanosized co-crystallites.* Journal of Solid State Chemistry, 2008. **181**(5): p. 1123-1132.
89. Raju, A.R., H.N. Aiyer, and C.N.R. Rao, *Oriented Films of $LaNiO_{3-\delta}$ and Other Members of the $La_{n+1}Ni_nO_{3n+1}$ Series, $LaCuO_{3-\delta}$ and $Pb(Zr_{0.52}Ti_{0.48})O_3$, Obtained by Nebulized Spray-Pyrolysis.* Chemistry of Materials, 1995. **7**(1): p. 225-231.
90. Ryll, T., et al., *Lanthanum nickelate thin films deposited by spray pyrolysis: Crystallization, microstructure and electrochemical properties.* Journal of the European Ceramic Society, 2012. **32**(8): p. 1701-1709.

91. Burriel, M., et al., *Enhanced high-temperature electronic transport properties in nanostructured epitaxial thin films of the $La_{n+1}Ni_nO3_{n+1}$ Ruddlesden-Popper series (n=1, 2, 3, ∞).* Chemistry of Materials, 2007. **19**(16): p. 4056-4062.
92. Jorgensen, J.D., et al., *Structure of the Interstitial Oxygen Defect in $La_2NiO_{4+\delta}$.* Physical Review B, 1989. **40**(4): p. 2187-2199.
93. Sayagués, M.J., et al., *Modulated Structure of $La_2NiO_{4+\delta}$ as a Mechanism of Oxygen Excess Accommodation.* Journal of Solid State Chemistry, 1996. **125**(2): p. 133-139.
94. Dragan, M.A., *Defect Chemistry, Transport Properties and Thermodynamic Stability of Acceptor Doped and Undoped Layered La_2NiO_4* 2006, PhD Thesis, RWTH Aachen.
95. Boehm, E., et al., *Oxygen diffusion and transport properties in non-stoichiometric $Ln_{2-x}NiO_{4+\delta}$ oxides* Solid State Ionics, 2005. **176**(37-38): p. 2717-2725.
96. Munnings, C.N., et al., *Oxygen transport in the $La_2Ni_{1-x}Co_xO_{4+\delta}$ system.* Solid State Ionics, 2005. **176**(23-24): p. 1895-1901.
97. Opila, E.J., et al., *Oxygen Tracer Diffusion in $La_{2-x}Sr_xCuO_{4-y}$ Single Crystals.* Journal of the American Ceramic Society, 1993. **76**(9): p. 2363-2369.
98. Minervini, L., et al., *Oxygen migration in $La_2NiO_{4+\delta}$.* Journal of Materials Chemistry, 2000. **10**(10): p. 2349-2354.
99. Yashima, M., N. Sirikanda, and T. Ishihara, *Crystal Structure, Diffusion Path, and Oxygen Permeability of a Pr_2NiO_4-Based Mixed Conductor $(Pr_{0.9}La_{0.1})_2(Ni_{0.74}Cu_{0.21}Ga_{0.05})O_{4+\delta}$.* Journal of the American Chemical Society, 2010. **132**(7): p. 2385-2392.
100. Parfitt, D., et al., *Molecular dynamics study of oxygen diffusion in $Pr_2NiO_{4+\delta}$.* Physical Chemistry Chemical Physics, 2010. **12**(25): p. 6834-6836.
101. Skinner, S., et al., *Evaluation of $La_2Ni_{1-x}Co_xO_{4\pm\delta}$ as a SOFC cathode material.* 2003: p. 552-560.
102. Kharton, V.V., et al., *Oxygen transport and electrochemical activity of La_2NiO_4-based cathode materials.* 2003: p. 561-570.
103. Sayers, R., et al., *Novel K_2NiF_4-Type Materials for Solid Oxide Fuel Cells: Compatibility with Electrolytes in the Intermediate Temperature Range.* Fuel Cells, 2008. **8**(5): p. 338-343.
104. Lou, Z., et al., *High performance $La_3Ni_2O_7$ cathode prepared by a facile sol–gel method for intermediate temperature solid oxide fuel cells.* Electrochemistry Communications, 2012. **22**(0): p. 97-100.
105. Woolley, R.J. and S.J. Skinner, *Novel $La_2NiO_{4+\delta}$ and $La_4Ni_3O_{10-\delta}$ composites for solid oxide fuel cell cathodes.* Journal of Power Sources, 2013. **243**(0): p. 790-795.

106. Litzelman, S.J., et al., *Opportunities and Challenges in Materials Development for Thin Film Solid Oxide Fuel Cells.* Fuel Cells, 2008. **8**(5): p. 294-302.
107. Pederson, L.R., P. Singh, and X.D. Zhou, *Application of vacuum deposition methods to solid oxide fuel cells.* Vacuum, 2006. **80**(10): p. 1066-1083.
108. Baumann, F.S., J. Maier, and J. Fleig, *The polarization resistance of mixed conducting SOFC cathodes: A comparative study using thin film model electrodes.* Solid State Ionics, 2008. **179**(21-26): p. 1198-1204.
109. Evans, A., et al., *Micro-solid oxide fuel cells: status, challenges, and chances.* Monatshefte für Chemie / Chemical Monthly, 2009. **140**(9): p. 975-983.
110. Beckel, D., et al., *Thin films for micro solid oxide fuel cells.* Journal of Power Sources, 2007. **173**(1): p. 325-345.
111. Dembinski, K., et al., *Crystal growth of La_2NiO_4 by the floating zone method with a CW CO_2 laser: Preliminary characterizations* Journal of Materials Science Letters, 1987. **6**(12): p. 1365-1367.
112. Lee, D., et al., *Strain Influence on the Oxygen Electrocatalysis of the (100)-Oriented Epitaxial $La_2NiO_{4+\delta}$ Thin Films at Elevated Temperatures.* The Journal of Physical Chemistry C, 2013. **117**(37): p. 18789-18795.
113. Moreno, R., et al., *Chemical Strain Kinetics Induced by Oxygen Surface Exchange in Epitaxial Films Explored by Time-Resolved X-ray Diffraction.* Chemistry of Materials, 2013. **25**(18): p. 3640-3647.
114. Yamada, A., et al., *Ruddlesden-Popper-Type Epitaxial Film as Oxygen Electrode for Solid-Oxide Fuel Cells.* Advanced Materials, 2008. **20**(21): p. 4124-4128.
115. Yamada, A., et al., *Anisotropic catalytic activity of the orientation controlled $Nd_2NiO_{4+\delta}$/YSZ hetero-epitaxial system for SOFC cathode.* Electrochemistry Communications, 2010. **12**(12): p. 1690-1693.
116. Sase, M., et al., *Enhancement of oxygen exchange at the hetero interface of $(La,Sr)CoO_3/(La,Sr)_2CoO_4$ in composite ceramics.* Solid State Ionics, 2008. **178**(35-36): p. 1843-1852.
117. Sase, M., et al., *Enhancement of Oxygen Surface Exchange at the Hetero-interface of $(La,Sr)CoO_3/(La,Sr)_2CoO_4$ with PLD-Layered Films.* Journal of the Electrochemical Society, 2008. **155**(8): p. B793-B797.
118. Crumlin, E.J., et al., *Oxygen Reduction Kinetics Enhancement on a Heterostructured Oxide Surface for Solid Oxide Fuel Cells.* The Journal of Physical Chemistry Letters, 2010: p. 3149-3155.
119. Chen, Y., et al., *Electronic Activation of Cathode Superlattices at Elevated Temperatures – Source of Markedly Accelerated Oxygen Reduction Kinetics.* Advanced Energy Materials, 2013. **3**(9): p. 1221-1229.
120. Tuller, H.L., S.J. Litzelman, and W. Jung, *Micro-ionics: next generation power*

sources. Physical Chemistry Chemical Physics, 2009. **11**(17): p. 3023-3034.

121. Nikbin, D., *Micro SOFCs: Why small is beautiful* The Fuel Cell Review, 2006. **3**: p. 21-24.
122. Shao, Z., et al., *A thermally self-sustained micro solid-oxide fuel-cell stack with high power density.* Nature, 2005. **435**(7043): p. 795-798.
123. Smith, H.M. and A.F. Turner, *Vacuum Deposited Thin Films Using a Ruby Laser.* Applied Optics, 1965. **4**(1): p. 147-148.
124. Hass, G. and J.B. Ramsey, *Vacuum Deposition of Dielectric and Semiconductor Films by a CO_2 Laser.* Applied Optics, 1969. **8**(6): p. 1115-1118.
125. Dijkkamp, D., et al., *Preparation of Y-Ba-Cu Oxide Superconductor Thin-Films Using Pulsed Laser Evaporation from High-Tc Bulk Material.* Applied Physics Letters, 1987. **51**(8): p. 619-621.
126. Eason, R., *Pulsed Laser Deposition of Thin Films: Applications-Led Growth of Functional Materials* 2007: Wiley.
127. Lowndes, D.H., et al., *Synthesis of Novel Thin-Film Materials by Pulsed Laser Deposition.* Science, 1996. **273**(5277): p. 898-903.
128. Montenegro, M.J. and T. Lippert, *Films for Electrochemical Applications*, in *Pulsed Laser Deposition of Thin Films: Applications-Led Growth of Functional Materials* R. Eason, Editor. 2007, Wiley. p. 563-584.
129. *Pulsed Laser Deposition System*. [cited 2014 02/26]; Available from: http://www2.physics.colostate.edu/groups/PattonGroup/systems/pld_desc.html.
130. Ashfold, M.N.R., et al., *Pulsed laser ablation and deposition of thin films.* Chemical Society Reviews, 2004. **33**(1): p. 23-31.
131. Hegde, M., *Epitaxial oxide thin films by pulsed laser deposition: Retrospect and prospect.* Journal of Chemical Sciences, 2001. **113**(5): p. 445-458.
132. Krebs, H.-U., et al., *Pulsed Laser Deposition (PLD) -- A Versatile Thin Film Technique*, in *Advances in Solid State Physics*, B. Kramer, Editor. 2003, Springer Berlin Heidelberg. p. 505-518.
133. Chen, L.-C., *Particulates generated by pulsed laser ablation*, in *Pulsed Laser Deposition of Thin Films*, D.B. Chrisey and G.K. Hubler, Editors. 1994, Wiley. p. 167-198.
134. Chrisey, D.B. and G.K. Hubler, eds. *Pulsed Laser Deposition of Thin Films*. 1994, Wiley.
135. Metev, S., *Process Characteristics and Film Properties in Pulsed Laser Deposition*, in *Pulsed Laser Deposition of Thin Films*, D.B. Chrisey and G.K. Hubler, Editors. 1994, Wiley. p. 255-264.
136. Horwitz, J.S. and J.A. Sprague, *Film Nucleation and Film Growth in Pulsed Laser Deposition of Ceramics*, in *Pulsed Laser Deposition of Thin Films*, D.B. Chrisey

and G.K. Hubler, Editors. 1994, Wiley. p. 229-254.

137. Foltyn, S.R., *Surface modification of materials by cumulative laser irradiation*, in *Pulsed Laser Deposition of Thin Films*, D.B. Chrisey and G.K. Hubler, Editors. 1994, Wiley. p. 89-113.
138. Greer, J., *Large-Area Commercial Pulsed Laser Deposition*, in *Pulsed Laser Deposition of Thin Films: Applications-Led Growth of Functional Materials* R. Eason, Editor. 2007, Wiley. p. 191-213.
139. Venables, J.A., *Introdution to Surface and Thin Film Processes*. 4 ed. 2000: Cambridge University Press. 144-183.
140. Oura, K., et al., *Surface Science: An Introduction*. 2003: Springer. 357-387.
141. Pechini, M., *Method of Preparing Lead and Alkaline Earth Titanates and Niobates and Coating Method Using the same to form A Capacitor*, 1967: US.
142. Sakka, S., *Handbook of Sol-Gel Science and Technology: Processing, Characterization, and Applications*. 2005: Springer.
143. Brinker, C.J. and G.W. Scherer, *Sol-Gel Science: The Physics and Chemistry of Sol-Gel Processing*, 1990, Academic Press.
144. Hill, S.J., ed. *Inductively Coupled Plasma Spectrometry and its Applications*. 2nd ed. 2007, Wiley-Blackwell.
145. Nave, C.R. *Bragg's Law for X-ray Diffraction*. [cited 2014 02/26]; Available from: http://hyperphysics.phy-astr.gsu.edu/hbase/quantum/bragg.html.
146. Speller, S. *Texture XRD, the diagram was obtained from a ppt slide*. [cited 2014 02/26].
147. Goldstein, J., et al., *Scanning Electron Microscopy and X-ray Microanalysis*. 3 ed. 2003: Springer.
148. Brandon, D. and W.D. Kaplan, *Microstructural Characterization of Materials*. 2 ed. 2008: Wiley. 261-332.
149. Goldstein, J., et al., *Scanning Electron Microscopy and X-ray Microanalysis*. 3 ed. 2003: Springer. 61-98.
150. Eaton, P. and P. West, *Atomic Force Microscopy*. 2010, Oxford University Press. p. 1-8.
151. Eaton, P. and P. West, *Atomic Force Microscopy*. 2010, Oxford University Press. p. 121-138.
152. Horcas, I., et al., *WSXM: A software for scanning probe microscopy and a tool for nanotechnology.* Review of Scientific Instruments, 2007. **78**(1): p. 013705-8.
153. *AFM setup*. [cited 2014 02/16]; Available from: http://www.ammrf.org.au/myscope/spm/background/.
154. Brydson, R., *Aberration-Corrected Analytical Electron Microscopy*. 2011: Wiley.
155. Pennycook, S.J., et al., *Aberration-corrected scanning transmission electron*

microscopy: from atomic imaging and analysis to solving energy problems. Philosophical Transactions of the Royal Society A: Mathematical, Physical and Engineering Sciences, 2009. **367**(1903): p. 3709-3733.

156. Pennycook, S.J., et al., *Transmission Electron Microscopy: Overview and Challenges.* AIP Conference Proceedings, 2003. **683**(1): p. 627-633.
157. Williams, D.B., *Transmission Electron Microscopy: A Textbook for Materials Science*. 2 ed. 2011: Springer.
158. van der Pauw, L.J., *A method of measuring the resistivity and Hall coefficient on lamellae of arbitrary shape.* Philips Technical Review, 1958. **20**: p. 220.
159. van der Pauw, L.J., *A method of measuring specific resistivity and Hall effect of discs of arbitrary shape.* Philips Research Reports, 1958. **13**: p. 1.
160. Kilner, J.A., B.C.H. Steele, and L. Ilkov, *Oxygen self-diffusion studies using negative-ion secondary ion mass spectrometry (SIMS).* Solid State Ionics, 1984. **12**: p. 89-97.
161. Chater, R.J., et al., *Development of a novel SIMS technique for oxygen self-diffusion and surface exchange coefficient measurements in oxides of high diffusivity.* Solid State Ionics, 1992. **53-56**(Part 2): p. 859-867.
162. Kilner, J., S. Skinner, and H. Brongersma, *The isotope exchange depth profiling (IEDP) technique using SIMS and LEIS.* Journal of Solid State Electrochemistry, 2011. **15**(5): p. 861-876.
163. Fischer, E. and J.L. Hertz, *Measurability of the diffusion and surface exchange coefficients using isotope exchange with thin film and traditional samples.* Solid State Ionics, 2012. **218**(0): p. 18-24.
164. Stephan, T., *TOF-SIMS in cosmochemistry.* Planetary and Space Science, 2001. **49**(9): p. 859-906.
165. Vickerman, J.C., *Molecular Surface Mass Spectrometry by SIMS*, in *Surface Analysis–The Principal Techniques*, J.C. Vickerman, Editor. 2009, Wiley. p. 113-205.
166. Crank, J., *The Mathematics of Diffusion*. 2 ed. 1975: Oxford University Press.
167. De Souza, R.A. and M. Martin, *Probing Diffusion Kinetics with Secondary Ion Mass Spectrometry.* MRS Bulletin, 2009. **34**(12): p. 907-914.
168. De Souza, R.A. and M. Martin, *Secondary ion mass spectrometry (SIMS) – a powerful tool for studying mass transport over various length scales.* physica status solidi (c), 2007. **4**(6): p. 1785-1801.
169. Brongersma, H.H., et al., *Surface composition analysis by low-energy ion scattering.* Surface Science Reports, 2007. **62**(3): p. 63-109.
170. Burriel, M., et al., *Absence of Ni on the outer surface of Sr doped La_2NiO_4 single crystals.* Energy & Environmental Science, 2014. **7**(1): p. 311.

171. Druce, J., T. Ishihara, and J. Kilner, *Surface composition of perovskite-type materials studied by Low Energy Ion Scattering (LEIS).* Solid State Ionics, 2014. **262**: p. 893-896.
172. SAMAVAT, F., B.V. KING, and D.J. O'CONNOR, *LOW ENERGY ION SCATTERING.* Surface Review and Letters, 2007. **14**(01): p. 31-41.
173. Leach, R., et al., *Guide to the Measurement of Smooth Surface Topography using Coherence Ccanning Interferometry*. 2008: National Physical Laboratory (NPL).
174. Woolley, R.J., *Ruddlesden-Popper phases as solid oxide fuel cell cathodes: electrochemical performance and in situ characterisation*, in *Department of Materials*, 2013, PhD thesis, Imperial College London.
175. Fähler, S., M. Störmer, and H.U. Krebs, *Origin and avoidance of droplets during laser ablation of metals.* Applied Surface Science, 1997. **109–110**(0): p. 433-436.
176. IJsselsteijn, R.P.J., et al., *Droplets and outgrowths on high-Tc laser ablated thin films*, in *High Tc Superconductor Thin Films*, L. Correra, Editor. 1992, Elsevier: Strassburg. p. 251-256.
177. Scarfone, C., et al., *Characterization of $BaTiO_3$ Thin Films Deposited by Pulsed-Laser Ablation.* MRS Online Proceedings Library, 1990. **201**: p. 183-188.
178. Dam, B., et al., *Stoichiometric transfer of complex oxides by pulsed laser deposition*, in *Laser Ablation*, E. Fogarassy, et al., Editors. 1996, Elsevier: Oxford. p. 679-684.
179. Dam, B., et al., *Non-Stoichiometric Transfer of Complex Oxides by Pulsed Laser Deposition at Low Fluences.* MRS Online Proceedings Library, 1995. **397**: p. 175-180.
180. Birkholz, M., P.F. Fewster, and C. Genzel, *Thin Film Analysis by X-Ray Scattering*. 2006: Wiley. p.143.
181. Wicklein, S., et al., *Pulsed laser ablation of complex oxides: The role of congruent ablation and preferential scattering for the film stoichiometry.* Applied Physics Letters, 2012. **101**(13): p. 131601-5.
182. Huijbregtse, J.M., et al., *High-quality off-stoichiometric $YBa_2Cu_3O_{7-\delta}$ films produced by diffusion-assisted preferential laser ablation* Journal of Applied Physics, 1999. **86**(11): p. 6528-6537.
183. Ohnishi, T., et al., *Improved stoichiometry and misfit control in perovskite thin film formation at a critical fluence by pulsed laser deposition.* Applied Physics Letters, 2005. **87**(24): p. 241919-3.
184. Kan, D. and Y. Shimakawa, *Controlled cation stoichiometry in pulsed laser deposition-grown $BaTiO_3$ epitaxial thin films with laser fluence* Applied Physics Letters, 2011. **99**(8): p. 081907-3.
185. Orgiani, P., et al., *Physical properties of $La_{0.7}Ba_{0.3}MnO_{3-\delta}$ complex oxide thin films*

grown by pulsed laser deposition technique. Applied Physics Letters, 2010. **96**(3): p. 032501-3.

186. Misra, D.S. and S.B. Palmer, *Laser ablated thin films of $Y_1Ba_2Cu_30_{7-\delta}$: the nature and origin of the particulates.* Physica C: Superconductivity, 1991. **176**(1–3): p. 43-48.
187. Willmott, P.R. and J.R. Huber, *Pulsed laser vaporization and deposition.* Reviews of Modern Physics, 2000. **72**(1): p. 315.
188. Arnold, C.B. and M.J. Aziz, *Stoichiometry issues in pulsed-laser deposition of alloys grown from multicomponent targets.* Applied Physics A, 1999. **69**(1): p. S23-S27.
189. Aguadero, A., et al., *In situ high temperature neutron powder diffraction study of oxygen-rich $La_2NiO_{4+\delta}$ in air: correlation with the electrical behaviour* Journal of Materials Chemistry, 2006. **16**(33): p. 3402-3408.
190. Ohring, M., *Materials Science of Thin Films*. 2nd ed. 2002: Academic Press. p. 423-424.
191. Kiselev, E.A., et al., *Phase equilibria and crystal structures of phases in the La-Fe-Ni-O system at 1370 K in air.* Inorganic Materials, 2007. **43**(2): p. 167-175.
192. Yang, L., et al., *Orientation control of $LaNiO_3$ thin films by RF magnetron sputtering with different oxygen partial pressure.* Journal of Crystal Growth, 2009. **311**(17): p. 4241-4246.
193. Iwazaki, Y., et al., *Artificial $SrTiO_3$/SrO superlattices by pulsed laser deposition.* Japanese Journal of Applied Physics Part 2-Letters, 1999. **38**(12A): p. L1443-L1446.
194. Ohring, M., *Materials Science of Thin Films*. 2nd ed. 2002: Academic Press. Ch.7.
195. Ferguson, J.D., et al., *Measurements of Surface Diffusivity and Coarsening during Pulsed Laser Deposition.* Physical Review Letters, 2009. **103**(25): p. 256103-1.
196. Read, M.S.D., et al., *Surface structures and defect properties of pure and doped La_2NiO_4.* Journal of Materials Chemistry, 2001. **11**(10): p. 2597-2602.
197. Tyunina, M. and S. Leppavuori, *Effects of laser fluence, size, and shape of the laser focal spot in pulsed laser deposition using a multielemental target.* Journal of Applied Physics, 2000. **87**(11): p. 8132-8142.
198. Singh, R.K. and J. Narayan, *Pulsed-laser evaporation technique for deposition of thin films: Physics and theoretical model.* Physical Review B, 1990. **41**(13): p. 8843-8859.
199. Balakrishnan, G., et al., *Epitaxial growth of cerium oxide thin films by pulsed laser deposition.* Thin Solid Films, 2013. **546**: p. 467-471.
200. Ohring, M., *Materials Science of Thin Films*. 2nd ed. 2002: Academic Press. p. 360.

201. Chang, C.C., et al., *Origin of surface roughness for c-axis oriented Y-Ba-Cu-O superconducting films.* Applied Physics Letters, 1990. **57**(17): p. 1814-1816.
202. Rice, D.E. and D.J. Buttrey, *An X-Ray Diffraction Study of the Oxygen Content Phase Diagram of $La_2NiO_{4+\delta}$.* Journal of Solid State Chemistry, 1993. **105**(1): p. 197-210.
203. Bassat, J.M. and et al., *Progressive change with T from hopping to random phase propagation in $La_{2-x}NiO_{4-\delta}$ ($\delta \geqq 0$).* Journal of Physics: Condensed Matter, 1994. **6**(40): p. 8285.
204. Kharton, V.V., et al., *Transport properties and stability of Ni-containing mixed conductors with perovskite- and K_2NiF_4-type structure.* Journal of Solid State Chemistry, 2004. **177**(1): p. 26-37.
205. Guan, L., et al., *Role of pulse repetition rate in film growth of pulsed laser deposition.* Nuclear Instruments and Methods in Physics Research Section B: Beam Interactions with Materials and Atoms, 2008. **266**(1): p. 57-62.
206. Eaton, P. and P. West, *Measuring AFM images*, in *Atomic Force Microscopy*. 2010, OUP Oxford. p. 91-92.
207. Eaton, P. and P. West, *AFM image artefacts*, in *Atomic Force Microscopy*. 2010, OUP Oxford. p. 123-124.
208. Ling, C.D., et al., *Neutron Diffraction Study of $La_3Ni_2O_7$: Structural Relationships Among n=1, 2, and 3 Phases $La_{n+1}Ni_nO_{3n+1}$.* Journal of Solid State Chemistry, 2000. **152**(2): p. 517-525.
209. Poltavets, V.V., et al., *The oxygen deficient Ruddlesden-Popper $La_3Ni_2O_{7-\delta}$ (δ=0.65) phase: Structure and properties.* Materials Research Bulletin, 2006. **41**(5): p. 955-960.
210. Pietsch, U., V. Holy, and T. Baumbach, *Determination of Layer Thicknesses of Single Layers and Multilayers*, in *High-Resolution X-Ray Scattering: From Thin Films to Lateral Nanostructures*. 2004, Springer. p. 143-178.
211. Pietsch, U., V. Holy, and T. Baumbach, *Lattice Parameters and Strains in Epitaxial Layers and Multilayers*, in *High-Resolution X-Ray Scattering: From Thin Films to Lateral Nanostructures*. 2004, Springer. p. 180-203.
212. Fewster, P.F., *Reciprocal space mapping.* Critical Reviews in Solid State and Materials Sciences, 1997. **22**(2): p. 69-110.
213. Detemple, E., et al., *Ruddlesden-Popper faults in $LaNiO_3/LaAlO_3$ superlattices* Journal of Applied Physics, 2012. **112**(1): p. 013509-5.
214. Houben, L., *Aberration-corrected HRTEM of defects in strained La_2CuO_4 thin films grown on $SrTiO_3$.* Journal of Materials Science, 2006. **41**(14): p. 4413-4419.
215. Zurbuchen, M.A., et al., *Morphology, structure, and nucleation of out-of-phase boundaries (OPBs) in epitaxial films of layered oxides.* Journal of Materials

Research, 2007. **22**(06): p. 1439-1471.

216. Galy, J., *(101) and (-101) Extended defects accounting for the non-stoichiometry of high-T_c superconducting $M_{2\pm\delta}CuO_{4\pm\delta}$ phases (M_2 = $La_{2-x}Sr_x$).* Acta Crystallographica Section B, 1992. **48**(6): p. 777-781.
217. Suzuki, T. and M. Fujimoto, *First-principles structural stability study of nonstoichiometry-related planar defects in $SrTiO_3$ and $BaTiO_3$.* Journal of Applied Physics, 2001. **89**(10): p. 5622-5629.
218. Tian, W., et al., *Transmission electron microscopy study of n= 1–5 $Sr_{n+1}Ti_nO_{3n+1}$ epitaxial thin films.* Journal of Materials Research, 2001. **16**(07): p. 2013-2026.
219. Matvejeff, M., et al., *Chemical stability and transport properties of ultrathin $La_{1.2}Sr_{1.8}Mn_2O_7$ Ruddlesden-Popper films.* Applied Physics Letters, 2009. **95**(15): p. 152110-3.
220. Matvejeff, M., T. Chikyow, and M. Lippmaa, *Interface growth of $La_{1.2}Sr_{1.8}Mn_{1.7}Ru_{0.3}O_7$ Ruddlesden–Popper films on $SrTiO_3$.* Journal of Crystal Growth, 2009. **311**(4): p. 1201-1205.
221. Iwazaki, Y., et al., *Thermal Stability of Artificial $SrTiO_3$/SrO Superlattice Epitaxially Grown on $SrTiO_3$ Single Crystal.* JAPANESE JOURNAL OF APPLIED PHYSICS PART 2 LETTERS, 2000. **39**(4A): p. 303-305.
222. Faucheux, V., S. Pignard, and M. Audier, *Structural study of lanthanum nickelate thin films deposited on different single crystal substrates.* Journal of Solid State Chemistry, 2004. **177**(12): p. 4616-4625.
223. Shibuya, K., et al., *Sr_2TiO_4 layered perovskite thin films grown by pulsed laser deposition.* Applied Physics Letters, 2008. **92**(24): p. 241918-3.
224. Wang, P., et al., *Aberration corrected STEM of defects in epitaxial n=4 Ruddlesden-Popper phase $Ca_{n+1}Mn_nO_{3n+1}$.* Journal of Physics: Conference Series, 2008. **126**(1): p. 012050.
225. Sasaki, H., et al., *Structural studies on the phase transition of $La_3Ni_2O_{6.92}$ at about 550 K.* Journal of the Physical Society of Japan, 1997. **66**(6): p. 1693-1697.
226. Fukamachi, T., et al., *^{139}La NMR studies of layered perovskite systems $La_3Ni_2O_{7-\delta}$ and $La_4Ni_3O_{10}$.* Journal of Physics and Chemistry of Solids, 2001. **62**(1–2): p. 195-198.
227. Choi, S., et al., *High Performance SOFC Cathode Prepared by Infiltration of $La_{n+1}Ni_nO_{3n+1}$ (n = 1, 2, and 3) in Porous YSZ.* Journal of the Electrochemical Society, 2011. **158**(8): p. B995-B999.
228. Tsipis, E.V., et al., *Oxygen non-stoichiometry of $Ln_4Ni_{2.7}Fe_{0.3}O_{10-\delta}$ (Ln=La, Pr).* Journal of Solid State Chemistry, 2007. **180**(6): p. 1902-1910.
229. Tilley, R.J.D., *Nonstoichiometry and Intrinsic Eletronic Conductivity*, in *Defects in Solids*. 2008, Wiley. p. 297-350.

230. Barsoum, M.W., *Diffusion and Electronic Conductivity*, in *Fundamentals of Ceramics*. 2003, Taylor & Francis. p. 175-241.
231. Bach, P.L., et al., *Strain-induced enhancement of the thermoelectric power in thin films of hole-doped $La_2NiO_{4+\delta}$.* APL Materials, 2013. **1**(2): p. 021101-1.
232. Shinomori, S., M. Kawasaki, and Y. Tokura, *Orientation-controlled epitaxy and anisotropic properties of $La_{2-x}Sr_xNiO_4$ with $0.5 \leq x \leq 1.5$ covering the insulator-metal transition.* Applied Physics Letters, 2002. **80**(4): p. 574-576.
233. Zapata, J., et al., *Planar defects in layered-structure mixed ionic-electronic $GdBaCo_2O_{5.5}$ and La_2NiO_4 epitaxial films and their role in charge transport. Poster presented at E-MRS Spring Meeting*, 2011, May 9-13, Nice, France.
234. Burriel, M., et al., *Influence of the Microstructure on the High-Temperature Transport Properties of $GdBaCo_2O_{5.5+\delta}$ Epitaxial Films.* Chemistry of Materials, 2010. **22**(19): p. 5512-5520.
235. Takamura, Y., et al., *Structural, magnetic, and electronic properties of (110)-oriented epitaxial thin films of the bilayer manganite $La_{1.2}Sr_{1.8}Mn_2O_7$.* Applied Physics Letters, 2005. **87**(14): p. 142508-3.
236. Takamura, Y., et al., *Thickness-dependent properties of (110)-oriented $La_{1.2}Sr_{1.8}Mn_2O_7$ thin films* Journal of Applied Physics, 2006. **99**(8): p. 08S902-3.
237. Simrick, N.J., A. Atkinson, and J. Kilner. *Annealed Thin-Film Silver Cathodes*. in *Proceedings of the 8th European SOFC Forum*. 2008. Lucerne, Switzerland.
238. Barnett, S.A., *A new solid oxide fuel cell design based on thin film electrolytes.* Energy, 1990. **15**(1): p. 1-9.
239. Sahiner, A., et al., *Electronic structure anisotropy and d-configuration in Ni-based materials.* Physical Review B, 1996. **53**(15): p. 9745-9752.
240. Greenblatt, M. and Z. Zhang, *Synthesis, Structure and Properties of Ruddlesden-Popper Nickelates, $Ln_{n+1}Ni_nO_{3n+1}$.* Abstracts of Papers of the American Chemical Society, 1994. **208**: p. 585.
241. Sreedhar, K., et al., *Low-Temperature Electronic Properties of the $La_{n+1}Ni_nO_{3n+1}$ ($n = 2, 3,$ and ∞) System: Evidence for a Crossover from Fluctuating-Valence to Fermi-Liquid-like Behavior* Journal of Solid State Chemistry, 1994. **110**(2): p. 208-215.
242. Wu, G., J.J. Neumeier, and M.F. Hundley, *Magnetic susceptibility, heat capacity, and pressure dependence of the electrical resistivity of $La_3Ni_2O_7$ and $La_4Ni_3O_{10}$.* Physical Review B, 2001. **63**(24): p. 245120.
243. Tarancón, A., *Strategies for Lowering Solid Oxide Fuel Cells Operating Temperature.* Energies, 2009. **2**(4): p. 1130-1150.
244. Chroneos, A., et al., *Oxygen diffusion in solid oxide fuel cell cathode and electrolyte materials: mechanistic insights from atomistic simulations.* Energy &

Environmental Science, 2011. **4**(8): p. 2774-2789.

245. Chroneos, A., et al., *Oxygen transport in perovskite and related oxides: A brief review.* Journal of Alloys and Compounds, 2010. **494**(1-2): p. 190-195.
246. Ziegler, J.F., M.D. Ziegler, and J.P. Biersack, *SRIM – The stopping and range of ions in matter (2010).* Nuclear Instruments and Methods in Physics Research Section B: Beam Interactions with Materials and Atoms, 2010. **268**(11–12): p. 1818-1823.
247. de Ridder, M., R.G. van Welzenis, and H.H. Brongersma, *Surface cleaning and characterization of yttria-stabilized zirconia.* Surface and Interface Analysis, 2002. **33**(4): p. 309-317.
248. Shin, H.H. and S. McIntosh, *On the H_2/D_2 isotopic exchange rate of proton conducting barium cerates and zirconates.* Journal of Materials Chemistry A, 2013. **1**(26): p. 7639-7647.
249. Gauquelin, N., et al., *Long-term structural surface modifications of mixed conducting $La_2NiO_{4+\delta}$ at high temperatures.* Monatshefte Fur Chemie, 2009. **140**(9): p. 1095-1102.
250. Fullarton, I.C., et al., *Study of oxygen ion transport in acceptor doped samarium cobalt oxide.* Ionics, 1995. **1**(1): p. 51-58.
251. Suntivich, J., et al., *Design principles for oxygen-reduction activity on perovskite oxide catalysts for fuel cells and metal–air batteries.* Nat Chem, 2011. **3**(7): p. 546-550.

List of Publications

Journal Publications from this Thesis

1. Wu, K.-T., Y.-A. Soh, and S.J. Skinner, "*Epitaxial Growth of Mixed Conducting Layered Ruddlesden-Popper $La_{n+1}Ni_nO_{3n+1}$ (n = 1, 2 and 3) Phases by Pulsed Laser Deposition*", Materials Research Bulletin, 2013. **48**(10): p. 3783-3789.
2. Aguadero, A., Fawcett, L., Taub, S., Woolley, R., Wu, K.-T., Xu, N., Kilner, J., and Skinner, S., "*Materials development for intermediate-temperature solid oxide electrochemical devices*", Journal of Materials Science, 2012. **47**(9): p. 3925-3948.
3. Wu, K.-T., Burriel, M., Téllez, H., Yang, F., McComb, D. and Skinner, S. J., "*Oxygen Diffusion and Surface Properties of Layered Ruddlesden-Popper $La_{n+1}Ni_nO_{3n+1}$ (n = 2 and 3) Epitaxial Films grown by Pulsed Laser Deposition*", in preparation
4. Wu, K.-T., Cavallaro, A., Yang, F., McComb, D. and Skinner, S. J., "*Structural, Electrical and Stability Characterisation of Layered Ruddlesden-Popper $La_3Ni_2O_{7-\delta}$ and $La_4Ni_3O_{10-\delta}$ Epitaxial Films grown by Pulsed Laser Deposition*", in preparation

Conference Publications from this Thesis

1. **Oral Presentation:** Wu, K.-T. and Skinner, S. J., "*Growth and Total Conductivity of Layered Ruddlesden-Popper* $La_{n+1}Ni_nO_{3n+1}$ (n = 1, 2 and 3) *Epitaxial Thin-Films*", Symposium C: Solid State Ionics, E-MRS Spring Meeting, Strasbourg, France, 14^{th}-18^{th} May 2012
2. **Oral Presentation:** Wu, K.-T., Soh, Y.-A. and Skinner, S. J., "*Growth of Layered Ruddlesden-Popper $La_{n+1}Ni_nO_{3n+1}$ (n = 1, 2 and 3) Epitaxial Films by Pulsed Laser Deposition (PLD)*", RSC Solid State Chemistry Group Christmas Meeting, Liverpool, UK, 19^{th}-20^{th} December 2011